ELECTRONIC STRUCTURE, INTERMOLECULAR INTERACTIONS AND ELECTRON EMISSION DYNAMICS VIA ANION PHOTOELECTRON IMAGING

by

Emily Rose Grumbling

A Dissertation Submitted to the Faculty of the

DEPARTMENT OF CHEMISTRY AND BIOCHEMISTRY

In Partial Fulfillment of the Requirements

For the Degree of

DOCTOR OF PHILOSOPHY

WITH A MAJOR IN CHEMISTRY

In the College of Science

THE UNIVERSITY OF ARIZONA

2010

THE UNIVERSITY OF ARIZONA

GRADUATE COLLEGE

As members of the Dissertation Committee, we certify that we have read the dissertation prepared by Emily Rose Grumbling
entitled Electronic Structure, Intermolecular Interactions and Electron Emission Dynamics via Anion Photoelectron Imaging
and recommend that it be accepted as fulfilling the dissertation requirement for the Degree of Doctor of Philosophy.

_____ Date: 16 November 2010
Andrei Sanov

_____ Date: 16 November 2010
Oliver L. A. Monti

_____ Date: 16 November 2010
W. Ron Salzman

_____ Date: 16 November 2010
Richard S. Glass

Final approval and acceptance of this dissertation is contingent upon the candidate's submission of the final copies of the dissertation to the Graduate College.
I hereby certify that I have read this dissertation prepared under my direction and recommend that it be accepted as fulfilling the dissertation requirement.

_____ Date: 16 November 2010
Dissertation Director: Andrei Sanov

STATEMENT BY AUTHOR

This dissertation has been submitted in partial fulfillment of requirements for an advanced degree at The University of Arizona and is deposited in the University Library to be made available to borrowers under rules of the Library.

Brief quotations from this dissertation are allowable without special permission, provided that accurate acknowledgment of source is made. Requests for permission for extended quotation from or reproduction of this manuscript in whole or in part may be granted by the head of the major department or the Dean of the Graduate College when in his or her judgment the proposed use of the material is in the interests of scholarship. In all other instances, however, permission must be obtained from the copyright holder.

SIGNED: _____

Emily Rose Grumbling

ACKNOWLEDGEMENTS

I am greatly indebted to a number of individuals and groups for their role in my education and/or contributions to the work presented in this dissertation; in the following I attempt to name and thank them all.

Thanks to Ed Autz and Lee Macomber of the Chemistry machine shop, and Mike Read and Marcus Perry of the electronics shop for their fabulous support. Any time I had a broken part or a new idea, they dropped everything to help, by fixing the problem or suggesting a certain approach; always willing to teach and always without complaint.

Thanks to Dr. Ian Jones for his enthusiasm in synthesizing benzyl azide and *p*-hydroxy phenylpentazole for my polynitrogen experiments, and to Professors Henry H. Hall and Eugene Mash for generously allowing these syntheses to occur in their labs. I must also acknowledge Dr. Arpad Somagyi for his interest in my proposed pentazole experiment. Thanks to Professor Jason Jones in the Department of Optical Sciences for his enlightening discussions on optical interferometry and for his willingness to share equipment.

Thanks to Mike Blumenfeld, Aaron Vannucci, Adam Daly and Jason Porter for their comaraderie throughout the PhD process.

I must particularly thank and acknowledge my group-mates over the years. Thanks to Lori Culberson for working with me on the cross-polarized pump-probe I_2^- experiment. Thanks to her and Dmitry Khuseynov for being such positive new presences in the lab, and for our exciting scientific discussions. Thanks to Kostya Pichugin for collaboration on the core-switching work and the years we put in together on many other experiments. I'm very grateful to Luis Velarde for his kind guidance in my early days of graduate school, and for initiating collaboration on the photoelectron-solvent scattering project. Thanks also to Terefe Habteyes, Dominique Villela, F. Ahu Akin and S. Eric Surber for all that I learned from them. Special thanks go to Richard Mabbs for welcoming my collaboration on several pedagogical manuscripts. Our discussions helped shape my understanding of photoelectron imaging and quantum mechanics in general; I have truly valued the experience.

Thanks to my research advisor, Andrei Sanov, a great teacher whose eloquence and appreciation for the beauty pervading science have inspired me. I thank him for accepting me into his group, for his patience and for the opportunities he opened up for me in the department and beyond.

Thanks to everyone who I worked with while a TA in the department, particularly Dr. Anne Padias, Dr. Lisa Dollinger, Dr. Deirdre Belle-Oudry, and Professors Scott Saavedra, Oliver Monti and Andrei Sanov. Teaching and working on course development was an incredibly enjoyable and educational experience for me. Thanks for making it so!

Endless thanks to graduate program coordinator Lori Boyd for her tireless efforts on behalf every graduate student in the department, and her knowledge and vigilance regarding form submission deadlines!

Thanks to Professors Hanna Reisler, Anna Krylov and Richard Zare for their interest in me as a scientist. Our interactions, however brief, have provided valuable mentoring.

Thanks to my dissertation committee, Professors Andrei Sanov, Richard Glass, Oliver Monti and W. Ron Salzman for their helpful feedback.

Thanks to all of my teachers. I must particularly acknowledge my undergraduate chemistry professors, Robert Olsen, Hilton Weiss, Craig Anderson and Simeen Sattar, for their commitment to my undergraduate education in Chemistry, and for facilitating my broader education.

I must also acknowledge the C. S. Marvel Foundation, the Arizona Imaging Fellowship Program, the University of Arizona and the National Science Foundation for supporting and funding various aspects of my graduate education.

Thanks to all of my friends in the Tucson community!

Thanks to my family of artists and writers (Amy, Megan, Audrey & Owen) for their wisdom, love and encouragement.

Infinite thanks to Joseph Baker for his patience, love and support.

My deepest gratitude goes out to everyone who helped me learn and grow as a scientist and as a human being during my time here.

Dedicated, with thanks,

to my teachers and to my family.

TABLE OF CONTENTS

TABLE OF CONTENTS - continued

TABLE OF CONTENTS – continued

TABLE OF CONTENTS – continued

LIST OF FIGURES

LIST OF FIGURES – continued

LIST OF FIGURES - continued

LIST OF FIGURES - continued

LIST OF FIGURES - continued

LIST OF FIGURES – continued

LIST OF FIGURES – continued

LIST OF FIGURES – continued

LIST OF FIGURES – continued

LIST OF TABLES

ABSTRACT

This dissertation explores the use of anion photoelectron imaging to interrogate electronic dynamics in small chemical systems with an emphasis on photoelectron angular distributions. Experimental ion generation, mass selection, laser photodetachment and photoelectron imaging were performed in a negative-ion photoelectron imaging spectrometer described in detail. Results for photodetachment from the simplest anion, H^-, are used to illustrate fundamental principles of quantum mechanics and provide basic insight into the physics behind photoelectron imaging from a pedagogical perspective. This perspective is expanded by introducing imaging results for additional, representative atomic and small molecular anions (O^-, NH_2^- and N_3^-) obtained at multiple photon energies to address the energy-dependence of photoelectron angular distributions both conceptually and semi-quantitatively in terms of interfering partial photoelectron waves. The effect of solvation on several of these species (H^-, O^-, and NH_2^-) is addressed in photoelectron imaging of several series of cluster anions. The 532 and 355 nm energy spectra for $H^-(NH_3)_n$ and $NH_2^-(NH_3)_n$ (n = 0-5) reveal that these species are accurately described as the core anion solute stabilized electrostatically by n loosely coordinated NH_3 molecules. The photoelectron angular distributions for solvated H^- deviate strongly from those predicted for unsolvated H^- as the electron kinetic energy approaches zero, indicating a shift in the partial-wave balance consistent with both solvation-induced perturbation (and symmetry-breaking) of the H^- parent orbital and photoelectron-solvent scattering. The photoelectron energy spectra obtained for the

cluster series $[O(N_2O)_n]^-$ and $[NO(N_2O)_n]^-$ indicate the presence of multiple structural isomers of the anion cores, the former displaying sharp core-switching at $n = 4$, the latter isomer coexistence over the entire range studied. The photoelectron angular distributions for detachment from the $O^-(N_2O)_n$ and $NO^-(N_2O)_n$ isomers deviate strongly from those expected for bare O^- and NO^-, respectively, in the region of an anionic shape resonance of N_2O, suggesting resonant photoelectron-solvent scattering. Partial-wave models for two-centered photoelectron interference in photodetachment from dissociating I_2^- is presented and discussed in the context of previous results.[10] New time-resolved photoelectron imaging results for I_2^-, for both parallel and perpendicular pump and probe beam polarizations, are presented and briefly discussed. Finally, new ideas and directions are proposed.

CHAPTER 1

GENERAL INTRODUCTION

1.1 Introduction

While molecular structure and reactivity are often described in terms of the geometrical coordination of atoms and their rearrangements, it is the interaction between atomic and molecular orbitals that determines these configurations. A highly developed understanding of electronic interactions is thus vital to a fundamental understanding of chemistry.

This fundamental perspective begins with the recognition of the quantum nature of electrons as having both particle- and wave-like properties. Electrons do not orbit nuclei with defined trajectories but are delocalized in orbitals, the one-electron wave function solutions to the time-independent Schrodinger equation. While the role of atomic and molecular orbitals is well-established throughout chemistry, the only chemical system for which the Schrodinger equation has been solved exactly is the hydrogen atom. The lack of analytical wave function solutions for an arbitrary chemical Hamiltonian necessitates the use of high-level theoretical approximations and sophisticated experimental approaches to elucidate the nature of electronic structure in chemical systems.

One of the most powerful experimental probes of electronic structure is photoelectron spectroscopy. Because the energy levels of electrons in molecules are quantized, the use of a monochromatic light source allows for determination of distinct

binding energies of electrons in a chemical system. For gas-phase systems, distinct peaks in the photoelectron spectrum correspond to removal of electrons from specific orbitals, with energy spacings equated to the difference in orbital energies of the system probed, within the framework of Koopman's theorem. The band structures, intensities and positions all reveal insights into the nature of the system's bonding and geometry.

Though it has historically been less emphasized, the spatial distribution of photoelectrons generated using a polarized or directional radiation source also reveals electronic structure information. In particular, the photoelectron angular distribution with respect to the electric field of the radiation is related through symmetry to the parent orbital from which the electron was detached. Angle-resolved photoelectron spectroscopy may be performed by rotating the polarization of the light source with respect to the photoelectron detector through a series of discrete angles, collecting signal at each step. Alternately, photoelectron imaging allows for measurement of a two-dimensional projection of the entire photoelectron distribution with 100% collection efficiency in a single experiment, and extraction of both the photoelectron energy spectrum and angular distribution.

1.2 Photoelectron imaging

Gas-phase charged particle imaging was first applied in the benchmark experiment by Chandler and Houston,[11] in which they detected state-specific gas-phase photofragment distributions. The fragments were ionized and then projected onto a two-dimensional position-sensitive detector using electric fields, revealing their spatial

distribution. Photoelectron imaging was first performed in the multiphoton ionization study of xenon atoms by Helm et al. in 1992,[12] and thus introduced as a detection scheme for photoelectron spectroscopy.

In 1997, Eppink and Parker refined the electron and ion imaging techniques with the introduction of velocity-mapping.[13,14] This approach has the advantage of minimizing image blurring due to the longitudinal component of the electron expansion and the initial spatial distribution of the gas-phase target by 1) focusing the electron cloud onto the plane of the detector and 2) mapping all components of the distribution with the same velocity in the plane of the detector onto the same point on the detector, regardless of their initial position within the imaging field. The introduction of velocity-mapping seeded a huge growth in the area of photoelectron imaging, particularly of gas-phase negative ions.[15]

1.3 Why negative ions?

The huge advances in negative ion spectroscopy pioneered by Lineberger laid the ground work for anion photoelectron imaging.[16] This technique is ideal for the study of electronic structure and dynamics for a variety of reasons.

As charged particles, anions may easily be mass-selected using electric fields, allowing for the exclusive examination of species of a desired mass-to-charge ratio. Anions also serve as a means for examining the structure of their neutral counterparts; removal of an electron from multiple orbitals of a negative ion corresponds to the generation of multiple electronic states of the neutral, including states typically forbidden

in optical absorption spectroscopy on the neutral species themselves. The energy spectra reveal the relative energy levels of these electronic states, including the optically "dark" states. Additionally, photodetachment from anions whose neutral counterparts have a different equilibrium geometry can result in generation of the neutral in vibrationally excited states. Anion photoelectron spectra thus often reveal neutral-molecule vibrational frequencies and assist in the assignment of bonding motifs.

The weaker long-range electron-neutral (i.e. charge-dipole or charge-quadrupole) interactions, as compared to the coulombic attraction between electrons and cations, result in valence electrons in anions more weakly bound than those found in neutrals. This means that the energy required for photodetachment of negative ions is much smaller than that required for photoionization; photodetachment may be performed using visible or near-ultraviolet radiation as opposed to the extreme ultraviolet or x-ray radiation required for photoionization. This makes photodetachment possible using any of a wide range of commercially available light sources, particularly pulsed or cw lasers, with less harmful radiation than that used in the corresponding photionization experiments. Weaker charge-neutral interactions also mean that anions have fewer bound states, increasing the ease of characterization of any existing excited states.[15]

Weakly-bound electrons in anions are also more sensitive to environmental effects than their counterparts in neutral species. Probing the electronic structure of solvated anions thus provides the opportunity to study intermolecular interactions. This can be achieved via photoelectron imaging of cluster anions of the general form $X^-(M)_n$, held together more strongly by charge-dipole or charge-quadrupole interactions than the

van der Waals interactions in neutral clusters. These microsolvation environments are particularly important because probing the mass-selected members of a given cluster series provides a systematic picture of the role of solvation on chemical structure and reactivity and provides a conceptual bridge between gas- and condensed-phase chemistry. [15,17,18]

Finally, electron-molecule dynamics are incredibly important in a variety of contexts. Several popular examples include electron transport in materials as it pertains to energy technology and the role of electron attachment in degradation (and mutation) of DNA. Gas-phase negative ions offer a unique opportunity for probing such interactions in a controlled environment, because they have a built-in electron. Photodetachment allows for in situ generation of an unbound electron in a particular environment. This could result in processes as direct as charge-transfer, or as subtle as a perturbation of the photoelectron wave.

This dissertation is concerned with the elucidation of electronic structure, electrostatic intermolecular interactions and electron emission dynamics. Herein, we explore the capacity of photoelectron imaging for illuminating such phenomena, with a particular emphasis on interpreting photoelectron angular distributions.

1.4 Conspectus of this Dissertation

In the following dissertation, I present a series of experimental photoelectron imaging studies on gas-phase anionic systems, providing a window into the nature of

electronic structure and photodetachment dynamics, emphasizing the utility of the experimental approach.

Chapter 2 outlines the technique of photoelectron imaging from the experimental perspective. The negative-ion photoelectron imaging spectrometer, on which all experiments were performed, is described in detail. Typical operation procedures and conditions are also discussed, along with data acquisition and analysis.

Highlights of efforts to introduce photoelectron imaging to a wider audience are presented in Chapter 3. This section is derived from one paper currently in revision with the *Journal of Chemical Education*,[19] and closely related to another recently published in *Chemical Society Reviews*.[20] The purpose of the manuscript is to elucidate how photoelectron imaging provides new, visual demonstrations of some fundamental concepts in quantum chemistry. We hope that the publication will help to encourage the inclusion of contemporary research methods in undergraduate education while raising an awareness of the field that is commensurate with its growing popularity as an experimental tool. It is also hoped that the inclusion of these ideas in this dissertation introduces conceptual strategies for thinking about photoelectron imaging that are beneficial to the reader.

Chapter 4 catalogues imaging results for photodetachment from representative atomic and molecular anions, including H^-, O^-, NH_2^- and N_3^-, obtained at a variety of wavelengths. Raw images, photoelectron energy spectra and angular distributions are presented and discussed. A particular emphasis is given to simple, instructive approaches to modeling the energy-dependence of the photoelectron anisotropy parameters.

Photoelectron imaging results are presented for $H^-(NH_3)_n$ and $NH_2^-(NH_3)_n$ (n = 0-5) in Chapter 5. These results build on those for unsolvated H^- and NH_2^- in the preceding chapter, introducing the solvent domain and allowing for examination of the effect of solvation on imaging results.

Chapter 6 further examines solvation effects with results for photoelectron imaging of the $[O(N_2O)_n]^-$ (n = 0-9) and $[NO(N_2O)_n]^-$ (n = 0-4) cluster series. The energy spectra indicate the presence of multiple anionic core isomers, demonstrating that cumulative electrostatic interactions may have a dramatic effect on chemical bonding. The photoelectron angular distributions for detachment from the $O^-(N_2O)_n$ and $NO^-(N_2O)_n$ isomers implicate a resonant interaction of the photoelectron with the solvent, demonstrating another way that photoelectron imaging can identify electron dynamics and the richness of imaging results.

In Chapter 7, we revisit the time-resolved photoelectron imaging of I_2^- performed by previous members of this group.[10] A new, simple model of two-centered partial-wave interference is outlined and discussed in the context of the old results. New results for two different pump-probe polarization schemes are presented for the purpose of addressing the timescale of coherence between the atomic fragments.

Finally, this dissertation concludes with a summary, ideas for future studies and an outlook on the future of photoelectron imaging.

CHAPTER 2

EXPERIMENTAL APPARATUS AND DATA ANALYSIS

2.1 General Overview

All experiments were carried out using a custom-built, negative-ion photoelectron imaging spectrometer, previously described in detail elsewhere.[21-23] The instrument is illustrated in Figure 2.1. In brief, ions are generated in a pulsed ion source, extracted into a time of flight (TOF) mass spectrometer and photodetached with a linearly polarized laser. The resulting photoelectrons are detected using a velocity-map photoelectron imaging assembly.

2.2 Vacuum systems

The instrument is divided into three regions, each maintained at a different level of vacuum by differential pumping, as illustrated in Figure 2.1. The source chamber (region I) is connected to the time of flight region (II) via a 4 mm-diameter orifice; the detection region (region III) is separated from the flight tube by a 4" pneumatic gate valve.

When the instrument is in use, the source chamber is pumped by a 10″ diffusion pump (Varian VHS-10, 3,650 L/s). The TOF region is pumped by a 6″ diffusion pump (Varian VHS-6, 1,550 L/s) and one turbomolecular pump (Turbotronik 361, by Oerlikon Leybold 400 L/s). The detection region (III) is pumped by a second Turbotronik 361. These pumps are water-cooled using a Neslab System 3 liquid-to-liquid heat exchanger.

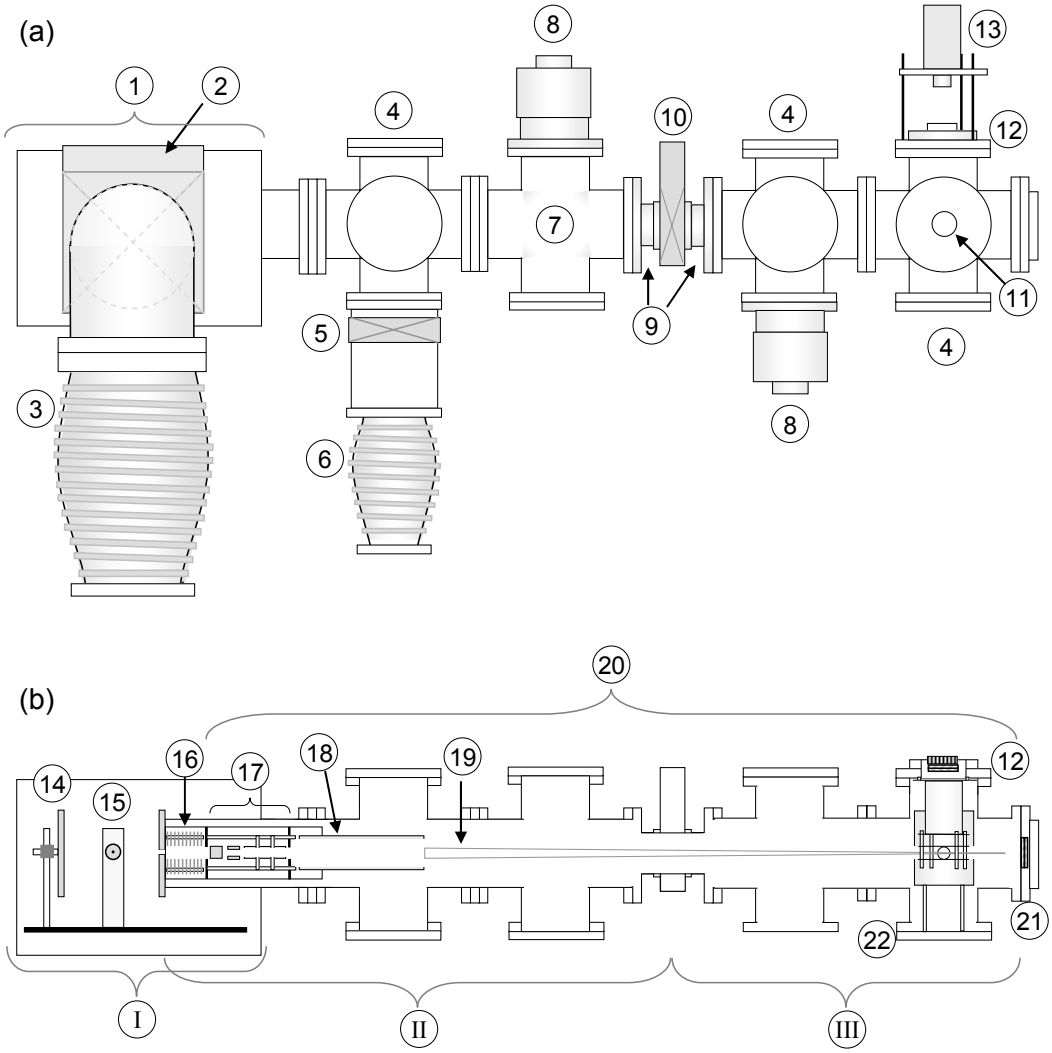

Figure 2.1 (a) Side exterior view and (b) cross-sectional interior view of the negative-ion photoelectron imaging spectrometer. Some key components are labeled and identified as follows. (1) Ion source chamber. (2) 10" gate valve (Vacuum Research Ltd. LP10). (3) 10" diffusion pump (Varian VHS-10). (4) 6-way CF cross with 8" flanges. (5) 6" gate valve (Chicago Allis Manufacturing). (6) 6" diffusion pump (Varian VHS-6). (7) 4-way CF cross with 8" flanges. (8) Turbomolecular pump (Turbotronik 361 by Oerlikon Leybold). (9) 8" to 4" reducing flange. (10) 4" gate valve. (11) Brewster window. (12) Flange with imaging detector and velocity-mapping assembly. (13) Mounted digital camera (CoolSnap HQ). (14) Repeller plate and mount. (15) Pulsed nozzle (General Valve Series 9) and mount. (16) Acceleration stack. (17) Ion Optics. (18) Potential switch. (19) Sketched ion beam trajectory. (20) Ion time of flight tube. (21) Flange with ion detector (Burle, Inc.). (22) Flange with μ-metal cup. Differentially pumped regions: (I) source chamber, (II) TOF region, (III) detection region.

The 6″ diffusion pump is backed by a Welch Duoseal Vacuum Pump (model 1397). The 10″ diffusion pump is backed by a Welch Duoseal Vacuum Pump (model 1373) that is also used to evacuate the source chamber (I) and time-of-flight region (II) if they have been vented to atmosphere. Both turbomolecular pumps are backed by a single Leybold Trivac mechanical pump. The base pressures of each region are $3\text{-}7\times10^{-6}$ Torr (source chamber), $2\text{-}4\times10^{-8}$ Torr (TOF region) and $1\text{-}4\times10^{-9}$ Torr (detection region). During imaging experiments, these pressures rise to $3\text{-}20\times10^{-5}$, $5\text{-}20\times10^{-8}$ and $2\text{-}10\times10^{-9}$ Torr, respectively.

When the instrument is not in use, the TOF gate valve is kept closed. The diffusion pumps are sealed by pneumatic gate valves (Vacuum Research Ltd model LP10 and Chicago Allis Manufacturing' 6" model) and turned off.

2.3 Ion source

Negative ions are generated via supersonic expansion of a neutral precursor bombarded by high-energy electrons using the techniques pioneered by the Lineberger group.[24] Figure 2.2 contains a detailed view of our source chamber components.

Gas precursors are delivered neat or as a mixture with argon (typically 2-20%), regulated at 12-40 psig. For liquid and solid precursors, 12-40 psig of argon is passed through a vessel containing the precursor sample, seeding a concentration determined by the sample's vapor pressure. The precursor gas expands supersonically into the source chamber through a solenoid-driven pulsed nozzle (General Valve Series 9 with a Kel-F poppet). The nozzle is typically held open for 150-200 μs, controlled by an Iota One

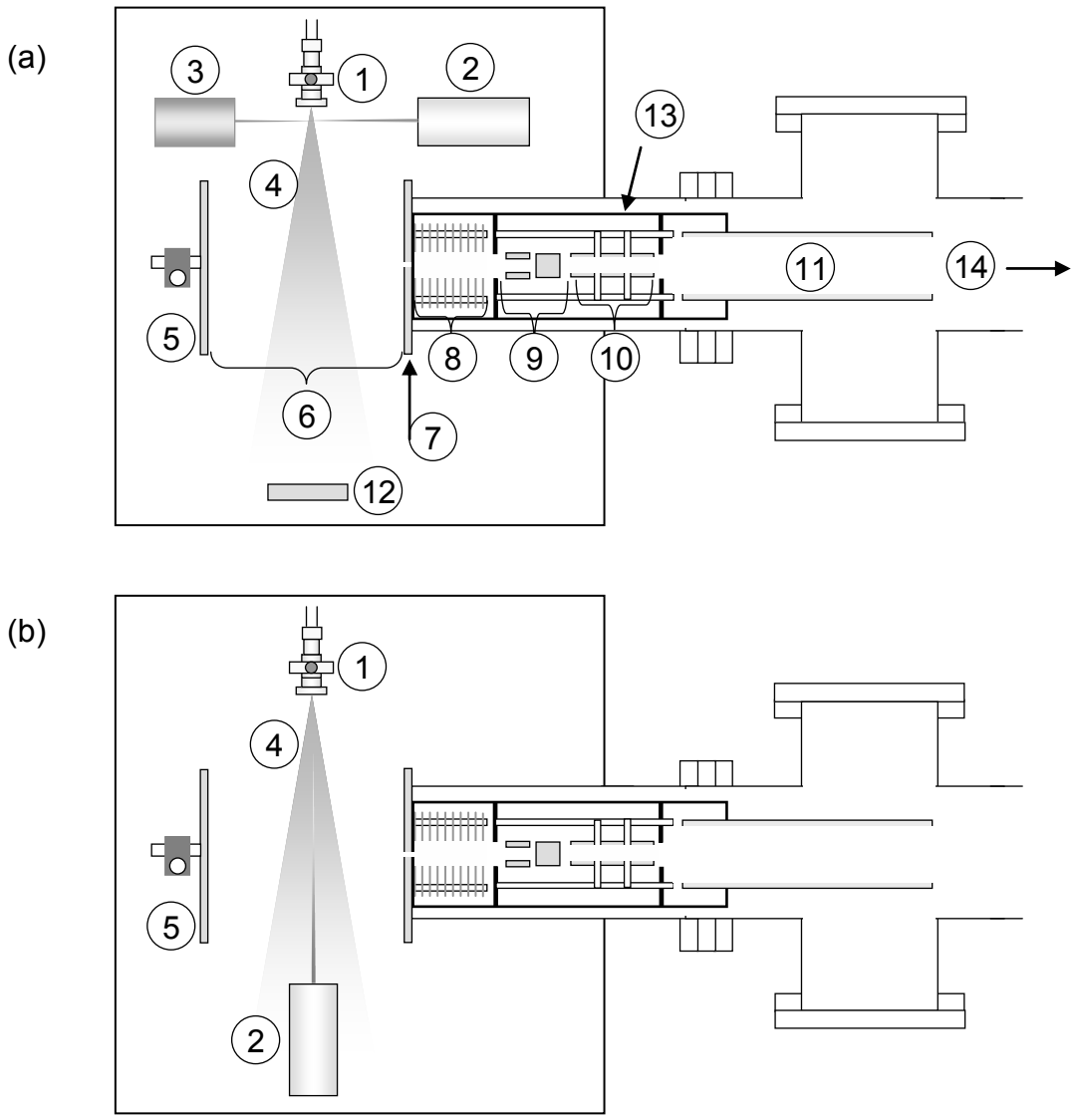

Figure 2.2 Expanded top view of the ion source chamber and TOF mass spectrometer components. Both (a) the perpendicular and (b) counter-propagating electron beam configurations are depicted. (1) Mounted pulsed nozzle (General Valve Series 9). (2) Electron gun. (3) Faraday cup. (4) Neutral gas and plasma expansion. (5) Mounted repeller plate. (6) First acceleration region of the TOF mass spectrometer. (7) Grounded plate. (8) Acceleration stack (second acceleration region of the TOF mass spectrometer). (9) Horizontal and vertical ion deflectors. (10) Einzel lens. (11) Potential Switch. (12) Fast Ion Gauge. (13) Floated housing for ion optics. (14) Ion drift region.

Pulse Driver (Parker Hannifin). The expanding gas mixture is bombarded with a continuous, high-energy (1 keV) electron beam from the thoriated iridium filament (floated at 1 kV by a Bertan 205B-03R power supply) of a custom-built electron gun described in detail elsewhere.[23] The electron beam is focused and tuned by altering the potential differences across a set of vertical and horizontal deflectors (supplied by two Agilent E3612A power supplies). The beam is focused using an Einzel lens (using a Keithley 247 High Voltage PS). The electron gun is positioned either so the beam intersects the expansion at a 90° angle [Figure 2.2 (a)] or in a counter-propagating configuration [Figure 2.2 (b)]. The high energy electrons ionize molecules or atoms upon impact, liberating low energy (<10 eV) "secondary" electrons and scatter out of the expansion. The slower electrons, entrained in the expanding mixture, continue to lose kinetic energy upon successive inelastic collisions. The expansion thus becomes a plasma with approximately no net charge.[24]

Secondary electrons may attach to neutral molecules or van der Waals clusters, yielding metastable anions. The metastable states either revert to their neutral form via autodetachment or are stabilized by energy release via one or more of the following mechanisms[24-26]:

$$MA + e^- \rightarrow (MA)^{-*} \rightarrow M + A^- \qquad \text{(dissociative attachment)} \qquad (2.1)$$

$$A + e^- + M \rightarrow (A)^{-*} + M \rightarrow A^- + M^* \qquad \text{(collisional energy release)} \qquad (2.2)$$

$$(M)_n + e^- \rightarrow [(M)_n]^{-*} \rightarrow [(M)_{n-x}]^- + xM \qquad \text{(evaporative cooling)} \qquad (2.3)$$

This ion generation method has the advantage of yielding high ion densities (initially $\sim 10^9$ cm^{-1}) with little ion loss over large expansion distances due to the

suppression of coulomb repulsion in the overall neutral environment.[27] The persistence of collisions throughout the expansion process can facilitate the formation of molecular anions that would not be formed via simple dissociative attachment or electron attachment. However, the primary mechanism of cluster anion formation is believed to be electron attachment to neutral clusters (equation 2.3), with energy released via evaporative cooling, rather than multiple association reactions of an ion with neutrals (unlike formation of positively charged clusters).[24] We have found cluster anion formation to be favored by directing the electron beam towards the throat of the nozzle, counter-propagating with respect to the expansion [Figure 2.2 (b)], as suggested by Robertson et al.[28]

With the electron gun in the perpendicular configuration [Figure 2.2 (a)], a Faraday cup is positioned to collect the remainder of the electron beam. The Faraday cup is grounded through an ammeter in order to monitor the current. This acts as a guide in tuning the electron gun for optimal beam trajectory. A fast ionization gauge (FIG-1 from Beam Dynamics, Inc.) is positioned opposite the nozzle; the signal is monitored on an oscilloscope. The appearance of a sharp drop in pressure immediately before the pressure jump due to the expansion reliably indicates the generation of anions within the source chamber. If this signal is present, the operator should move on to optimization of the downstream components and extraction timing to steer the ions toward their detector.

In the counter-propagating configuration [Figure 2.2 (b)] the fast ion gauge is replaced by the electron gun. The nozzle is grounded and doubles as a Faraday cup,

collecting some of the electrons from the beam. Connecting the nozzle to the ammeter can also be useful for optimizing the electron beam trajectory.

2.4 Time-of-flight mass spectrometer

The plasma expands freely until it enters the extraction region (or first acceleration stage) of an adapted[22,29] Wiley-McLaren[30] time-of-flight mass spectrometer. The spectrometer extracts the ions with a pulsed repeller plate, accelerating them further in a second stage. The ion trajectory is optimized by tuning vertical and horizontal deflectors and focused transversely in space with a decelerating Einzel lens. The ions drift through a field-free flight tube, finally arriving at the detector in packets, separated by mass-to charge ratio. The spectrometer is illustrated in Figure 2.1; Figure 2.2 contains a more detailed view of the acceleration stages and their components.

The expansion enters the region between two metal plates, the repeller plate and the grounded plate separating the source chamber from the flight region. Approximately 2 ms after the nozzle is fired, the repeller plate is pulsed with a negative voltage (typically between –400 V and –800 V) by a DEI PVM-420 high-voltage pulse generator (~10 ns rise time), creating an electric field (E_1) in the extraction region. This field pushes a cylindrical volume element of the negative ions in the expansion through an aperture (~ 4 mm diameter) in the center of the grounded plate. On the other side, they enter the ion acceleration stack, a series of ten round, 3″-diameter parallel plates, each with a centered 1″ through-hole. The neighboring plates are connected via 1 MΩ resistors, with the first plate grounded and the last plate floated at +1950 V (with a

Hewlett Packard model 6516A DC power supply), generating an electric field (E_2). The acceleration stack and downstream ion optics are encased in a floated metal housing to keep the ions referenced to the +1950 V of the final acceleration electrode.

Once the ions have exited the acceleration stack, they pass through a set of horizontal and vertical deflectors used to optimize the ion trajectory. The deflectors are floated by the same power supply that floats the acceleration stack and are grounded through an isolation transformer. Each pair may be biased up to ±120 V about the +1950 V float by Agilent E3612A power supplies that are floated by the same source. They then enter a three-electrode Einzel lens for transverse focusing. Each electrode is a 1.5″×1.5″ stainless steel cylindrical shell. The first and last electrodes are floated at +1950 V, and the center is varied between +500 V and +1000 V (as tuned by a Bertan Model 205B-03R power supply).

After focusing, the ions enter the potential switch, a 24 inch-long, 3 inch diameter stainless steel tube. The switch is pulsed from ground to +1950 V by a Directed Energy, Inc PVX-4140 high-voltage pulser (~15 ns rise time) using voltage from the ion optic float power supply at the time the repeller plate was fired, and drops back to ground after a variable 4-50 μs. This switch has the effect of re-referencing the ions to the ground potential for the field-free leg of the flight. Only the ions inside the potential switch during the re-referencing maintain their trajectory and kinetic energy upon exiting the switch. Ions that reach the end of the switch before it has dropped to ground are deflected, as are the heavier ions that are still upstream of the switch at the time of the voltage drop. The potential switch thus has a windowing effect on the mass spectrum,

suppressing all signal outside of a bracketed range.[31] This is can help to minimize saturation of the ion detector, but also necessitates the collection of spectra in these windowed sections, rather than in a single shot.

The ions travel field-free, until they reach the ion detector on the downstream side of the detection region (shown in detail in Figure 2.3). There, they pass through a grounded wire mesh (33 lines/inch, maximum transmission of 70%, Buckbee-Mears, Inc) positioned millimeters before the ion detector (a dual chevron microchannel plate assembly from Burle, Inc.). The mesh shields the flight tube from the voltage on the ion detector and homogenizes the field in the region just before the detector for a smooth additional acceleration of the ions before impact. The detector is floated by the divided voltage output from a Bertan 05B-03R power supply.[21-23] A bias across the plates of ≈1.5 V accelerates a cascade of electrons through the channels of the first and then the second MCP upon each impact. The cascade ultimately hits the metalized backing (the anode) whose AC-coupled output signal is further amplified (100:1, Phillips Scientific Model 6931) and monitored on an oscilloscope (Tektronix, Inc. TDS model 3032) whose trace may be averaged and recorded. The front, rear and anode plates are typically floated at ≈ 1 kV, 2.5 kV and 2.5 kV, respectively.

The time-of-flight for a given mass m with charge z is of the general form:

$$t(m) = a\sqrt{\frac{m}{z}} + t_0 . \tag{2.4}$$

The recorded time distribution (TOF spectrum) is converted via Jacobian transformation to a mass distribution (mass spectrum) as follows:

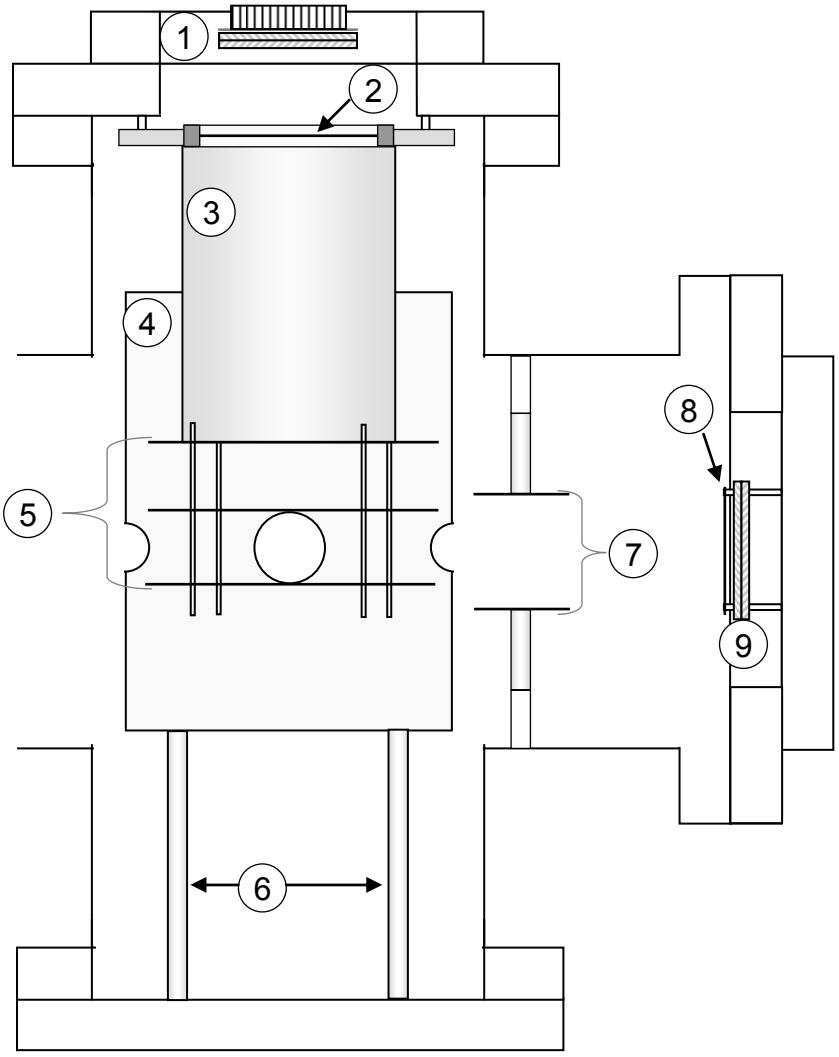

Figure 2.3 Detection region (side cross-section). (1) Photoelectron imaging detector (dual chevron MCP from with phosphor screen and optical output coupler by Burle, Inc). (2) Floated wire mesh. (3) Photoelectron flight tube. (4) μ-metal cup with ion and laser through-holes. (5) Velocity-mapping lens. (6) Mounting posts for μ-metal cup. (7) Post-imaging ion deflector. (8) Grounded wire mesh. (9) Ion detector.

$$P(m) = \frac{dt}{dm} P(t) = \frac{a}{2\sqrt{zm}} P(t). \tag{2.5}$$

Calibration is performed using two characterized ion peaks as a reference. For example, identifying (via photodetachment spectra) two TOF peaks centered at t_1 and t_2 as due to singly-charged ions of masses m_1 and m_2, respectively, allows for determination of a and t_0, via

$$a = \frac{t_1 - t_2}{m_1^{1/2} - m_2^{1/2}} \tag{2.6}$$

and

$$t_0 = t_1 - \frac{t_1 - t_2}{m_1^{1/2} - m_2^{1/2}}. \tag{2.7}$$

For optimally focused ions, a is typically ≈ 3.8 μs/Da$^{1/2}$, and t_0 between 0 and 0.3 μs.

When the repeller plate voltage is pulsed, the ions are distributed over a range of positions and energies. The longitudinal spatial focusing and the energetic focusing may be optimized by varying the ratio of E_2 to E_1. In practice this is done by tuning the voltage applied to the repeller plate to optimize the TOF resolution. Tuning the electron gun deflectors and Einzel lens also greatly affects the focusing of ion packets, most likely by altering the initial energy or spatial distributions of the ions formed. In general, there is some compromise between spatial and energetic focusing.[30] Ideally, the ions should be spatially focused for optimization of their overlap with the finite diameter of the laser beam (typically ≈ 0.5 cm), but a wide distribution of energies can lead to broadening in the photoelectron spectra for small (faster-moving) ions.

Due to the windowing effect of the potential switch, an entire mass spectrum typically must be accumulated in segments. In general, ions in each time window are reoptimized and the voltage on the ion detector is rescaled to optimize the quality of the recorded trace. The intensity scale is thus arbitrary for a given time-window; the relative intensities are even considered qualitative within a given window. Time-of-flight and mass spectra for an ammonia sample (30% in argon) are shown in Figure 2.4 as examples.

2.5 Laser Systems

When ions of interest have been identified, they are intersected with a linearly polarized laser pulse from one of two commercial laser systems. The first is a flashlamp-pumped, neodymium-doped yttrium aluminum garnet (Nd:YAG) laser (Quanta-Ray Lab 130-50 from Spectra Physics). The system is Q-switched at 50 Hz, yielding output pulse durations of approximately ten nanoseconds (ns). The fundamental output wavelength is 1064 nm (corresponding to the $^4I_{11/2} \leftarrow {}^4F_{3/2}$ transition of Nd^{3+}), with a maximum energy output of 200 mJ/pulse. The fundamental is frequency-doubled (to 532 nm) in a Type II potassium dideuterium phosphate (KDP) crystal, yielding a maximum energy of 70 mJ/pulse. This output may be used as is or doubled through a second KDP crystal to generate the fourth harmonic (266 nm, 15 mJ/pulse) or frequency-mixed with residuals of the fundamental to yield the third harmonic (355 nm, 30 mJ/pulse).

The second system is a regeneratively amplified femtosecond (1 fs = 10^{-15} s) pulsed laser (Spectra-Physics). The second harmonic (532 nm, 4.0 W) from a diode-

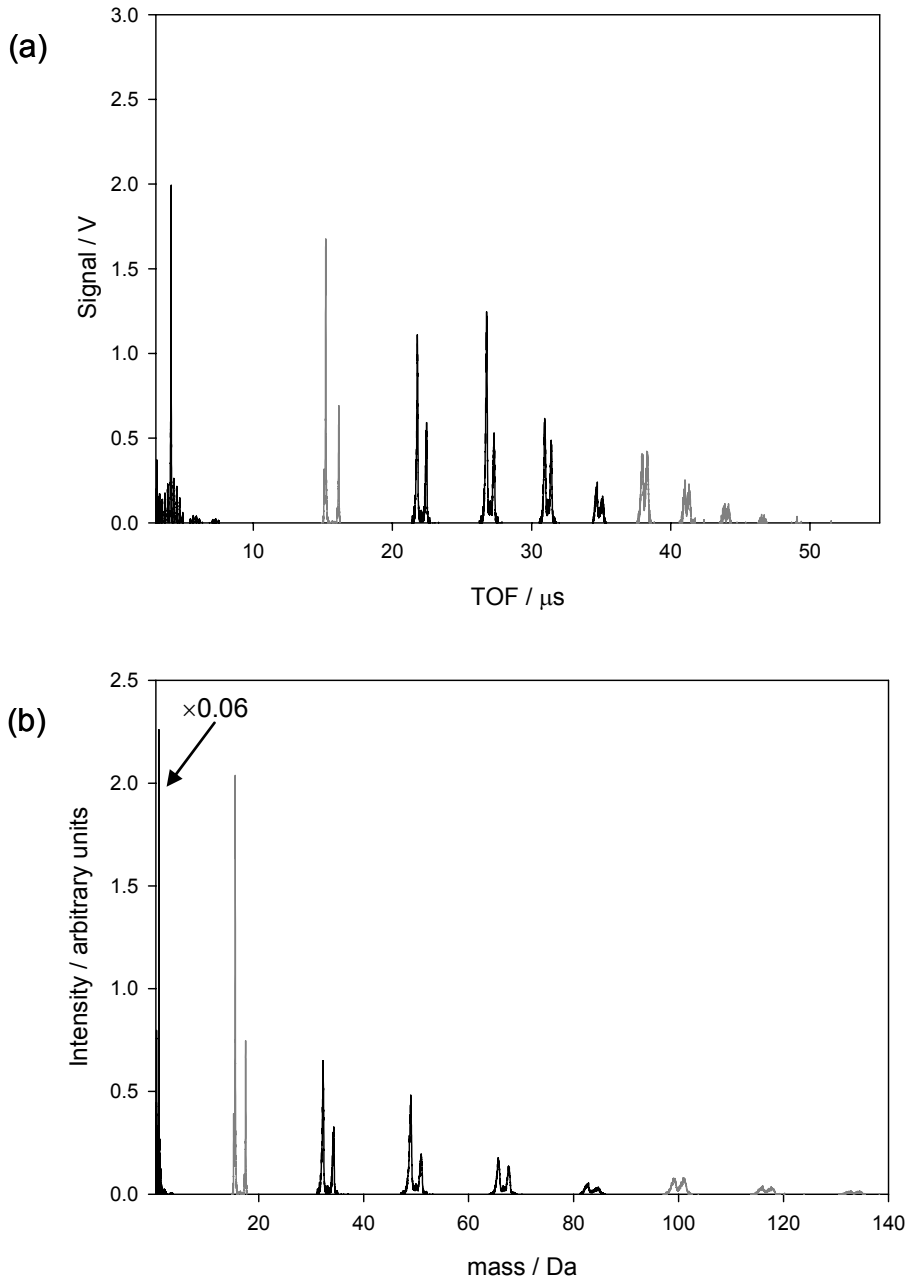

Figure 2.4 (a) TOF and (b) mass spectrum for expansion of 30% ammonia in argon. The signal was obtained in four windows (four different potential switch pulse durations). The distinct sections are shown in alternating black and gray lines. The first section of the mass spectrum was multiplied by 0.06 to fit it on the vertical scale. The spectrum displays two mass series: $H^-(NH_3)_n$ and $NH_2^-(NH_3)_n$, respectively.

pumped, neodymium-doped yttrium vanadate ($Nd:YVO_4$) continuous wave laser (Millennia V, Spectra-Physics) pumps the gain medium of a mode-locked titanium-doped sapphire (Ti:Sapph) laser (Tsunami, Spectra-Physics). The 82 MHz-pulsed output (temporal FWHM ≈ 80 fs) of the Tsunami is broadly tunable over 750-820 nm and serves as the seed beam for a regenerative amplifier (Spitfire, Spectra-Physics). Inside the amplifier, the seed beam is temporally and spectrally broadened by a grating, to minimize peak power and protect the downstream optics. The seed is then injected into the regeneration cavity which contains another Ti:Sapph rod as a gain medium, pumped by the 527 nm output of an intracavity-doubled, diode-pumped, neodymium-doped yttrium lithium fluoride (Nd:YLF) laser, pulsed at 1 kHz with an average power of up to 10 W (typically 7-8 W). The seed beam is Q-switched using Pockels cells. One in 82,000 seed pulses is amplified by ≈ 20 passes through the cavity, selected by the timing of the Pockels cells to arrive after saturation of the gain medium by the Evolution's pump pulse, amplifying 1000 pulses per second. Now amplified, the chirped beam passes through a compressor assembly, returning each pulse to an optimal temporal profile.

The femtosecond system typically yields 1 mJ/pulse at 790 nm, pulsed at 1 kHz. The horizontally polarized output is directed through a Single Shot Autocorrelator from Spectra-Physics. To determine the temporal FWHM, a 5% reflective mirror is rotated into the beam path, allowing a fraction of the output to travel into the autocorrelation optics. The FWHM is typically ≈ 120 fs. If desired, this output may be frequency-doubled using a Super Tripler (by Optronics) in doubling mode. Within the doubler, the beam is focused, collimated, and directed through a 0.2 mm thick, double-antireflection-

coated (400nm/800nm) type I β-barium borate (BBO) crystal (MiniOptic Technology, Inc.), generating up to 330 μJ/pulse of the second harmonic (now vertically polarized). A schematic of the laser configurations is given in Figure 2.5.

2.6 Time-resolved experiments

Time-resolved imaging experiments, in which one laser pulse (the pump pulse) excites the system of interest and a second (the probe pulse) photodetaches an electron after a chosen delay time, require specific beam arrangements. For one-color experiments, either the fundamental or the second harmonic is passed through a 50% beamsplitter to yield separate pump and probe beams of the same color; one beam is delayed with respect to the other and both are recombined downstream with a second 50% beamsplitter, resulting in a net 50% power loss in each beam. For two-color experiments, a fraction of the fundamental (50% or 70%, separated with the corresponding 800 nm beamsplitter) is directed through the doubler and the beams are recombined at a dichroic mirror with minimal energy loss. The beams are ultimately directed into the laser-ion interaction region collinearly, typically slightly focused with a Fresnel lens (f = 2 m) positioned about 1.3 m before the laser-ion interaction region. The two-color pump-probe configuration is illustrated in Figure 2.5.

The delay between the pump and probe pulses is created by changing the relative path lengths of the pump and probe beams. One of the beams is offset onto two mirrors mounted on a digitally-controlled translation stage (Newport ILS-100C), with a smallest-motion increment of 0.5 μm. The other beam is offset to generate approximately the

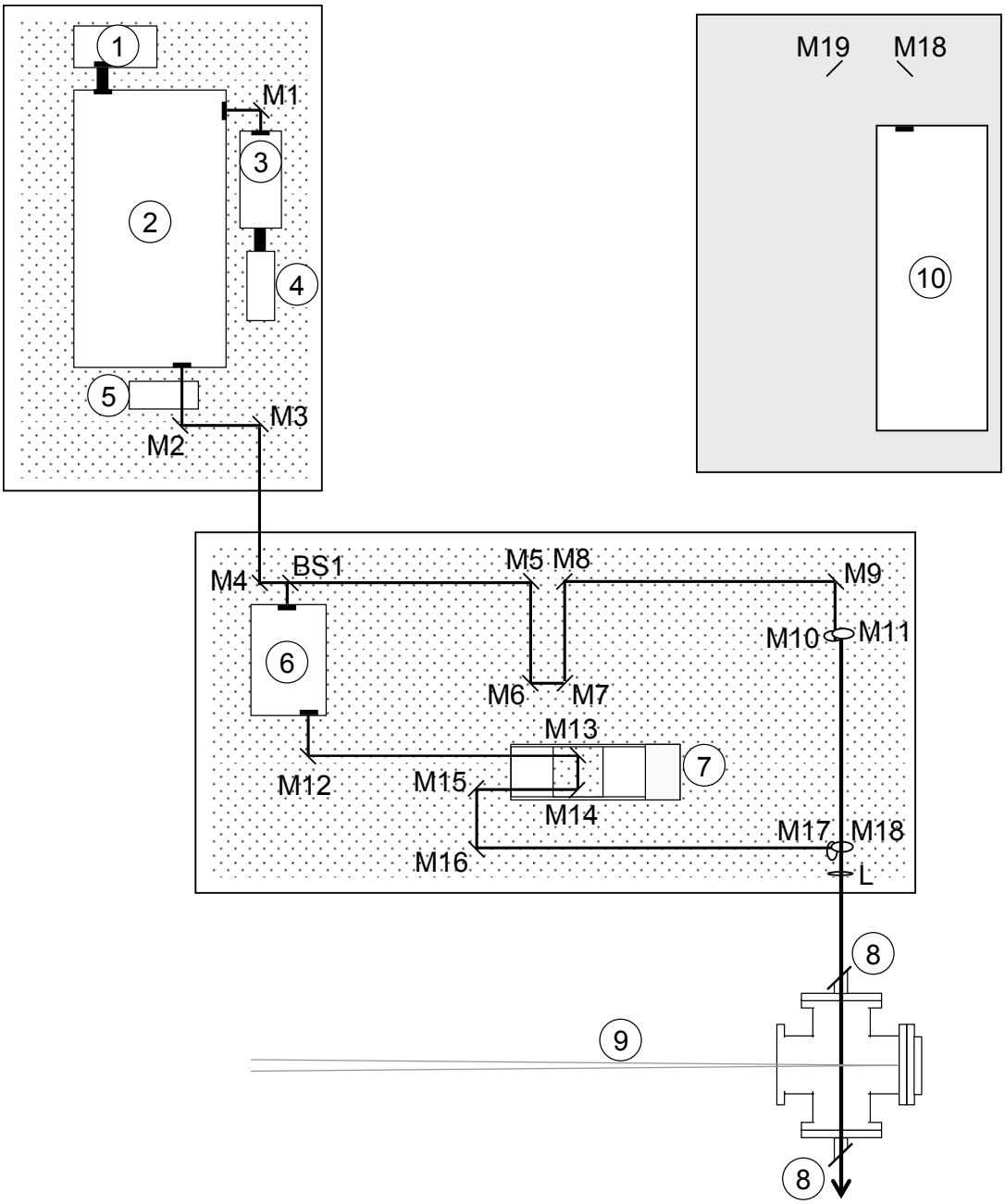

Figure 2.5 Top view of optical tables, configured for a two-color pump-probe experiment. (1) Evolution X. (2) Spitfire. (3) Tsunami. (4) Millennia V. (5) Single-shot autocorrelator. (6) Doubler. (7) ILS 100CC linear translation stage. (8) Brewster window. (9) Ion beam. (10) YAG laser. In this configuration, M1-M10 are 800 nm dichroic mirrors, M11-M17 are 400 nm dichroic mirrors. BS1 is an 800 nm beamsplitter (either 50 or 70% reflective). A fresnel lens (L) with a focal length of 2 meters gently focuses the beams just upstream of the first Brewster window. See text for details.

same path length as the first beam when its translating mirrors are centered on the translation stage, allowing for both positive and negative delays. Pump-probe delays are set by first finding the spatial and temporal overlap (or "zero-delay") between the two beams' pulses. This can be achieved for one-color experiments (pump and probe both from either the fundamental or the 2nd harmonic) by scanning the stage position until fringes, signatures of interference arising due to very slight deviations from collinearity, are observed in the cross-section of the overlapping beams. For a two-color experiment (using the fundamental as a pump and the 2nd harmonic as a probe, or vice versa), the collinear beams are passed through a BBO crystal (type I for parallel polarization, type II for perpendicular) followed by a prism to separate the beams by wavelength. Observation of the third harmonic indicates the temporal alignment of the two pulses. Maximizing the fringe contrast (one color experiment) or power of the 3rd harmonic (two-color experiment) optimizes the overlap.

The exact stage position for the zero delay is typically determined as the average of the positions for first appearance of the fringe or 3rd harmonic determined by scanning the stage in each direction. A delay of Δt is introduced by moving the stage

$$d = \frac{\Delta t \cdot c}{2}, \tag{2.8}$$

where c is the speed of light and d is the stage's offset from the zero-delay position; the factor of two accounts for the double pass of the beam. The resolution of a time-resolved experiment is no better than the temporal width of the convolved pulses, $\approx$ 250 fs.

For a one-color experiment, one may alternately monitor the pump-probe delay corresponding to a given stage position via spectral interference of the combined beams. The spectrum of the collinear pump and probe beams will display fringes whose spacing, $\Delta\nu$, is the reciprocal of the delay between the components.[32] Subtracting the individual pump and probe spectra yields an interferogram. Figure 2.6 (a) contains sample combined and individual pump and probe profiles as well as the corresponding interferogram. For any two adjacent interferogram peaks n and $n-1$,

$$\Delta t = \frac{1}{\Delta \upsilon} = \frac{1}{c\left(1/\lambda_n - 1/\lambda_{n-1} \right)}, \tag{2.9}$$

where λ_n is the peak wavelength of the nth fringe. Alternately, the experimentally determined interferogram may be transformed to a function of energy [see Figure 2.6 (b)] and fit to the product of a gaussian and a cosine function with a period of $h/\Delta t$, where h is Planck's constant. The delay-range for which this method is useful is limited by the resolution of the spectrometer used to record the spectra (Ocean Optics SD2000) and the FWHM of the laser's spectral profile.

Regardless of the experiment, the photon beam (or beams) enters and exits the laser-ion interaction region though fused silica windows mounted at the Brewster angle with respect to the propagation direction of the laser beams (see Figure 2.5). For a two-color experiment, the 800 nm beam must be delayed by an extra 650 fs (97.5 μm on the stage) to correct for the additional relative delay induced upon passing through the window. For most experiments, the laser's electric field is oriented parallel to the plane

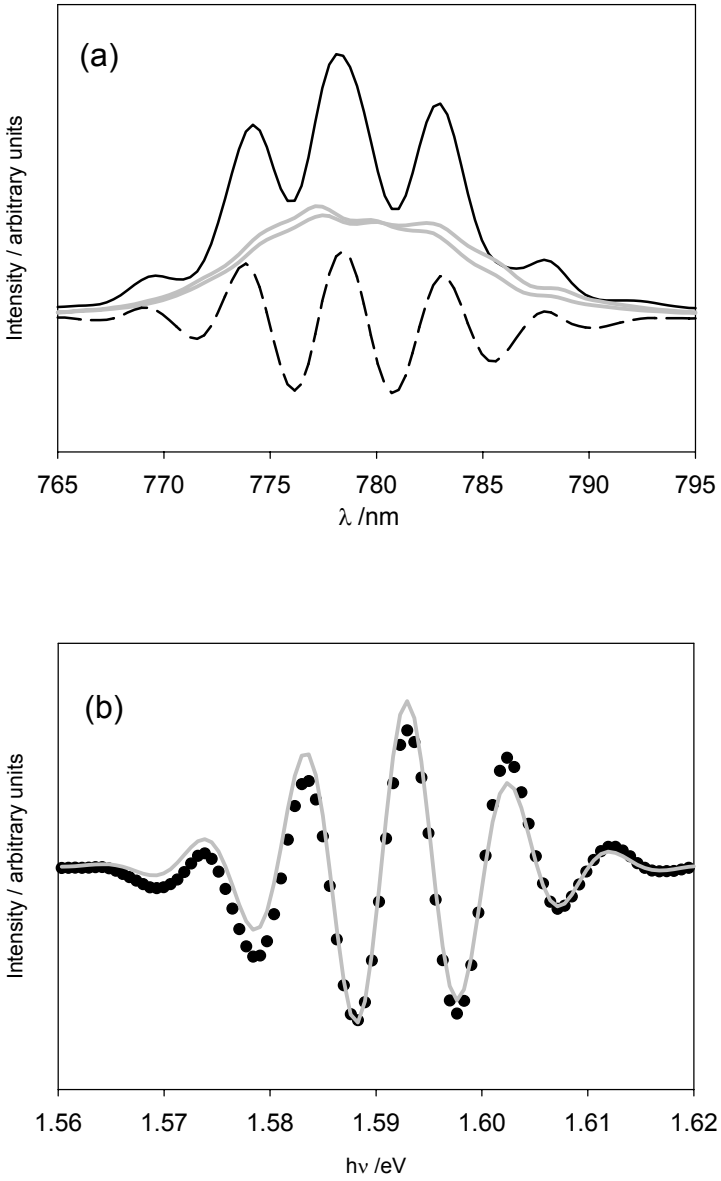

Figure 2.6 Pump-probe (780 nm + 780 nm) spectral interference. (a) The spectral profile for the pump and probe together is displayed as a solid black line. The individual pump and probe spectra are solid grey lines. The pure interferogram (dashed line) was obtained by subtracting the individual pump and probe profiles from the pump + probe trace. In this case, the beams were offset by 400 ± 37 fs from the determined zero-delay. (b) Experimentally determined interferogram (circles) plotted as a function of energy along with a fit to the data (grey line). The ≈ 0.0098 eV fringe spacing in the fit, corresponds to a delay of 420 fs.

of the imaging detector, collinear with the ion propagation direction, taken as the laboratory frame's z-axis.

2.7 Photoelectron Imaging Assembly

The laser-ion interaction region is located between the bottom two electrodes of the velocity-mapping lens of the photoelectron imaging assembly modeled after the designs of Eppink and Parker[13,14] and similar to that of Bordas and co-workers.[33] This imaging lens (illustrated in Figures 2.3 and 2.7) has three functions. First, it accelerates the photoelectrons perpendicularly to the ion path, towards the imaging detector. It also longitudinally focuses the electron cloud onto the plane of the detector. Finally, it maps identical velocity-components of the photoelectron distribution onto the same position of the detector, regardless of the position from which any given electron was detached.

The lens consists of three circular electrodes made of oxygen-free high-conductivity copper. The bottom plate is floated at a negative potential, varying down to –330V (supplied by a Hewlett-Packard 6516A DC power supply). The middle plate is grounded and the top plate is floated at a positive potential (up to +900V, by a Bertan model 205B-03R power supply). The optimal ratio of voltages for the top and bottom plates, determined empirically, is ≈ –2.73. Changing the magnitude of the imaging voltages (while maintaining the optimal ratio) either shrinks (higher voltage) or expands (lower voltages) the radius of the image by a factor of $\sqrt{\frac{V_{old}}{V_{new}}}$ by speeding up the projection process and reducing the electron flight time. All plates are 4" in diameter and

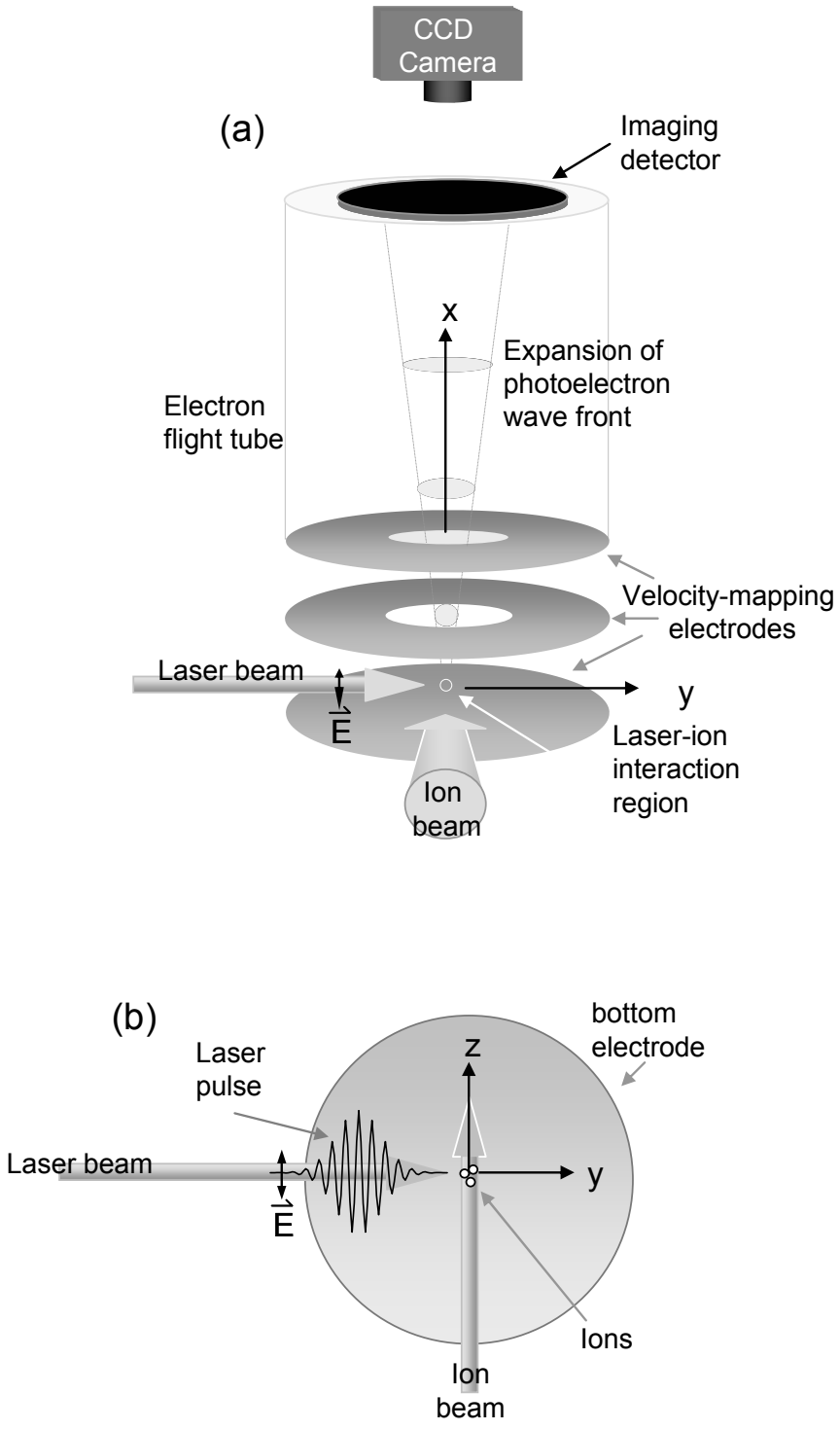

Figure 2.7 (a) Illustration of the velocity-mapping photoelectron imaging assembly and (b) top view of laser and ion beams with laboratory frame axes indicated.

are mounted approximately 1” apart; the top two plates have 1” round holes at their centers through which the electrons travel. Once accelerated by the imaging lens, the photodetached electrons travel field-free through a metal tube floated at the potential of the top electrode. This flight tube is lined and wrapped with μ-metal to shield from magnetic fields. Before impacting the detector, the electrons pass through a fine nickel mesh (33 lines/inch, maximum transmission of 70%, Buckbee-Mears, Inc), positioned just inside the flight tube and floated at the same potential. The mesh shields the electron flight region from the voltage supplied to the detector just downstream. The imaging lens and roughly half the flight tube are contained within a μ-metal cup which shields the imaging lens from magnetic fields. The μ-metal cup has four through-holes for entrance and exit of the ion and laser beams.

The imaging detector consists of a dual chevron microchannel plate (MCP) assembly coupled to a P47 phosphor screen (Burle, Inc.). The first of two outputs from a Burle Model PF1054 power supply floats the phosphor screen at typically +6.50 kV; the second, +3.00 kV output is sent into a voltage divider which provides +2.00 kV and +3.00 kV to the input of the first (bottom) and exit of the second (top) MCP’s respectively. The exit of the second MCP is pulsed (DEI PVM-4150 pulse generator) up another 1.01 kV (Bertan model 205B-05R power supply) for a total bias of 2.01 kV across the two MCP’s during the 200 ns window coinciding with the arrival of photoelectrons. This pulsed-bias approach helps to discriminate against noise. Electron impacts upon the front (bottom) of the assembly are multiplied within the MCP’s assembly. Upon striking the phosphor screen, the electrons from the second MCP

generate photons coupled to an external window using a fiber optic bundle. The resulting signal is recorded by a thermoelectrically cooled digital camera (CoolSnap HQ by Roper Scientific, 1392×1040 CCD array of 6.45μm × 6.45 μm pixels) monitored via computer interface.

The imaging assembly is only turned on after ion optimization because the voltage from the bottom electrode affects the ion path and the position of incidence on the detector. Increasing the electric field within the vertical ion deflector compensates somewhat for the deflection induced by the imaging lens. Tuning this deflector plays a major role in optimizing the laser-ion overlap. Another helpful tool is the post-ion imaging deflector, a pair of electrodes through which the ions travel just downstream of the laser-ion interaction region and pictured in Figure 2.3. Applying a potential difference across the electrodes can be used to deflect all ions, allowing only the neutral species to reach the detector. Maximizing the flux of neutrals effectively maximizes the number of anions that are photodetached.

2.8 Timing and signal optimization

All pulsed components are triggered by the outputs from two digital delay generators (Berkeley Nucleonics Corporation Model 555 and Stanford Research Systems DG535). All trigger pulses are transmitted through RG 58/U coaxial cables with BNC connectors. High voltage pulses travel through coaxial cable with SHV or MHV connectors, as appropriate. Figure 2.8 contains a schematic of the triggering times and on-times for the pulsed components.

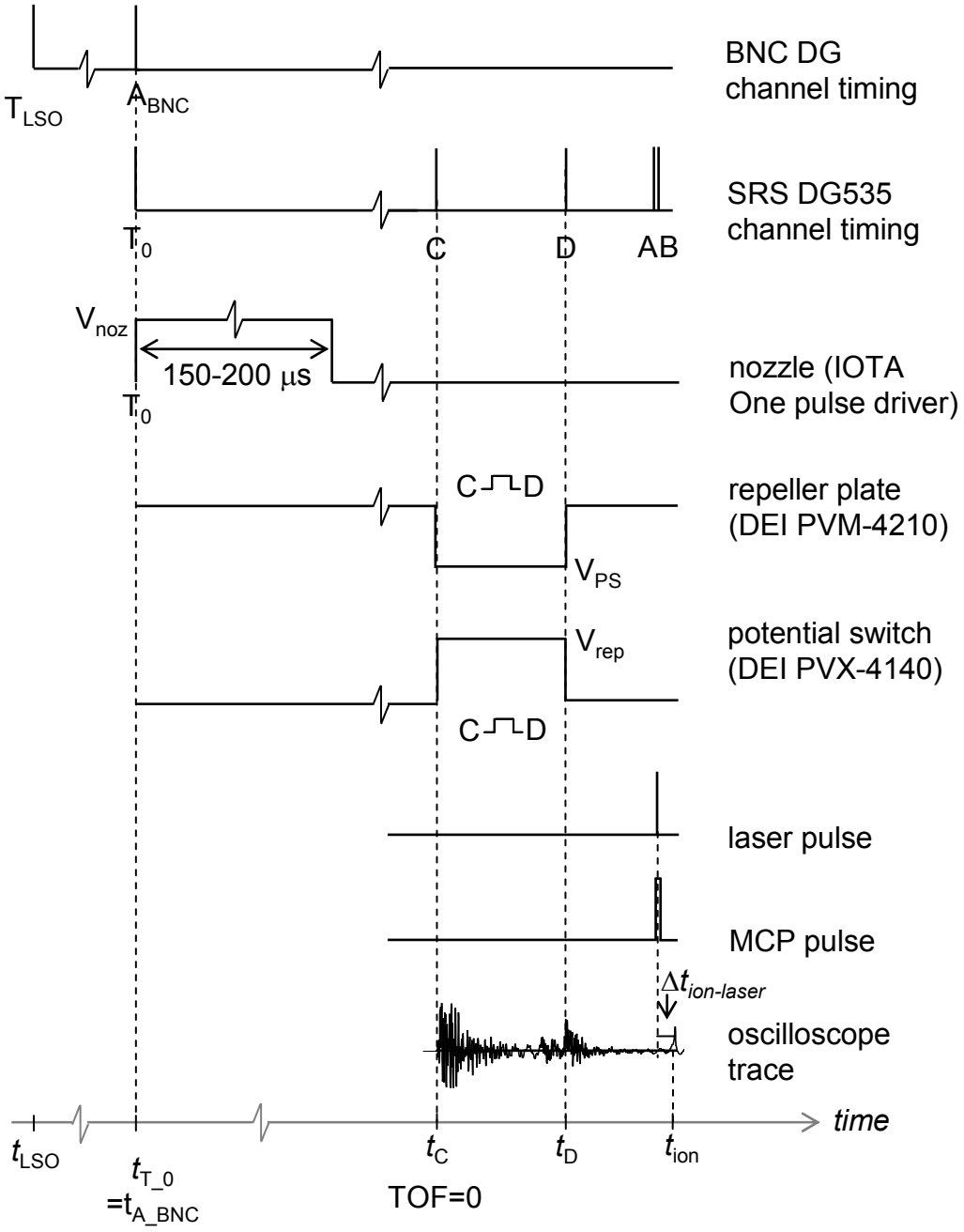

Figure 2.8 Experimental timing scheme. See text for details.

Because the femtosecond laser is not configured for external triggering, photoelectron imaging experiments are always timed relative to the pulses of the laser system used. The laser SYNC output (T_{LSO}) from the Spitfire (or YAG) is connected to the trigger input of the BNC delay generator. The laser pulse is delayed by Δt_{offset} (and divided by 14 in the case of the fs system) to generate an output (A_{BNC}) to trigger the SRS DG535 which triggers all other experimental components. The nozzle is triggered by the T_0 output of the SRS DG535.

The SRS DG 535 has four channels, (A, B, C and D) that trigger the other pulsed components. The C $\sqcap$ D output gates the high voltage pulses of the repeller plate and the potential switch; time C thus corresponds to $t = 0$ in the time-of-flight spectrum, and is used to trigger the oscilloscope on which the ion signal is monitored. Laser pulses, detected by a fast photodiode (Thorlabs DET 210) placed behind the exit Brewster window, are monitored on the second channel of the oscilloscope. The laser is timed to intersect the ions of interest approximately 15 cm upstream of the ion detector by tuning the offset (A_{BNC} output) between the BNC and SRS delay generators. Optimal overlap occurs when the laser reaches the detection region $\Delta t_{ion\text{-}laser}$ on the order of μs before the ions reach the detector, approximated by the empirical relation

$$\Delta t_{ion-laser} = 0.264 \ \ \mu s \cdot Da^{-1/2} \cdot \sqrt{m}\,, \tag{2.10}$$

where m is the mass in Da, or, alternately,

$$\Delta t_{ion-laser} = 0.0720 t\,, \tag{2.11}$$

These expressions are the best fits to a large record of optimized experimental parameters for a variety of ions on different days and are useful starting points for

optimizing laser-ion overlap. The optimal offset is largely insensitive to the specific voltage settings of the spectrometer components.

For the femtosecond source, there are 14 laser pulses per triggered experimental cycle, each separated by 1 ms. The first pulse triggers the nozzle, and photodetachment is performed by either the third or fourth pulse. Twelve pulses are not used and the 15^{th} pulse triggers the nozzle again, becoming the first pulse of the next cycle. For the YAG source, there is one pulse per experimental cycle (one per 20 ms) and the photodetachment pulse for one cycle doubles as the trigger for the following experimental cycle. This timing is thus dependent on the stability of the pulse rate for each laser system; the timing jitter of 0.5 ns for the YAG and <250 ps for the femtosecond system compare favorably to the minimum tuning increment of 10 ns used to optimize the temporal laser-ion overlap. The A $\sqcap$ B output gates the pulsing of the top MCP plate in the imaging assembly (see section 2.6). This pulse duration must bracket the arrival time of the laser in order to detect the resulting photoelectrons; for optimal signal collection, the laser must arrive within 70 ns after the SRS A output.

The C and D delays are tuned as part of ion optimization. Once the ion signal has been optimized, the imaging assembly is turned on and the photoelectron signal is optimized by tuning the vertical ion deflector, the Einzel lens and the A, B and A_{BNC} delays. The channel timing references and typical delay settings for each are as follows:

$$A_{BNC} = L_{SO} + 20\text{–}120\ \mu s \tag{2.12}$$

$$T_0 = A_{BNC} \tag{2.13}$$

$$A = T_0 + 4\text{–}100\ \mu s \tag{2.14}$$

$$B = A + 200\ ns \tag{2.15}$$

$$C = T_0 + 1.7\text{–}2.2\ ms \tag{2.16}$$

$$D = C + 4\text{–}90\ \mu s \tag{2.17}$$

2.9 Data Acquisition

The photoelectron signal collected by the digital camera is fed to the computer and monitored using either the Winview (Roper Scientific), V++ 4.0 (Precision Digital Imaging Systems) or Cool Image[6] software interfaces. For signal optimization, either Winview or Cool Image is run in a "focus" mode in which the software displays successive 3-second accumulations. For collection of one-photon (static) images, the signal is typically accumulated for a total of five minutes in five or ten second intervals, corresponding to 15,000 (YAG) or 21,300 (fs laser) experimental cycles. Background images are obtained by shifting the laser and MCP pulses together to an earlier time, at which there is no laser-ion overlap and thus no photodetachment signal, and collecting for an identical time period. The background noise is subtracted from each to yield the raw photoelectron image. Images are typically collected in multiple five- or ten-minute batches and combined for signal averaging.

For time-resolved experiments, four separate images are collected, typically as sixty cycles of the following sequence: 1) background accumulation (both beams blocked) 2) signal from the pump beam alone, 3) signal from the probe beam alone and 4) signal with both beams entering the interaction region. This sequence is implemented

by a pair of mechanical shutters (Uniblitz Electronics), one in each beam path, connected to the computer interface. Each step in the collection cycle lasts for 5 seconds, with a 1 second pause between each step to accommodate the opening and closing of the shutters. Shutter actuation is controlled by the data acquisition software which allows for modification of collection sequences. The raw two-photon signal is obtained from the four images by subtracting the one-photon pump and probe images from the pump + probe image and adding in the background image to account for the double subtraction.

2.10 Analysis of photoelectron images

In the absence of the imaging assembly, a single photoelectron may be thought of a wave front expanding spherically from the detachment center, with cylindrical symmetry about the laser's electric field vector.[19,20] The imaging lens has the effect of projecting the wave front towards the position-sensitive detector, while simultaneously focusing (i.e. flattening) the wave front longitudinally onto the plane of the detector. The voltages of the imaging electrodes are optimized to overlap the focal plane with the surface of the imaging detector.

Interaction of the photoelectron with the detector constitutes an act of measurement and thus collapses the photoelectron wave front onto an eigenfunction of the measurement operator, in this case the position operator. Eigenfunctions of the position operator are delta functions of the coordinates. The electron thus registers on the detector as a single impact point (within the resolution of the detector). Detection of a very large number of electrons results in a statistical accumulation of impact points,

approaching the limit of a smooth distribution. For the case of photodetachment of an atomic anion, this distribution corresponds to the square modulus of the wave function of a single photoelectron immediately before hitting the detector.

In practice, there are millions of target ions distributed over a finite volume in the laser-ion interaction region in every experimental cycle. Typically, a countable number of electrons are photodetached at different positions within the laser-ion interaction region in a given experimental cycle. The velocity-map imaging assembly has the effect of focusing all photoelectron wave fronts identically onto the plane of the detector, regardless of the point of origin of each wave front. This means that identical velocity components of the photoelectron distribution are mapped onto the same point on the detector, regardless of the position of the anion from which each electron was detached.

Raw images may thus be thought of as 2-dimensional (2-D) projections of the three-dimensional (but cylindrically symmetric) photoelectron probability distribution. The axis of cylindrical symmetry, determined by the electric field vector of the laser, is taken as the z-axis and is parallel to the ion propagation direction. The laser beam defines the y-axis, and the detector is parallel to the plane defined by the laser and ion beams (the yz plane). The photoelectrons are projected in the positive x-direction. The photoelectron expansion and laboratory frame coordinates are displayed in Figure 2.7.

In order to quantitatively analyze the data, the 3-D distributions are reconstructed from the 2-D images. Because the axis of cylindrical symmetry is parallel to the plane of the detector, this may be done via inverse Abel transform,[34] implemented using the Gaussian BAsis Set EXpansion (BASEX) program developed by the Reisler group.[35]

BASEX reads the image as a matrix of intensities, which is expanded in the 2-D projections of 3-D gaussian basis functions that are restricted to be identical for a given r and ±z (where the origin is the image center). The program determines the coefficients on the 2-D basis functions, translates them to the 3-D basis functions and returns a cross-sectional slice through the center of the reconstructed 3-D distribution as a matrix of intensities as a function of r (in pixels) and θ (in degrees). When swept through all angles φ about the z-axis, this cross-section traces out the reconstructed 3-D distribution. The raw and reconstructed photoelectron images for 800 nm photodetachment of H^- are displayed in Figure 2.9.

The program also returns the angle-integrated intensities of the reconstructed image over the entire radial range of the image in user-chosen increments (typically 0.5 pixels). During projection onto the detector, the transverse expansion of the photoelectron wave front is linear with time; the radial coordinate of a reconstructed image is directly proportional to the speed of this expansion. The kinetic energy corresponding to a given r is thus

$$eKE = \frac{1}{2} m(k \cdot r)^2 = Cr^2 , \tag{2.18}$$

where k is a proportionality constant and C is the calibration constant determined from one or more peaks in the photoelectron energy spectrum of a standard. In general,

$$C = \frac{eKE_c}{r_c^{\,2}} , \tag{2.19}$$

where eKE_c is the peak electron kinetic energy of the calibrant (typically defined as the difference between the photon energy and literature detachment energy) and r_c is the

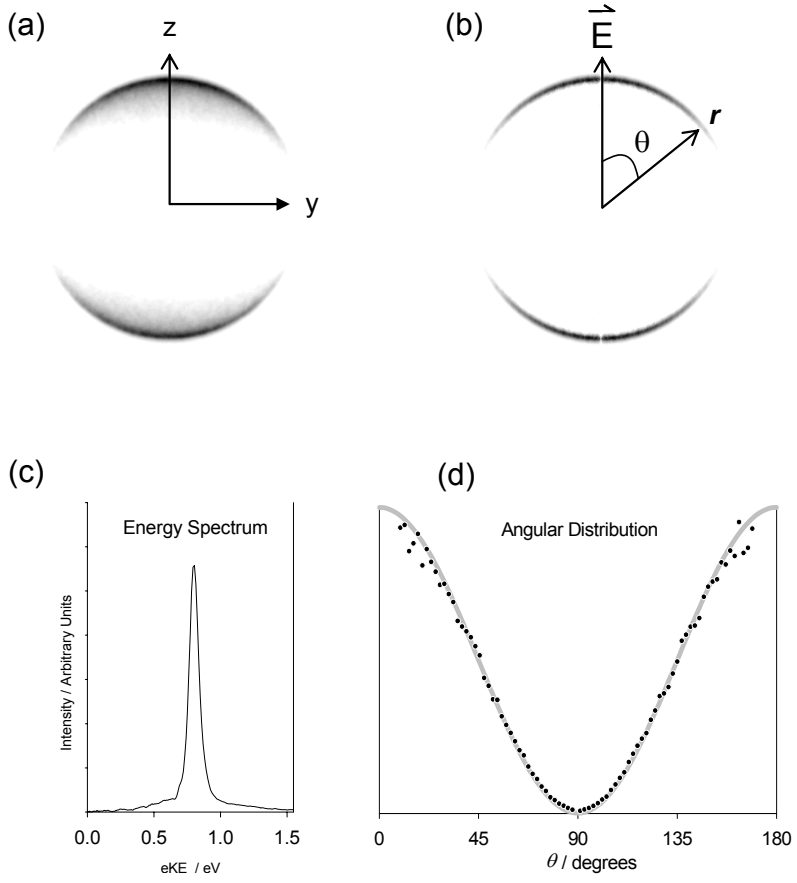

Figure 2.9 (a) Raw and (b) reconstructed photoelectron images, (c) photoelectron energy spectrum and (d) angular distribution for 800 nm photodetachment from H^-.

pixel corresponding to the peak intensity. For *n* calibration peaks, C is best determined as the average

$$C_{avg} = \frac{1}{n}\sum_{i=1}^{n}\frac{eKE_i}{r_i^2}. \tag{2.20}$$

It is important that the calibration peaks occur near the maximum radial range of the signal to be acquired due to the nonlinear scaling of energy with radius.

The radial distribution, *I(r)*, is converted to the energy distribution, *I(eKE)*, by Jacobian transformation:

$$I(eKE) = I(r)\frac{dr}{d(eKE)} = \frac{I(r)}{k\sqrt{2m\cdot eKE}} \propto \frac{I(r)}{\sqrt{eKE}}. \tag{2.21}$$

Since an image's intensity scaling is arbitrary, the proportionality is sufficient to obtain the photoelectron spectrum. The 800 nm photoelectron spectrum for H^- is displayed in Figure 2.9 (c).

BASEX also generates an intensity map of the reconstructed image as a function of polar coordinates (*r* and θ). This allows for integration over a chosen radial range, typically taken as the full-width at half-maximum of a given transition, yielding the photoelectron angular distribution (PAD), $I(\theta)$.

Photoelectron angular distributions for an *n*-photon detachment process using linearly polarized light can be expanded in the following general form,[36-38, 39,40]

$$I(\theta) = \frac{d\sigma}{d\Omega} = \frac{\sigma_{total}}{4\pi}\left[1 + \sum_{i=1}^{n}\beta_{2i}P_{2i}(\cos\theta)\right], \tag{2.22}$$

where σ_{total} is the total photodetachment cross-section, P_{2i} is the $2i^{th}$ order Legendre polynomial, β_{2i} are constants, termed $2i^{th}$ order anisotropy parameters. Because the

image intensity scaling is arbitrary and the ion flux is not quantified, experimental angular distributions do not quantitatively indicate the total photodetachment cross-section. In this dissertation, we shall only consider angular distributions resulting from photodetachment using linearly polarized light.

For all one-photon processes (and some 2-photon processes), only the leading term of the summation is required. Experimental data are thus fit to the following form:

$$I(\theta) = K\left[1 + \beta_2\left(\frac{3}{2}\cos^2\theta + \frac{1}{2}\right)\right], \tag{2.23}$$

and "β" will be used interchangeable with "β_2" The K and β_2 parameters are extracted by performing a linear least squares fit of the reconstructed I(θ) vs $P_2(\cos\theta)$. The angular distribution is totally characterized by the anisotropy parameter. The distribution ranges from purely parallel (a $\cos^2\theta$ distribution, $\beta_2 = 2$) to purely perpendicular ($\sin^2\theta$, $\beta_2 = -1$) and everything in between. A distribution for which $\beta_2 = 0$ is perfectly isotropic. The PAD for 800 nm photodetachment from H^- is displayed in Figure 2.9 (d). The anisotropy parameter for this transition, $\beta = 1.92 \pm 0.04$, is quite close to the upper extreme β-value.

In Chapter 3, these results for H^- are used to discuss key concepts of quantum mechanics, emphasizing the educational potential for photoelectron imaging results. Chapter 4 discusses the chemical significance of photoelectron angular distributions in the context of experimental results for relatively simple systems of importance to later chapters.

CHAPTER 3

PHOTOELECTRON IMAGING AS A CLASSROOM TEACHING TOOL

In this chapter, we present a pedagogical introduction to the technique of photoelectron imaging. This chapter is derived from an article currently in revision for the Journal of Chemical Education whose purpose is to demonstrate how the contemporary technique of photoelectron imaging may be used to demonstrate fundamental quantum principles. The discussion is aimed at advanced undergraduate students and their educators.

3.1 Introduction

The photoelectric effect is usually discussed in physical chemistry courses as part of the introduction to wave-particle duality and the quantization of light. This observation of electron-release upon irradiation of a metal surface had characteristics that could not be explained by the physics of the day. First, increasing the light's intensity increased the number of electrons released, contrary to the classical expectation that it should increase the speed with which they depart. On the other hand, increasing the frequency of the radiation does increase the speed (or kinetic energy) with which the electrons are ejected, although the classical expectation that there should be an increase in the number of electrons released is not realized! Finally, decreasing the frequency to a certain point (unique to the type of metal) abruptly causes the electron emission to cease,

regardless of the light intensity.

These observations necessitated an alternate description of light as having particle-like, in addition to wave-like, attributes. Light is indivisible beyond discrete packets, now called photons (a termed coined by G. N. Lewis in 1926), each with energy defined by the light's frequency. The photoelectric effect was explained by Albert Einstein in one of the papers[41] of his *annus mirabilis*, as a one-photon, one-electron process, where part of the photon's energy is spent in overcoming the binding force, with the excess converted into kinetic energy of the released electron (or "photoelectron"). For photons above the cutoff frequency, electrons may be liberated with maximum kinetic energy (eKE) of

$$eKE = h\nu - \Phi, \tag{3.1}$$

where Φ, the work function of the metal, is the smallest photon energy for which electrons may be liberated. The photoelectric effect is one of the strongest indications of the quantization of light energy, and the most commonly used classroom example of this phenomenon.

Applying the light source instead to atoms and molecules also reveals quantized energy levels in matter. Photoelectron spectroscopy has become an extremely useful and versatile tool for probing the energies of atomic and molecular orbitals. This is usually done through interpretation of the photoelectron energy spectrum, which reflects the probability of the emitted electrons having a certain kinetic energy. The photoelectron spectrum contains the probability of removal of an electron from a given orbital and the amount of energy required to do so, often yielding information about the energy spacing

of electronic and vibrational levels.

It is less appreciated that photoelectrons produced using polarized radiation have characteristic distributions of the directions of their velocities. These distributions, referred to as photoelectron angular distributions, are generally anisotropic. This arises due to the quantization of angular momentum. Students of chemistry generally appreciate that orbitals have defined shapes and symmetries based upon their orbital angular momentum. Similarly, the angular distribution of the photoelectrons is dependent on the shape of the orbital from which it was removed. These shapes may be probed by visualizing the photoelectron cloud in an imaging experiment. In particular, careful interpretation of photoelectron angular distributions for isolated molecular systems yields insight into the structure and symmetry of the parent orbitals from which the electrons were ejected.

Photoelectron imaging combines photoelectron spectroscopy with a photographic approach to quantify the photoelectron distributions upon detachment from gas-phase chemical systems. This elegant experimental technique probes both electronic energy eigenvalues and the properties of the corresponding wave functions.

While negative-ion photoelectron imaging requires the specialized equipment outlined in Chapter 2, we propose that both framing the technique as a thought-experiment and actual experimental results have great potential as educational tools. The visual nature of the photoelectron image makes it an automatic object of curiosity for a student. This curiosity can be used to stimulate an interest in the information content of the image and allow considerable insight into the quantization of energy and the wave-

like nature of matter. The simplest negative ion, H^- for which imaging results have been reported previously,[42] is an ideal tutorial system, relating most directly to the only fully-solved chemical Hamiltonian, that of the hydrogen atom. In the following, we use our independent results for H^- as a new context for discussion of concepts that are key to quantum chemistry.

3.2 Wave-particle duality of matter

Wave-particle duality is at the heart of quantum mechanics. Einstein's explanation of von Lennard's photoelectric effect measurements clearly showed that light has particle-like as well as wave-like properties. Though not typically emphasized in the context of the photoelectric effect or photoelectron spectroscopy, objects with a non-zero inertial mass (which classically would be considered particles) also behave like waves. The characteristic wavelength (λ) is dependent on the particle's momentum, p, according to the de Broglie relation, $\lambda = h/p$, where h is Planck's constant.

As chemists we rely upon this principle; our description of molecular structure is based upon electron wave functions that define molecular orbitals and the corresponding probability densities. A similar approach holds for free electrons with the key distinction that electrons in molecules are in bound, spatially localized states, while a free electron is a boundless, propagating wave.

When an electron is photodetached from a negative ion, its behavior should be viewed as wave-like. As the electron departs, its average separation from the remaining neutral increases with time. However, the direction in which the electron travels is

usually fundamentally undefined. A photoelectron ejected from a molecule can be thought of as a spherically expanding wave front, like an inflating balloon whose surface becomes increasingly distant from its center. In photoelectron imaging, we probe photoelectrons after a set expansion time by flattening these spherical waves, focusing them onto the plane of the detector.

3.3 Quantum measurement and probability densities

The interaction of the electron wave front with the detector constitutes an act of measurement, which collapses (projects) the wave function into one of the eigenfunctions of the measurement operator. Since the eigenfunctions of the position operator are delta-functions of the coordinates, measurement results in a single observable impact spot. Thus, even though quantum mechanical descriptions of electrons are cast in terms of wave functions, each individual electron is seen as hitting the detector in a single spot, which reinforces the intuitive perception of electrons as microscopic particles.

A single measurement cannot reveal the inherently delocalized probability distribution associated with a photoelectron; by measuring we obtain only one of the possible outcomes. However, by repeating the same experiment many times we accumulate a statistical distribution of measured impact points, a probability density of photoelectrons. The Born interpretation of quantum mechanics equates the square modulus of the wave function with a probability density. Thus, the distribution measured for many photoelectrons is equivalent to the square modulus of the wave function for a

single photoelectron immediately before hitting the detector.

The accumulation of a photoelectron image, and hence the photoelectron probability density, is illustrated in Figures 3.1 (a)-(c) for 800 nm photodetachment of H^-. The relatively few events in Figure 3.1 (a) seem randomly distributed, but by the time as few as ~200 events have been accumulated [Figure 3.1(b)] a circular pattern begins to emerge. The pattern is much better defined in Figure 3.1 (c), which is the result of approximately 200,000 event measurements. The velocity-mapping electrodes have the effect of flattening the spherical wave front onto the detector, restricting the expansion to the plane of the detector. The distance from any point to the image center is proportional to the electron speed in the plane of the detector due to the now circular expansion.

As mentioned in Chapter 2, the photoelectron spectrum is obtained by integrating the reconstructed image over all angles and performing the appropriate Jacobian transformation. The resulting spectrum, displayed in Figure 2.9 (c), peaks at eKE = 0.80 eV. For $h\nu$ = 1.55 eV, this corresponds to an electron binding energy eBE = $h\nu$ – eKE = 0.75 eV**,** which is the electron affinity of atomic hydrogen. The only difference between this relationship and that for the photoelectric effect (equation 3.1) is the replacement of the work function Φ with the eBE. The imaging result thus provides an alternative demonstration of the concepts involved in the photoelectric effect and photoelectron spectroscopy. In addition to the radial coordinate, the photoelectron signal intensity in Figures 3.1 (c) and (d) also varies with respect to angle θ, reflecting the angular dependence of the free-electron probability density., the photoelectron angular

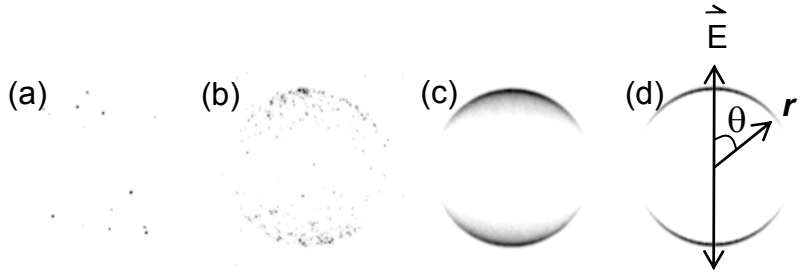

Figure 3.1 Recording of photoelectron impacts after detachment from H^- using 800 nm (1.55 eV) photons. Electrons impact the detector as localized, seemingly random spots. (a) Image corresponding to detection of approximately 15 photoelectrons. (b) Emerging pattern due to many (here ~200) electron-impacts. (c) The noise-subtracted, intensity-scaled distribution for ~200,000 photoelectrons. Darker areas indicate a greater number of electron impacts. (d) Reconstructed cross-section of the 3-D distribution. The electric field polarization vector for the laser radiation is vertical in the plane of the image.

distribution is calculated by integrating the slice in Figure 3.1 (d) with respect to r and plotting the result as a function of θ as shown in Figure 3 (b).

Our focus now turns to the connection between the photoelectron angular distribution and the parent atomic orbital. In the following, we consider the transformation of the electron from a bound 1s atomic orbital to an evolving photoelectron wave upon absorption of a photon:

$$H^- (1s^2) + h\nu \rightarrow H (1s^1) + e^- , \tag{3.2}$$

using simple selection rules.

3.4 Conservation of angular momentum

We extract physical significance from the photoelectron angular distribution $I(\theta)$ by first considering the $\Delta l = \pm 1$ selection rule for a one-photon, electric-dipole allowed transition (within the nonrelativistic, one-electron approximation). In this picture, the absorbed photon carries one quantum of angular momentum. This angular momentum is conserved by transfer to the electron during photodetachment. Since for the H^- 1*s* orbital $l = 0$, the free electron must have $l = 1$, corresponding to a "*p* wave," like an atomic *p*-orbital, but with a different (unbound and time dependent) radial component.

The image in Fig. 3.1 c) is consistent with the photoelectron having p_z character—the image shows a single node perpendicular to the z-axis corresponding to a cosine-squared angular distribution, like that of a p_z orbital. This limiting distribution, calculated as $I(\theta) \propto |Y_{10}|^2$, where Y_{10} is the angular part of the wave function, the spherical harmonic for $l = 1$ and $m_l = 0$, is superimposed with the experimental data in

Figure 2.9 (d). However, our analysis to this point does not address the apparent lack $p_{x,y}$ character which is related to the $l = 1$ and $m_l = \pm 1$ spherical harmonics. In the following, we use another formulation of the electric-dipole selection rule to examine why the free-electron p-wave in this case is polarized along the z-axis.

3.5 The transition dipole moment

Under the one-electron and electric-dipole approximations, the transition dipole moment, defined as

$$\vec{\mu}_{fi} = \int_{\substack{all \\ space}} \psi_f^*(r,\theta,\phi)\ \hat{\mu}\ \psi_i(r,\theta,\phi)\ d\tau = \left\langle \psi_f \left| \hat{\mu} \right| \psi_i \right\rangle, \tag{3.3}$$

must be non-zero for a transition to be allowed. In Eq. (4), $\hat{\mu} = e\vec{r}$ is the dipole operator, $d\tau$ is the infinitesimal volume element, while ψ_i and ψ_f are the wave functions corresponding to the initial (bound) and final (free) states of the electron, respectively. The transition amplitude is proportional to the scalar product of $\vec{\mu}_{fi}$ and the electric field vector. The transition probability P is given by:

$$P \propto \left| \vec{\mu}_{fi} \cdot \vec{\varepsilon} \right|^2 = \left| \mu_{fi,x} \varepsilon_x \right|^2 + \left| \mu_{fi,y} \varepsilon_y \right|^2 + \left| \mu_{fi,z} \varepsilon_z \right|^2, \tag{3.4}$$

where $\vec{\varepsilon}$ is the laser light electric field vector.

For z-polarized laser light, $\varepsilon_x = \varepsilon_y = 0$. Thus only the z component of the transition moment is important in this case. The condition for the absorption of a photon is therefore:

$$\mu_{fi,z} = \int_{\substack{all \\ space}} \psi_f^*(r,\theta,\phi)\ \hat{\mu}_z\ \psi_i\ (r,\theta,\phi)\ d\tau = \left\langle \psi_f \middle| \hat{\mu}_z \middle| \psi_i \right\rangle \neq 0\,. \tag{3.5}$$

The integration in Eq. (3.5) is over all space. However, for the case of H^- photodetachment, only the angular components of the wave functions need be considered to understand the photoelectron angular distribution. The angular part of the final state wave function is identical to the angular part of a hydrogenic orbital and can be expressed as a spherical harmonic function, $Y_{\ell,m}$. Considering only the angular components and recalling that $d\tau = r^2 \sin\theta dr d\theta d\phi$, the condition in Eq. (3.5) simplifies to

$$\int_0^{2\pi}\int_0^{\pi} Y_f^*(\theta,\phi) z Y_i(\theta,\phi) \sin\theta d\theta d\phi = \left\langle Y_f \middle| z \middle| Y_i \right\rangle \neq 0\,, \tag{3.6}$$

where Y_i and Y_f are the spherical harmonics corresponding to the initial (bound) and final (free) states of the electron, respectively. For photodetachment from the 1*s* orbital of H^-, $Y_i = Y_{00}$ and $Y_f = Y_{l,\,m}$ where $l = 1$, so m has possible values of 0 and ±1. Since Y_{00} is an even function, while z is odd, the integral in Eq. (3.6) is nonzero only if Y_f^* is odd with respect to the z-axis. Therefore, the only allowed free-electron wave in this case is that for which $m = 0$, corresponding to the p_z wave.

This result can be illustrated pictorially using the common visualizations of the real p_x, p_y, and p_z angular functions instead of those for p_0 and $p_{\pm1}$:

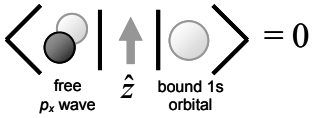

(3.7)

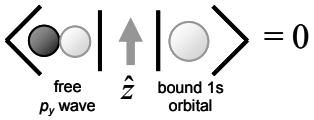

(3.8)

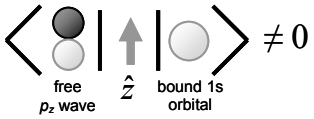

(3.9)

Again, the only final state that corresponds to a nonzero value of the z component of the transition dipole moment for photodetachment from the bound 1s orbital is the p_z (l = 0, m_l = 0) wave. Thus, the only free-electron waves allowed in the one-photon, one-electron photodetachment of $H^-(1s^2)$ using linearly z-polarized light are p_z waves, with intensity peaking in the laser polarization direction (at 0° and 180°). This prediction is in agreement with the experimental angular distribution seen in Figures 3.1 (b)-(d) and (f).

3.6 Extension to other anions

Using H^- as an example, we have shown that the photoelectron angular distribution is related through symmetry to the orbital from which it was detached. It is noteworthy that the results for H^- are also consistent with the classical expectations. The interaction of the oscillating electric field of light (described as classical electromagnetic wave) with bound electrons (described as particles or a charged cloud) would result in an

external force parallel to the electric field vector and should therefore eject electrons predominantly along the laser polarization axis. This classical prediction is in qualitative agreement with the photoelectron angular distribution observed for H^-. However, classical theory generally fails to predict the nature of photoelectron angular distributions; Chapter 4 contains many photoelectron images in which the intensity peaks in the direction perpendicular to the light's electric field vector. Such cases emphasize the necessity for a quantum mechanical explanation of photodetachment.

In general, for atomic orbitals with $l_i > 0$, conservation of angular momentum allows for two possible types of outgoing waves ($l_f = l_i \pm 1$), each containing its own radial and angular components. The photoelectron wave functions in such cases are actually coherent superpositions of both allowed wave types. The relative contributions of each "partial" wave are dependent upon the kinetic energy of the photoelectron. This leads to energy dependence of the photoelectron angular distributions, as will be seen and discussed in Chapter 4.

Photodetachment from molecular anions, while conceptually much more complicated, can also be interpreted using a partial-wave approach, though all possible orientations of the molecule in the laboratory frame must be considered. For the case that the timescale of molecular rotation is much longer than the detachment timescale (typically assumed to be the case), the photoelectron distribution may be modeled as the incoherent average of the distributions that would result from each possible molecular orientation. Approaches for treating molecular photodetachment are outlined in Chapter 4.

3.7 Summary

Photoelectron imaging combines traditional photoelectron spectroscopy with "photography" of quantum objects, yielding snapshots of photoelectron probability densities. Imaging experiments provide a layered approach to the quantum nature of chemical systems: they probe both a system's quantum energy levels and the properties of its wave functions. The unique visual accessibility of imaging makes it a potentially effective teaching tool.

The straightforward experimental result for H^- may be directly connected to fundamental concepts in quantum chemistry. This example (and even others) could be easily incorporated into an introductory quantum chemistry course to extend the traditional discussion of the photoelectric effect and photoelectron spectroscopy into the area of matter waves. In working through this example, we have touched upon the core quantum-mechanical concepts of conservation of angular momentum, the transition dipole moment, components of the hydrogenic orbitals, the Born interpretation of the wave function, and the theory of quantum measurement.

CHAPTER 4

PHOTOELECTRON ANGULAR DISTRIBUTIONS VIA PARTIAL-WAVE INTERFERENCE MODELS

4.1 Introduction

Many theoretical approaches have been applied to the problem of photoelectron cross-sections and angular distributions. This introduction contains an overview of the relevant considerations.

The differential photodetachment cross-section for linearly polarized light in the dipole approximation is proportional to the orientation average of the square of transition dipole moment:[37,43-46]

$$\frac{d\sigma}{d\Omega} \propto \int \left| \mathbf{u} \cdot D_k^{FI} \right|^2 d\Omega', \tag{4.1}$$

where σ is the total photodetachment cross-section, Ω the solid angle, k is the photoelectron's wave vector, **u** is the unit vector in the direction of the laser polarization, D_k^{FI} the transition dipole matrix element between the final and initial states of the system and Ω′ the solid angle defining the orientation of the molecular frame with respect to the laboratory frame. The integral, over all orientations of the system with respect to the molecular frame and, therefore, polarization of the incident radiation, is unimportant for atoms but necessary for molecules.

Under the one-electron approximation and according to Koopman's theorem, the initial and final states ($\left|\psi_i\right\rangle$ and $\left|\psi_f\right\rangle$) may be approximated as the parent orbital from which the electron is detached and the free electron wave function, respectively:

$$D_k^{FI} = \left\langle \psi_f \left| \mathbf{r} \right| \psi_i \right\rangle \approx \left\langle k \left| \mathbf{r} \right| \psi_{PO} \right\rangle, \tag{4.2}$$

where **r** is the vector position operator, $\left|k\right\rangle$ is the continuum state of the photoelectron and $\left|\psi_{PO}\right\rangle$ the parent orbital. The free electron may be expanded as a superposition of partial-waves or described as a plane wave accompanied by incoming spherical waves.[43] The incoming spherical waves are often neglected, an approach that is expected to be most valid for anion photodetachment or in the limit of extremely large photon energies.[43 47,48] Because a plane wave is not necessarily orthogonal to the bound orbitals, complete or partial orthogonalization, such as Schmidt orthogonalization, or a careful choice of coordinate system is required for a rigorous computation.[49,50]

Differential photodetachment, photoionization and scattering cross-sections have been shown to have the general form under the electric dipole (one-photon) approximation:

$$\frac{d\sigma}{d\Omega} \propto 1 + \beta(\frac{3}{2}\cos^2\theta + \frac{1}{2}), \tag{4.3}$$

where Ω is the solid angle.[36,37,43-45] This may be generalized to

$$\frac{d\sigma}{d\Omega} \propto 1 + \sum_{n=1}^{n} \beta_{2i} P_{2i}(\cos\theta) \tag{4.4}$$

for an *n*-photon process, where P_{2i} is the 2ith Legendre polynomial.[37-40] Using the plane-wave approximation including spherical incoming waves (the central potential model)

for atomic anion photodetachment, Bethe,[51] Cooper and Zare[37,44,45] found the first anisotropy parameter to have the following analytical form:

$$\beta_2 = \frac{l_i(l_i-1)^2 + (l_i+1)(l_i+2)\left(\frac{\chi_{l_i+1}}{\chi_{l_i-1}}\right)^2 - 6l_i(l_i+1)\frac{\chi_{l_i+1}}{\chi_{l_i-1}}\cos(\delta_{l_i+1}-\delta_{l_i-1})}{(2l_i+1)\left[l_i + (l_i+1)\frac{\chi_{l_i+1}}{\chi_{l_i-1}}\right]}. \qquad (4.5)$$

In the above expression, l_i is the orbital angular momentum quantum number of the parent orbital and δ_l is a phase-shift incurred by an l-type scattered wave. The radial dipole integral,

$$\chi_l = \int_0^\infty r \cdot R_{nl_i}(r) R_{kl}(r) dr\,, \qquad (4.6)$$

has been interpreted as the square root of the total cross-section for a scattered l-wave.[1] This result has been quite successful in reproducing experimental photoelectron angular distributions, often by approximating the square of the radial dipole integral using the appropriate Wigner-law[52] cross-sectional energy dependence ($\sigma_l \propto eKE^{l+1/2}$), in spite of the fact that it is only valid in the limit of a detachment threshold.

We cautiously note, however, that this "geometric" approach neglects electron relaxation and correlation, configuration interaction, anionic resonances, interchannel coupling, relativistic effects, certain long-range interactions and environmental effects, which may affect PAD's greatly in some cases.[53] Much theoretical work has addressed these issues for atomic and molecular photoionization and photodetachment.[49,50,54-61] In general, the applicability of existing theoretical models depends upon the level of approximation used and the system considered. The simplest models often agree quite

well with experimental results and can prove useful in conceptualizing the underlying physics.

This chapter presents imaging results for photodetachment of representative atomic and small molecular anions. The experimental results are discussed and used to introduce simple partial-wave strategies for interpreting photoelectron angular distributions. This chapter is intended as an accessible illustration of the basics of photoelectron imaging while laying the groundwork for addressing more complicated systems in later chapters.

4.2 Experimental details and results

All ions were generated from a neutral precursor, mass selected and photodetached in the negative ion photoelectron imaging spectrometer described in Chapter 2. Below are relevant experimental details for generation and photoelectron imaging of hydride, oxide, amide, and azide anions (H^-, O^-, NH_2^-, and N_3^- and NO^-).

4.2.1 Hydride

Atomic hydrogen anions were generated using a precursor of either neat ammonia or 20% ammonia in argon. CAUTION: Ammonia gas is highly corrosive and toxic; all gas lines should be tested for leaks and proper ventilation employed as a first requirements for working with this gas.

The ions are understood to be formed via resonant dissociative electron attachment to ammonia, with the lowest capture resonance peaking at ~ 5.65 eV, and

yielding both $NH_2^- + H^\cdot$ and $NH_2^\cdot + H^-$ fragmentation pathways, with the anions in their ground electronic states.[62-64] The cluster anion series $H^-(NH_3)_n$ and $NH_2^-(NH_3)_n$ are also efficiently formed in the expansion (see the mass spectra in Figure 2.4 and elsewhere[65,66]).

The anions were separated and characterized in the time-of-flight mass spectrometer. Photodetachment of H^- was performed at 787 nm using the fundamental of the regeneratively amplified femtosecond titanium sapphire laser, and 532 and 355 nm using the second and third harmonics, respectively, of the yttrium aluminum garnet laser. The top and bottom imaging electrodes set to +900 and −330 V, respectively. For all H^- photodetachment experiments the laser beam was slightly focused using a lens of focal length 2 m positioned about 1 m before the laser-ion interaction region. Images and background were recorded in five 5-minute batches for individual images corresponding to ~21,400 (fs laser) or 15,000 (YAG laser) experimental cycles. Three images were collected at 355 nm and five at 532 and 800 nm, respectively. Images were analyzed both individually (for anisotropy statistics) and cumulatively (for figures). The raw and Abel-transformed cumulative images are displayed in Figure 4.1, some of which were also reported previously.[19,20] Figure 4.2 contains the corresponding energy spectra and photoelectron angular distributions. The peak electron kinetic energies, binding energies and average anisotropy parameters are tabulated in Table 4.1. The photoelectron anisotropy parameters are plotted as a function of eKE in Figure 4.3, with error bars corresponding to ± one standard deviation.

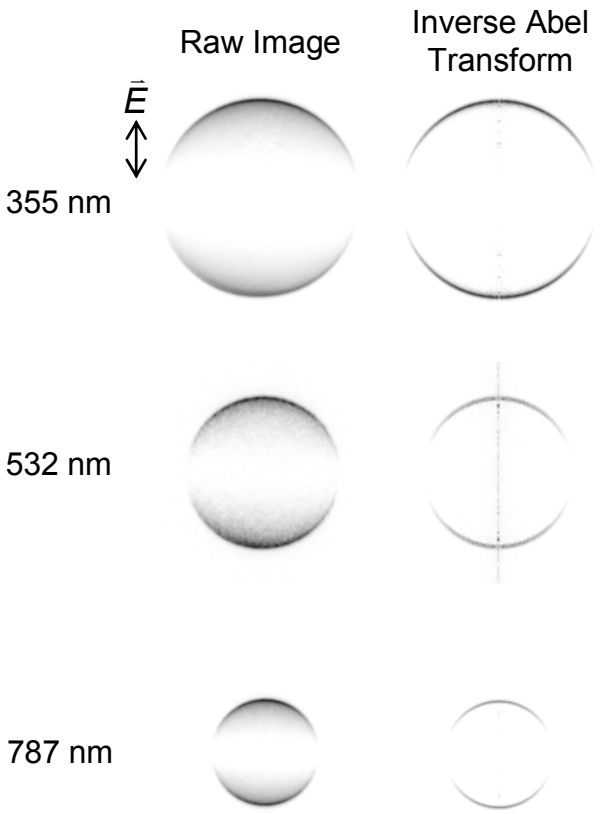

Figure 4.1 Raw and Abel-inverted images for photodetachment from H^- at 355 nm, 532 nm and 787 nm as indicated. Intensity scaling is arbitrary.

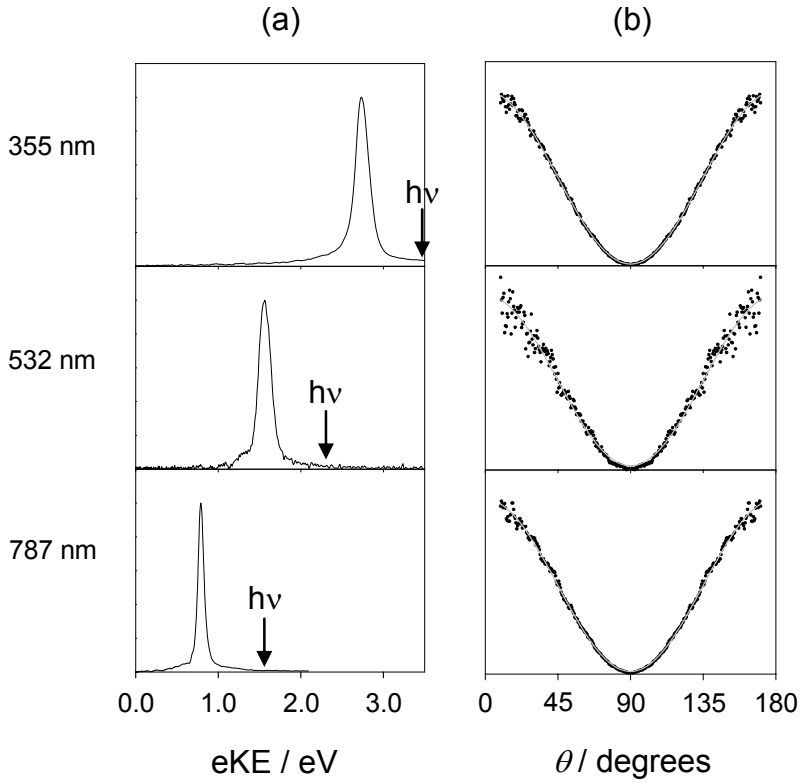

Figure 4.2 Photoelectron (a) energy spectra and (b) angular distributions for photo-detachment from H^- at 355 nm, 532 nm and 787 nm as indicated. Intensities are arbitrarily scaled for identical peak intensities.

	Transition	PO	λ /nm	hν /eV	eKE /eV	eBE /eV	ΔE_{pix} / eV	FWHM / eV	β
H^-	$^2S \leftarrow ^1S$	1s	355	3.49	2.74	0.75	0.020	0.20	1.95 ± 0.04
			532	2.33	1.58	0.75	0.015	0.18	1.89 ± 0.10
			787	1.58	0.83	0.75	0.011	0.11	1.93 ± 0.08
O^-	$^3P \leftarrow ^2P$	2p	266	4.66	3.20	1.46	0.021	0.19	–0.11 ± 0.02
	$^1D \leftarrow ^2P$				1.25	3.41	0.013	0.12	–0.86 ± 0.11
	$^3P \leftarrow ^2P$		355	3.49	2.03	1.46	0.017	0.07	–0.55 ± 0.04
	$^1D \leftarrow ^2P$				0.07	3.42	0.003	0.04	–0.10 ± 0.05
	$^3P \leftarrow ^2P$		399	3.11	1.65	1.46	0.015	0.13	–0.655 ± 0.001
	$^3P \leftarrow ^2P$		798	1.55	0.09	1.46	0.004	0.05	–0.18 ±0.02
NH_2^-	$^2B_1 \leftarrow ^1A_1$	b_1	351†	3.53†	2.75†	0.78†			0.34 ± 0.05†
			355	3.49	2.72	0.77	0.020	0.20	0.46 ± 0.03
			390	3.18	2.40	0.78	0.019	0.14	0.20
			488‡	2.54‡	1.77‡	0.77‡			–0.024 ± 0.012‡
			532	2.33	1.56	0.77	0.015	0.15	–0.08 ± 0.06
			786	1.58	0.81	0.77	0.011	0.10	–0.68 ± 0.01
N_3^-	$^2\Pi_g \leftarrow ^1\Sigma_g$	π_g	266	4.66	2.00	2.66	0.017	0.14	–0.82
			355	3.49	0.83	2.66	0.011	0.10	–0.35
			391	3.17	0.50	2.67	0.008	0.092	–0.16

† From the work of Wickham-Jones et al.[3]
‡ From the work of Celotta et al.[2]

Table 4.1 Summary of photodetachment results for H^-, O^-, NH_2^-, and N_3^-. The detachment wavelength, photon energy, peak eKE, and corresponding eBE of each observed transition are listed, along with the corresponding parent orbital (PO). The energy increment corresponding to one pixel (ΔE_{pix}) at the peak eKE, full-width at half-maximum (FWHM) and anisotropy parameters (β, plus or minus two standard deviations where applicable) of each transition are also listed.

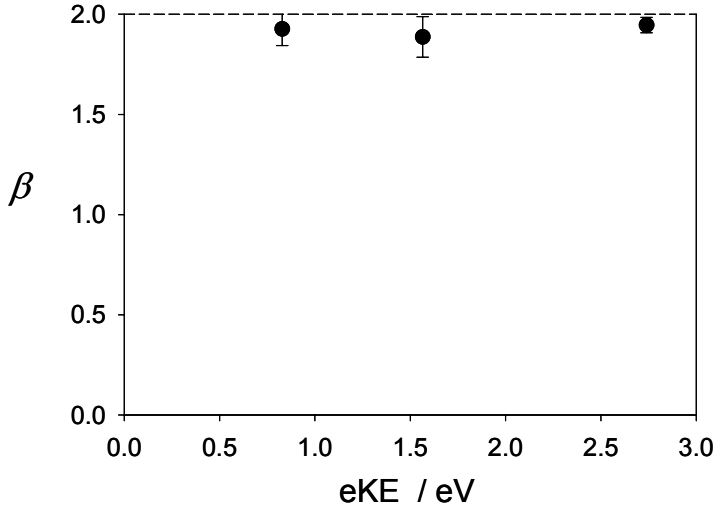

Figure 4.3 Photoelectron anisotropy parameters (β) vs. electron kinetic energy (eKE) for the $^{2}S \leftarrow ^{1}S$ H^- photodetachment transition. Error bars correspond to plus or minus two standard deviations .

4.2.2 Oxide

Oxide anions were generated using either a precursor of neat to 20% N_2O in argon or a mixture of 15% O_2 in CO_2, regulated into the pulsed nozzle at 20 psig. Dissociative electron attachment (by slow, secondary electrons in the expansion) to N_2O and CO_2 is understood to result in formation of O^-.[67-71] Electron attachment to atomic oxygen generated by collision-induced dissociation of N_2O, O_2 or CO_3 in the expansion may also contribute to the ion yield. Images were collected for photodetachment from O^- at 266, 355, 399 and 800 nm, with the top and bottom imaging electrodes at 900 V and –330 V, respectively and the laser beam mildly focused by a Fresnel lens (f = 2 m) positioned approximately 1.2 m upstream of the laser-ion interaction region. The raw and Abel-inverted images in Figure 4.4 each correspond to a combination of three individual images each collected over 90,000 (266 nm and 355 nm) or 69,300 (399 nm and 800 nm) experimental cycles. The cumulative photoelectron energy spectra and angular distributions are displayed in Figure 4.5. The angular distributions, computed over the full width at half-maximum of each transition in the individual reconstructed images, were fit to the form of equation 4.3. The average anisotropy parameters are reported along with an uncertainty of plus or minus two standard deviations for each transition in Table 1, and plotted vs eKE in Figure 4.6.

4.2.3 Amide

Amide (NH_2^-) was formed under the same conditions as H^-. Photodetachment was performed at 355, 390, 532, and 786 nm. Cumulative images, corresponding to the

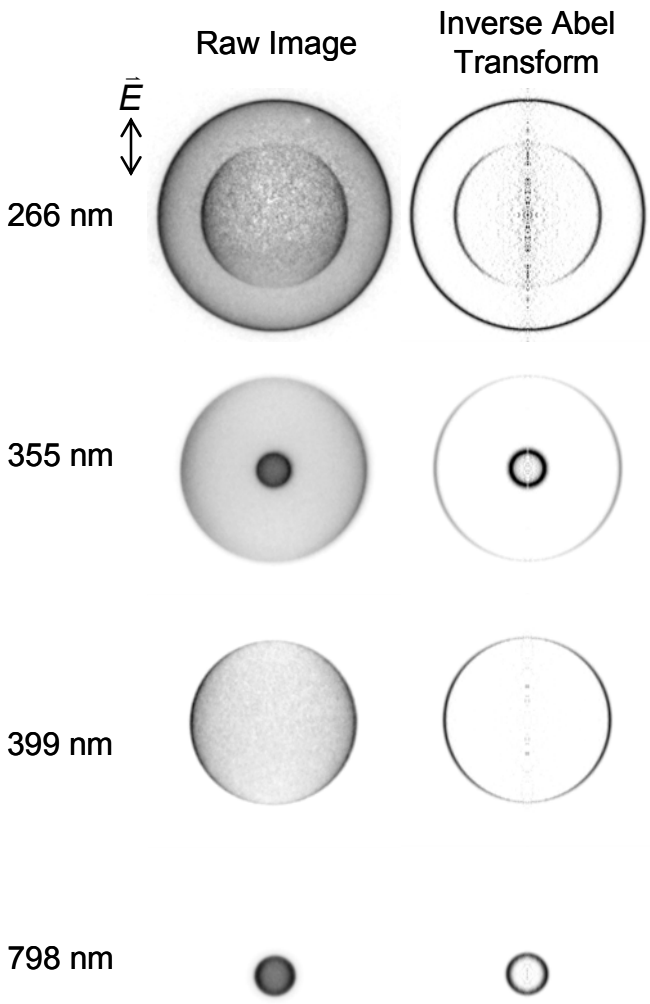

Figure 4.4 Raw and Abel-inverted photoelectron images for 266, 355, 399 and 798 nm photodetachment of O^-.

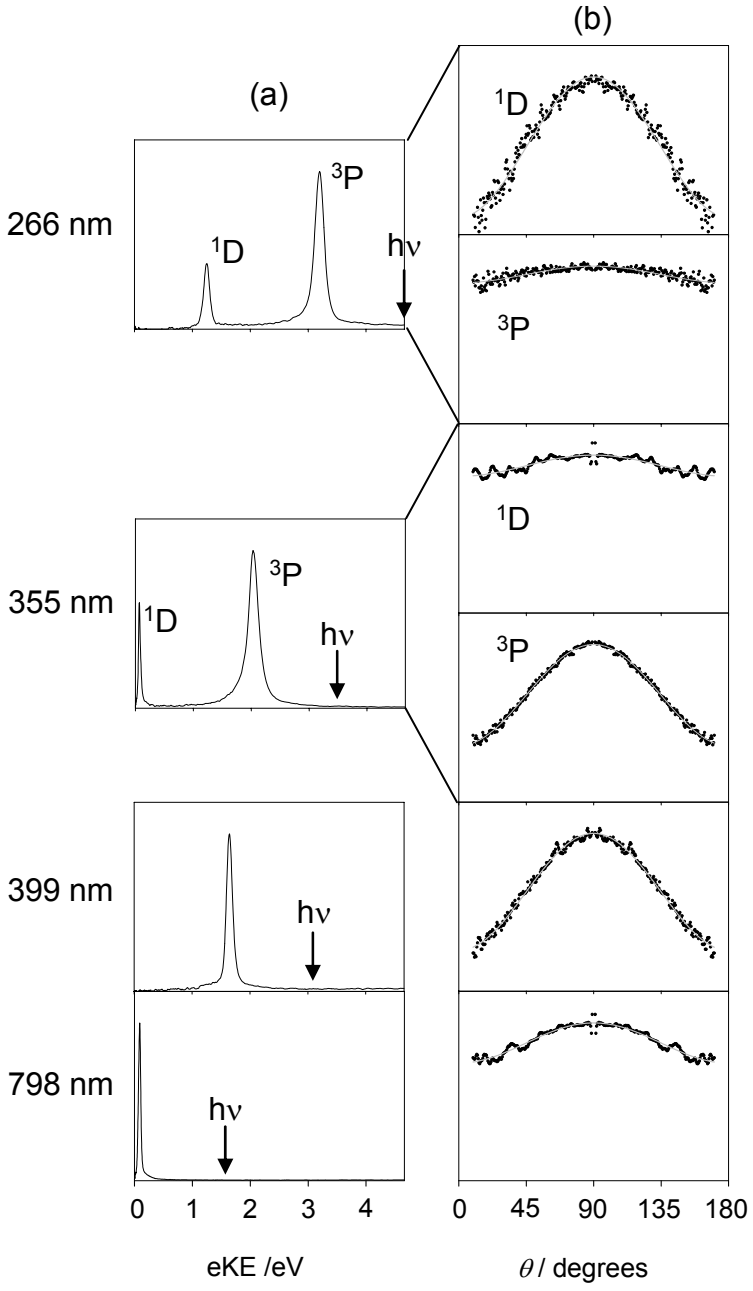

Figure 4.5 Photoelectron (a) energy spectra and (b) angular distributions for photo-detachment from O^- at 266 nm, 355 nm, 399 nm, and 798 nm as indicated. See text for details.

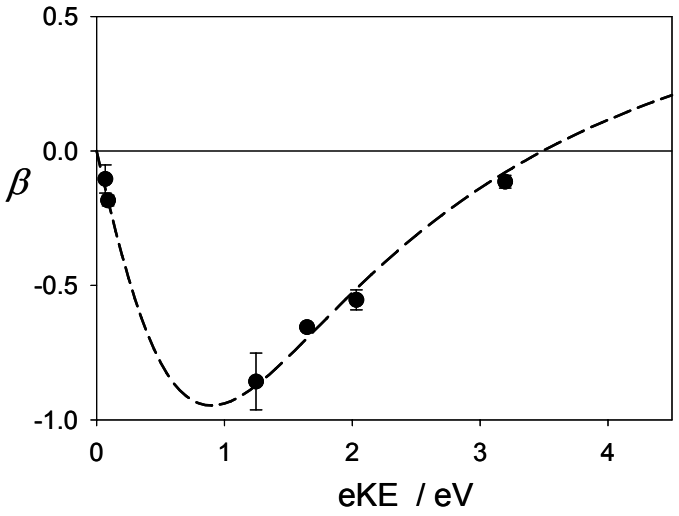

Figure 4.6 Photoelectron anisotropy parameters for photodetachment from O^- plotted as a function of electron kinetic energy (eKE). Error bars correspond to plus or minus two standard deviations. The Wigner-Bethe-Cooper-Zare fit to the experimental data is displayed as a dashed curve for $l_i = 1$, $A = 0.55$ and $\cos\delta = 0.96$ as reported by Hanstorp et al.[1]

sum of five (355 nm and 532 nm), three (786 nm) or fifteen (390 nm) individual images, are displayed for Figure 4.7 along with the corresponding Abel-inversions. The individual images correspond to 150,000 (355 nm, 532 nm), 42,000 (786 nm) or 21,000 (390 nm) experimental cycles. The energy spectra, peak energies and angular distributions, displayed in Figure 4.8, were derived from the cumulative images. The anisotropy parameters are taken as the average plus or minus two standard deviations of the results for individual images (with the exception of the 390 nm result, for which only the cumulative image was analyzed due to the signal-to-noise level) and plotted vs eKE in Figure 4.9. The results are summarized in table 4.1.

4.2.4 Azide

Azide ions were generated by dissociative electron attachment to benzyl azide,[72,73] which was prepared as follows based upon a common synthesis.[74] CAUTION: Though no problems were encountered during this synthesis, some azides are known to be explosive. A careful analysis of safety hazards should be performed before attempting to recreate this synthesis. Some important considerations are as follows, though they should not be taken as complete or comprehensive list: sodium azide (NaN_3) may explode when heated and should not come into contact with heavy metals, particularly lead or copper, or alkyl halides, as even more explosive heavy metal or alkyl azides may form. Caution should be taken to avoid heating, high pressures and shock to the reaction mixture, product and byproducts. The target itself may be explosive, though no incidents have been reported. Contact of azides with acids or water may release hydrogen azide

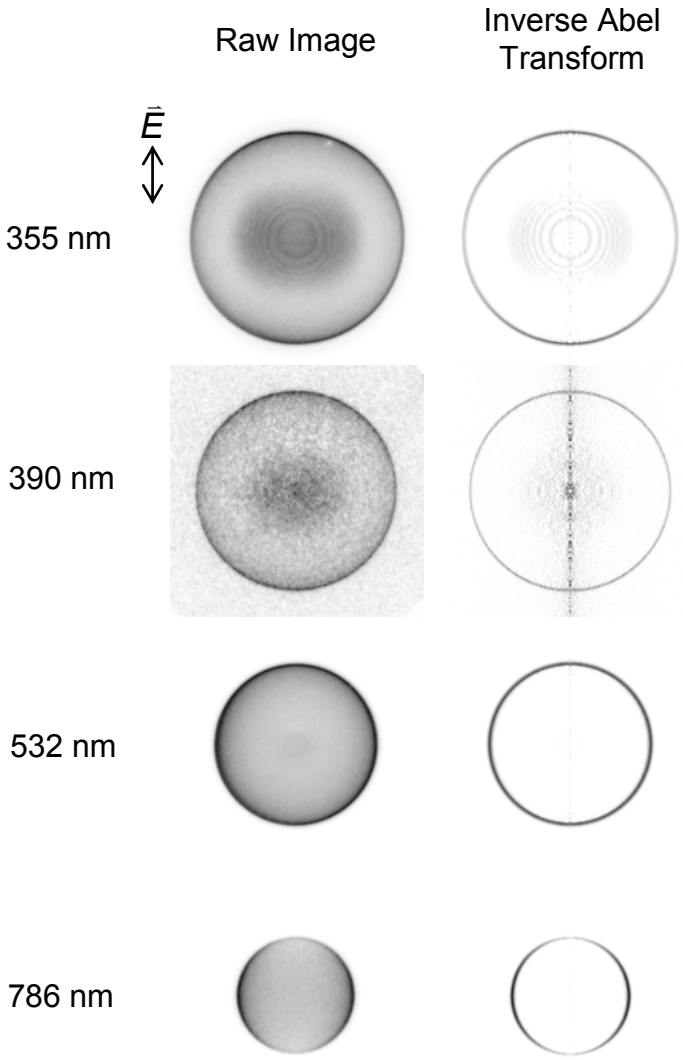

Figure 4.7 Raw and Abel-inverted photoelectron images for 355 nm, 390 nm, 532 nm and 786 nm photodetachment from NH_2^-, as indicated. Intensity scaling is arbitrary.

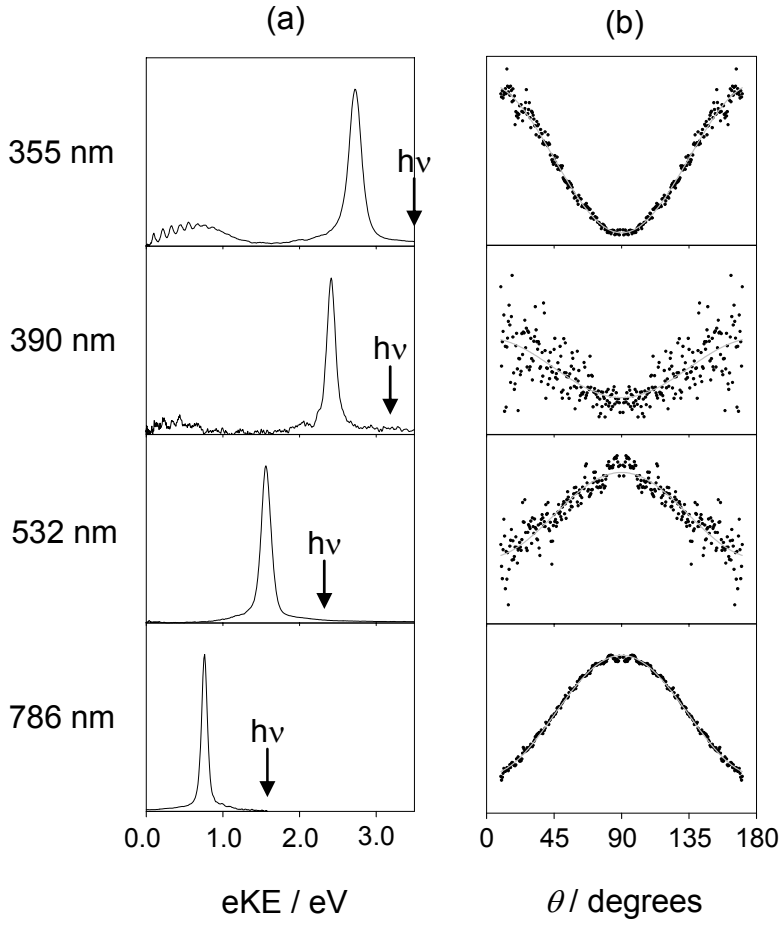

Figure 4.8 Photoelectron (a) energy spectra and (b) angular distributions for 355 nm, 390 nm, 532 nm and 786 nm photodetachment from NH_2^-. Intensities are arbitrarily scaled for identical peak intensities. Photoelectron angular distributions correspond to the lowest-eBE transition.

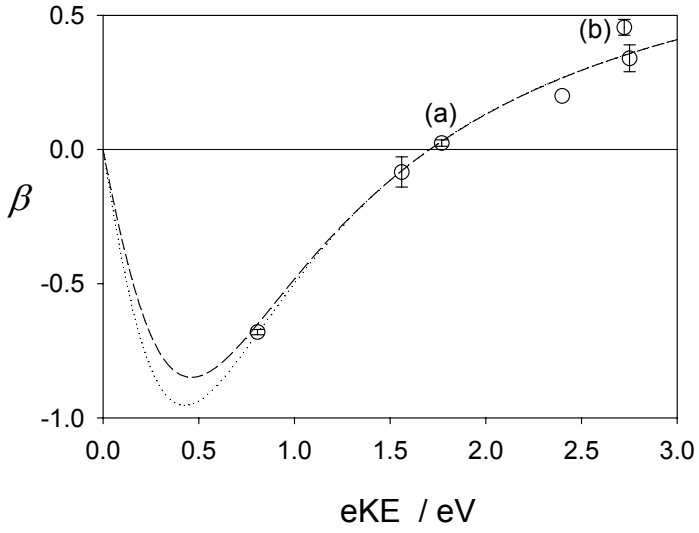

Figure 4.9 Photoelectron anisotropy parameters for the $^2B_1 \leftarrow {}^1A_1$ NH_2^- photodetachment transition at 355 nm, 390 nm, 532 nm and 786 nm plotted vs. eKE. Literature results for (a) 488 nm (Celotta et al.[2]) and (b) 363.8 nm (Wickham-Jones et al.[3]) photodetachment are also included. The dashed line is the Wigner-Bethe-Cooper-Zare curve fit to all data points ($l_i = 1$ $A = 1.09$, $\cos\delta = 0.934$). The dotted line is a fit to the group theoretical model. See text for details.

(HN_3) gas, which is highly toxic and explosive. Proper safety precautions should be taken including performing the synthesis behind a blast barrier in a fume hood in addition to routine personal protective equipment and proper disposal of waste. [75-82]

The following was performed in collaboration with Dr. Ian Jones, an expert synthetic organic chemist: ~3 mmol of sodium azide (NaN_3) were dissolved in 5 mL of dimethyl sulfoxide (DMSO) in a round-bottomed flask. Approximately 0.35 mL (~3 mmol) of benzyl bromide were added slowly and dropwise to the sodium azide solution with stirring behind a barrier in a fume hood. The mixture was allowed to stir for approximately 12 hours upon which the mixture was slightly yellow and any salt or precipitates had dissolved. The flask contents were poured into a separatory funnel, along with one water washing of the flask and ~30 mL diethyl ether. The aqueous layer was washed three times with ether. The separated ether washings were dried over magnesium sulfate and rotavapped to remove the ether. (Note: use CAUTION when rotavapping.) The flask contents were filtered over a small silica gel column with pentanes as the mobile phase. The filtrate was collected in a vial and rotavapped to remove the pentanes. The flask was rinsed with a small quantity of diethyl ether which was added to the vial and further rotavapped. The product's identity was verified by ^1H NMR, which also revealed the presence of ether. The mixture was further evaporated to remove the remaining ether, yielding 337 mg of benzyl azide, an 86.7% yield.

Benzyl azide was seeded in argon by passing the argon carrier gas with a stagnation pressure of ~25 psig through a stainless steel sample holder containing ~100

mg of benzyl azide approximately six inches upstream of the nozzle. Azide formation is expected to occur via dissociative secondary electron attachment to benzyl azide.[72,73]

Azide was identified in the time-of-flight mass spectrum and photodetached with the second harmonic from the Ti:Sapph laser (391 nm) and the third (355 nm) and fourth (266 nm) harmonics of the Nd:YAG laser. Images and background were collected in 5 minute batches, each corresponding to 21,300 (391 nm) or 15,000 (355 and 266 nm) experimental cycles, with the imaging electrodes set to 900 and –330 V, respectively. Figure 4.10 contains the background-subtracted sums of all images collected at each respective wavelength (five each at 391 and 355 nm, ten at 266 nm), along with their Abel inversions. Only the cumulative images were analyzed and no statistics are reported. The energy spectra and angular distributions for the sole transition are plotted in Figure 4.11. Peak energies and angular distributions are listed in table 4.1.

4.3 Discussion

In the following, we discuss the imaging results for H^-, O^-, NH_2^-, N_3^- and NO^- with an emphasis on interpreting the photoelectron angular distributions.

4.3.1 Photodetachment from an s-orbital (H^-)

All of the photoelectron images for H^- (Figure 4.1) contain a single transition corresponding to removal of a photoelectron from the 1s orbital of hydride:

$$H^- (^1S, 1s^2) + h\nu \rightarrow H (^2S, 1s^1) + e^-(eKE). \quad (4.7)$$

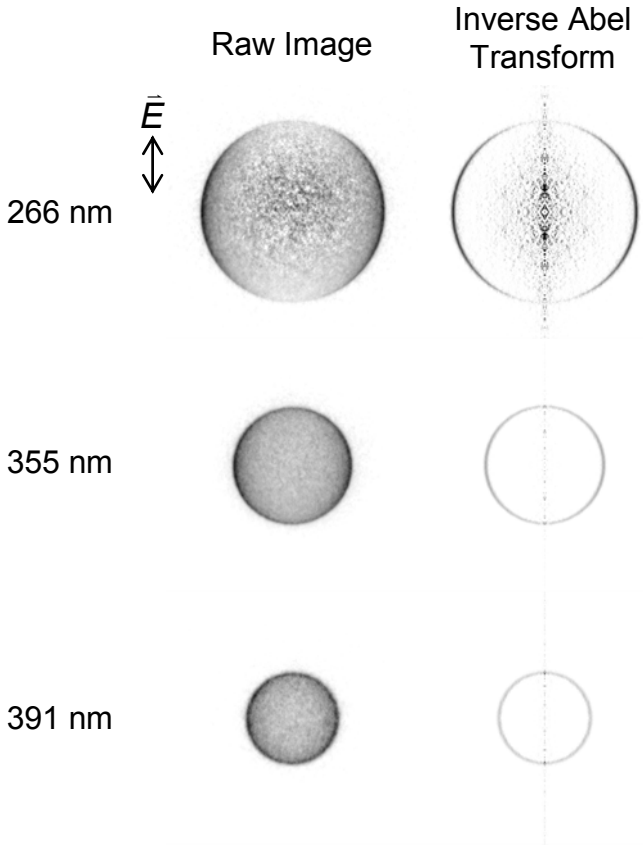

Figure 4.10 Raw and Abel-inverted photoelectron images for 266 nm, 355 nm and 391 nm photodetachment of N_3^-. Intensity scaling is arbitrary.

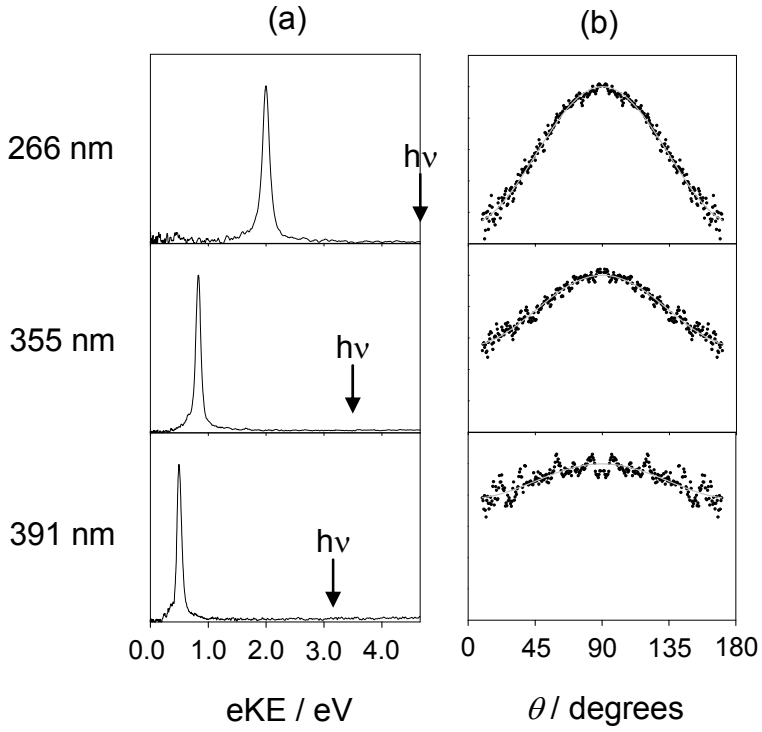

Figure 4.11 Photoelectron (a) energy spectra and (b) angular distributions for 266 nm, 355 nm and 391 nm photodetachment from N_3^-. Intensities are arbitrarily scaled for identical peak intensities.

The spin-orbit splitting is not resolved. The photoelectron kinetic energy spectra peak at 1.70 eV (355 nm), 1.57 eV (532 nm) and 0.83 eV (800 nm), respectively, each corresponding to a vertical detachment energy of 0.75 eV, the electron affinity of atomic hydrogen.[83,84]

All of the images are extremely anisotropic. The reconstructed angular distributions (Figure 4.2) peak strongly parallel to the direction of the laser polarization, dropping to nearly zero intensity at θ = 90°, regardless of the photoelectron kinetic energy. Fitting the angular distributions of each individual image to the analytical form yields average β parameters of 1.95 ± 0.04 (355 nm), 1.89 ± 0.10 (532 nm), and 1.92 ± 0.04 (800 nm), with the uncertainties corresponding to plus or minus two standard deviations among the individual images for each wavelength. These results are in good, though not perfect agreement with the Bethe-Cooper-Zare prediction (see equation 4.5) of $\beta = 2$ for photodetachment from an s-orbital ($l_i = 0$). This is the largest possible value for β, corresponding to a $\cos^2\theta$ distribution.

Insight into the underlying physics of s-orbital photodetachment may be gained by considering simple selection rules. First, angular momentum must be conserved. In the one-electron approximation, this means that the photon's angular momentum (s = 1) is transferred to the electron removed during the detachment process, requiring $\Delta l = \pm 1$ between the initial and final states of the electron. Because l cannot be negative, $l_i = 0$ requires $l_f = 1$. This implies that the photoelectron, despite being an unbound wavepacket evolving radially in time, is in an angular momentum eigenstate, particularly one with a defined orbital angular momentum quantum number of l = 1, corresponding to the

angular distribution of a p-orbital. In fact, the experimentally observed angular distributions are essentially the same as those corresponding to a p_z orbital (the square of the spherical harmonic for $l = 1$, $m_l = 0$, is $\left|Y_1^0\right|^2 \propto \cos^2\theta$). The exclusion of the p_x and p_y waves is apparent upon application of the transition dipole selection rule:

$$\langle p_x | z | s \rangle = 0 \tag{4.8}$$

$$\langle p_y | z | s \rangle = 0 \tag{4.9}$$

$$\langle p_z | z | s \rangle \neq 0, \tag{4.10}$$

where $|s\rangle$ is the initial, bound s-state of the electron and $|p_x\rangle$, $|p_y\rangle$ and $|p_z\rangle$ are the three linearly dependent (orthogonal) p-waves. (For linearly polarized light, we have a $\Delta m_l = 0$ selection rule.)

The only allowed symmetry for the photoelectron wave is that parallel to the laser's electric field vector, corresponding to $l = 1$ and $m_l = 0$. In this sense, the H^- photoelectron images are experimental snapshots of the probability distributions corresponding to an unbound p_z orbital.

The nearly $\cos^2\theta$ angular distributions presented here for H^- are consistent with the results of other researchers for the near-threshold regime.[84-86] Similar angular distributions have been reported for photodetachment from s-orbitals in other closed-shell systems; anisotropy parameters of $\beta \geq 1.94$ have been reported for Ag^- and Cu^- at a variety of wavelengths,[87-89] with uncertainties on the order of the deviations from the

Cooper-Zare limit. These results, along with those for H^- presented in this chapter, show no significant deviation from the Cooper-Zare prediction of $\beta = 2$.

It should be emphasized that the one-electron approach outlined here for s-orbital detachment is approximate. For example, detachment from an s-orbital from an atom that also possesses unpaired electrons (e.g. in p- or d-orbitals) has been predicted to yield varying values of β as a result of exit-channel L-S coupling, though this does not apply to the case of H^- (or detachment from the s orbital of any closed shell species).[53] Even in the absence of L-S coupling effects, relativistic interactions may induce deviations from $\beta = 2$ for s-orbital detachment.[53] It has been suggested that small deviations from $\beta = 2$ observed for detachment from s-orbitals are manifestations of relativistic (K^-)[53,90] or L-S coupling (Fe^-)[89] effects, and there is a need for more definitive experiments to elucidate these interactions.

At higher energies (outside of the ranged employed in this study), additional H^- photodetachment exit channels emerge corresponding to excited states of the neutral atom. In this regime, the one-electron picture is expected to be a poor approximation and l (or L) may no longer be a good quantum number for photodetachment due to interchannel coupling.[53] Accessible anionic Feshbach and shape resonances are expected to also influence the electron exit channels.[91-96] In the regime examined here, however, the simple Cooper-Zare model holds up remarkably well.

4.3.2 Photodetachment from a p-orbital (O^-)

Photodetachment[1,97-99] and photoelectron imaging[5,23,100,101] results have been reported for O^- at a variety of wavelengths by a several groups. In the following, independent imaging results for O^- are reported in order to demonstrate characteristic angular distributions for photodetachment from a p-orbital.

Two transitions are apparent in the 266 and 355 nm images and energy spectra, corresponding to removal of an electron from a fully-occupied p orbital to yield the ^3P state of the neutral, or from the singly occupied orbital to yield the ^1D state of the neutral. Both possibilities correspond to removal of a p-electron, so the angular distributions may be treated identically within the non-relativistic, one-electron approximation.

In the case of photodetachment from a non-s atomic orbital, both the $l = l_{l+1}$ and $l = l_{i-1}$ waves will contribute to the photoelectron wave function. Therefore,

$$I(\theta) = \left|\Psi(\theta)\right|^2 \approx \left| \sum_{l_i+1, l_i-1} C_l e^{i(\delta_l + \frac{l\pi}{2})} Y_l^m \right|^2, \tag{4.11}$$

where the phase shift of $l \cdot \pi/2$ is due to the centrifugal barrier, δ_i is any additional phase shift of the l^{th} partial-wave, $Y_{l,m}$ are the spherical harmonics, arbitrarily taken to be unnormalized. While this approximation does not generally yield the correct analytical form of the angular distribution over the entire range, it is accurate at $\theta = 0°$, 180°.

Because, for a one-photon process,

$$I(\theta) \propto 1 + \beta_2 \cdot \left(\frac{3}{2} \cos^2(\theta) - \frac{1}{2} \right), \tag{4.12}$$

we may define the ratio of parallel ($\theta = 0°$) to perpendicular photoelectron intensities as:

$$\rho = \frac{I_{par}}{I_{perp}} = \frac{I(0^\circ)}{I(90^\circ)} = \frac{1+\beta_2 \cdot \left(\frac{3}{2}\cos^2(0^\circ) - \frac{1}{2}\right)}{1+\beta_2 \cdot \left(\frac{3}{2}\cos(90^\circ) - \frac{1}{2}\right)} = \frac{1+\beta_2}{1-\frac{\beta_2}{2}}, \tag{4.13}$$

and thus obtain an expression for β_2

$$\beta_2 = \frac{\rho - 1}{1 + \frac{\rho}{2}}. \tag{4.14}$$

So, any model for a LF photoelectron probability distribution (constructed from partial-wave functions) need only be accurate at θ = 0° and 90° to successfully model photoelectron anisotropy for a one-photon process.

For the case of p-orbital photodetachment, the initial state has $l_i = 1$ and $m_l = 0$, ±1 (in other words, we must consider detachment from a superposition of the three p-orbitals in the laboratory frame). We can approximate the asymptotic angular form of the photoelectron wave function according to the $\Delta l = \pm 1$, $\Delta m_l = 0$ one-electron selection rules. Thus we may model the photoelectron as a linear combination of outgoing s and $d_{0,\pm1}$ waves. Considering the transition dipole matrix elements for detachment from p_x, p_y and p_z orbitals (using the real basis) yields the same result, with the following non-zero matrix elements:

$$\langle s | z | p_z \rangle \neq 0 \tag{4.15}$$

$$\langle d_z | z | p_z \rangle \neq 0 \tag{4.16}$$

$$\langle d_{xz} | z | p_x \rangle \neq 0 \tag{4.17}$$

$$\langle d_{yz} | z | p_y \rangle \neq 0 . \tag{4.18}$$

Because the $l = 2$, $m_l = \pm 1$ partial-waves have zero intensity at $\theta = 0°, 90°$, we will neglect their contributions and write:

$$\Psi_{PE}(0^\circ) \propto C_0 Y_{00}(0^\circ) + e^{i(\delta+\pi)} C_2 Y_{20}(0^\circ), \tag{4.19}$$

and

$$\Psi_{PE}(90^\circ) \propto C_0 Y_{00}(90^\circ) + e^{i(\delta+\pi)} C_2 Y_{20}(90^\circ) \tag{4.20}$$

where we define a relative phase shift $\delta = \delta_2 - \delta_0$. Arbitrarily taking the spherical harmonics to be unnormalized yields:

$$I_{par} \propto \left|\Psi_{PE}(0^\circ)\right|^2 = C_0^{\,2} - 4C_0C_2\cos(\delta) + 4C_2^{\,2} \tag{4.21}$$

and

$$I_{perp} \propto \left|\Psi_{PE}(90^\circ)\right|^2 = C_0^{\,2} + 2C_0C_2\cos(\delta) + C_2^{\,2} \tag{4.22}$$

$$\rho = \frac{I_{par}}{I_{perp}} = \frac{C_0^{\,2} - 4C_0C_2\cos(\delta) + 4C_2^{\,2}}{C_0^{\,2} + 2C_0C_2\cos(\delta) + C_2^{\,2}}. \tag{4.23}$$

So

$$\beta = \frac{\dfrac{C_0^{\,2} - 4C_0C_2\cos(\delta) + 4C_2^{\,2}}{C_0^{\,2} + 2C_0C_2\cos(\delta) + C_2^{\,2}} - 1}{1 + \dfrac{C_0^{\,2} - 4C_0C_2\cos(\delta) + 4C_2^{\,2}}{2C_0^{\,2} + 4C_0C_2\cos(\delta) + 2C_2^{\,2}}}, \tag{4.24}$$

Yielding

$$\beta = \frac{C_0^{\,2} - 4C_0C_2\cos(\delta) + 4C_2^{\,2} - (C_0^{\,2} + 2C_0C_2(\delta) + C_2^{\,2})}{C_0^{\,2} + 2C_0C_2\cos(\delta) + C_2^{\,2} + \dfrac{1}{2}C_0^{\,2} - 2C_0C_2\cos(\delta) + 2C_2^{\,2}} \tag{4.25}$$

$$\beta = \frac{-4C_0C_2\cos(\delta) + 2C_2^{\,2}}{C_0^{\,2} + 2C_2^{\,2}}. \tag{4.26}$$

If $C_l = \chi_l$, where χ_l is the radial dipole integral[44,45] for a partial-wave of type *l*, (see equation 4.5), we arrive at the Bethe-Cooper-Zare result for $l_i = 1$. This approach for arriving at this expression will prove useful for modeling the photoelectron angular distributions for more complicated systems, for which performing a complete plane wave expansion of the continuum state would be much more involved. It is worth noting that if the spherical harmonics had been taken as normalized, then C_l^2 would be equal to the total photodetachment cross-section for a given *l*-type partial-wave, so are in the above form proportional to the total cross-section. According to the Wigner threshold laws,[52] the total scattering cross-section of an *l*-type partial-wave, σ_l, is dependent on the particle's momentum. In the case of partial photoelectron waves for near-threshold anion photodetachment, it is also dependent upon *l*:[52]

$$\sigma_l \propto k^{2l+1} \propto eKE^{l+1/2}. \tag{4.27}$$

The *l*-dependence indicates that a photoelectron angular distribution resulting from combinations of partial-waves with different orbital angular momentum quantum numbers will depend upon the photoelectron kinetic energy. We note that this approximation is only rigorous in the vicinity of the photodetachment threshold. Assuming the validity of the Wigner law throughout the relevant energy range (and not just near threshold), we write

$$\frac{C_{l_i+1}}{C_{l_i-1}} = \frac{\chi_{l_i+1}}{\chi_{l_i-1}} = A \cdot \varepsilon, \tag{4.28}$$

for some constant A inversely related to the size of the parent orbital and $\varepsilon \equiv eKE$.[1] Coupling this approximation with the Bethe-Cooper-Zare equation allows for modeling

the anisotropy parameter as a function of electron kinetic energy. Dividing the numerator and denominator in expression 4.26 by C_0 and combining it with equation 4.28 yields the Wigner-Bethe-Cooper-Zare expression for detachment from a p-orbital:

$$\beta = \frac{2A^2\varepsilon^2 - 6 \cdot A\varepsilon\cos(\delta)}{1 + 2 \cdot A^2\varepsilon^2}. \tag{4.29}$$

The experimentally determined β-values for the O^- detachment transitions are plotted in Figure 4.6 as a function of electron kinetic energy. These results are consistent with others reported for O^- photodetachment.[1,98,101] The Wigner-Bethe-Cooper-Zare model prediction is also plotted for parameters $A = 0.55$ and $\cos\delta = 0.96$ as reported by Hanstorp et al.,[1] in good agreement with our results, even for eKE's as large as 3.2 eV (which is somewhat counterintuitive given the nature of the approximation for cross-sectional energy dependence).

In general, PAD's for photodetachment from an s-orbital are independent of *eKE*. Photodetachment from a p-orbital yields isotropic distributions near zero *eKE* but, as eKE increases the anisotropy parameters become negative, typically reaching a minimum below 2 eV. As the eKE increases further, the anisotropy parameters increase, becoming positive before ultimately leveling off near $\beta = 1$. Angular distributions for photodetachment from a d-orbital are qualitatively similar to those for p-orbital detachment, with the important difference that anisotropy parameters for d-orbital detachment approach $\beta = 0.2$ as the *eKE* approaches zero.

It should be emphasized that the Wigner-law cross-sectional behavior of partial-waves with *eKE* is only valid for near-threshold behaviors for long-distance potentials

that fall off faster than r^{-2}. While it is not immediately clear at what energies the Wigner approximation becomes inadequate, the Wigner dependence is understood to be the first term in an expansion of the "true" [46,102,103] cross-section which may be expressed as follows[46]:

$$\sigma_l \propto k^{2l+1}\left(a_0 + a_1 k^2 + a_2 k^4 + \ldots\right). \tag{4.30}$$

In general, the Wigner (zeroth-order) term alone seems to be sufficient to fit the experimental energy-dependence of photoelectron angular distributions for photodetachment from atomic anions even at kinetic energies in excess of 3 eV. This implies that the ratio of partial-wave cross-sections do not diverge from the Wigner prediction as quickly as the absolute cross-sections, though it is also possible that fitting the scaling coefficient (A in equation 4.28) to experimental data induces some error cancellation.

Corrections to the Wigner (zeroth order) term have been computed using the zero-core contribution (ZCC) model for photodetachment from s, p, and d-orbitals[103] and analytically for different long-range potentials, including r^{-2}, r^{-3}, r^{-4}.[102] Such corrections are necessary in the limit of high electron kinetic energies or when different long-range interaction potentials (i.e. for molecular photodetachment where the corresponding neutral has a significant dipole moment). The Wigner approximation may be avoided by computing the relative cross-sections for a given experiment.

Again, we note that the Bethe-Cooper-Zare approach has been predicted to fail for detachment from open-shell systems due to L-S coupling and correlation effects even

in the non-relativistic approximation.[53] However, as shown in this section and other works,[1,104] it generally performs quite well.

4.3.3 Molecular anions

As one may expect, understanding photoelectron angular distributions for molecular anion photodetachment is more of a challenge than for atomic systems, as l is not a rigorous quantum number for molecules. Also, as molecules are not spherically symmetric, the photoelectron distribution must be averaged over all molecular orientations.[54] Nonetheless, a partial-wave approach may be taken to gain insight into near-threshold PAD's.

One qualitative approach is to apply the dipole moment selection rule using group theory. Assuming the timescale of rotation is longer than that of the photodetachment process, each principal orientation (of which there are typically three) of the molecule may be considered separately, first in the molecular frame. For a given orientation, only partial-waves transforming like the direct product of the irreducible representations of the laser and parent orbital under the point group's symmetry elements are allowed. The functions corresponding to the irreducible representation of the direct product must be transformed to the laboratory frame. The allowed LF partial-waves are identified by the spherical harmonics corresponding to the LF functions. [46,105]

At low electron kinetic energies, one may neglect all partial-waves corresponding to $l > 1$. This has been termed the s&p approach.[105] Because the waves from each unique orientation add incoherently with the others, all orientations of the molecule must be

considered. The corresponding angular distributions are thus qualitatively described by combining the angular probability distributions of the contributing partial-waves. For example, if the analysis yields any number of s waves, the photoelectron angular distribution should be effectively isotropic for small eKE's. If p-waves are present, the photoelectron intensity may be polarized parallel or perpendicular to the electric field vector of the laser. Recalling that $\sum_{m=-l}^{l}\left|Y_l^m\right|^2 = (2l+1)/4\pi$, it becomes apparent that if the ratio of the number of parallel to perpendicular p-waves is >0.5, then β>0; for a ratio <0.5, β<0. While this approach is purely qualitative and only applicable to detachment from small molecular anions at low kinetic energies, its application has accurately predicted the character of the photoelectron angular distributions for photodetachment from a variety of anions.[15,105]

The LF partial-waves may be combined with the Wigner threshold law to obtain a semi-quantitative model of the photoelectron energy dependence. The approach is similar to that outlined in section 4.3.2. In some cases, it may be appropriate to model anion photodetachment as interfering partial-waves emitted from multiple centers, with additional phase shifts parameterized by the internuclear distance and the photoelectron's de Broglie wavelength. [15,106]

In some cases, the parent molecular orbital has symmetry quite close to that of an atomic orbital. In such cases it one may simply approximate the PAD energy-dependence using the Bethe-Cooper-Zare equation coupled with the Wigner approximation.

In the next two sections, photoelectron imaging results for detachment from NH_2^- and N_3^- are presented. For these anions, the relevant parent orbitals are very atomic-like, allowing their photoelectron angular distributions to be discussed in atomic terms, in the non-relativistic and one-electron approximations.

4.3.4 Photodetachment from a p-like HOMO (NH_2^-)

Photodetachment has been previously performed on NH_2^-, yielding experimental photodetachment cross-sections and anisotropy parameters for several electron kinetic energies. [24, 26, 45, 46] In the following, the first photoelectron imaging results for NH_2^- are reported, yielding anisotropy parameters at new wavelengths and allowing for examination of their energy dependence. The NH_2^- images are displayed in Figure 4.7 and the corresponding energy spectra in Figure 4.8.

The 355 nm image displays multiple features, corresponding to photodetachment from the b_1 HOMO and a_1 HOMO−1 of NH_2^- respectively yielding the ground ($^2B_1$) and first excited ($^2A_1$) states of the neutral.[107]

The narrow b_1^{-1} transition (detachment from the b_1 HOMO) is apparent in all of the images in Figure 4.7. Though a small relative intensity peaks corresponding to excitation of the $v_1' = 1$ and $v_2' = 1$ vibrational modes (0.5% and 0.9%) of the neutral, and P, Q, and R branches within the dominant transition have been observed,[3] we do not resolve them here. The relative narrowness of the transition (for example, as compared with those for O^- at similar *eKE*'s) and the virtual lack of a vibrational progression is due

to the quite similar equilibrium geometries of the ground states of the anion and the neutral.[2,3,66]

The a_1^{-1} transition (detachment from the a_1 HOMO–1) is broad with some vibrational resolution at 355 nm [see Figure 4.8 (a)]. The onset of the broad transition is approximately 1.35 eV below the peak of the narrow transition, consistent with the reported energy difference of 1.38 eV[108] between the $^2A_1$ and $^2B_2$ states of NH_2. Parts of this transition are also visible in the 390 nm and 532 nm images. The observed spacing between the lowest-eBE peaks of the a_1^{-1} transition, 0.12 eV (~970 cm^{-1}), is close to that determined via emission spectroscopy for the low-lying bending mode of the $^2A_1$ state, 1158 cm^{-1} (0.14 eV).[108] The excitation of the bending mode upon removal of an electron from the a_1 HOMO–1 is consistent with significant differences in the equilibrium geometries of the anion and excited neutral states. The HNH bond angle and bond length have been reported for the anion as 101.7° and 1.040 Å, and 102.5° and 1.034 Å for the neutral.[109] The $^2A_1$ excited state of the neutral is expected to have a slightly shorter bond-length and an HNH angle of ~144°, understood to deviate from linearity due to Renner-Teller interactions generating a potential barrier at the linear geometry.[110] The significant difference in initial and final equilibrium geometries in the NH_2 ($^2A_1$) ← NH_2^- ($^1A_1$) transition is consistent with the observed vibrational progression.

The anisotropy parameters for the b_1^{-1} transitions in Figures 4.7 and 4.8 are plotted vs. eKE in Figure 4.9 along with several reported by other researchers.[2,3] This transition corresponds to the removal of an electron from a non-bonding (b_1) HOMO of NH_2^- of the same symmetry as a p_x atomic orbital. In fact, this orbital, plotted in Figure

4.12 from a B3LYP/aug-cc-pVT computation in Gaussian 03,[111] is predominantly a p-orbital centered on the nitrogen atom, perpendicular to the plane of the molecule. In order to model the energy-dependence of the anisotropy parameters, we thus approximate the parent orbital as an atomic p-orbital, with l_i = 1, an approximation previously for this system.[3] A nonlinear least-squares fit of equation 4.29 (equivalent to the Cooper-Zare equation for l_i = 1 approximating the cross-sectional energy-dependence with the Wigner law) to the experimental anisotropy parameters yields fit parameters A = 1.09 and $\cos\delta$ = 0.934. The corresponding result is plotted as the dashed curve in Figure 4.9.

We may also consider the allowed partial-waves using a group theoretical approach building on the s&p approach,[46,105] but additionally includes d-waves and ultimately energy-dependence. We must consider the principal orientations of the molecule in the laboratory frame (LF); the p-like orbital may be oriented along the LF X, Y and Z axes. We first consider these orientations in the molecular frame (MF) by taking the electric field vector of the laser to be along the x, y and z MF axes, determine the allowed symmetry of the partial-waves in the MF, then transform these waves into the laboratory frame. This process is illustrated in Figure 4.9.

In order for the transition dipole matrix element to be nonzero, the partial-waves emitted in each principal orientation must transform as the direct product of the irreducible representations corresponding to the parent orbital and the laser's electric field vector in the C_{2v} point group.

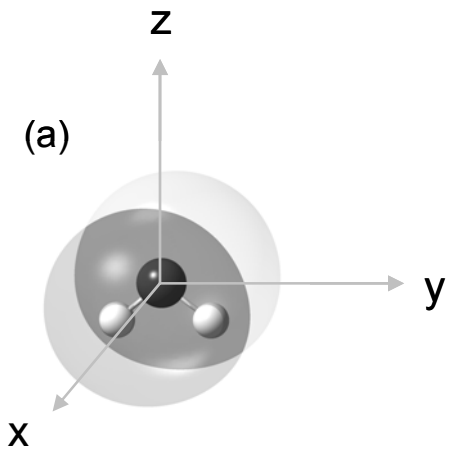

b_1 HOMO $\qquad\qquad$ a_1 HOMO−1

(c)

MF			LF
$\vec{\varepsilon}$	$\Gamma_{las} \times \Gamma_{HOMO} = \Gamma_{PW}$	Γ_{PW} functions	PW's
x	$b_1 \times b_1 = a_1$	z, x^2, (y^2, z^2)	s, p_z, d_{z^2}
y	$b_2 \times b_1 = a_2$	xy	xz
z	$a_1 \times b_1 = b_1$	x, xz	p_x, d_{xz}

Figure 4.12 The computed (B3LYP/aug-cc-pVTZ) (a) HOMO and (b) HOMO−1 for NH_2^- (isosurface values of 0.02). The b_1 HOMO has the symmetry of an atomic p_x orbital centered on the nitrogen with the node in the plane of the molecule; the a_1 HOMO−1 is similar to an atomic p_z orbital. (c) Table outlining the allowed partial-waves (PW) for photodetachment from each principal orientation of the b_1 HOMO. Group theoretical selection rules are considered in the MF, with the functions translating as the resulting irreducible representations converted into LF partial-waves.

With the laser polarization oriented along the MF x-axis both the parent orbital and the laser's electric field vector have b_1 symmetry. Because

$$b_1 \otimes b_1 = a_1, \tag{4.31}$$

(and according to the C_{2v} character table) the allowed partial-waves must transform in the MF like isotropic, x, x^2, y^2 or z^2 functions. This corresponds to s, p_z and d_0 waves in the laboratory frame (where we have neglected the functions that do not correspond to waves with symmetry of the LF spherical harmonics).

For the MF y orientation, the direct product becomes

$$b_1 \otimes b_2 = a_2, \tag{4.32}$$

corresponding to waves that transform like the function xy in the MF, and thus a d_{yz} wave in the laboratory frame. Finally, the MF z orientation yields

$$b_1 \otimes a_1 = b_1, \tag{4.33}$$

corresponding to functions x and xz in both the MF and LF, meaning that p_x and d_{xz} waves are allowed.

The photoelectron probability distribution is the sum of the square of the partial-waves resulting for each principal orientation. Following the approach of section 4.3, we may neglect the LF d_{yz} waves. However, the presence of the p_x wave requires integration over φ. This yields asymptotic intensities of

$$I_{par} = \int_0^{2\pi} d\varphi \left(\left| C_0 Y_0^0(0^\circ, \varphi) + e^{i(\delta+\pi)} C_2 Y_2^0(0^\circ, \varphi) \right|^2 + \left| C_1 Y_1^0(0^\circ, \varphi) \right|^2 \right) \tag{4.34}$$

$$= 2\pi (C_0{}^2 - 4C_0 C_2 \cos(\delta) + 4C_2{}^2 + C_1{}^2) \tag{4.35}$$

and

$$I_{par} = \int_0^{2\pi} d\varphi \left(\left| C_0 Y_0^0(90^\circ, \varphi) + e^{i(\delta+\pi)} C_2 Y_2^0(90^\circ, \varphi) \right|^2 + \left| \frac{C_1}{\sqrt{2}} \left[Y_1^{-1}(90^\circ, \varphi) + Y_1^1(90^\circ, \varphi) \right] \right|^2 \right)$$

(4.36)

$$= 2\pi (C_0{}^2 + 2C_0 C_2 \cos(\delta) + C_2{}^2 + \frac{1}{4} C_1{}^2) \,. \tag{4.37}$$

It follows that

$$\rho = \frac{C_0{}^2 - 4C_0 C_2 \cos(\delta) + 4C_2{}^2 + C_1{}^2}{C_0{}^2 + 2C_0 C_2 \cos(\delta) + C_2{}^2 + \frac{1}{4} C_1{}^2} \tag{4.38}$$

and

$$\beta = \frac{\dfrac{C_0{}^2 - 4C_0 C_2 \cos(\delta) + 4C_2{}^2 + C_1{}^2}{C_0{}^2 + 2C_0 C_2 \cos(\delta) + C_2{}^2 + \frac{1}{4} C_1{}^2} - 1}{1 + \dfrac{C_0{}^2 - 4C_0 C_2 \cos(\delta) + 4C_2{}^2 + C_1{}^2}{2C_0{}^2 + 4C_0 C_2 \cos(\delta) + 2C_2{}^2 + \frac{1}{2} C_1{}^2}} \tag{4.39}$$

$$= \frac{C_0{}^2 - 4C_0 C_2 \cos(\delta) + 4C_2{}^2 + C_1{}^2 - (C_0{}^2 + 2C_0 C_2 \cos(\delta) + C_2{}^2 + \frac{1}{4} C_1{}^2)}{C_0{}^2 + 2C_0 C_2 \cos(\delta) + C_2{}^2 + \frac{1}{4} C_1{}^2 + \frac{1}{2} C_0{}^2 - 2C_0 C_2 \cos(\delta) + 2C_2{}^2 + \frac{1}{2} C_1{}^2} \tag{4.40}$$

$$\beta = \frac{-12C_0 C_2 \cos(\delta) + 6C_2{}^2 + \frac{3}{2} C_1{}^2}{3C_0{}^2 + 6C_2{}^2 + \frac{3}{2} C_1{}^2} \,. \tag{4.41}$$

Making use of the Wigner law for the p-waves yields

$$\left| \frac{C_1}{C_0} \right|^2 \propto B^2 \varepsilon \,, \tag{4.42}$$

$$\beta = \frac{6A^2\varepsilon^2 + \frac{3}{4}B^2\varepsilon - 12A\varepsilon\cos(\delta)}{3 + 6A^2\varepsilon^2 + \frac{3}{2}B^2\varepsilon}. \quad (4.43)$$

Artificially fixing $\delta = 0$ and fitting the above expression to the experimental data yielded fit parameters of A = 1.16 and B = 0.47. The corresponding curve is plotted as a dotted line in Figure 4.9. The fit is nearly identical to the Cooper-Zare prediction near zero eKE and above 1 eV; the two models fit the experimental data similarly for the eKE range of the experimental data points.

The HOMO-1 is plotted in Figure 4.12 (b) (isosurface = 0.02). The orbital has a_1 symmetry, and is similar to a p_z orbital centered on the nitrogen, though there is some bonding character between the two hydrogens. The s&p treatment predicts s and p_z waves (and thus $\beta > 0$) for photodetachment from an a_1 MO; this prediction does not agree with the perpendicular ($\beta < 0$) character apparent for this transition in the 266 and 355 nm images in Figure 4.7. This contradiction implies that this orbital, while not entirely non-bonding, is actually closer to an atomic p-orbital (which, according to the WBCZ model, should indeed yield $\beta < 0$) than a hybridized bonding orbital. The inability of the C_{2v} point group to describe approximately ungerade symmetry along the z axis may limit the use of a group theoretical determination of allowed partial-waves. While we cannot rule out relativistic or resonance effects, the inconsistency with the a_1^{-1} transition suggests that molecular orbitals with nearly atomic-orbital symmetry may be best described in atomic terms.

4.3.5 Photodetachment from a d-like HOMO (N_3^-)

The photoelectron energy spectra for detachment from N_3^- (Figure 4.11) each contain a single, relatively narrow band peaking at eBE ≈ 2.66 eV corresponding to the N_3 X $^2\Pi_g \leftarrow N_3^-$ X $^1\Sigma_g$ photodetachment transition. The lack of an observable vibrational progression reflects the similar geometries of the anion and neutral ground states and is consistent with previous theoretical and photodetachment studies.[73,112] The HOMO, computed at the B3LYP level in Gaussian 03[113] (isosurface = 0.02) is illustrated in Figure 4.13. While the orbital extends over the linear three-atom framework (with a node at the central nitrogen), the symmetry is quite like that of an atomic d_{xz}-orbital centered on the central nitrogen; the HOMO may thus be treated, in rough approximation, as corresponding to $l_i = 2$.

The anisotropy parameters are plotted vs eKE in Figure 4.13. The data were fit to a WBCZ curve under the d-orbital approximation of the HOMO (l_i = 2) with fit parameters of $A = 0.22$ and $\cos\delta = 0.95$. The resulting function fits the data quite well.

4.4 Summary

The results presented in this chapter illustrate characteristic photodetachment dynamics for isolated atomic and atomic-like systems in the absence of electron correlation, relativistic, or resonance effects. Chapters 5 and 6 will address photodetachment from anions in a solvated environment.

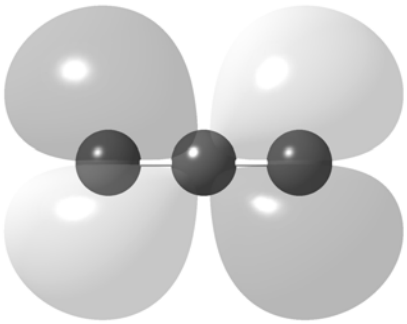

Figure 4.13 Computed (B3LYP/aug-cc-pVTZ) π_g HOMO of N_3^- (isosurface value = 0.02).

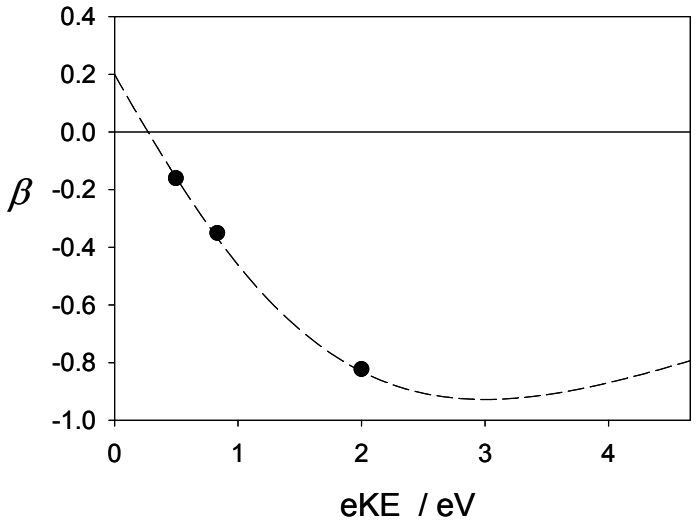

Figure 4.14 Photoelectron anisotropy parameters for the N_3 $^2\Pi_g \leftarrow N_3^-$ $^2\Sigma_g$ transition. The Wigner-Bethe-Cooper-Zare fit to the data is plotted as dashed curve ($l_i = 2$, $A = 0.22$, $\cos\delta = 0.95$).

CHAPTER 5

PARTIAL-WAVE BALANCE AND CHARGE-TRANSFER-TO-SOLVENT IN $H^-(NH_3)_n$ and $NH_2^-(NH_3)_n$ (n = 0-5)

5.1 Introduction

In Chapter 4, we examined the angular distributions for direct photodetachment from a variety of anions in the gas phase. The energy spectra revealed the electron binding energies and thus quantized energy levels of the corresponding neutral. The presence or lack of vibrational progressions also provides a qualitative comparison between the equilibrium geometries of the anion's ground electronic state and electronic states accessed in the neutral. The photoelectron angular distributions are related through symmetry to the parent orbital from which the electron was detached; the energy dependence of these distributions may be modeled using a partial-wave approach to the photoelectron's composition. In general, photoelectron imaging provides two very powerful lenses through which to examine the chemical structure of isolated molecules. Because chemical dynamics generally involve intermolecular interactions, we may ask what can be learned about more complicated chemical environments.

The examination of a series of mass-selected cluster anions of the form $X^-(M)_n$ allows for the systematic study of solvation effects, one solvent molecule at a time. Anions are stabilized more strongly by solvation than the corresponding neutrals due to their net charge. Solvation thus increases the energy gap between the ground states of the anion and its corresponding neutral. This results in a monotonic increase in vertical

detachment energy (VDE) as *n* increases along a solvation series. If the electronic structure of the solute is approximately preserved, the energy spectra retain their general spectral features, though commonly with peak broadening, along a solvation series. Any drastic spectral changes along a solvation series indicate chemistry or physics beyond those of electrostatic charge-solvent interactions or simple photodetachment. Though solvation can affect the bonding structure and geometry of the anion core (as we shall see in Chapter 6), the first system we will address, ammoniated H^- and NH_2^-, may be considered in terms of electrostatic perturbation of the anion core.

As mentioned in previous chapters, photoelectron angular distributions for one-photon photodetachment have the general form[37,44,45]

$$I(\theta) = \frac{\sigma_{tot}}{4\pi}\left[1 + \beta(\frac{3}{2}\cos^2\theta + \frac{1}{2})\right], \tag{5.1}$$

where β is a parameter that defines the polarization of the PAD with respect to the electric field vector of the detachment source, and likewise may be altered by solvation. The angular distribution may be described in terms of partial-waves of defined orbital angular momentum *l*. The types of waves allowed are determined by the parent-orbital symmetry and their relative cross-sections are energy dependent, making the angular distribution (and thus β) energy dependent as well.

In the perturbative regime, solvation is expected to affect a PAD in several ways. First, the solvation-induced shift in VDE necessarily results in a shift in eKE relative to the unsolvated species for photodetachment at a given wavelength. The eKE shift may affect the partial-wave composition of the photodetached electron, potentially altering

the PAD in a manner that can be accounted for with knowledge of the energy-dependence of angular distributions for the solute alone. Second, the electrostatic interaction between an anion and a solvent molecule perturbs the anion electronic wave function, changing the types, relative phases, and/or amplitudes of allowed partial-waves emitted upon photodetachment. Finally, the departing electron may interact with the solvent molecules after or during photodetachment in a way that may be thought of as scattering or exit-channel interactions. The first, pure eKE effect is expected to be always present. The second and the third types of solvation-induced perturbation are both generally expected to occur to some degree, though in certain cases one may dominate. (In Chapter 6 we will discuss cases where anionic resonances of the solvent dominate.)

Separation and understanding of the latter two perturbative effects depends on understanding of the energy-dependence of the PAD's for the unsolvated anion. For atomic anions, this dependence is often modeled by coupling the Bethe-Cooper-Zare model [37,44,45] with the Wigner threshold law,[1,52] as described in Chapter 4. For detachment from the simplest orbitals, atomic s-orbitals, the Bethe-Cooper-Zare model predicts only one allowed partial-wave (a p-wave), independent of electron kinetic energy, corresponding to $\beta = 2$. While electron correlation and/or relativistic effects, could alter PAD's from the Wigner-Bethe-Cooper-Zare (WBCZ) prediction,[53] the theory is generally consistent with experimental results for detachment from small atomic anions and molecular anions. In particular, the WBCZ equation models the energy dependence of photoelectron anisotropy parameters for H^- and NH_2^- fairly well (as

shown in Chapter 4). In this chapter we continue to use the non-relativistic, one-electron approximation when considering the effects of solvation on the photoelectron angular distributions for H^- and NH_2^- photodetachment.

As the simplest anion, one with an energy-independent PAD within the Cooper-Zare framework, H^- is perhaps the most ideal solute for probing the effects of solvation on photoelectron imaging results. Photoelectron spectroscopy on solvated H^- was first performed by the Bowen group.[65,114] Their 488 nm spectra for $H^-(NH_3)_{n=1-2}$ contained relatively narrow dominant bands, with binding energies successively larger than the 0.75 eV electron affinity of atomic hydrogen, consistent with electrostatic solute-solvent interactions. These bands also each had a weaker satellite band at approximately 0.43 eV higher in binding energy, attributed to activation of stretching modes in the ammonia solvent upon photodetachment due to differences in the equilibrium geometries of the anion and the neutral. An additional feature in the $H^-(NH_3)$ spectrum was attributed to the presence of a second isomer, the $(NH_4^+)^{2-}$ double Rydberg anion.[65,114] The group's results are in agreement with theoretical studies predicting the structure of these clusters as an ion-dipole complex with the ammonia loosely coordinated to the hydride through one of its hydrogens,[115-121] along with a stable tetrahedral form for n = 1.[109,118-123] The group's spectra for $NH_2^-(NH_3)_{n=0-2}$ indicated only the solvated NH_2^- isomer in these analogous clusters, [66] consistent with theoretical structure predictions,[109] with up to two vibrational quanta of ammonia excited upon photodetachment.

We now revisit these cluster series via photoelectron imaging. In the following, we present 532 and 355 nm imaging results for $H^-(NH_3)_n$ and $NH_2^-(NH_3)_n$ up to n = 5.

The resulting photoelectron energy spectra are consistent with those previously reported by the Bowen group up to n = 2, but the different wavelengths and inclusion of additional members of each series results in some new features. Specifically, the NH_2 A $^2A_1 \leftarrow NH_2^-$ X $^1A_1$ detachment transition is accessed (as discussed in Chapter 4); we also observe signatures of autodetachment and photofragmentation in some of the larger clusters probed, suggestive of metastable charge-transfer states.

The photoelectron angular distributions, previously unreported for either series for $n > 0$, are examined from the perspectives of perturbation of the electron both pre- and post-detachment. In particular, we create a simple, nonrelativistic, one-electron model for the energy dependence of PAD's for detachment from a parent state with some s- and some p-character and apply it directly to solvated H^- and NH_2^-.

5.2 Experimental

All experiments for this study were performed on the pulsed negative-ion photoelectron imaging spectrometer described in detail in Chapter 2. For these experiments, the neutral precursor was neat or 30% ammonia in argon, yielding the $H^-(NH_3)_n$ and $NH_2^-(NH_3)_n$ cluster series (see the mass spectrum in Figure 2.4)

For each image, the cluster anions of interest were intersected with a linearly polarized laser pulse about 15 cm upstream of the ion detector, between the bottom two electrodes of a velocity-map imaging assembly. Photodetachment was performed with both the second (532 nm) and third (355 nm) harmonics of a nanosecond-pulsed Nd:YAG (50 kHz, QuantaRay by Spectra-Physics) laser. In each experiment, the beam

was slightly focused with a Fresnel lens (f = 2 m) placed approximately 1.2 m upstream of the laser-ion interaction region, to yield laser fluences of 1.6×10^6 W/cm^2 and 1.3×10^6 W/cm^2, respectively, in the region of laser-ion overlap. The experiment was triggered at 50 Hz from the synchronized output of the laser.

Five individual images were obtained for each species at each wavelength, with the exception of $H^-(NH_3)_{n=0-3}$ at 355 nm for which only three were collected. Three-dimensional photoelectron distributions were reconstructed via inverse Abel transform using the BASEX program developed by the Reisler group.[35] All individual images were obtained over 15,000 experimental cycles. We report the cumulative raw images and energy spectra for each species at each wavelength, and the average and standard deviation of the anisotropy parameters determined for each individual image. The bare H^- and NH_2^- peaks were used for energy calibration.

5.3 Results

In the following we present our 355 nm and 532 nm photoelectron imaging results for $H^-(NH_3)_{n=0-5}$ and $NH_2^-(NH_3)_{n=0-5}$. The cumulative raw images and photoelectron energy spectra for each cluster series at each wavelength are presented in Figures 1-4. Peak eBE's (approximate vertical detachment energies) and average anisotropy parameters are indicated in italics for the lowest-eBE peaks originating from direct detachment from the core anion. The energy spectra were derived from the sum of all images collected at the same wavelength for a given cluster.

5.3.1 355 nm photoelectron energy spectra for $H^-(NH_3)_n$

Photoelectron images and energy spectra for $H^-(NH_3)_n$ (n = 0-5) obtained at 355 nm are displayed in Figure 5.1. Peak eBE's and average anisotropy parameters are indicated for the lowest-eBE transitions.

The n = 0 spectrum corresponds to photodetachment from bare H^-. Its single feature reflects removal of a 1s electron, yielding the neutral atom in its ^2S ground state. The hyperfine structure is not resolved. (See Chapters 3 and 4 for more details of H^- photodetachment.)

Photodetachment from singly solvated (n = 1) species yields a similar spectral feature (termed feature I) shifted to a higher eBE, along with a bump (feature II) on its high eBE tail with a peak eBE greater than that of the primary transition by about 0.4 eV. Features I and II persist through n = 5, shifted together, monotonically, to successively higher eBE's and somewhat broadened; we note that solvation-induced broadening of the transition competes with improving energy resolution as n increases and eKE decreases. These features were previously observed for n = 1-2 by the Bowen group, [65,114] and we adopt their assignment of the dominant peaks (I) to direct photodetachment from H^- solvated by n ammonia molecules and the weaker feature (II) to photodetachment with activation of an asymmetric ammonia stretching mode. We do not observe the third peak identified by the Bowen group for n = 1 (VDE = 0.472 eV), assigned to direct photodetachment from the tetrahedral, double-Rydberg state described as $(NH_4^+)^{2-}$.

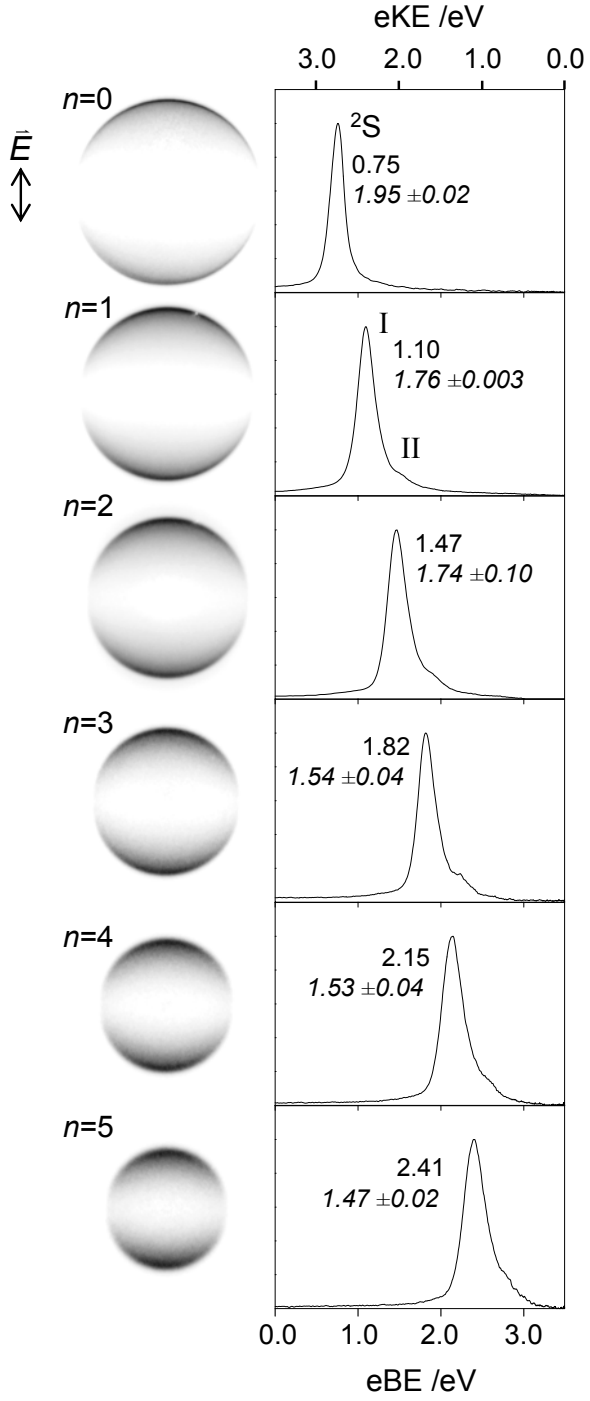

Figure 5.1 Photoelectron images and energy spectra for photodetachment from $H^-(NH_3)_n$ (n = 0-5) at 355 nm. Image intensities are arbitrarily scaled; spectra are scaled for matching peak intensities. Anisotropy parameters and peak binding energies are indicated for the dominant transition. See text for details.

5.3.2 532 nm photoelectron energy spectra for $H^-(NH_3)_n$

The summed 532 nm images and resulting spectra for $H^-(NH_3)_n$ are displayed in Figure 5.2. The spectral features are generally consistent with those obtained at 355 nm, with a few exceptions. First, band II is not visible for $n = 3$, most likely due to threshold cross-sectional effects. Second, for $n = 5$, there is a spike in intensity near the high-eBE cutoff (eBE = 2.33 eV, eKE = 0), which we tentatively assign as a new feature, labeled III.

5.3.3 355 nm photoelectron energy spectra for $NH_2^-(NH_3)_n$

Figure 5.3 contains photoelectron images and energy spectra for $NH_2^-(NH_3)_{n=0-5}$. Photodetachment of unsolvated NH_2^- has been performed previously, with the lowest binding energy transition assigned to removal of an electron from the b_1 HOMO of NH_2^- to generate the neutral amidogen radical in its $^2B_1$ ground state. [2,3,66] While one high-resolution study[3] revealed P,Q, and R rotational branches for this transition, these features are not resolved in our spectrum due to a lower instrumental resolution. The nonetheless narrow width of this transition (and lack of a vibrational progression) is consistent with the small geometry change between the ground states of the anion and the neutral. [3,109,124]

A second, broad transition also appears in the spectrum for $n = 0$, attributed to removal of an electron from the a_1 HOMO−1 orbital of the anion, yielding the $A\ ^2A_1$ state of the neutral. The band's onset is higher in binding energy than the peak of the $^2B_1$ transition by about 1.35 eV, a spacing closely matching that between the ground and first

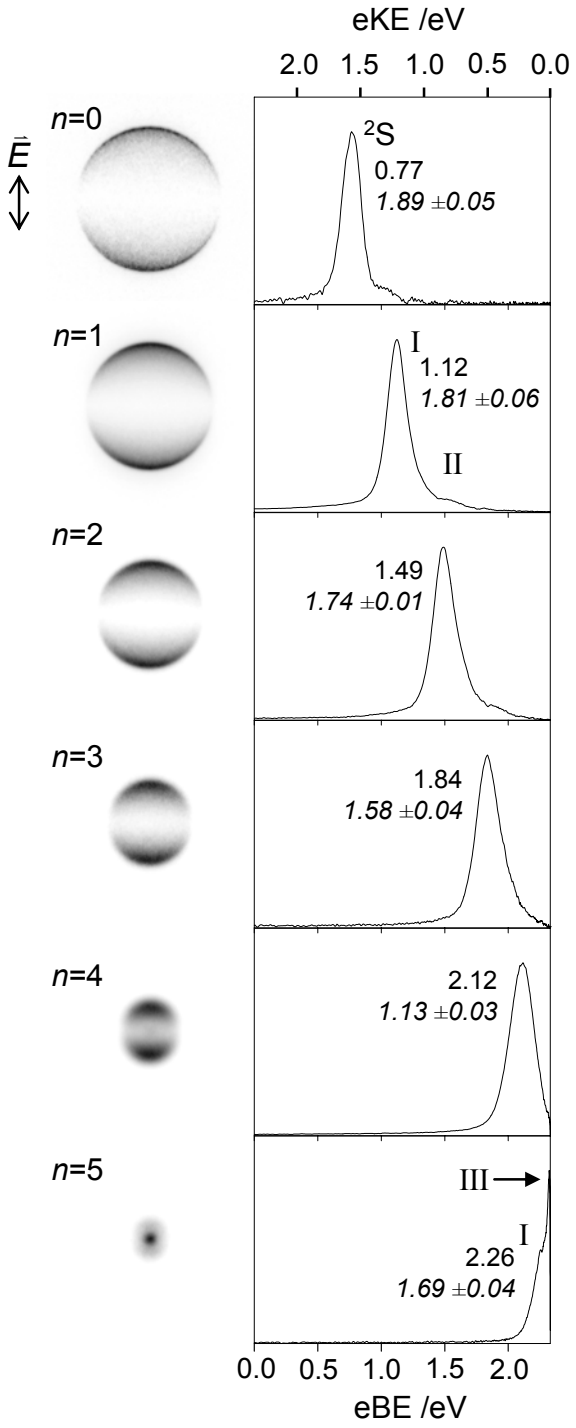

Figure 5.2 Photoelectron images and energy spectra for photodetachment from $H^-(NH_3)_n$ (n = 0-5) at 532 nm. Image intensities are arbitrarily scaled; spectra are scaled for matching peak intensities. Anisotropy parameters and peak binding energies are indicated for the dominant transition.

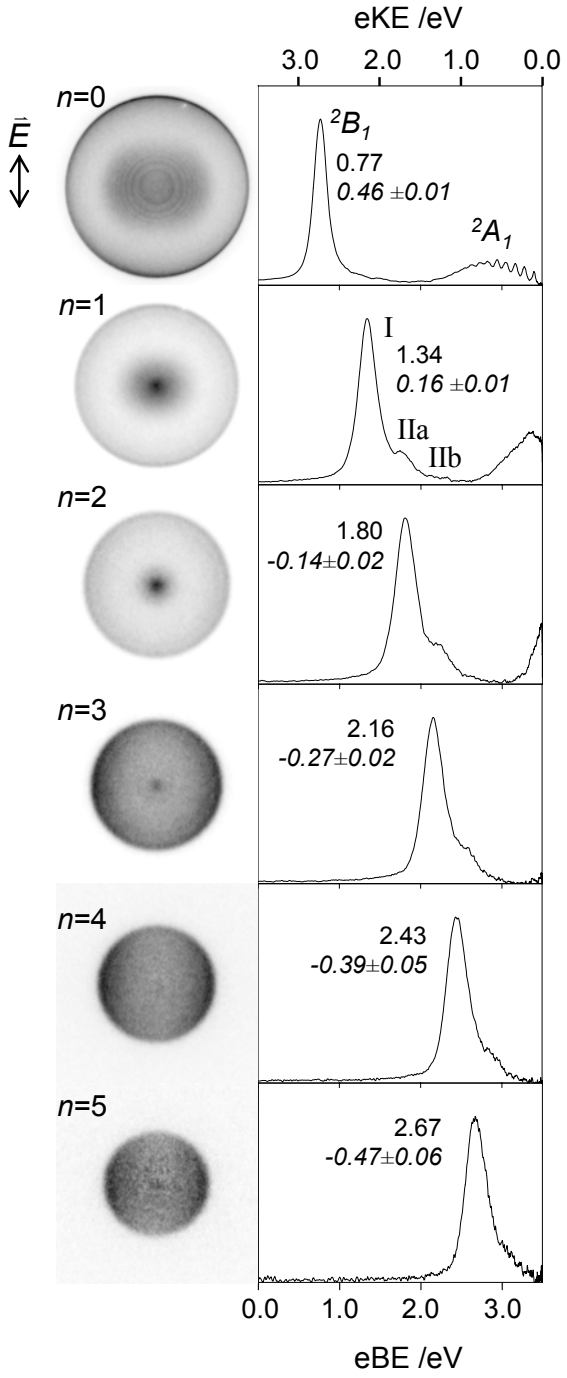

Figure 5.3 Photoelectron images and energy spectra for photodetachment from $NH_2^-(NH_3)_n$ (n = 0-5) at 355 nm. Image intensities are arbitrarily scaled; spectra are scaled to match peak intensities. Anisotropy parameters and peak binding energies are indicated for the dominant transition.

excited states of the neutral (≈ 1.38 eV).[108] The vibrational energy spacing within this band, ≈ 0.12 eV, is consistent within our resolution with the reported[108] bending mode frequency (≈ 0.14 eV) in the $\tilde{A}\ ^2A_1$ state of neutral NH_2. The extent of the vibrational progression indicates a significant geometry change along the bending coordinates between the $\tilde{X}\ ^1A_1$ state of the anion and the neutral $\tilde{A}\ ^2A_1$ state (and thus between the $^2A_1$ and $^2B_1$ states of the neutral). (See Chapter 4 for a more detailed discussion of NH_2^- photodetachment.)

Both features persist in the spectrum for n = 1, shifted to higher binding energies and somewhat broadened. Features IIa and IIb, respectively, reflect activation of one and two NH_3 vibrational quanta,[66] analogous to those observed for $H^-(NH_3)_n$,[65,114] and $OH^-(NH_3)_{n=1,2}$.[125] All features persist as n increases unless clipped or suppressed at or near the high-eBE cutoff (hν = 3.49 eV).

5.3.4 532 nm photoelectron energy spectra for $NH_2^-(NH_3)_n$

The results for $NH_2^-(NH_3)_n$ at 532 nm are displayed in Figure 5.4. For n = 0, the lower-eBE peak is consistent with that in the 355 nm spectrum, but the photon energy is only sufficient to catch the onset of the transition accessing the $^2A_1$ excited state of the neutral. For n = 1, only features I and II are seen.

The n = 2 spectrum contains the same two features seen for n = 1, shifted to higher binding energies, as well as a sharp spike near the high-eBE cutoff (eKE = 0) that appears to be distinct from feature II. This spike (III) persists through n = 5, while direct

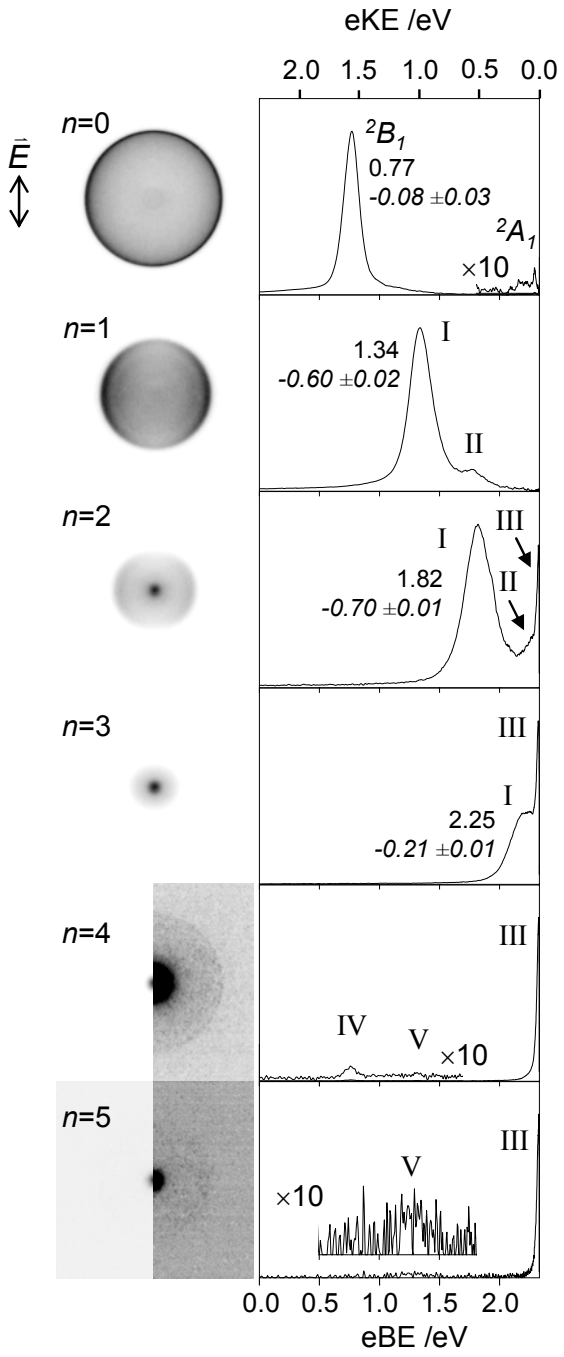

Figure 5.4 Photoelectron images and energy spectra for photodetachment from $NH_2^-(NH_3)_n$ (n = 0-5) at 532 nm. Image intensities are arbitrarily scaled; those for n = 4,5 are shown in split scale to emphasize the less intense features. Spectra are scaled for matching peak intensities, with details for n = 0, 4, 5 enhanced by a factor of ten. Anisotropy parameters and peak binding energies are indicated for the dominant transition. See text for details.

photodetachment of the cluster becomes energetically inaccessible. Because these features are absent from the 355 nm spectra, they are not the result of direct photodetachment.

The n = 4 spectrum contains two additional, weak features, labeled IV and V, at roughly the same binding energies as those for NH_2^- and $NH_2^-(NH_3)$, respectively. Feature V may also be present (at the same eBE) for n = 5. The n = 4, 5 energy spectra are enhanced and images shown in split scale in Figure 4 to emphasize features IV and V.

To better understand features III, IV and V, we repeated 532 nm image collection for $NH_2^-(NH_3)_n$, n = 2-4 at twice the laser fluence. This resulted in no change in the ratio of peak intensities of bands I to III for n = 2 or n = 3, indicating that feature III is not the result of a two-photon process. The ratios of the peak intensities of bands IV and V to that of band I approximately doubled (for n = 4), indicating that peaks IV and V are the result of a two-photon process.

5.3.5 Photoelectron angular distributions

Multiple images were obtained for each species at each wavelength. Anisotropy parameters were computed for each image over the full width at half-maximum (FWHM) of all type I transitions, with the exception of those for $H^-(NH_3)_5$ and $NH_2^-(NH_3)_3$ at 532 nm, for which β was calculated over the lower-eBE halves of the transitions to minimize the contribution from peak III. The average β for all images for a given n at a given wavelength are reported in Figures 5.1-5.4 along with the standard deviation.

Anisotropy parameters for 786 nm and 390 nm photodetachment of NH_2^- (previously reported in Chapter 4) and 786 nm photodetachment of $H^-(NH_3)_{n=0\text{-}2}$ are also included in the respective plots of β vs eKE. The energy spectra are consistent with the 355 nm results for these species and are not reproduced here.

The average anisotropy parameters for $H^-(NH_3)_{n=0\text{-}5}$ and $NH_2^-(NH_3)_{n=0\text{-}5}$ are plotted vs. eKE in Figures 5.5 (a) and 5.5 (b), respectively. Error bars correspond to ± one standard deviation. Anisotropy parameters reported elsewhere for 488 nm photodetachment[2] and 352 nm photodetachment[3] of NH_2^- are also plotted in Figure 5.5 (b).

5.3.6 Photoelectron angular distributions for $H^-(NH_3)_n$

The anisotropy parameters obtained for $H^-(NH_3)_n$ at a given wavelength (closed symbols in Figure 5.5 (a) monotonically decrease in magnitude with increasing solvation number, dropping most rapidly near eKE = 0. The anisotropy parameters for solvated H^- are all smaller in magnitude than those for bare H^-; those for n = 2, 4, and 5 display a clear energy-dependence. These PAD's will be discussed further in Section IV.

5.3.7 Photoelectron angular distributions for $NH_2^-(NH_3)_n$

The angular distributions for photodetachment from NH_2^- are plotted as open circles in Figure 5.5 (b). The β-parameters for ammoniated NH_2^- are not strikingly different from those for bare NH_2^- at similar energies.

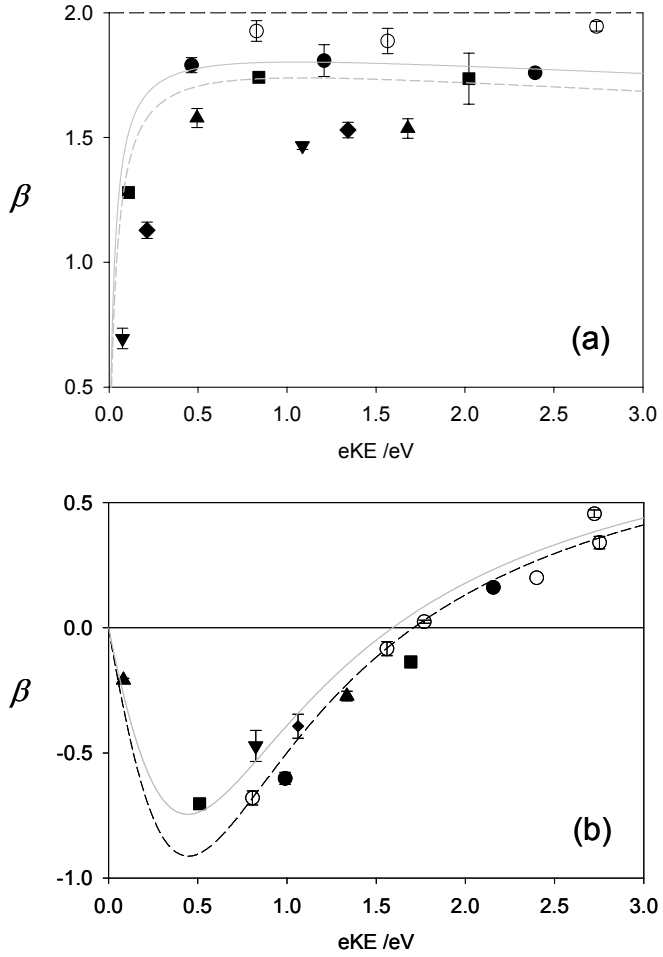

Figure 5.5. (a) Average anisotropy parameters for $H^-(NH_3)_n$ at 532 nm (n = 0-5), 355 nm (n = 0-5), and 786 nm (n = 0-2). The dashed black line at $\beta = 2$ corresponds to the WBCZ prediction for bare H^-. The solid and dashed grey lines are our models for detachment from a perturbed s-orbital having 2.6% and 3.5% p-character, respectively. (b) Average anisotropy parameters for $NH_2^-(NH_3)_n$ at 532 nm (n = 0-5), 355 nm (n = 0-5) and 786 nm (n = 0). Two data points from other studies on bare NH_2^- are also included. The WBCZ fit for photodetachment from bare NH_2^- is plotted as a dashed line. The grey line, corresponding to the model prediction for photodetachment from a p-orbital with 10% s-character. In both plots, open circles correspond to n = 0; closed circles, n = 1; squares, n = 2; point-up triangles, n = 3; diamonds n = 4; point-down triangles, n = 5. Error bars correspond to ± one standard deviation.

5.4 Discussion of photoelectron energy spectra

The *n*-dependence of the energy spectra presented in Section III suggests that both the $H^-(NH_3)_n$ and $NH_2^-(NH_3)_n$ (n = 0-5) cluster series are accurately described as an anionic solute (H^- and NH_2^-, respectively) solvated by *n* ammonia molecules. However, the spectra contain a few unexpected features. Specifically, bands III, IV and V do not result from direct photodetachment from the solvated anion core. Bands IV and V are the result of a two-photon process, while band III is not.

We first consider the nature of band III. This sharp feature appears near zero eKE in the 532 nm energy spectra for $NH_2^-(NH_3)_{n=2\text{-}5}$ and $H^-(NH_3)_5$. Of these species, photodetachment has only been reported for $NH_2^-(NH_3)_2$ (at 488),[66] but in this case, feature III was not observed due to the ~0.2 eV low-eKE cutoff of the spectrometer.

The type III features are essentially identical on the eKE scale, regardless of the cluster for which they are observed; this suggests that they correspond to autodetachment from metastable excited anionic states. Ammonia's known ability to solvate electrons (and the lack of appropriate excited states in the H^- and NH_2^- cores) leads us to assign these features as signatures of autodetachment from a charge-transfer to solvent state (CTTS) accessed upon 532 nm absorption. We note that these signals are only observed for clusters that have a photodetachment threshold near the photon energy.

The binding energies of the two-photon features, IV and V, in our 532 nm spectrum for $NH_2^-(NH_3)_4$ are coincident with those of NH_2^- and $NH_2^-(NH_3)$, respectively. We find it most likely that these species are generated as photoproducts formed after 532 nm excitation of the n = 4 species. While we cannot rule out the

existence of a bound or metastable solvated NH_2^- excited state, it is likely that one 532 nm photon generates a charge-transfer state that reverts back to the original core, with the excess energy released via evaporation of three or four ammonia molecules.

We now briefly compare our results to those obtained in the Neumark group for the analogous $I^-(NH_3)_{n=4\text{-}15}$ cluster series, which was studied via both direct photodetachment and femtosecond photoelectron spectroscopy (FPES). [126,127] The one-photon photoelectron spectra of $I^-(NH_3)_{n=0\text{-}8}$ exhibited a monotonic increase in binding energy along the cluster series, consistent with electrostatic solvation of the iodide core. The difference in vertical detachment energy from $n = 1$ to $n = 0$, $\Delta VDE_{1,0} \approx 0.25$ eV, indicates that I^- is stabilized somewhat less by solvation with ammonia than either H^- ($\Delta VDE_{1,0} \approx 0.34$ eV) or NH_2^- ($\Delta VDE_{1,0} \approx 0.57$ eV). However, change in VDE with n varies smoothly for all three cluster series (see Figure 5.6), suggesting that a solvent shell has not been completed within the size range examined.

Time-resolved two-photon signal for $I^-(NH_3)_{n=4\text{-}15}$ was assigned to excitation of a CTTS state, followed by its photodetachment at pump-probe delays of up to ≈ 2.5 ps. The smooth temporal evolution of the excited state's binding energy and photodetachment cross-section was attributed to solvent rearrangement to accommodate the electron, with excited-state lifetimes ranging from 12 to 53 ps. While no autodetachment was directly observed (presumably due to the detector's low-eKE cutoff of ≈ 0.2 eV), the authors viewed this as the most likely relaxation mechanism due to the lack of observation of photofragments.[126] Our present observation of both autodetachment and photofragment signatures in the 532 nm photoelectron spectrum for

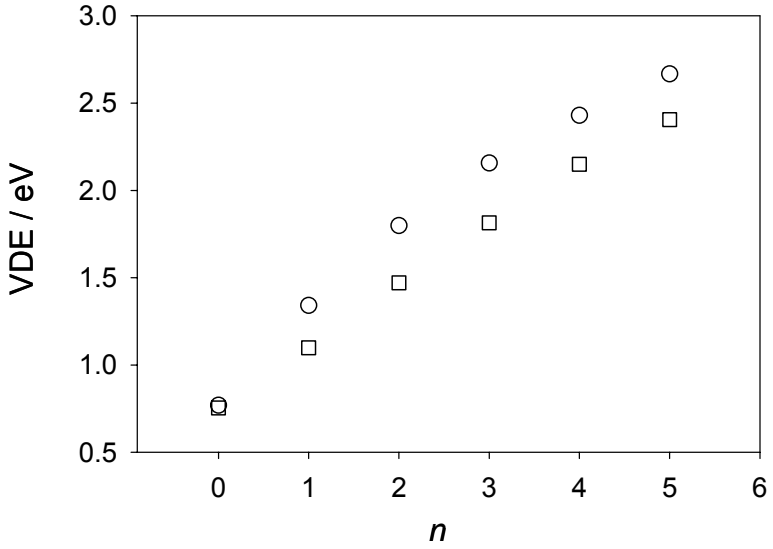

Figure 5.6. Vertical detachment energies (VDE's) vs n for $H^-(NH_3)_{n=0\text{-}5}$ (squares) and $NH_2^-(NH_3)_{n=0\text{-}5}$ (circles). Values were taken from 355 nm photodetachment results.

$NH_2^-(NH_3)_4$ suggests that charge-transfer-to solvent followed by charge recombination is possible in small clusters.

5.5 Discussion of photoelectron angular distributions

Free photoelectrons may be thought of in terms of scattered partial-waves with defined orbital angular momentum quantum number l.[43] In the case of detachment from atoms, $l = l_i \pm 1$, where l_i is the orbital angular momentum quantum number of the parent orbital. According to the derivations of Bethe,[51] Cooper and Zare, [37,44,45] the anisotropy parameter, β (from equation 5.1) has the following analytical form:

$$\beta = \frac{l_i(l_i-1)^2 + (l_i+1)(l_i+2)\left(\frac{\chi_{l_i+1}}{\chi_{l_i-1}}\right)^2 - 6l_i(l_i+1)\frac{\chi_{l_i+1}}{\chi_{l_i-1}}\cos(\delta_{l_i+1}-\delta_{l_i-1})}{(2l_i+1)\left[l_i+(l_i+1)\frac{\chi_{l_i+1}}{\chi_{l_i-1}}\right]}, \qquad (5.2)$$

where l_i the parent orbital, $\delta_{li\pm1}$ the phase shift and $\chi_{li\pm1}$ the radial dipole matrix element for the $l = l_i \pm 1$-type partial-wave. Taking into account the Wigner threshold law,[52] we may approximate[1]

$$\frac{\chi_{l_i+1}^{\ 2}}{\chi_{l_i-1}^{\ 2}} \propto \frac{\sigma_{l_i+1}}{\sigma_{l_i-1}} = A \cdot \varepsilon, \qquad (5.3)$$

where σ_l is the total cross-section for l-type partial-waves, A is a proportionality constant related to the size of the anion and $\varepsilon \equiv$ eKE. While the Wigner-law cross-sectional

energy dependences are only rigorous near threshold, this approximation has been used to accurately fit the energy-dependence of photoelectron anisotropy parameters for a variety of atomic systems [1,5] (see Chapter 4).

Detachment from an s-orbital ($l = 0$) reduces equation 5.2 to $\beta = 2$, corresponding to a cosine squared angular distribution, independent of eKE. This limit, corresponding to evolution of pure p-waves,[20,84] is indicated in Figure 5.5 (a) by the dashed black line. Our experimental results for bare H^-, plotted as open circles in the same figure, are close to this upper limit, consistent with other reported angular distributions for this system,[85,86] and do not display striking energy-dependences. The small deviations of our experimentally-determined results for H^- from $\beta = 2$ may be due to signal-to-noise or background subtraction issues, though (as previously discussed in sections 4.1, 4.3.1 and 5.1) we cannot rule out correlation or relativistic effects. In the non-relativistic, one-electron approximation, any significant deviation of anisotropy parameters for $H^-(NH_3)_{n>0}$ from $\beta = 2$ must be solvation-induced.

On the other hand, photoelectron angular distributions for detachment from bare NH_2^- [open circles in Figure 5.5 (b)] are strongly energy dependent, with $\beta > 0$ for eKE > 1.7 eV and $\beta < 0$ for eKE < 1.7 eV. However, as seen in Figure 5 (b), the PAD's for $NH_2^-(NH_3)_{n=1\text{-}5}$ show no remarkable deviations from the zero-solvation limit. Because the b_1 HOMO of NH_2^- transforms identically to a p_x-orbital under the symmetry operations of the C_{2v} point group we thus use the $l_i = 1$ approximation to model the energy-dependence of the photoelectron anisotropy,[3] as discussed in the previous Chapter. The WBCZ fit to the data for bare NH_2^-, is plotted in Figure 5.5 (b) as a black

dashed line to serve as a zero-solvation reference (with fit parameters of A = 1.09 and $\cos\delta$ = 0.934 as described in Chapter 4).

We may quantify the effect of solvation on β for cluster ions via the scaled anisotropy differential[5,8]

$$D_n(eKE) = \frac{\beta(eKE) - \beta_{WBCZ}(eKE)}{n^{0.8}}, \tag{5.4}$$

where β(eKE) is the experimentally determined anisotropy parameter for a solvated anion and β_{WBCZ}(eKE) is the WBCZ prediction for detachment from the bare anion at the same electron kinetic energy. The exponent of 0.8 was empirically determined for the best continuity in D(eKE) for $NO^-(N_2O)_n$ obtained at different wavelengths (see Chapter 6 for further discussion). Figure 5.7 contains the anisotropy differentials for $H^-(NH_3)_n$ (closed circles) and $NH_2^-(NH_3)_n$ (closed squares), as well as the deviations, $\Delta\beta$(eKE), in the experimental anisotropy parameters of bare H^- (open circles) and NH_2^- (open squares) from the Wigner-Bethe-Cooper-Zare predictions.

The anisotropy differentials for ammoniated H^- are largest near zero eKE (≈ 0.4). At around 0.5 eV, they flatten to a level (≈ 0.2) slightly greater than $\Delta\beta$ for bare H^-. Anisotropy differentials for ammoniated NH_2^- are consistently smaller in magnitude than those for H^-. They are also quite similar to the $\Delta\beta$'s for bare NH_2^- at similar energy ranges. The significance of these differentials depends upon the quality of the zero-solvation prediction; we note that the WBCZ curve was mostly fit to data in the higher-eKE range examined here. Nonetheless, the plot suggests that the solvent has a greater effect on β for the H^--based clusters than those with NH_2^- at their core.

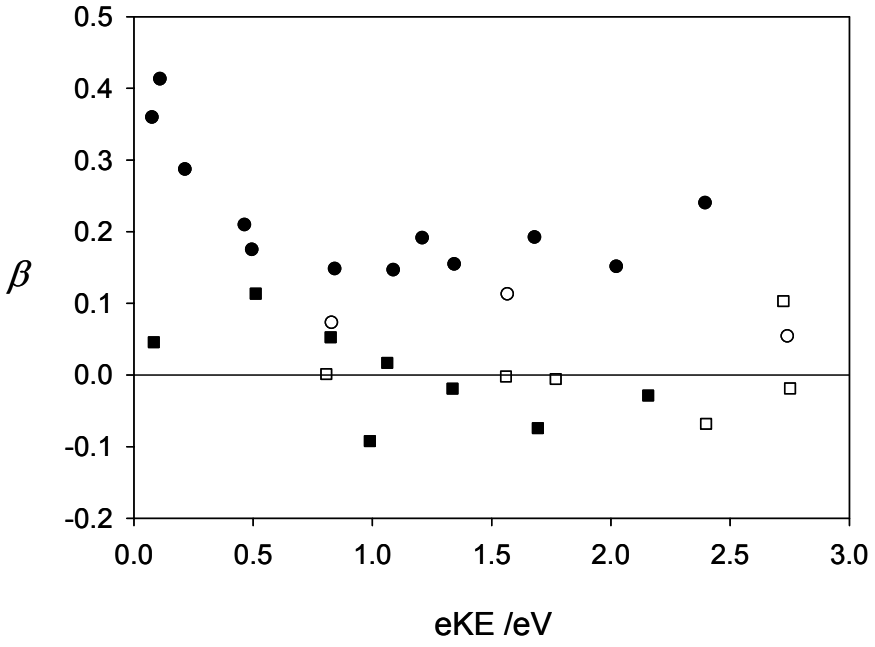

Figure 5.7 Anisotropy differentials for $H^-(NH_3)_n$ (solid circles) and $NH_2^-(NH_3)_n$ (solid squares) vs eKE. The difference between the experimental and theoretical β's for bare H^- (open circles) and NH_2^- (open squares) are also plotted. See text for details.

In the following, we discuss the observed deviations in β from the bare H^- limit from two perspectives: perturbation of the parent s-orbital and perturbation of the emitted photoelectron wave.

5.5.1 Perturbation of H^-

In a field-free environment, the electron density in the hydride anion is spherically symmetric. The presence of a solvent molecule breaks the spherical symmetry. In the case of $H^-(NH_3)$, such a perturbation may be approximated as a pure charge-dipole interaction polarizing the charge density along a single axis. The parent orbital, now lacking inversion symmetry, must be mathematically described as a linear combination of even and odd functions, so we shall choose to combine the initial s-function with an arbitrary p-type function polarized along the direction of the interaction.

We now build a model for photodetachment from an initial state with some combination of s- and p-character, with a treatment similar to that applied in Chapter 4. The initial state may be constructed as

$$|\psi_i\rangle = \sqrt{1-f}\,|s\rangle + \sqrt{f}\,|p\rangle, \tag{5.5}$$

where f is the fractional net p-character of the state. This decomposition is illustrated in Figure 5.8 (b). For a perturbed s-orbital, f will be quite small. While detachment from a pure s-orbital is expected to yield only p-type photoelectron waves, the presence of some p character will introduce s- and d-type partial-waves. For $f > 0$, the photoelectron angular distribution will thus be energy-dependent.

(a)

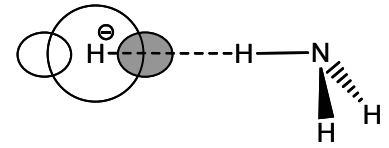

(b)

LF orientation	LF orbital component	hν →	allowed partial waves (LF)	
X	s	$\Delta l = \pm 1$	p_z	+
	p_x		d_{xz}	
Y	s		p_z	+
	p_y	$\Delta m_l = 0$	d_{yz}	
Z	s		p_z	+ +
	p_z		s, d_{z^2}	

Figure 5.8 (a) Conceptual illustration of component s and p functions. (b) Graphical representation for determination of partial-wave contributions from both parent orbital components for each principal orientation. See text for details.

According to equation 5.1, we may write

$$\beta = \frac{\rho - 1}{1 + \rho/2}, \tag{5.6}$$

where

$$\rho = \frac{I(0^\circ)}{I(90^\circ)}, \tag{5.7}$$

as long as I(90°) ≠ 0. We thus need only know the ratio of the photoelectron intensities at 0° and 90° in order to estimate β.

We may write

$$I(\theta) \approx I_X(\theta) + I_Y(\theta) + I_Z(\theta) \ , \tag{5.8}$$

where X, Y and Z indicate that the orientation of the perturbation axis is along the x, y and z axes, respectively, in the laboratory frame.

The allowed partial-waves must be determined for each principal orientation of the parent orbital separately. The electric field vector of the laser is taken as the laboratory frame z-axis. The following treatment is similar to the group theoretical approach used in the s&p model[46,105] applied to molecular orbital photodetachment. However, here we consider an initial (bound) state with two atomic-like components (with well-defined orbital angular momenta) so we make use of the one-electron spectroscopic selection rules (Δl = ±1, Δm_l = 0)[20] rather than group theoretical considerations to determine the allowed partial-waves for each component (noting that the p_x and p_y orbitals may be decomposed as a combination of $p_{\pm 1}$ orbitals). We will also not neglect energy-dependence or partial-waves for which $l > 1$. We construct the

parallel and perpendicular intensities by inspection. The process for each principal orientation is described in the following; it is also graphically illustrated in Figure 8 (b).

Orientations X and Y each yield a p_z wave and a linear combination of $d_{\pm 1}$ waves which we may neglect entirely due to their lack of intensity at 0° and 90°. These orientations each contribute an intensity at 0° and 90° proportional to the square of the $l = 1$, $m_l = 0$ spherical harmonic.

Orientation Z yields p_z, s and d_0 waves. The net intensities for each orientation should be the average of those resulting from the two possible orientations (up and down) for the parent components along the corresponding axis. Because the p-wave is antisymmetric while s and d_0 waves are not, any effects on the photoelectron intensity due to p-wave interference will cancel. For simplicity, we choose to consider one orientation and neglect the s-p_z and the p_z-d_0 partial-wave cross-terms.

We thus construct the parallel and perpendicular intensities:

$$I(0^\circ) \propto \left|\sqrt{f} C_0 Y_{00}(0^\circ) + \sqrt{f} \cdot e^{i(\delta_2+\pi)} C_2 Y_{20}(0^\circ)\right|^2 + 3\left|\sqrt{1-f} \cdot e^{i(\delta_1+\pi/2)} C_1 Y_{10}(0^\circ)\right|^2, \quad (5.9)$$

and

$$I(90^\circ) \propto \left|\sqrt{f} C_0 Y_{00}(90^\circ) + \sqrt{f} \cdot e^{i(\phi_2+\pi)} C_2 Y_{20}(90^\circ)\right|^2, \quad (5.10)$$

where Y_{lm} are the spherical harmonics, C_l the coefficient on partial-wave of type-l, the phase shifts of $\pi/2$ and π due to interactions of the p and d waves (respectively) with the centrifugal barrier,[20] and δ_1 and δ_2 additional phase shifts induced by interaction of the partial-waves with the neutral fragment. We have made use of the lack of φ-dependence of the contributing spherical harmonics. We note that complete orientation averaging

could easily be performed by expanding the initial state in the basis of LF spherical harmonics for any angle of the charge-dipole interaction axis with respect to the laser's electric field polarization vector, which would yield the same result as considering the principal orientations only.

We arbitrarily choose to define the spherical harmonics as unnormalized, incorporating the necessary normalization in the constants C_l. Equations 5.9 and 5.10 may be simplified:

$$I(0^\circ) \propto fC_0^{\,2} + 3(1-f)C_1^{\,2} + 4fC_2^{\,2} - 4fC_0C_2\cos(\delta_2) \tag{5.11}$$

$$I(90^\circ) \propto fC_0^{\,2} + fC_2^{\,2} + 2fC_0C_2\cos(\delta_2)\,. \tag{5.12}$$

Dividing both equations by C_0^2 and taking their ratio yields

$$\rho = \frac{fC_0^{\,2} + 3(1-f)C_1^{\,2} + 4fC_2^{\,2} - 4f\cdot C_0C_2\cos(\delta_2)}{fC_0^{\,2} + fC_2^{\,2} + 2fC_0C_2\cos(\delta_2)} \tag{5.13}$$

Using equation 5.13 to solve for β gives

$$\beta = \frac{2(1-f)C_1^{\,2} + 2fC_2^{\,2} - 4fC_0C_2\cos(\delta_2)}{fC_0^{\,2} + 2fC_2^{\,2} + (1-f)C_1^{\,2}} \tag{5.14}$$

In the limits that f goes to zero and one, corresponding to detachment from pure s- and p-states, respectively, equation 5.14 is equivalent to the respective Cooper-Zare expressions for $l_i = 0$ and $l_i = 1$ if $C_l^2 = \chi_l^2$. Making this substitution and dividing the numerator and denominator by χ_0^2 gives

$$\beta = \frac{2(1-f)\frac{\chi_1^{\,2}}{\chi_0^{\,2}} + 2f\frac{\chi_2^{\,2}}{\chi_0^{\,2}} - 4f\chi_0\chi_2\cos(\delta_2)}{f + 2f\frac{\chi_2^{\,2}}{\chi_0^{\,2}} + (1-f)\frac{\chi_1^{\,2}}{\chi_0^{\,2}}}. \tag{5.15}$$

Assuming the Wigner law[52] scaling of partial-waves, we may write

$$\frac{\chi_1^{\,2}}{\chi_0^{\,2}} \propto \frac{\sigma_1}{\sigma_0} = B \cdot \varepsilon^{1/2}, \tag{5.16}$$

where B is another proportionality constant. Combining equations 5.3, 5.15 and 5.16 now yields an expression for β as a function of electron kinetic energy.

$$\beta(\varepsilon) = \frac{2(1-f)B^2\varepsilon + 2fA^2\varepsilon^2 - 4fA\varepsilon\cos(\delta_2)}{f + 2fA^2\varepsilon^2 + (1-f)A^2\varepsilon} \tag{5.17}$$

For $f = 0$ (corresponding to an unperturbed s-orbital), equation 5.17 reduces to equation 5.2 (the WBCZ equation) for the case of $l_i = 0$. In the limit of $f = 1$, equation 5.17 again reduces to the WBCZ equation, this time for $l_i = 1$, corresponding to detachment from a p-orbital. Equation 5.17 is thus consistent with the WBCZ model in these extremes. We note that the general approach of this model is a simple, alternate way to arrive at the Cooper-Zare equation; the approach can similarly be coupled with group theoretical selection rules and/or additional phase shifts for simple models of the energy-dependence of β for photodetachment from molecular anions.[6,46]

For ($f > 0$) we note that as $\varepsilon \rightarrow 0$, the s-waves dominate and $\beta \rightarrow 0$. According to this model, perturbation of an s-orbital ($0 < f < 0.5$) will render β energy-dependent with the effects greatest near threshold. To illustrate this effect, we have plotted equation 5.17 for $f = 0.026$ (solid grey curve) and 0.035 (dashed grey curve) in Figure 5.5 (a). As δ is

typically small for atomic anion photodetachment, it has been artificially fixed at zero; we have also arbitrarily set $A = B = 1$. This first-order perturbation model qualitatively agrees with the experimentally determined trends in β for a given n. In fact, the two plotted curves overlap quite well with the experimental data for $H^-(NH_3)$ and $H^-(NH_3)_2$, respectively.

We note that any number of solvent molecules could be viewed as introducing additional p-components in the parent orbital at different positions relative to the first, depending on the cluster geometry. Considering all relevant orientations of these additional components would yield s, d_0, and p partial-waves, but with a smaller relative contribution from p-waves. This additional contribution can easily be accounted for by increasing the value of f in equation 5.17.

While this model is nonetheless likely a less rigorous approximation for photodetachment from the $H^-(NH_3)_{n>1}$ clusters, s partial-waves ($l = 0$) resulting from any solvation-induced p-character ($l_i = 1$) in the parent orbital will dominate over partial-waves induced by higher-l_i parent orbital components at low eKE's. (In other words, it is reasonable to neglect all solvation-induced components of the parent orbital that correspond to $l_i>1$ at low kinetic energies.)

5.5.2 Perturbation of NH_2^-

We now consider the angular distributions for solvated NH_2^-. In a simple electrostatic picture, the electron density within the molecule should be perturbed along the solvent-interaction axis. The non-bonding b_1 HOMO of NH_2^- has the same symmetry

as a p_x orbital. Solvation should break the inversion symmetry of this orbital. This can also be done mathematically by introducing a gerade function. Regardless of the initial solvation geometry, the first-order perturbation term can be taken as a totally symmetric (or s-like) function.

Under this crude approximation, we may also use equation 5.17 to model β vs eKE for photodetachment from solvated NH_2^-, treating the parent orbital as a p-orbital with some s-character ($0.5 < f < 1$). The model suggests that perturbation should alter the PAD's resulting from p-orbital photodetachment much less than those for photodetachment from an s-orbital for similar electron kinetic energies. The prediction for $f = 0.90$ is plotted in Figure 5.5 (b), with $A = B$, using the A and δ parameters determined for bare NH_2^-.

5.5.3 Perturbation of the photoelectron

We now briefly consider perturbation of the photoelectron itself. If the autodetachment signal discussed in section 5.4 indeed occurs upon geometrical relaxation of a metastable charge transfer-to-solvent state, then we may reasonably suspect the presence of anionic resonances of the solvent network. It is thus possible that some of the photoelectrons resulting from direct detachment (i.e. the type I transitions) are influenced by the charge-transfer exit channel. This effect can be thought of as resonant scattering—or diffraction— of the photoelectron wave front through the solvent, resulting in additional partial-wave phase shifts or interferences that may

noticeably alter photoelectron angular distributions from the zero-solvation prediction. (Direct evidence for such a phenomenon will be presented in Chapter 6.)

Theoretical momentum-transfer cross-sections for electrons in ammonia have been reported for the relevant energy range (< 2.5 eV).[128] While there are some disagreements in absolute magnitude between the reported cross-sections, they all increase rapidly as the electron energy approaches zero, with predicted cross-sections $>10^{-15}$ cm^2. For comparison, we note that the peak momentum-transfer cross-section for N_2O (whose corresponding resonance directly correlates with large anisotropy differentials for $O^-(N_2O)_n$ and $NO^-(N_2O)_n$, as will be shown in Chapter 6) is approximately 4×10^{-15} cm^2. We may thus expect solvation-induced perturbation of the photoelectron to affect the photoelectron angular distributions for ammonia-solvated anions at eKE's < 1 eV. The results for the H^--based clusters are consistent with this expectation, but we have only a few data points for the NH_2^--based clusters in this energy range. Of these, the deviations for the three lowest-eKE points do seem to roughly follow the same trend, but the lowest-eKE point has a very small anisotropy differential. This could be because the zero solvation limit approaches $\beta = 0$ at eKE = 0; loss of anisotropy necessarily manifests as a small D(eKE).

5.6 Conclusions

We have reported 532 nm and 355 nm photoelectron imaging results for the $H^-(NH_3)_{n=0\text{-}5}$ and $NH_2^-(NH_3)_{n=0\text{-}5}$ cluster series. The corresponding energy spectra agree

with previous results[65,66,114] for both series for n = 0-2, indicating that the cluster series may be described as the notation implies: H^- or NH_2^- cores electrostatically bound to n neutral NH_3 molecules. The 532 nm energy spectra for $NH_2^-(NH_3)_{n=2\text{-}5}$ and $H^-(NH_3)_5$ contain features indicative of autodetachment, suggesting that metastable charge-transfer-to-solvent precursor states may be accessible for these clusters at this wavelength. The 532 nm energy spectrum for $NH_2^-(NH_3)_4$ also contains two-photon features that we tentatively assign to detachment from $NH_2^-(NH_3)_{n=0,1}$ photofragments.

We observed significant deviations in anisotropy with respect to the zero solvation limit for $H^-(NH_3)_n$, but minimal deviations for $NH_2^-(NH_3)_n$. From the perspective of the parent orbital, this is superficially unexpected, as NH_2^- interacts more strongly with the solvent (as indicated by the ΔVDE's). However, the simple model applied suggests that perturbation of an s-orbital will have a prominent effect on the corresponding PAD's, but that the effects are not as pronounced with a p-type parent orbital, in agreement with the experimental observations. In general, is may be reasonable to assume that perturbation of parent p orbitals will have a negligible effect on photoelectron angular distributions.

While we cannot definitively separate the roles of pre- and post-photodetachment perturbation on the photoelectron angular distributions for ammoniated H^- and NH_2^-, our results indicate that anisotropic environmental effects manifest more substantially for isotropic systems. The nature of the parent orbital, not only the solvent, must be considered when evaluating effects of solvation on photoelectron angular distributions. Further study of photodetachment from simple orbitals in the vicinity of different

solvents will prove valuable to unraveling the interplay of environmental effects pre- and post-photodetachment.

CHAPTER 6

BONDING STRUCTURE AND PHOTODETACHMENT DYNAMICS IN $[O(N_2O)_n]^-$ (n = 0-9) and $[NO(N_2O)_n]^-$ (n = 0-4)

We shall now further examine solvation effects on photoelectron angular distributions and bonding structure using imaging results for two heterogeneous nitrous oxide cluster anion series. The results presented in this chapter have been reported previously,[4-6,8,100] and sections from two journal articles[4,5] (of which I was a primary author) have been reproduced in part or whole in the following. While the work was highly collaborative, this chapter emphasizes my contributions. For clarity, the collaboration is briefly described. Kostyantyn Pichugin and I together performed the experiments for the 355 and 266 nm photoelectron imaging study of $[O(N_2O)_{n=1-9}]^-$. I analyzed the results, while Kostyantyn Pichugin performed ab initio computations on $[O(N_2O)_{n=1-4}]^-$. Luis Velarde performed the photofragmentation study of $[O(N_2O)_{n=1-9}]^-$.[4] Photoelectron imaging was performed on $NO^-(N_2O)_n$ at 355, 532 and 786 nm primarily by Luis Velarde with help from Terefe Habteyes, Kostyantyn Pichugin and myself.[8,100] I performed the experiments and data analysis for the 266 nm photoelectron imaging study of $NO^-(N_2O)_{n=0-4}$.[5]

6.1 Introduction

As mentioned in Chapter 5, solvated anions are usually stabilized by ion-neutral interactions. On a pairwise basis, these mostly electrostatically controlled interactions

tend to be weaker than the covalent bonds in either the solute or the solvent, but their combined effect for many solvent molecules (and generally accounting for the many-body interactions)[129] can easily exceed a typical covalent bond energy. To the contrary, the corresponding neutral states are usually stabilized to a much lesser degree due to the weaker strength of van der Waals bonding. As a result, solvation tends to increase the vertical detachment energy (VDE) of anionic species. In the absence of chemical rearrangements, the increase is expected to be gradual and monotonic with the number of solvating molecules. Discontinuities in this trend usually signal abrupt changes in the structure of the core anion.

A classic example of such behavior was reported by DeLuca et al.[130] for the $(CO_2)_n^-$, n = 2-13 cluster series, later expanded by Tsukuda et al.[131] for the n = 2-16 range. The photoelectron spectra of the size-selected $(CO_2)_n^-$ cluster anions obtained by these authors display two different photodetachment band series: one corresponding to higher VDE's is observed for the n = 2–6 and n = 14 clusters, and the other, with lower VDE's, is observed in the n = 6-13 range. The VDE discontinuities at n = 6 and 14 cannot be accounted for by ordinary solvation and are attributed to qualitative changes in the cluster core structure. Specifically, these changes have been described as a core-switching (at n = 6) from the covalent dimer anion $(O_2CCO_2)^-$, whose structure was originally proposed by Fleischman and Jordan,[132] to the monomer CO_2^- and back (at n = 14).[130,131]

A study by Tsukuda et al. [133] revealed a somewhat similar phenomenon for $(NO)_n^-$. For this cluster series, the VDE was found to increase by nearly 0.8 eV from n =

2 to n = 3, while only moderate consecutive increases (~ 0.1 eV) were observed in the n = 3–7 range. The VDE trend for n = 3–7 is consistent with stepwise solvation of a charged cluster core, but the abrupt changes occurring between n = 1 and 2 and between n = 2 and 3 once again signal qualitative changes in the core-anion structure. In this case, a gradual assembly (or building up) of the core anion is observed as the $(NO)_n^-$ cluster size increases. Specifically, the core anions in these clusters are described as (obviously) NO^- for n = 1, a covalently bound dimer anion for n = 2, and (preferentially) a covalently bound trimer anion for n = 3. That is, in the $n \leq 3$ range, the excess electron delocalizes and promotes covalent bonding between all available NO moieties. In larger clusters, the size of the anionic core no longer increases with n and the additional NO molecules play the role of neutral solvents.[133]

In this Chapter, we shall consider the dimer anion of NO. Multiple isomers of $N_2O_2^-$ have been the subject of an increasing number of studies,[134-140] in part due to the interest in the possible role of their neutral analogues as intermediates in atmospheric processes.[140] Posey and Johnson, using pulsed supersonic expansion of distinct precursor gas mixtures ionized by a fast electron beam, identified three distinct forms of $N_2O_2^-$: (i) the $O_2^-\cdot N_2$ ion-molecule complex, observed in the expansion of O_2 seeded in nitrogen; (ii) the C_{2v} symmetry Y-shaped NNO_2^- anion (analogous to CO_3^-), formed in the expansion of pure N_2O; and (iii) an NO dimer anion, *cis*- or *trans*-$ONNO^-$, generated by seeding NO in the Ar carrier gas.[134] In this work, we are primarily concerned with the Y-shaped (NNO_2^-) isomer[134,136,138,140] and changes in its structure under solvation by N_2O.

Dissociative electron attachment to N_2O is understood to be a preliminary step in

the formation of NNO_2^- in electron-impact anion sources.[25,67,69,70,141-146] This process yields N_2 and O^- and in the presence of third bodies may be followed by the $O^- + N_2O \rightarrow NNO_2^-$ association reaction involving additional N_2O molecules in the presence of a third body.[134] Such processes in neutral N_2O clusters have been shown to yield an anionic cluster series, often termed $O^-(N_2O)_n$.[7,25,70,141,144,145,147] In their thermodynamics study on this series for n = 2–7, Hiraoka et al. suggested an $NNO_2^-(N_2O)_{n-1}$ structural form for these clusters.[7] Based upon the accepted NNO_2^- structure for the n = 1 member of this cluster series, they also suggested that the first effective solvent shell in $NNO_2^-(N_2O)_{n-1}$ is completed at n = 3, corresponding to preferential solvation of the two equivalent anionic oxygen sites. This cluster series, generated by dissociative electron attachment to supersonically expanding N_2O, is a prime candidate for photoelectron imaging; photoelectron energy spectra can elucidate the structural motifs of the core anion, and photoelectron angular distributions provide another dimension of information.

When interpreting photoelectron angular distributions in the photodetachment of cluster anions, several solvent-induced effects must be considered,[8] as discussed in Chapter 5. First, the anion-neutral solvation interaction typically stabilizes the electronic state of the anion more than that of the neutral, resulting in increased electron binding energies (eBE) for solvated species.[18,148] As the relative partial-wave contributions to the photoelectron wave function depend upon the electron's kinetic energy (eKE), a solvation-induced shift in eBE (and, therefore, eKE) affects the angular distribution. Second, the solvent perturbs the electronic structure of the anion solute, possibly accommodating some of the excess charge.[18,149] This perturbation of the initial state may

also affect the partial-wave composition of the photoelectron wave function. Third, the wave function of the photoelectron itself may be perturbed by interactions with the solvent molecules.

These effects are expected to be manifest to varying degrees in cluster anion photodetachment. Several studies suggest that solvent-induced perturbation of the photoelectron has a particularly pronounced effect when the asymptotic electron kinetic energy is in the vicinity of an anionic resonance of the solvent. In one case, 266 nm photodetachment from $I^-\cdot CH_3I$ yielded photoelectrons that were markedly more isotropic than those detached from $I^-\cdot H_2O$, $I^-\cdot Ar$, or $I^-\cdot CH_3CN$. [104] This was attributed to scrambling of the nascent photoelectron angular distribution via one of several possible electron-CH_3I scattering resonances [150] near the 1.2 eV kinetic energy of the photoelectrons in that particular measurement.[104] A similar observation was made upon comparison between detachment from anionic acetone clusters $(Acn)_n^-$ (n = 5-15) to their hydrated analogues, $Acn^-(H_2O)_m$ (m = 5-10). [151] In this case, the smaller anisotropies for detachment from the homogeneous clusters were attributed to an electron-acetone scattering resonance in the eKE range accessed in the experiment.

Previously, our group reported another case of dominant photoelectron-solvent interactions evidenced by photoelectron anisotropy shifts upon solvation of NO^- by N_2O in cluster-anion photodetachment at 786, 532 and 355 nm.[8] A fit to experimentally determined anisotropy parameters *(β)* for detachment from bare NO^- using the Wigner-Bethe-Cooper-Zare potential model[44,45,51,52] was used as a basis for comparison. To examine the effect of both eKE and n on the photoelectron anisotropy for the $NO^-(N_2O)_n$

cluster anions, a new parameter – the scaled "anisotropy differential" – was introduced, calculated as:

$$D(\mathrm{eKE}) = \frac{\beta(\mathrm{eKE}) - \beta_{CZ}(\mathrm{eKE})}{n^{0.8}}, \tag{6.1}$$

where β(eKE) is the experimentally determined photoelectron anisotropy parameter for a given cluster of solvation number n corresponding to a transition centered at a specific eKE, while β_{cz}(eKE) is the Cooper-Zare prediction for detachment from the core anion in the absence of solvation but at the same electron kinetic energy as the β(eKE) measurement. The exponent of 0.8 is an empirical parameter that accounts for the nonlinear contribution of multiple solvent molecules, determined to best overlap the data sets obtained at different wavelengths. [8]

When plotted as a function of eKE, the resulting anisotropy differentials peaked at approximately the same energy as a computed momentum-transfer cross-section for electron collisions with N_2O (~2.25 eV). [9] The same analysis for 355 nm detachment from $NO^-(H_2O)_n$ (n = 1-3, peak eKE = 0.9-2.13 eV) yielded a less pronounced loss of anisotropy with a different energy dependence, confirming that the effect is specific to the N_2O solvent. Since the electrostatic (solvation) interactions of NO^- with H_2O are stronger than with N_2O, it was concluded that the anisotropy loss is not primarily due to perturbation of the initial bound state. [8]

Most of the photoelectron imaging data in the previous work (summarized above) corresponded to the low-energy side of the scattering resonance implicated in the analysis. In this chapter we shall revisit the $NO^-(N_2O)_n$ cluster series at 266 nm,

extending the observation range to larger electron kinetic energies. In addition, the results peripherally reveal the signature of another core anion for n = 1-4, assigned to the $ONNNO^-$ structure first proposed by Hiraoka et al. [7] and characterized spectroscopically by Continetti and coworkers.[152] We examine the coexistence of the NO^- and $ONNNO^-$ cluster cores under stepwise solvation by N_2O and suggest the possibility of gradual core-*shifting* (rather than abrupt core-*switching*[4,130,131,153] attributed to the interplay between the relative stabilities of the NO^- and $ONNNO^-$ anions and the preferential solvation of the smaller NO^- core.

In the following, 355 and 266 nm photoelectron imaging results for $[O(N_2O)_{n=0-9}]^-$ and 266 nm results for $[NO(N_2O)_n]^-$ are presented. These results allow us to evaluate 1) the identity of the anion core (i.e., over what framework the excess electron resides) and 2) the effects of solvation on the corresponding photoelectron angular distributions. From photoelectron spectroscopy, we identify the anion core for the $[O(N_2O)_n]^-$ as covalently bound NNO_2^- in the smaller (n = 1-3) clusters, while in the larger (n > 3) clusters O^- is determined to be the dominant ionic core. However, for $[NO(N_2O)_n]^-$, two cores (NO^- and $ONNNO^-$) are identified as coexisting through the cluster size range considered (n = 1-4). The photoelectron angular distributions for the $O^-(N_2O)_{n=4-9}$ and $NO^-(N_2O)_{n=1-4}$ clusters at these wavelengths deviate strongly from the unsolvated limit in the vicinity of anionic $^2\Pi$ anionic resonance of N_2O providing further evidence for the resonant photoelectron-solvent scattering phenomenon previously proposed.[8,100]

6.2 Experimental

Experiments are performed in a negative-ion photoelectron imaging spectrometer described in detail in Chapter 2 and elsewhere.[105] The instrument combines velocity-map[13,14] imaging[11,34,154] detection of photoelectrons[16,155] with the negative-ion techniques pioneered by Lineberger.[24]

In brief, ions are formed in a low-pressure (10^{-7} Torr base, $\leq 10^{-4}$ Torr operational) chamber upon supersonic expansion of neat N_2O from a pulsed nozzle (General Valve Series 9) operating at 50 Hz, bombarded by a 1 keV electron beam. For enhanced production of cluster anions, the electron beam propagates counter to the expansion, aimed at the nozzle's orifice.[28] Negative ions are extracted into a Wiley-McLaren[30] time-of-flight mass spectrometer, where they are accelerated to ~2.5 kV and focused using an Einzel lens. Ions are detected using a dual-microchannel plate (MCP) detector, with the output read from a digitizing oscilloscope, yielding time-of-flight mass spectra.

Nanosecond pulses (50 Hz) of the third or fourth harmonic from a Nd:YAG laser (Spectra Physics Corp., model Lab 130-50), entering the detection region through a Brewster window and timed to intersect the target anions, propagate perpendicularly to the ion trajectory. Upon detachment, photoelectrons are projected by velocity-mapping electrodes onto a two-dimensional position-sensitive dual-microchannel-plate (MCP) detector coupled to a phosphor screen (Burle, Inc), allowing the amplified photoelectron signal to be recorded with a digital camera. The detector's surface is parallel to the plane defined by the laser and ion propagation directions. The laser beam is in some cases

focused with a lens (f = 2 m) placed approximately 1 m before the laser-ion interaction region. The laser polarization is linear in the direction parallel to the ion beam and the surface of the imaging MCP detector, vertical with respect to the image orientation in the page.

Three-dimensional photoelectron probability distributions were reconstructed from the raw images using the BASEX program.[35] Angular distributions were calculated over the full width at half-maximum of the O^--based transitions and the entire Franck-Condon envelope of the NO^--based transitions. The O^- transitions were used for energy calibration in all cases. The absolute energy resolution of the imaging technique scales as $eKE^{1/2}$. Under the conditions used in this study, the full widths at half maximum for the 266 nm O^- detachment transitions are 145 meV and 243 meV, at electron kinetic energies of 1.24 eV and 3.18 eV, respectively.

6.3 Imaging Results for $[O(N_2O)_n]^-$ (n = 0-9) at 355 and 266 nm

In this section, we present photoelectron imaging results for the $[O(N_2O)_n]^-$, n = 0–9 cluster anion series. Figure 6.1 shows the 355 nm results, while Fig. 6.2 displays the 266 nm data.

The raw photoelectron images and the corresponding spectra shown in Figures 6.1 and 6.2 are hereafter referred to as datasets 6.1.n and 6.2.n, respectively, with n = 0–9 referring to the cluster size. All images for a given wavelength are displayed on the same velocity scale. The intensity scales are chosen arbitrarily to highlight the most relevant features of the individual images; therefore, they do not reflect the absolute cross-

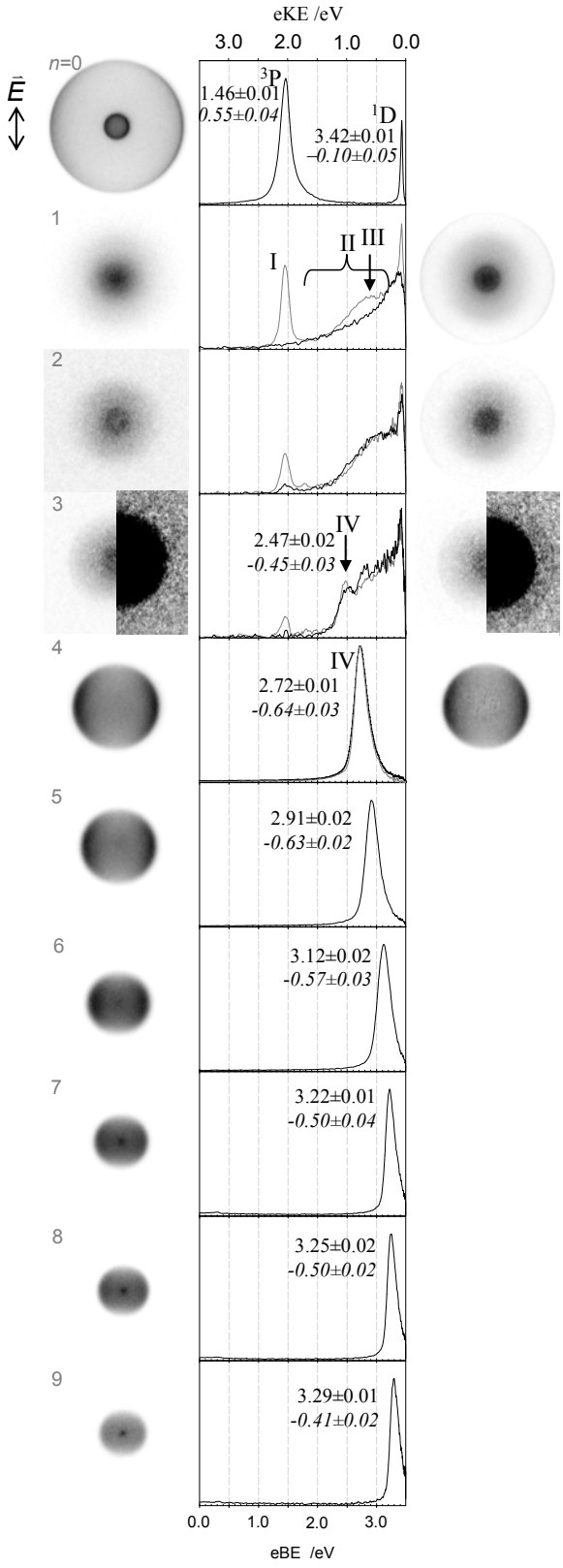
eKE /eV
3.0
2.0
1.0
0.0
n=0
$\vec{E}$
^{3}P
1.46±0.01
0.55±0.04
^{1}D
3.42±0.01
–0.10±0.05
1
I
II
III
2
3
2.47±0.02
-0.45±0.03
IV
4
IV
2.72±0.01
-0.64±0.03
5
2.91±0.02
-0.63±0.02
6
3.12±0.02
-0.57±0.03
7
3.22±0.01
-0.50±0.04
8
3.25±0.02
-0.50±0.02
9
3.29±0.01
-0.41±0.02
0.0
1.0
2.0
3.0
eBE /eV

Figure 6.1 Photoelectron images and energy spectra for $[O(N_2O)_n]^-$ at 355 nm. Cluster size, n, is indicated for each row. The left column contains images obtained with a laser fluence of 1.1×10^6 W/cm^2; the corresponding energy spectra are the black curves in the middle column. Images obtained with an increased laser fluence of 3.7×10^6 W/cm^2 (right column) reveal two-photon features, and the corresponding photoelectron spectra are plotted as grey curves in the middle column. The vertical double arrow in the $n = 0$ photoelectron image defines the laser polarization axis for all images. All images are shown on the same velocity scale. The photoelectron spectra are normalized to the corresponding maximum intensities. The vertical detachment energies along with anisotropy parameters for bands with clearly defined maxima are indicated next to the corresponding spectral features. These results appeared in a previous publication.[4] See the text for band assignments and further details.

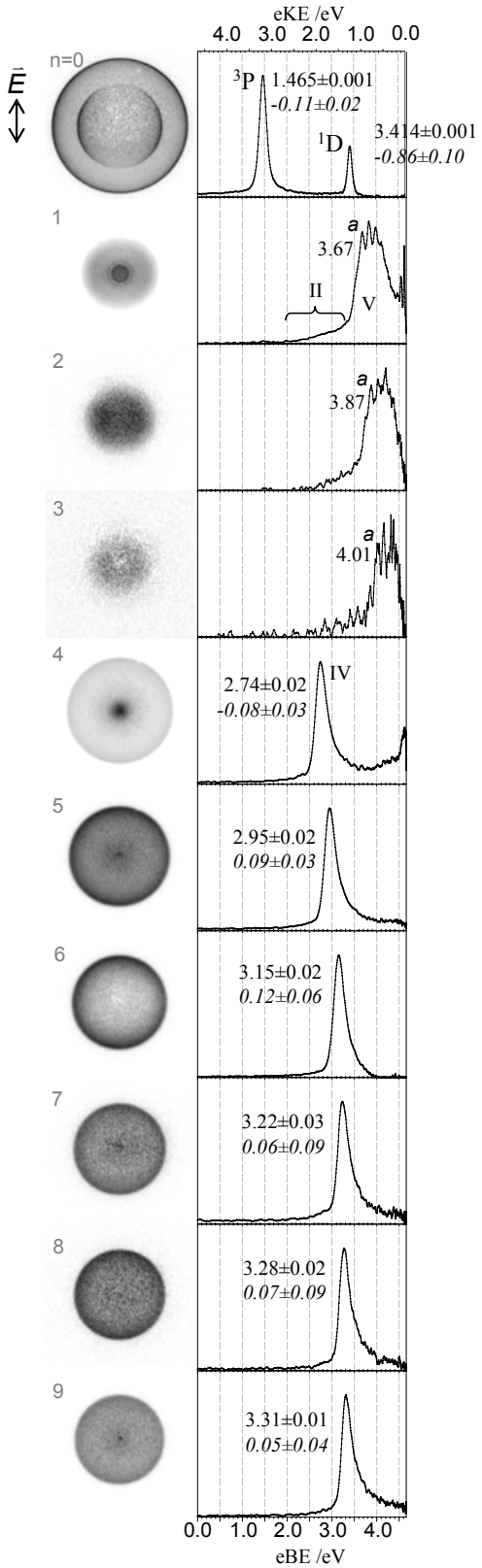
eKE /eV
4.0 3.0 2.0 1.0 0.0
n=0
$\vec{E}$
^{3}P 1.465±0.001
-0.11±0.02
^{1}D 3.414±0.001
-0.86±0.10
1
a
3.67
II
V
2
a
3.87
3
a
4.01
4
2.74±0.02
-0.08±0.03
IV
5
2.95±0.02
0.09±0.03
6
3.15±0.02
0.12±0.06
7
3.22±0.03
0.06±0.09
8
3.28±0.02
0.07±0.09
9
3.31±0.01
0.05±0.04
0.0 1.0 2.0 3.0 4.0
eBE /eV

Figure 6.2 Photoelectron images and the corresponding photoelectron spectra for the $[O(N_2O)_n]^-$, n = 0–9 cluster anion series obtained at 266 nm (with a laser fluence of 1.0×10^6 W/cm^2). The images and energy spectra are the combination of all 266 nm images obtained for a given cluster. All images are shown on the same velocity scale. The spectra are normalized to the corresponding maximum intensities. The average vertical detachment energies and anisotropy parameters (in italics) of the component images for bands with clearly defined maxima are indicated next to the corresponding spectral features. Uncertainties correspond to two standard deviations in the results for the component images. The results for n = 1-3 appeared in a previous publication; those for n = 0, 4-9 correspond to the combination of the results first reported for these clusters[4] with additional data; the combined VDE's and β's have also been published.[5]

sections. The $O(^3P, ^1D) \leftarrow O^-(^2P)$ photodetachment transitions[97] in datasets 6.1.0 and 6.2.0 were used for electron kinetic energy (eKE) calibration of the rest of the data. Although the fine structure of these transitions is not resolved in the present case, photoelectron imaging is capable of such resolution, as demonstrated recently by Cavanagh et al.[101]

The first column of Figure 6.1 contains the sum of three to five 355 nm images (each corresponding to approximately 30,000 experimental cycles) obtained with a laser fluence of 1.1×10^6 W/cm^2; the corresponding energy spectra are displayed as black traces in the middle column. For n = 1-4, image collection was repeated at a higher laser fluence (3.7×10^6 W/cm^2) for higher signal-to-noise, revealing new spectral features. The higher-fluence images are shown in the right-hand column in Figure 6.1 with corresponding spectra plotted in grey in the energy spectra (middle column). Peak eBE's (approximate VDE's) for the primary transitions are indicated, corresponding to the average of the values determined for the individual images, plus or minus two standard deviations.

The images and energy spectra in Figure 6.2 correspond to the combination of all individual images (with background subtraction) obtained for a given cluster at 266 nm. For n = 1-3, six individual images were obtained, each corresponding to 15,000 experimental cycles. For n = 0, 4-9, three images were obtained, each corresponding to 90,000-270,000 experimental cycles, collected in 30,000-cycle batches with background subtraction. Peak eBE's and anisotropy parameters are indicated for n = 0, 4-9, corresponding to the average of the results for the individual images, plus or minus two

standard deviations.

Overall, the photoelectron images and the corresponding spectra in Figs. 6.1 and 6.2 include two types of features. The first are narrow bands, suggestive of atomic or atomic-like transitions. Others exhibit broader and more complex structures, as typically seen in detachment from molecular anions. These features, as well as energetic and angular considerations, provide the basis for structural characterization of each cluster species.

6.3.1 355 nm photoelectron spectra for $[O(N_2O)_n]^-$

The unsolvated O^- photoelectron spectrum at 355 nm (Fig. 1.0) shows two peaks corresponding to the $O(^3P, ^1D) \leftarrow O^-(^2P)$ transitions with the detachment energies of 1.46 and 3.42 eV, respectively. Similar features (without any measurable solvation-induced shifts) are also present in high laser fluence results in 6.1.1–6.1.3. The intensities of these signals increase relative to other spectral features upon slight focusing of the laser beam. The selective relative signal enhancement indicates that the unshifted O^- transitions in $[O(N_2O)_n]^-$, n = 1–3 result from a two-photon process, ascribed to the photodissociation of the $N_2O_2^-$ cluster core and evaporation of solvent molecules, followed by photodetachment from the O^- photofragment.

For brevity, we will refer to these two-photon bands as type I transitions. Similar O^- fragment signatures were seen in the previous studies of NNO_2^- at 532 and 266 nm,[134,138] as well as in the photoelectron spectroscopy studies of the $ONNO^-$ isomer at 355 and < 420 nm.[133,134] As discussed in the section 6.1, past experiments under similar

ion-source conditions have yielded almost exclusively the covalent, Y-shaped (NNO_2^-) isomer of $N_2O_2^-$.[134,138] This isomer is expected to be dominant among the n = 1 species in our experiment. Although the 355 nm photon energy is insufficient for direct detachment of Y-shaped NNO_2^-,[138] the observed type I signals are consistent with its photodissociation, followed by O^- fragment photodetachment. In addition to the type I transitions, dataset 1.1 contains a broad band labeled II. This feature is ascribed to photodetachment of the $ONNO^-$ isomer,[133,134,139] which may be present to some extent in the ion beam. However, the apparent enhancement of this feature for n = 1 at the higher laser fluence implies that some of the signal in this energy range is the result of a 2-photon process (this was not discussed in the original publication[4]), indicated as feature III, at a binding energy quite close to the vertical detachment energy (VDE) of NO_2^-.[6]

For n = 2 and 3 (Figures 6.1.2 and 6.1.3, respectively), type I (O^- fragment) features are also observed, as well as analogues of band II. While the former do not show any solvation-induced shift, band II moves to progressively higher binding energies as n increases, consistent with solvent stabilization of the $ONNO^-$ anion, and apparently the result of direct (one-photon) detachment, with no two-photon feature analogous to III. These observations suggest similar molecular-anion core structures persisting in the n = 1–3 cluster size range. However, Fig. 1.3 (n = 3) contains an additional peak (labeled IV) at eBE = 2.47 eV.

The n = 4–9 data are similar to n = 0 in that we noticed no changes in the overall structure of the photoelectron spectra with respect to the laser flux conditions. The absolute signal levels are significantly larger for n = 4–9, compared to n = 1–3, and the

corresponding photoelectron spectra are strikingly different. Each of the larger species exhibits just one intense (and relatively narrow) atomic-like transition, which peaks at progressively higher binding energies as n increases. The comparison of spectra 1.3 and 1.4–1.9 in Figure 6.1 suggests that the type IV transition, observed for n = 3, belongs to this progression. For n = 4 and 5, type IV features are centered at eBE = 2.72 and 2.91 eV, respectively, compared to 2.47 eV for n = 3. By interpolation, this spectral series is consistent with O ^{3}P ← O^- ^{2}P photodetachment transition for $O^-(N_2O)_n$, progressively shifted due to solvation with N_2O. The angular distributions of the type III transitions for n = 3 are also qualitatively similar to the corresponding transition in unsolvated O^- n = 0 at the same wavelength, as reflected by the β values included in Figure 6.1. In summary, the 355 nm photoelectron imaging results suggest a molecular-anion core for the $O^-(N_2O)_n$, n = 1–3 clusters, and an O^- core for n = 4–9. The exact nature of the covalent core cannot be established based on these data alone, but the results are consistent with both the *Y*-shaped NNO_2^- and $ONNO^-$ isomers identified by Posey and Johnson.[134] Although we expect the NNO_2^- structure to be dominant under the ion-generation conditions employed in the present work, only ONNO− undergoes direct photodetachment at 355 nm, possibly resulting in band II in the photoelectron spectra shown in Figures 6.1.1-6.1.3.

6.3.2 266 nm photoelectron spectra for $[O(N_2O)_n]^-$

In the 266 nm data presented in Fig. 2, a new molecular-type transition (labeled V) appears for n = 1–3. Band V shows partially resolved vibrational structure,

particularly clear in dataset 2.1, which allows us to identify it as a signature of the Y-shaped NNO_2^- anion (depicted in Figure 6.3 as structure V) arising from detachment to yield the $^3A_2$ state of the neutral, as previously characterized.[138] In order to quantify the solvation-induced shift of band V, we identify the first (lowest-eBE) vibrational peak (labeled a) and use it as a marker (i.e., the detachment energies indicated in Figs. 2.1-2.3 correspond to transition a).

The $ONNO^-$ signal (band II, most prominent in dataset 2.1) appears as a weak, low-eBE tail of band V, at a small fraction of the NNO_2^- signal intensity. The two-photon signal from the O^- fragment, seen at 355 nm for n = 1-3, is not observed at 266 nm. Although its absence may be attributed partially to a smaller 266 nm O^- channel dissociation cross-section (compared to 355 nm), we believe that the lower 266 nm laser fluence is primarily responsible for the reduction of the two-photon signal.

We also note that the photoelectron spectrum in Fig. 2.3 contains no band that can be attributed to the O^- cluster core. This may seem surprising, as the 355 nm results strongly suggest the presence of some $O^-(N_2O)_3$ clusters (feature IV in spectrum 6.1.3). However, using band II (arising from the $ONNO^-$ cluster core) as a reference, the signal due to $O^-(N_2O)_3$ in Fig. 2.3 is not expected to rise above the noise level.

The 266 nm spectra for the larger clusters (n > 3) are consistent with those obtained at 355 nm, suggesting atomic anion (O^-) cluster cores. The VDE's indicated for the type IV bands in Figures 6.1 and 6.2 differ only within the experimental uncertainty. For n = 4, the higher-energy $O(^1D) \leftarrow O^-(^2P)$ photodetachment transition is also

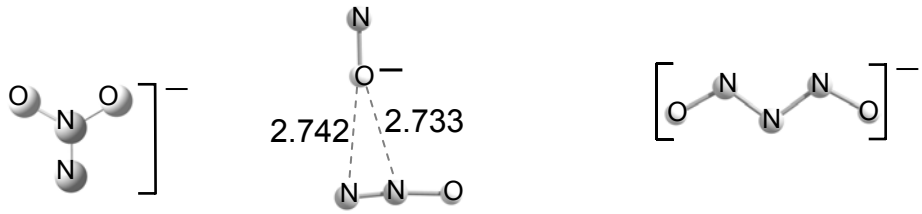

V VI VII

Figure 6.3. Relevant covalent isomers for $[O(N_2O)]^-$ and $[NO(N_2O)]^-$. Drawn to scale based on parameters reported by Pichugin[6] (isomer V, NNO_2^- at the MP2/aug-cc-pVDZ) and Hiraoka et al. [$NO^-(N_2O)$ and $ONNNO^-$, at the ROHF/6-31+G and RHF/6-31+G levels]. The intermolecular distances for isomer VI are indicated in Angstroms. All other geometric parameters are found in the original references.[6,7]

observed at a near-zero eKE. This transition is inaccessible for $n > 4$ due to the additional solvent stabilization. While some of the 266 nm images for $n \geq 7$ do show faint central features (eKE $\approx$ 0), the corresponding contributions to the photoelectron spectra in the low-eKE range are negligibly small.

In summary, the 266 nm photodetachment data indicate the same abrupt change in the $[O(N_2O)_n]^-$ cluster-core structure occurring at $n = 4$, as seen in the 355 nm data. The switch from broad molecular transitions in the $n = 1$–3 range to atomic-like bands for $n \geq 4$ suggests a molecular-to-atomic anion ($NNO_2^- \rightarrow O^-$) core switching.

6.3.3 Photoelectron angular distributions for $O^-(N_2O)_n$ (n = 0,4-9)

The corresponding anisotropy parameter values for the O^- based transitions (observed for $n = 4$–9) are plotted in Figure 6.4 (a). The $O^-(N_2O)_n$ photodetachment transitions analyzed correspond to the final ^3P state of solvated oxygen, while for bare O^- both the ^3P and ^1D neutral pathways are included. The Cooper-Zare curve for O^-, using the parameters of Hanstorp et al.,[1] (as discussed in Chapter 4) is also shown in Figure 6.4 (a). In the low-eKE range, the 355 nm anisotropy parameters for the O^- -based clusters fall close to the O^- Cooper-Zare curve, but deviate from it increasingly with increasing eKE. The 266 nm angular distributions (for peak eKE's between 1.35 and 1.92 eV) show stronger deviations from the Cooper-Zare curve; these transitions are nearly isotropic – in fact slightly positive – in stark contrast to the strongly negative values of the Cooper-Zare curve for bare O^- in the corresponding energy region.

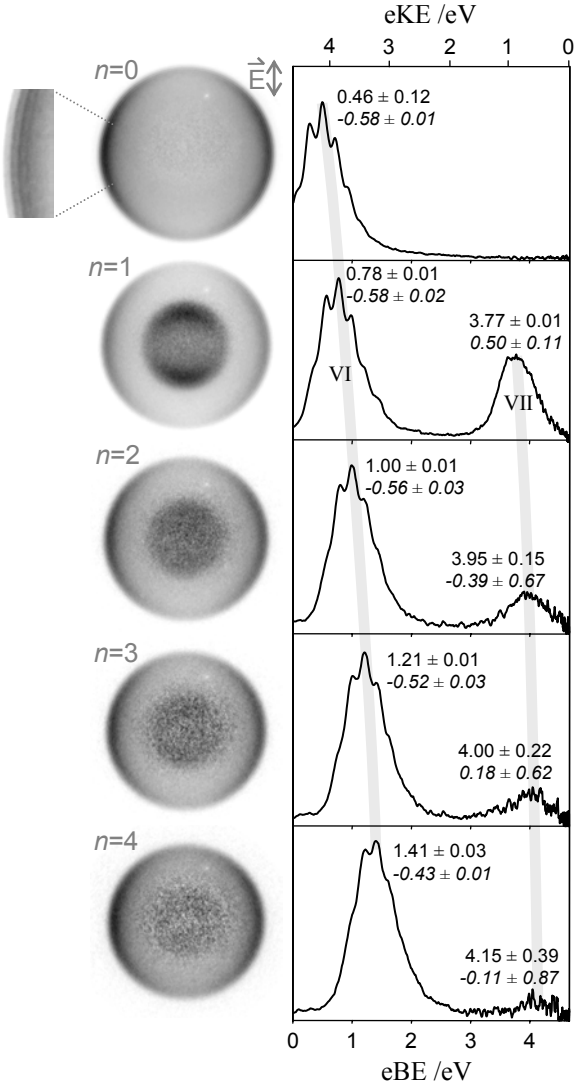

Figure 6.4 Photoelectron images and energy spectra for $[NO(N_2O)_{n=0\text{-}4}]^-$, obtained at 266 nm. Laser polarization is vertical in the plane of the page. Peak eKE's (in eV, top value) and anisotropy parameters (italicized value) are indicated for each type VI band as well as type VII bands. Anisotropy parameters were determined for the angular distributions over the entire Franck-Condon envelope of each transition. The gray lines are intended to aid the eye in recognizing the shifts in VDE along the solvation series.

6.4 Imaging Results for $[NO(N_2O)_n]^-$ (n = 0-4) at 266 nm

The 266 nm photoelectron images and spectra for $NO^-(N_2O)_n$ (n = 0-4) presented in Figure 6.4.1 correspond to the combination of three individual images (each between 90,000 and 270,000 experimental cycles, collected on separate days in 15,000 batches with background subtraction). The laser fluence was 1.0×10^6 W/cm^2. The average vertical detachment energies (VDE's) and anisotropy parameters for the individual images are indicated, with uncertainties corresponding to plus or minus two standard deviations for each transition.

6.4.1 Photoelectron energy spectra of $[NO(N_2O)_n]^-$ at 266 nm

The n = 0 image shows limited vibrational structure which is more apparent in the magnified inset in Figure 6.4.0. The NO^- spectral band (labeled VI) progressively shifts to higher VDE's with the addition of each solvent molecule, as expected in general along a solvation series and seen for this system previously[8,156,157] at various other wavelengths. For $n \geq 1$ we note a second, higher-eBE transition (labeled VII), peaking parallel to the laser polarization direction in contrast to the NO^--based transitions. This second feature, while absent for n = 0, persists through n = 4, though its relative intensity decreases along the series. This feature is attributed to a second isomer of the n = 1 species. The n = 1 photoelectron spectrum is similar to that obtained by the Continetti group at the same wavelength, with the notable difference that their spectrum contains features consistent with photodetachment from O^-, while ours does not. The O^- signal, observed by the Continetti group using a laser fluence of ~2×10^8 W/cm^2, was attributed

to photodissociation of the parent anion species, generating O^-, followed by photodetachment of the fragment with a second photon from the same laser pulse.[152] In our experiment a much lower laser fluence of ~1×10^6 W/cm^2 was used. The absence of similar features in our n = 1 spectrum, therefore, supports the Continetti group's assignment of this feature to a two-photon process.

6.4.2 Photoelectron angular distributions for $[NO(N_2O)_n]^-$

Photoelectron anisotropy parameters (β) were calculated over the Franck-Condon envelope of each transition. The β values for the NO^- based transitions (band VI), including bare NO^-, are plotted in Figure 6.4 (b) as a function of the transition's peak eKE, along with the previous results for this cluster series at 786, 532 and 355 nm,[8] with error bars of plus or minus two standard deviations. The data point for bare NO^- at 266 nm in Figure 6.4 (b) reflects the results of the new measurement, as the present work was carried out with significantly lower experimental backgrounds and greater data accumulation times (as evidenced by the excellent quality of the photoelectron image in Figure 6.2.0).

6.5 Discussion of solvent-mediated core anion isomerization

In the following we discuss the identities of the anion cores indicated by the photoelectron spectra for both cluster series.

6.5.1 Core-switching in $[O(N_2O)_n]^-$

The present study is the first investigation of the $[O(N_2O)_n]^-$ cluster series in the size range up to n = 9 via photoelectron spectroscopy. The experimental results reveal a transition from the molecular (NNO_2^-) to atomic (O^-) cluster core structure occurring between n = 3 and 4. Although both core types may coexist, to a degree, through the entire cluster size range studied, an overwhelming predominance of clusters with the molecular core is seen for n = 1–3, while the atomic anion based clusters clearly dominate for n = 4–9. Accordingly, the $[O(N_2O)_n]^-$ anion population can be described as a combination of the competing distributions of the $NNO_2^-(N_2O)_{n-1}$ and $O^-(N_2O)_n$ clusters. Judging by the signal levels, the $NNO_2^-(N_2O)_{n-1}$ distribution peaks at n = 1 and decreases as the cluster size increases, with a very quick falloff after n = 3 where the $O^-(N_2O)_n$ series emerges.

The core-switching phenomenon is expected to depend on the relative stabilities of the $O^-(N_2O)_n$ and $NNO_2^-(N_2O)_{n-1}$ cluster anions. For n = 1, covalent bonding in NNO_2^- is energetically favored over the solvation of O^- by N_2O. However, O^- could be solvated more effectively than NNO_2^- due to the more localized charge of the atomic anion. As the number of solvent molecules increases, the difference between the solvent stabilization energies for $O^-(N_2O)_n$ and $NNO_2^-(N_2O)_{n-1}$ may exceed the extra covalent bond energy in NNO_2^-, making the O^--based clusters more energetically favorable overall. Similar arguments were made previously for the core-switching in $(CO_2)_n^-$.[130,131,153]

The relative stabilities of the $NNO_2^-(N_2O)_{n-1}$ and $O^-(N_2O)_n$ clusters, ΔE_n, can be estimated from the solvent evaporation and bond dissociation energies and expressed approximately as[158]

$$\Delta E_n = D_0(NNO_2^-) + \Delta_{n-1}VDE(NNO_2^-) - \Delta_n VDE(O^-). \quad (6.2)$$

In equation 6.1, $D_0(NNO_2^-)$ is the $NNO_2^- \rightarrow O^- + N_2O$ bond dissociation energy, while $\Delta_{n-1}VDE(NNO_2^-)$ and $\Delta_n VDE(O^-)$ are the shifts in the NNO_2^- and O^- photoelectron band positions due to the interaction with $(n - 1)$ and n N_2O solvent molecules, respectively. Specifically,

$$\Delta_{n-1}VDE(NNO_2^-) = VDE[NNO_2^-(N_2O)_{n-1}] - VDE[NNO_2^-] \quad (6.3)$$

$$\Delta_n VDE(O^-) = VDE[O^-(N_2O)_n] - VDE[O^-]. \quad (6.4)$$

In determining $\Delta_{n-1}VDE(NNO_2^-)$, we will use the solvation-induced shift of band V's peak (a) identified in Figures 6.2.1–6.2.3.

Two independent measurements of the $NNO_2^- \rightarrow O^- + N_2O$ dissociation are available in the literature, giving the rather disparate $D_0(NNO_2^-)$ values of 1.40±0.03eV[139] and 0.57±0.05eV.[140] In both cases, the dissociation energy is determined from the maximum fragment kinetic energy release in the dissociative photodetachment of NNO_2^-, but via two different pathways: $O(^3P) + N_2O + e^-$ at 532 nm[139] and $N(^4S) + NO_2 + e^-$ at 266 nm.[140] The latter channel has a better Franck-Condon overlap with the parent NNO_2^- owing to the bent equilibrium geometry of NO_2. It is therefore expected to yield a less excited NO_2 photofragment (compared to the N_2O fragment in the other channel) and provide a more accurate determination of $D_0(NNO_2^-)$.

Though the VDE's for both the O^- and NNO_2^- cluster core types are not available for all cluster sizes studied due to the size-dependent core-preference, we have estimated the "missing" VDE values by interpolating or extrapolating the observed band positions for the series of each core-type. Figure 6.5 displays plots of the cluster-size-dependent detachment energies for $O^-(N_2O)_n$ and $NNO_2^-(N_2O)_{n-1}$, determined from bands IV and VI (peak a), respectively. The solid symbols indicate the direct experimental results, while the open symbols show the interpolated or extrapolated "missing" values.

Since the solvent-induced shift in the VDE between $n-1$ and n is approximately equal to the binding energy of the n^{th} solvent molecule to the cluster, we estimate that the sequential binding energies of the first, second, third, and fourth N_2O's to O^- are 0.37, 0.34, 0.30, and 0.25 eV, respectively. These numbers are strikingly close to the corresponding values of 0.37, 0.34, 0.30, and 0.28 eV for the sequential binding energies of N_2O to OH^- determined previously by Lineberger and co-workers.[159]

From the data summarized in Fig. 3 and the two aforementioned values of $D_0(NNO_2^-)$, the relative stabilities of the $O^-(N_2O)_n$ and $NNO_2^-(N_2O)_{n-1}$ cluster anions can be calculated using equation 6.2. The relative stabilities calculated using each D_0 are listed in Table 6.1. Positive ΔE_n indicate that the corresponding NNO_2^- based clusters are more stable than those with the O^- core. The estimated ΔE_n values based on $D_0 = 1.40$ eV[139] (first column in Table 1) suggest that from the thermodynamic standpoint the $NNO_2^- \rightarrow O^-$ core-switching is not expected at $n = 4$, where our experimental data clearly indicates that the O^- based clusters become the predominant species. However, the relative stabilities derived from $D_0 = 0.57$ eV[140] (second column in Table 1) do show

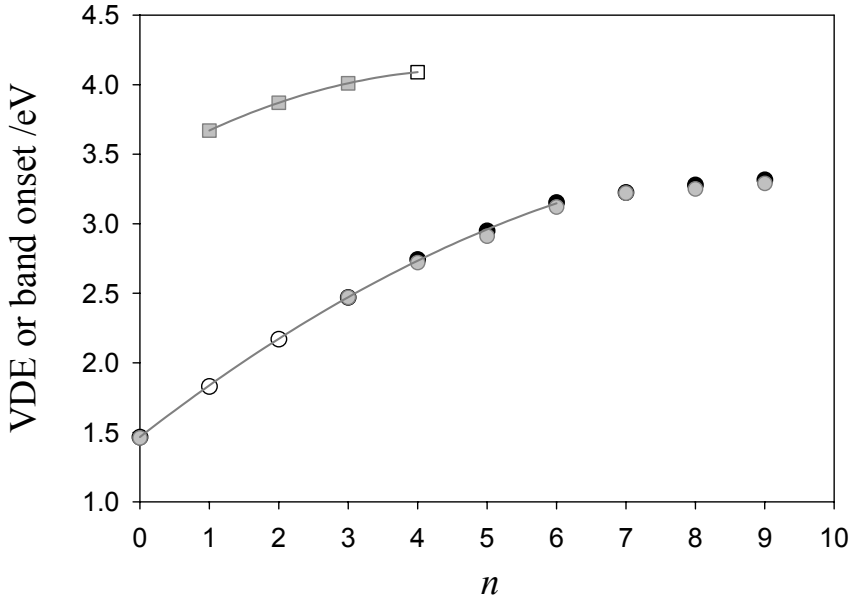

Figure 6.5 The detachment energies (VDE or band onset energy) for detachment from $O^-(N_2O)_n$ at 266 nm (solid grey circles) and 355 nm (solid black circles) and $NNO_2^-(N_2O)_{n-1}$ at 266 nm (solid grey squares), corresponding to the bands in the photoelectron spectra in Figures 6.1 and 6.2. The solid symbols indicate the direct experimental results, while the open symbols show the interpolated or extrapolated "missing" values.

n	Experiment[a]	Experiment[b]	MP2[c]	CCSD[d]	CCSD[e]
1	1.03	0.20	0.33	1.01	0.98
2	0.89	0.06	0.24	0.91	...
3	0.73	–0.10	...	...	...
4	0.56	–0.29	≤0.07	≤0.62	...

[a]Based on the value $D_0(NNO_2^-$ = 1.40±0.03 eV by Osborn et al.[139]

[b]Based on the value $D_0(NNO_2^-)$ = 1.40±0.03 eV by Li et al.[140]

[c]UMP2/aug-cc-pVDZ

[d]CCSD/6-31+G*//MP2/aug-cc-pVDZ

[e]CCSD/aug-cc-pVDZ

Table 6.1 Relative stabilities (ΔE_n /eV) of the $NNO_2^-(N_2O)_{n-1}$ and $O^-(N_2O)_n$ cluster anions. Positive values indicate that the corresponding NNO_2^- -based clusters are more stable than those with the O^- core.

that the core-switching should occur at around n = 3, which agrees well with the first appearance of the type III transitions at this cluster size in our experiment.

It is also instructive to compare the experimental estimates of the relative stabilities for the $[O(N_2O)_n]^-$ series with theoretical predictions. Computations were performed by a co-worker[4,6] for $O^-(N_2O)_n$ and $NNO_2^-(N_2O)_{n-1}$, n = 1–4, using the GAUSSIAN 03 program package.[111] The details of the computations (including the stable structures isolated) may be found elsewhere.[4,6] In brief, the geometries were optimized at the unrestricted second-order Møller-Plesset perturbation theory (UMP2/aug-cc-pVDZ) level, followed by harmonic frequency calculations at the same theory level to verify that the stationary points found correspond to true potential minima. The computed energies were corrected for zero-point vibrational energies and basis set superposition errors.[160] Due to internal instabilities[161,162] in the Hartree-Fock (HF) wave functions for all $[O(N_2O)_{n=1-4}]^-$ except for NNO_2^-, energies were also computed using the coupled-cluster with single and double excitations (CCSD) method for some of the cluster structures of interest. No instabilities were detected for the wave functions with the CC calculations.

The relative stabilities ΔE_n, defined as the energy differences between the most stable $O^-(N_2O)_n$ and $NNO_2^-(N_2O)_{n-1}$ structures computed from the MP2 and CC results are summarized in the last four columns of Table 6.1. Although both the MP2 and CC calculations find that NNO_2^- is more stable than $O^-(N_2O)$, there is a significant discrepancy in the computed relative energies: MP2 estimates that NNO_2^- is more stable by mere 0.33 eV, while CC methods return an about 1 eV difference. Nonetheless, both

the MP2 and CC energies are consistent with the lack of $O^-(N_2O)$ signatures in the experimental data (Figs. 6.1.1 and 6.2.1). The relative stabilities determined by both the MP2 and CC methods indicate that the energy difference between the $O^-(N_2O)_n$ and $NNO_2^-(N_2O)_{n-1}$ clusters decreases steadily with increasing n, which is consistent with the assumption of O^- being solvated more effectively than NNO_2^- and is necessarily for the core switching to occur. However, both the MP2 and CC methods predict that the NNO_2^- based species remain favored energetically even for n = 4, where the experiment indicates a nearly complete switch to the O^- core type.

Specifically, MP2 predicts the $NNO_2^-(N_2O)_3$ to be more stable than $O^-(N_2O)_4$ by only 0.07 eV, while the CCSD/6-31+G*//MP2/aug-cc-pVDZ estimates a 0.62 eV difference. We note also that MP2 provides a better quantitative agreement with the estimates of ΔE_n based on $D_0(NNO_2^-)$ = 0.57 eV,[140] which are in accord with the present experimental observations. The CC calculations closely match the relative stabilities based on the 1.40 eV value of $D_0(NNO_2^-)$,[139] which are not in agreement with the present experimental results. This outcome is surprising, since one should not expect MP2 performance to be superior to the CC methods, especially given the wave function instability problems mentioned above; the observed agreement of the MP2 results with the experiment is likely serendipitous. To conclude, we have obtained two sets of relative stabilities ΔE_n of the $NNO_2^-(N_2O)_{n-1}$ vs. $O^-(N_2O)_n$ cluster structures, summarized in columns 1 and 2 of Table 6.1. These estimates are based on our own experimental data and the two available (yet drastically different) measurements of the NNO_2^- bond

dissociation energy. One of the ΔE_n series supports and the other contradicts the simple thermodynamic model of the experimentally observed NNO_2^- to O^- core-switching.

Although the present experimental results are compelling, the discrepancies between past experimental measurements and theoretical models call for caution in concluding that the suggested thermodynamic mechanism is the only possible explanation for the observed core-switching. Alternatively, it could be possible for the larger clusters ($n \geq 4$) to be formed initially with the O^- core and remain trapped in the corresponding (possibly metastable) state on the timescale of our experiment (tens of microseconds). Such a kinetic model would imply the existence of a barrier for the association reaction of O^- with any one of the surrounding N_2O solvent molecules. Certainly, additional experimental data on NNO_2^- bond dissociation energy would help to draw a confident conclusion on the core-switching mechanism. At present, the work of Li and Continetti[140] is believed to provide a more accurate determination of $D_0(NNO_2^-)$, supporting the thermodynamic picture of the core-switching reported here.

While we have not focused on the $ONNO^-$ isomer, we note again that it may coexist somewhat for n = 1-3 as evidenced by the tail in the one-photon signal. The two-photon signal in the overlapping energy range (feature IV) suggests that NO_2^- is formed upon 355 nm excitation of unsolvated $N_2O_2^-$. However, as no 46 amu peak was observed in the 355 nm photofragmentation of this species,[4] this feature warrants further study. We have performed a 400 nm + 800 nm pump-probe experiment on NNO_2^- to monitor the O^- fragment (which turns out to be generated on a timescale comparable to the temporal resolution of the experiment), but the higher-eBE component would not have

been accessible with the 800 nm probe. The evolution of two-photon feature IV could be monitored in a 400 nm + 400 nm pump-probe experiment. Additionally, 355 nm photofragmentation of the n = 1 species at a higher laser fluence could test for the presence of an NO_2^- photofragment.

Finally, we note very weak (unlabeled) features in the higher-fluence spectra for n = 2-3 peaking at eBE ≈ 1.8 eV which are not apparent in the lower-fluence spectra. This value is quite close to the extrapolated VDE ≈ 1.84 for $O^-(N_2O)$ (see Figure 6.5), suggesting that fragmentation of the $NNO_2^-(N_2O)_{n-1}$ core also yields singly solvated O^-. Photofragmentation of the n = 2,3 species performed by a co-worker[4,100] revealed a dominant fragment peak at 60 amu. Comparison of these results with those for $NNO_2^-(H_2O)$ by the same coworker and $CO_3^-(H_2O)$[163,164] by the Bowen group led us to conclude previously[4] that this mass fragment was most likely covalent NNO_2^-, formed upon excitation of the NNO_2^- core, internal conversion to the ground state and evaporation of all solvent molecules. The 1.8 eV feature in Figures 6.1.2 and 6.1.3 suggests that 355 nm excitation of the NNO_2^- core may also result in internal conversion to the $O^-(N_2O)$ isomer. This possibility also warrants further investigation; a 400 nm + 400 nm pump-probe experiment could also help to elucidate this process.

6.5.2 Isomer coexistence in $[NO(N_2O)_n]^-$

Two distinct transition types, labeled bands VI and VII and corresponding to different core anions, are apparent in the $[NO(N_2O)_n]^-$ photoelectron images and spectra in Figure 6.4. Each transition is shifted to successively higher eBE's as n increases;

solvation stabilizes the anion more than the corresponding neutral and thus the anion-neutral energy gap increases with increasing n. We again take the difference between a band's estimated VDE for anion clusters of size n and size n–1 as an estimate of the stabilization of the anion cluster by addition of the n^{th} solvent molecule. Type VI transitions are assigned to photodetachment from NO^- or an N_2O-solvated NO^- core, while the higher-eBE transitions (type VII) are ascribed, based on the following arguments, to the $ONNNO^-$ core anion (see Figure 6.3 for illustrations of the two isomers of $N_3O_2^-$).

Band VII is not present for $n = 0$, but seen for $n \geq 1$. For $n = 1$, it peaks at approximately 3.8 eV, consistent with the feature observed by Resat et al.,[152] who assigned it to a w-shaped (C_{2v} symmetry) covalent $ONNNO^-$ structure. This structure, first proposed by Hiraoka et al. (RHF/6-31+G),[7] was computed by Snis and Panas [B3LYP/6-311+G(d)][165] to have VDE's of 3.92 eV and 3.93 eV for detachment to the $^2B_2$ and $^2A_1$ states of the neutral, respectively. Both of these values are in good agreement with the observed maximum of band VII.

More recently, it was proposed[166] that $NO_2^-(N_2)$, structurally related to the computed[69] cyclic intermediate of dissociative electron attachment to nitrous oxide, $O^-(N_2)$, could be responsible for this transition. While the positive β of band VII is consistent with our experimental observations for detachment from unsolvated NO_2^-,[6] we find the $NO_2^-\cdot N_2$ structure incompatible with the VDE reported here and in the work of Resat et al.[152] The VDE for NO_2^- ($X\,^2A_1 \leftarrow X\,^1A_1$) is ≈ 2.8 eV.[6,167-169] We may estimate

the VDE of $NO_2^-(N_2)$ to be only slightly greater than that of the bare ion because N_2 should interact weakly with the anion. The cyclic $O^-(N_2)$ isomer was predicted to be stable by only 0.18 eV with respect to $O^- + N_2$,[69] consistent with a relatively weak electrostatic interaction; assuming a similar stabilization of NO_2^- we expect the VDE for $NO_2^-(N_2)$ to be approximately 3.0 eV, which is significantly different from the 3.8 eV value observed for transition VI in Figure 6.3.1. For further comparison, we note the VDE for $NO_2^-(NO)$ is ≈ 3.1 eV.[169]

The positive photoelectron anisotropy parameter for transition VII is consistent with detachment from a totally symmetric orbital.[20] According to the s&p approach, photodetachment from a C_{2v} symmetry molecule, such as $ONNNO^-$, with positive anisotropy is likely to originate from an a_1 orbital. (We caution, however, that this argument is best suited for low-eKE transitions in small, relative to the de Broglie wavelength of the photoelectron, anions, and that the approach failed for photodetachment from the a_1 HOMO−1 of NH_2^-.) Therefore, the observed properties of transition VII are consistent with detachment from an a_1 orbital. Some possible contribution from b_2 orbital photodetachment could help account for the magnitude of the anisotropy parameter, consistent with the predictions of Snis and Panas for the $ONNNO^-$ anion.[165]

Unlike our observations for the $[O(N_2O)_n]^-$, n = 1-9 cluster anions,[4] there is no clear size-dependent core-switching between the $NO^-(N_2O)_n$ and $ONNNO^-(N_2O)_{n-1}$ isomers in the $[NO(N_2O)_n]^-$ series. Based on the data in Figure 6.3, the two isomers

coexist for all degrees of solvation examined (n = 1–4), and we make two additional observations regarding their coexistence.

First, the successive solvation-induced shifts in peak eBE for isomer VII are somewhat smaller than those for isomer VI throughout the cluster series. This is easily seen upon examination of the differing slopes of the grey trend lines sketched in Figure 6.3. Assuming that peak eBE in each case corresponds to the vertical detachment energy, this trend suggests that upon solvation core isomer VII ($ONNNO^-$) is stabilized less efficiently than core isomer VI (NO^-). The validity of the above assumption may be questioned at small eKE's, where near-threshold effects on photodetachment cross-sections may skew the observed peak positions away from values that correspond to the true VDE's, as discussed previously for other systems.[170,171] Qualitatively, however, the less efficient stabilization of isomer VII is consistent with the more diffuse charge density in $ONNNO^-$, compared to the smaller NO^- anion.

Second, the intensity of the bands corresponding to an $ONNNO^-$ cluster core is observed to decrease along the solvation series relative to that of the NO^- core. This may also be due in part to the increasing proximity of transition VII to eKE = 0 (as photodetachment cross-sections tend to decrease with decreasing eKE).[52,172] However, the eKE effect alone does not appear to be sufficient to account for the rapid decrease in the relative intensity of transition VII observed with increasing n. We therefore conclude that the relative population of the $ONNNO^-$ based clusters decreases with increasing solvation relative to that of the NO^- based isomers.

Both of these observations suggest that increasing solvation favors, in a thermodynamic sense, the smaller NO^- core. A more quantitative discussion of the solvation-dependent energetics of isomer VII would require modeling the partial-wave composition of the photodetached electrons, which affects the scaling of the low-eKE cross-sections.[171]

6.6 Discussion of the photoelectron angular distributions: evidence for resonant photoelectron-solvent scattering

We now move on to the solvation effects on the photoelectron angular distributions in the photodetachment of $NO^-(N_2O)_n$, n = 1–7 (type VI transitions in Figure 6.3) and $O^-(N_2O)_n$, n = 4–9. The anisotropy values (β) for the two cluster series, derived from the present work as well as past measurements,[4,6,8,100] are plotted in Figures 6.4 (a) and (b), respectively, as functions of eKE. The following analysis closely follows the procedure outlined previously.[8,100]

In examining the angular distributions in photodetachment of cluster anions, it is instructive to separate the effects of solvation on the initial and final states of the detached electron from pure kinetic-energy effects. Namely, solvation-induced changes in eKE for a given transition (as indicated, for example, by the band shifts in Figures 6.1-6.3) is presumed to affect partial-wave composition of the photoelectrons in the same way as a red-shift of the detachment wavelength would. The resulting anisotropy variation can be described approximately using the Bethe[51] and Cooper-Zare[37,44,45] central-potential model, assuming Wigner scaling of partial-wave cross-sections[1,52]

which, as discussed in Chapter 4, is not strictly valid throughout the energy range examined, but generally agrees quite well with experimental data. This variation is purely eKE-induced and does not reflect the solvent-induced perturbation of the initial- or final-state wave functions. In this paradigm, the Cooper-Zare curve β_{cz}(eKE) provides a zero-solvation reference, which describes pure eKE effects on anisotropy, while discounting such effects as photoelectron-solvent scattering and perturbation of the shape of the parent electron orbital.

The solid curves in Figures 6.6 (a) and (b) are obtained by fitting the Cooper-Zare model equation[37,44,45] under the Wigner approximation[52] to the experimental data for bare O^- (l = 1), and NO^- (with effective l = 2) respectively (see Chapter 4 for details). The model uses two fitting parameters: A, related to the spatial extent of the negative ion, and φ, the relative phase of the $l \pm 1$ partial-waves.[37,44,45] The O^- curve in Figure 6.6 (a) has been well-studied and our data for unsolvated O^- are fit well over the entire energy range using the previously reported values of A = 0.55 eV^{-1} and $\cos\delta$ = 0.96,[1,101] with respective standard errors of 0.045 and 0.053. The resulting curve closely matches the curve first computed by Cooper and Zare.[44] The NO^- curve in Figure 6.6 (b) has been adjusted relative to that initially reported by our group[8] to fit the new 266 nm data. The new fit parameter values used in Figure 6.4 (b) are A = 0.336 eV^{-1} and $\cos\delta$ = 0.896, obtained via a nonlinear regression with respective standard errors of 0.031 and 0.039. The old values of A = 0.383 eV^{-1} and $\cos\delta$ = 0.881 are well within two standard errors of the new fit and the adjustment does not appreciably affect the analysis or conclusions of this or the previous work.

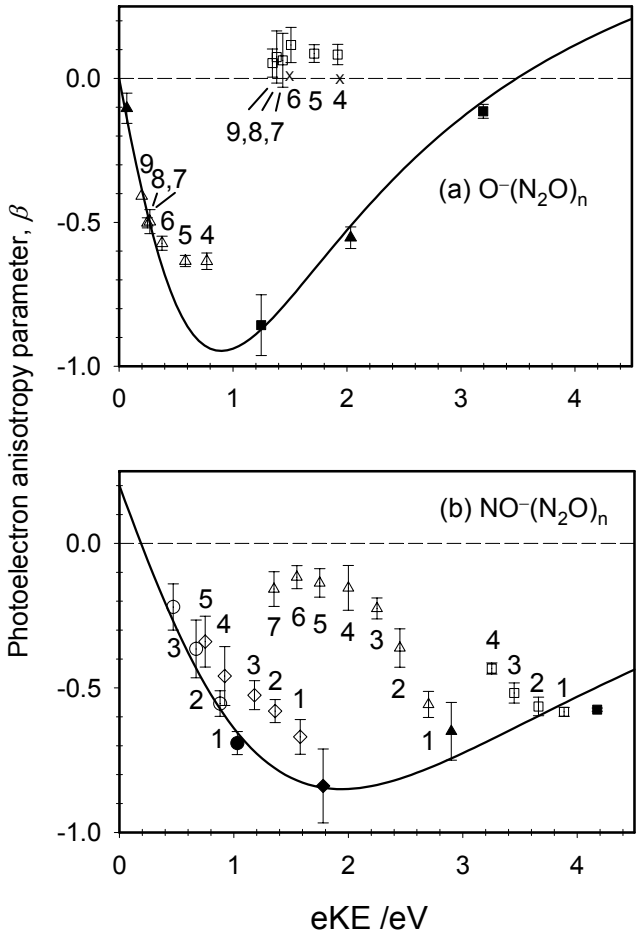

Figure 6.6 (a) Summary of the photoelectron anisotropy parameter (β) values determined for the $O^-(N_2O)_n$, n = 0, 4-9 cluster series at 355 nm (triangles) and 266 nm (squares). Data points corresponding to the unsolvated O^- (i.e., n = 0) transitions yielding both the ^3P and ^1D neutral states are included (filled symbols). The Wigner-Bethe-Cooper-Zare curve for O^- from Chapter 4 is also plotted as a zero-solvation reference. Results for n = 4, 6 obtained with the 266 nm laser polarization perpendicular to the plane of the detector are also plotted (as ×'s). (b) Similar summary of the β values for the $NO^-(N_2O)_n$ cluster series plotted vs electron kinetic energy: circles, 786 nm;[8] diamonds, 532 nm;[8] triangles, 355 nm;[8] squares, 266 nm.[5] Filled symbols correspond to bare NO^- (i.e., n = 0), while open symbols are used to show the results for solvated clusters (n>0). The integers next to the cluster data points indicate the corresponding solvation numbers n. A Cooper-Zare curve (using the l = 2) approximation, is plotted as a solid line. Error bars correspond to two standard deviations.

The effects of solvent-induced perturbations of the final and initial photoelectron wave functions can now be quantified by calculating the difference between the experimental β values for cluster anions and the Cooper-Zare predictions for the unsolvated core anions at the observed transition's peak eKE. In comparing the results for clusters of different sizes, the difference between the experimental values, β(eKE), and the Cooper-Zare predictions, β_{cz}(eKE), should be normalized by the corresponding degree of solvation. Since the cumulative effect of several solvent molecules is not expected to scale linearly with n, an empirical scaling exponent is introduced, as described in the previous publication,[8] giving rise to the normalized solvent-induced anisotropy differential D(eKE) defined by equation 6.1

The deviations of the $O^-(N_2O)_n$ and $NO^-(N_2O)_n$ photoelectron anisotropies from the corresponding O^- and NO^- Cooper-Zare curves are most pronounced at eKE ~ 2 eV (see Figure 6.4). The D(eKE) values for both the $O^-(N_2O)_n$ and $NO^-(N_2O)_n$ cluster series, including all available cluster sizes and wavelengths studied, are plotted in Figure 6.7. Note that the anisotropy differentials for the O^- based clusters fall close to those for the NO^- based clusters for comparable eKE's. We also note that adjusting the phase parameter in the O^- Cooper-Zare curve (using, for example, $\cos\delta = 0.925$, as done by other groups [1,101] does not significantly alter the anisotropy differentials for the O^- -based clusters. While the large VDE's of the O^- based clusters prohibit comparison in the eKE = 2-4 eV range, the overlap between the $O^-(N_2O)_n$ and $NO^-(N_2O)_n$ anisotropy differentials at eKE < 2 eV is remarkable.

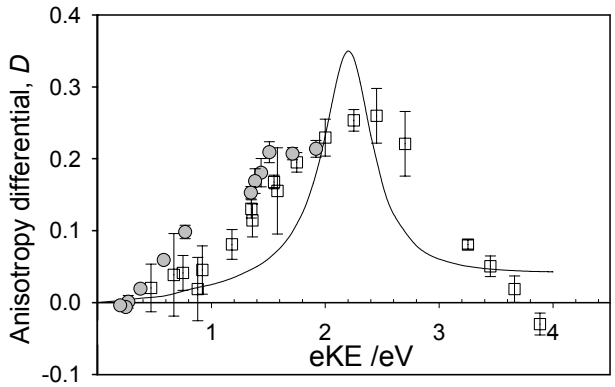

Figure 6.7 Anisotropy differentials D(eKE), calculated according to equation 6.1 for $NO^-(N_2O)_n$ (open squares) at 786 nm (n = 1-3), 532 nm (n = 1-5), 355 nm (n = 1-7), and 266 nm (n = 1-4), and for $O^-(N_2O)_n$ (gray circles) at 355 and 266 nm (n = 4-9). Error bars correspond to plus or minus 2 standard deviations. A computed $^2\Pi$ momentum-transfer cross-section for electron-N_2O scattering[9] is also plotted with arbitrary scaling relative to D(eKE).

This agreement suggests that the observed anisotropy deviations are not primarily due to the effects of solvation on the parent orbitals of the O^- or NO^- cores, consistent with our observation in Chapter 5 that parent-orbital perturbation effects are less pronounced for photodetachment from non-isotropic orbitals and the lack of a similar effect for $NO^-(N_2O)_n$ as discussed previously by our group.[8] Instead, the trend exhibited by the normalized anisotropy differentials reflects the properties of the solvent, N_2O, which is what the two cluster types studied have in common. The overall *D*(eKE) dependence, derived from the combination of the $O^-(N_2O)_n$ and $NO^-(N_2O)_n$ data, mirrors the main trend of the momentum-transfer cross-section[173] for $N_2O + e^-$ scattering.[9] The corresponding curve, taken from the work of Winstead and McKoy[9] is plotted in Figure 6.4. The broad *D*(eKE) maximum is near 2.4 eV, quite close to the $^2\Pi$ electron-N_2O scattering resonance peaking at 2.25 eV. The broader width of the *D*(eKE) curve compared to that of the resonance is likely due to the spread in effective energies of the photoelectrons undergoing scattering interaction with the solvent.[70] As discussed previously,[8] the effective "near-field" energy of this interaction, while difficult to quantify, is expected to differ appreciably from the "far-field" eKE measured in the experiment.

The foregoing discussion demonstrates that the observed solvent-induced decrease in photoelectron anisotropy magnitude may be attributed to scrambling of photoelectron angular distributions due to interaction with solvent molecules. Such scrambling appears to be particularly effective in the presence of solvent-based anionic resonances.[8,104] However, we now address the possibility that a scattering resonance may

not only depolarize (scramble) a photoelectron's angular distribution, but may in fact repolarize it in a different direction, by turning to another observation from the 266 nm $O^-(N_2O)_n$ anisotropy values.

As seen in Figure 6.4 (a), the 266 nm β values in the eKE = 1.3–1.9 eV range not only deviate very strongly from the values expected in the photodetachment of bare O^-, but are also opposite in sign, all ranging between zero and +0.12.

In view of the unexpected nature of this result, we felt it was necessary to test for the possibility that the sign change is due to a systematic error in our imaging system. We carried out additional measurements on $O^-(N_2O)_4$ and $O^-(N_2O)_5$, collecting photoelectron signals for 150,000 experimental cycles (with corresponding background subtraction), with the laser polarization aligned in the direction perpendicular to the plane of the detector. In this configuration, the photoelectron angular distribution should appear isotropic in the image plane, regardless of the nature of the transition probed. This is confirmed by the anisotropy parameters obtained (–0.005 and 0.007, respectively), both well within the confidence limits of the expected $\beta = 0$ value. Therefore, although the magnitudes of the proper $O^-(N_2O)_n$ 266 nm anisotropy values in Figure 6.4 (a) are small (0.08 ± 0.04 and 0.12 ± 0.06, respectively), the above test suggests that their sign is in fact significant. The change in the apparent character of cluster photodetachment transitions may mean that an accessible scattering resonance has the capacity to repolarize a photoelectron.

The lifetime of the resonance is likely ~1 fs,[174] which is expected to be long enough to completely scramble the original angular distribution, considering the

attosecond timescales of electronic motions.[175] However, this view does not necessarily imply that electrons passing through a resonance are re-emitted isotropically. In fact, in the $N_2O + e^-$ case, the electrons were both predicted[9] and observed[176] to scatter with a *p*-like distribution polarized preferentially in the backward and forward scattering directions. Applying this result to cluster-anion photodetachment requires not only explicit knowledge of the cluster's geometry, but also the phase shifts associated with scattering events, which may result in new interference effects.

We thus speculate that photoelectrons resonantly scattered by solvent molecules, though stripped of their nascent angular distributions, will not necessarily have completely isotropic final angular distributions. In the absence of complete scrambling, the final distribution's character may be determined by the cluster geometry and specific details of the solvent-based resonance. In this light, the fact that the above observation of possible photoelectron repolarization is made for the $O^-(N_2O)_n$ cluster anions, but not for $NO^-(N_2O)_n$, is likely due to differences in the geometric structures and the solvation numbers of the two cluster types studied.

6.7 Summary

Our photoelectron imaging results for $[O(N_2O)_n]^-$ and $[NO(N_2O)_n]^-$ revealed the presence of multiple isomers for the core anions. For $[O(N_2O)_n]^-$, the covalent NNO_2^- core is preferred for n = 1-3, with a clear switch to an atomic O^- core for $3 < n \leq 9$. This switch is attributed to the more favorable solvation of O^- relative to NNO_2^-, overcoming the additional stability of the covalent bonds in the molecular anion and resulting in a net

thermodynamic preference for the atomic anion core in the clusters for n>3. In contrast, the $[NO(N_2O)_n]^-$ cluster series demonstrates a clear coexistence between an NO^- and (tentatively assigned) $ONNNO^-$ core for n = 1-3.

These results also facilitate examination of the effect of solvation by N_2O on photodetachment from O^- and NO^-. In both cases, the photoelectron anisotropy parameters deviate strongly from the corresponding zero-solvation reference curves, with the solvation-number-scaled anisotropy differentials D(eKE) for the O^- based clusters following the same trend as those for the clusters with NO^- cores in the eKE-range common for the two datasets. The scaled anisotropy differentials peak in the vicinity of the known electron-N_2O $^2\Pi$ scattering resonance. While the trend in D(eKE) is broadened relative to the momentum transfer cross-section for electron-N_2O scattering, the qualitative agreement is quite striking, especially considering that the scattering process is expected to be affected by the cluster environment. We therefore conclude that the solvation effect on the photoelectron angular distributions in these cases is primarily due to resonant interaction of photoelectrons with the N_2O solvent, rather than a solvent-induced perturbation of the parent-anion electronic wave function.

Additionally, photoelectron anisotropy parameters for 266 nm detachment from O^- under N_2O solvation appear to be slightly positive – opposite in sign to the expected values for detachment from bare O^- in the same eKE-range. The corresponding data points fall close in energy to the electron-N_2O scattering resonance. If this observation is indeed due to resonant photoelectron-solvent scattering, one possible explanation is that autodetachment from the N_2O^- resonance state is not necessarily isotropic. This

explanation is consistent with the p-type (forward-backward) nature of the $e^- + N_2O$ scattering interaction in the vicinity of the $^2\Pi$ resonance.

These results emphasize the complex nature of chemistry in solvated environments while demonstrating that photoelectron-solvent interactions must be considered in the analysis of photoelectron imaging results for cluster anions.

CHAPTER 7

A REVISITATION OF PHOTOELECTRON INTERFERENCE IN A DYNAMIC MOLECULAR SYSTEM

This chapter presents a new, partial-wave approach for examining the effects of coherence on photoelectron angular distributions for the time-resolved (780 nm + 390 nm) photoelectron imaging of I_2^- performed previously by coworkers.[10] It also presents new results for revisitation of their experiment, using two different pump-probe polarization schemes. I obtained these data in collaboration with Lori Culberson.

7.1 Introduction

Ultrafast pump-probe spectroscopy is a powerful technique for studying photodynamics of chemical systems. In general, this involves the initiation of a dynamic chemical process with an ultrashort laser pulse (on the order of femtoseconds or picoseconds in duration) that is probed by another laser pulse arriving after a defined delay time (Δt). Repeating the experiment for a variety of pump-probe delays allows for monitoring the evolution of the dynamic process in real time. While pump-probe photoelectron spectroscopy is useful for monitoring the evolution of electronic energies in the time domain, pump-probe photoelectron imaging also yields the corresponding photoelectron angular distributions, which provides an extra dimension of information related to the real-time evolution of electronic structure.

In general, a photoelectron distribution resulting from a two-photon process is not necessarily cylindrically symmetric. However, in the unique case of parallel linear pump and probe beam polarizations, the distribution is cylindrically symmetric about the laser polarization vector and has the following form[40,177]

$$I(\theta) = \frac{\sigma_{tot}(\Delta t)}{4\pi}[1 + \beta_2(\Delta t)P_2\cos(\theta) + \beta_4(\Delta t)P_4\cos(\theta)], \quad (7.1)$$

where $\sigma_{tot}(\Delta t)$ is the total detachment cross-section, P_i is the i^{th} order Legendre polynomial and β_i the i^{th} order β-parameter, all at a pump-probe delay of Δt, where θ is the angle with respect to the pump (and probe) laser beam polarizations. While we have previously referred to the second order anisotropy parameter as "β," we will now include the subscript to emphasize that higher-order terms may be present for multiphoton processes.

The molecular iodine anion is an excellent model system for anion pump-probe photoelectron spectroscopy; the fundamental (800 nm) and harmonics (400 or 267 nm) of a fs Ti:saphhire laser are ideal for 1) excitation from the anion's ground $X\,^2\Sigma_u^+$ state to the repulsive $A'\,^2\Pi_{g,1/2}$ state (~800 nm) and 2) photodetachment from the evolving I^- fragment (~390 or 267 nm). This photodissociation process has been studied for bare[178-183] and solvated[184-193] I_2^- via a variety of methods, and was the first process to be studied by time-resolved photoelectron imaging, by Davis and co-workers.[194] Davis et al. performed 793 nm + 267 nm time-resolved photoelectron imaging of I_2^- collecting images corresponding to pump-probe delays of up to ~1250 fs. They reported the appearance of sharp, I^--like features in the photoelectron energy spectrum as early as 300

fs into the dissociation process with minor evolution of the band position (further shifting by ~0.010 eV) through ~1 ps, yielding eKE's expected for detachment from bare I^-, consistent with their previous observations from time-resolved photoelectron spectroscopy.[178,180] The β_4 anisotropy parameter was observed to be largely time-independent and always smaller in magnitude than 0.1. The β_2 anisotropy parameter dropped steadily from $\beta_2 \approx -0.1$ at the zero-delay ($\Delta t \approx 0$ fs) to $\beta_2 \approx -0.55$ ($\Delta t \approx$ 200-350 fs). These delays are concurrent with the evolution of the photoelectron energy spectrum from broad to sharp atomic-like features, attributed to changes in the nature of the parent orbital during the dissociation process. Between $\Delta t \approx$ 350 fs and 600 fs, β_2 increased, peaking at $\beta_2 \approx -0.44$ near 600 fs. This change was correlated to the slight shift in the atomic-like peak in the energy spectrum. Finally, a small drop occurred at a pump-probe delay between 700 and 800 fs (to an average value of –0.52) which does not correlate to a change in the energy spectrum. The researchers suggest that this change is due to localization of the electron on one or the other of the I^- atoms enabled by coupling of the $A'\ ^2\Pi_{g,1/2}$ dissociative state with an ungerade state correlating to the same product channel, perhaps mediated by the electric field (500 V/cm^2) in the laser-ion interaction region.

A similar experiment, 780 nm + 390 nm time-resolved photoelectron imaging was performed (again with linear, parallel pump-probe polarization) for pump-probe delays from 0 to 5 ps by Mabbs et al.[10] In their experiment, the dissociation asymptote also appeared to have been reached by Δt = 700 fs from the energetic perspective (peak

eKE = 0.12 eV, matching that expected for detachment from bare I^- with a 390 nm, or 3.18 eV, probe). However, significant evolution of the anisotropy parameter (β_2) persisted through Δt = 2.5 ps. This variation in β_2 appeared to have a periodic component, oscillating from –0.2 to –0.35 and back over a period of 2.5 ps. This timescale corresponds to an internuclear separation of 36 Å (determined from classical trajectory calculations assuming 0.58 eV kinetic energy in the fragments) and is quite similar to the deBroglie wavelength of a 0.12 eV photoelectron, λ = 35.4 Å. The oscillation in β was thus attributed to the interference of the photoelectron effectively emitted from two centers, as first predicted by Cohen and Fano.[106] The oscillation in β_2 was fit to the following generic functional form:

$$\beta_2(t) = a + b\cos\left(\frac{2\pi R(t)}{\lambda} + \alpha\right), \tag{7.2}$$

where a and b are parameters, $R(t)$ is the time-dependent internuclear distance parameterized using a classical dissociation trajectory, α an additional phase shift (set arbitrarily to zero), and λ the de Broglie wavelength. A least squares fit of the data to equation 7.2 yielded a = –0.267 ± 0.006, b = 0.082 ± 0.008 and λ = 42.7 ± 1.1 Å, close to the photoelectron de Broglie wavelength of 35.4 Å. In this picture, preservation of the gerade symmetry of the dissociative $A'\,^2\Pi_{g,1/2}$ state requires the excess electron to be delocalized between the two iodine atoms, even at internuclear distances greater than 30 Å. The dissociating system is a coherent superposition of the two possible charge-localized states, (I_A^- + I_B) and (I_A + I_B^-), with the electron collapsing onto one state or the other only upon coupling of the gerade state with an ungerade state. Coincidentally, the

delocalization timescale (2.5 ps, as evidenced by the apparent end of the oscillation in β_2) is similar in magnitude to the de Broglie timescale (or oscillation period of β_2).

It was further proposed that the apparent difference in the $\beta_2(\Delta t)$ variation timescales between the experiments of Davis et al.[194] and Mabbs et al.[10] In the experiment by Davis et al,[194] the 267 nm probe resulted in a photoelectron de Broglie wavelength of ~10Å (less than one-third that in the experiment of Mabbs et al.[10]), resulting in a smaller $\beta_2(\Delta t)$ oscillation period of approximately 800 fs.

The present hypothesis regarding the two-centered interference dynamics is that the oscillations in β_2 with Δt are controlled by two, in principle distinct, timescales: 1) the de Broglie timescale, τ_{dB} and 2) the electron localization (or decoherence) timescale, τ_{loc}, which defines. The former, τ_{dB}, is determined by the photoelectron's de Broglie wavelength and the speed of dissociation of the diatomic. The delocalization timescale is believed to be dependent upon the external (imaging) field strength and the dissociation speed. This hypothesis suggests that the interference dynamics (and thus the temporal evolution of β_2) may be manipulated by altering the photon energy and electron extraction fields in the experiment (affecting τ_{db} and τ_{loc}, respectively).

In this chapter, we revisit several aspects of these results. First, we make use of the partial-wave approach outlined in Chapter 4 to model the photoelectron interference for the purpose of considering the delocalization timescales. In addition, new, preliminary imaging results for 778 + 389 nm photodetachment for 1) different extraction voltages and 2) a cross-polarized pump-probe configuration are presented and

discussed in the context of the previously reported pump-probe photoelectron imaging experiments on I_2^-.

7.2 Partial-wave treatment of photodetachment from dissociating I_2^-

In the following we consider photodetachment from dissociating I_2^-. We determined the photoelectron partial-waves resulting from each principal orientation. We then model the angular component of the photoelectron wave function for detachment at some internuclear distance R as a linear combination of the partial-waves emitted from each atomic fragment, I_a and I_b, separated by R. Determining the ratio, ρ, of the intensities of the photoelectron wave parallel and perpendicular to the laser polarization [$\rho = I_{par}/I_{perp} = |\Psi(0°)|^2 / |\Psi(90°)|^2$] allows for determination of β_2 by the relation $\beta_2 = (\rho-1)/(1+\rho/2)$ (equation 4.14; see section 4.3.2 for discussion of this approach). In this treatment, we neglect the higher-order terms in the angular distribution.

7.2.1 Photodetachment from the σ_u HOMO

Because I_2^- exhibits strong spin-orbit coupling, it cannot be said to exist in a pure Λ state (Hund's case a).[187] The dissociative A′ state relevant here (i.e., that accessed at the pump wavelength) has been described as a combination of $^2\Pi_g$ and $^2\Sigma_g$ states, with 90% Π character in the Franck-Condon region and 67% Σ character in the asymptotic limit. However, the photoelectron angular distribution will depend upon the symmetry of

the *orbital* from which the electron is be detached, which is the same (σ_u) for both pure Λ states.

This antibonding orbital may be approximated as a linear combination of two in-phase, collinear p orbitals separated along the internuclear axis, as illustrated in Figure 7.1 for each principle orientation of the dissociating molecule in the laboratory frame.

For perpendicular alignment of the internuclear axis with respect to the probe beam's electric field vector (parallel either to the laboratory frame x and y axes), the HOMO is approximated by two collinear p_x orbitals or two collinear p_y orbitals separated along the corresponding axis. In general, detachment from p_x and p_y orbitals may yield outgoing partial photoelectron waves with $l = 2$ and $m_l = \pm 1$ due to the angular momentum selection rules for a one electron process, $\Delta l = \pm 1$ and $\Delta m = 0$. Because these waves have zero amplitude at $\theta = 0^\circ, 90^\circ$, their contribution (in the limit of separated atomic orbitals) to the photoelectron signal may be neglected in this model.

If the internuclear axis is parallel to the electric field vector, the system may be approximated (in the dissociation asymptote) as two p_z orbitals separated along the z-axis by distance R. If an electron were photodetached from either p_z orbital in the absence of the other, we could construct the relative parallel and perpendicular components of the photoelectron wave function as a superposition of the selection rule-allowed outgoing partial-waves, as was done for detachment from a p_z orbital in Chapter 4. Thus, the net photoelectron wave function may be treated as a linear combination of both s and d_0 partial-waves emitted from both atomic centers, with phases indicated in Figure 7.2.

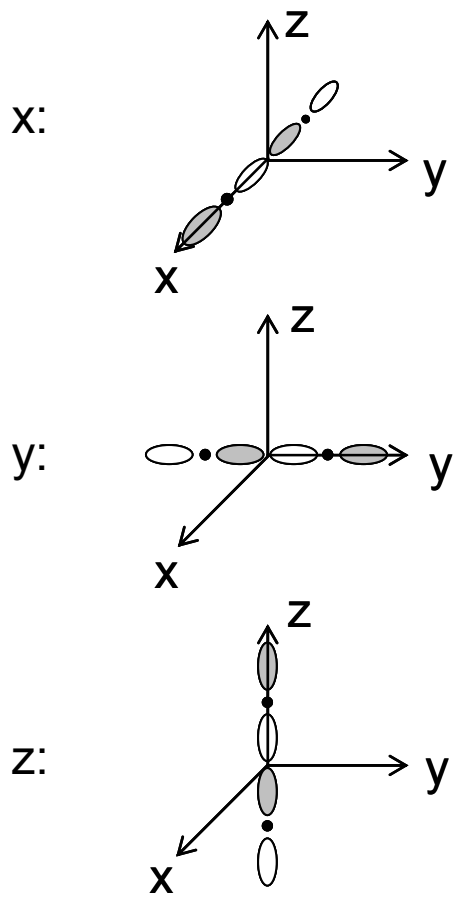

Figure 7.1 Illustration of principal orientations of the HOMO of dissociating I_2^-, decomposed into atomic orbitals, in the laboratory frame. The pump and probe beams' polarizations are parallel to the laboratory frame z-axis. The detector is parallel to the yz plane. See text for details.

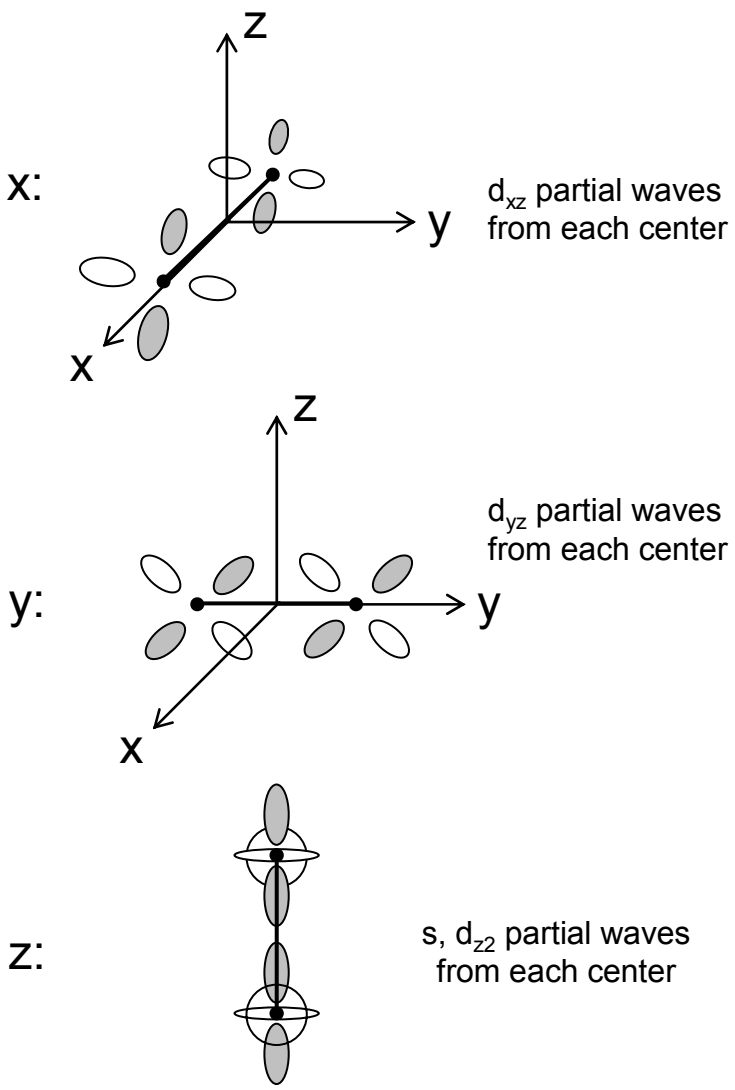

Figure 7.2 Partial photoelectron waves for photodetachment from dissociating I_2^- in each principal orientation. While the sketches look like atomic orbitals, they are meant to indicate evolving photoelectron partial-waves of the same angular symmetry. The partial-waves resulting from the x and y orientations shall be neglected in this treatment because the do not contribute to the photoelectron intensity parallel or perpendicular to the probe's electric field vector.

7.2.2 Two-centered interference

Because the waves emitted from each atomic center have the same kinetic energy profile the relative phase of the two wave fronts will evolve identically in time. However, the initial positions of the two component wave fronts are different by the internuclear distance at the time of photodetachment, introducing an additional phase shift of $\frac{2\pi R}{\lambda}$ between the partial-waves emitted from each center. In the velocity-mapped photoelectron image, this R-dependent phase shift will result in a periodic deviation (as a function of pump-probe delay time) in β relative to the result for detachment from the corresponding isolated atomic anions (the p-orbital detachment limit).

Photofragmentation of I_2^- via the dissociative A' state has been observed to preferentially yield fragment ejection parallel to the laser polarization vector.[187] Because the time scale of rotation (~ns) is much longer than the time scale of the experiment (~ps) we assume that rotation may be neglected for the time scale considered and that the anions are preferentially excited (and dissociated) when the internuclear axis is parallel to the laser polarization axis. Thus, we shall approximate the cross-section for photodissociation to be proportional to $\cos^2(\gamma)$, where γ is the angle between the internuclear axis and the laser polarization axis.

7.2.3 The pure s-wave approximation

We now model the angular distribution for a photoelectron detached from dissociating I_2^-. We model the HOMO as a linear combination of two p_z orbitals

separated by an internuclear distance, *R*, along the axis parallel to the laser's polarization (the LF z-axis). Because the kinetic energy of the photoelectron is small in the dissociation limit (0.12 eV for 390 nm photodetachment from isolated I^-), as we shall neglect the contribution of d_z waves to the photoelectron wave function as a first approximation. In the following, we consider coherent photodetachment from the p_z orbitals (corresponding to the asymptotic dissociation limit) on the atoms of dissociating I_2^-.

The parallel contributions from both photoelectron emission sites add coherently, as do the perpendicular contributions. We treat the wave function at $\theta = 0^\circ$ and 90° using the formalities of plane waves, as was done in Chapter 4. For this treatment, we assume the internuclear axis to be parallel to the laser's electric field, with an internuclear separation of *R* (see Figure 7.2). Because the other principle orientations will not contribute in this model, the *R*-dependent interference thus only affects the parallel wave function intensity; the perpendicular component is independent of *R* in this principal orientation.

$$\Psi_{par,s} = c\left(1 + e^{i(2\pi R/\lambda + \alpha)}\right), \tag{7.3}$$

$$\left|\Psi_{par,s}\right|^2 = c^2\left[2 + 2\cos\left(\frac{2\pi R}{\lambda} + \alpha\right)\right], \tag{7.4}$$

$$\Psi_{perp,s} = c(1+1) \tag{7.5}$$

$$\left|\Psi_{perp}, s\right|^2 = 4c^2 \tag{7.6}$$

$$\rho_s = \frac{\left|\Psi_{par,s}\right|^2}{\left|\Psi_{perp,s}\right|^2} = \frac{1+\cos\left(\frac{2\pi R}{\lambda}+\alpha\right)}{2}, \tag{7.7}$$

where α is any additional phase shift between the two wave fronts. The "s" denotes that we have only considered s-type waves. This results in

$$\beta_2 = \frac{\frac{1+\cos\left(\frac{2\pi R}{\lambda}+\alpha\right)}{2}-1}{1+\frac{1+\cos\left(\frac{2\pi R}{\lambda}+\alpha\right)}{4}}. \tag{7.8}$$

This results is plotted as the black line in Figure 7.3 (a).

In order to connect this result to the previous experimental results,[10] we approximate the corresponding time-dependence of the anisotropy parameter using the semi-classical dissociation trajectory as was done previously.[10,195] At small Δt (short pump-probe delays and thus small R) the interaction between the fragments results in a variable average separation velocity. However, for Δt > ~100 fs, the average fragment separation velocity has reached its asymptotic limit of v_f = 13.3 Å/ps. Ignoring the trajectory's deviation from linearity near $\Delta t = 0$, we may approximate R as

$$R = v_f \cdot \Delta t + R_0, \tag{7.9}$$

where R_0 is the extrapolated intercept of the linear region (Δt > 100 fs) of the dissociation trajectory, approximately 2.42 Å. Substituting equation 7.9 into 7.8 gives the anisotropy parameter as a function of pump-probe delay time, plotted in Figure 7.3 (b). The LCAO

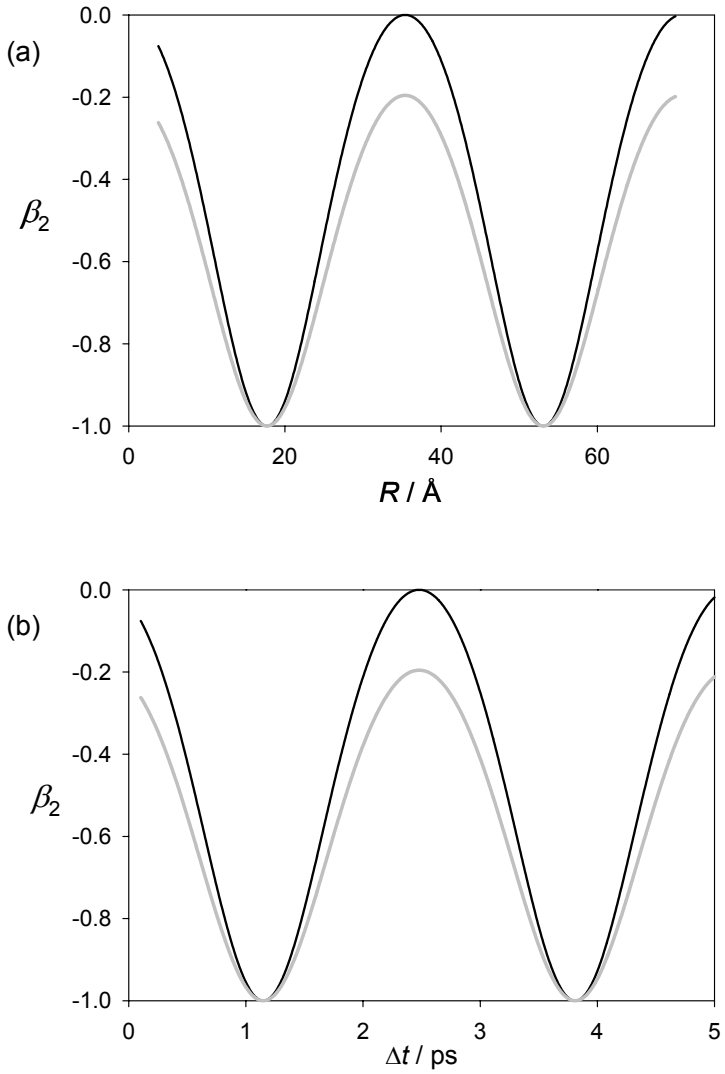

Figure 7.3 Simple two-centered interference models of β_2 vs. (a) R and (b) Δt for 780 nm + 390 nm pump-probe photoelectron imaging of I_2^- assuming a de Broglie wavelength of 35.4 Å and zero phase additional phase shift, α, between the two centers. Black lines correspond to the pure interfering s-wave approximation. Grey lines correspond to the inclusion of d_0-waves emitted from both centers. See text for details.

approximation and the approximations to the dissociation trajectory mean that the model is most accurate at larger (>700 fs) time delays.

7.2.4 Inclusion of d waves

We shall now consider both the s- and d-type waves emitted from each atomic center. The angular component of the photoelectron wave front emitted from I_a is thus constructed as

$$\psi_a \propto 1 + A \cdot \varepsilon \cdot e^{i(\delta+\pi)} Y_{20}(\theta), \tag{7.10}$$

where $A \cdot \varepsilon$ is the Wigner relative partial-wave scaling (see section 4.3.2 for a more in-depth discussion of modeling β for p-orbital photodetachment).

The wave front emitted from fragment I_b is the same, but it will have an additional R-dependent phase shift relative to that emitted from I_a:

$$\psi_b \propto e^{i(2\pi R/\lambda)} \cdot \psi_a \propto e^{i(2\pi R/\lambda+\alpha)} \left(1 + A \cdot \varepsilon \cdot e^{i(\delta+\pi)} Y_{20}(\theta)\right). \tag{7.11}$$

So,

$$\rho_{s,d} = \frac{\left|\Psi(0^\circ)\right|^2}{\left|\Psi(90^\circ)\right|^2} = \frac{\left|\psi_a(0^\circ,\varepsilon,\delta) + \psi_b(0^\circ,\varepsilon,\delta)\right|^2}{\left|\psi_a(90^\circ,\varepsilon,\delta) + \psi_b(90^\circ,\varepsilon,\delta)\right|^2} \tag{7.12}$$

$$= \frac{\left|\left(1 + e^{i(2\pi R/\lambda+\alpha)}\right)\psi_a(0^\circ\varepsilon,\delta)\right|^2}{\left|2 \cdot \psi_a(90^\circ,\varepsilon,\delta)\right|^2} = \frac{\left|\left(1 + e^{i(2\pi R/\lambda+\alpha)}\right)\right|^2 \cdot \left|\psi_a(0^\circ,\varepsilon,\delta)\right|^2}{4 \cdot \left|\psi_{Pa}(90^\circ,\varepsilon,\delta)\right|^2}. \tag{7.13}$$

$$= \frac{I_{par,s}(R,\lambda,\alpha) \cdot I_{par,I^-}(\varepsilon,A,\delta)}{I_{perp,s}(R,\lambda,\alpha) \cdot I_{perp,I^-}(\varepsilon,A,\delta)} = \rho_s(R,\lambda,\alpha)\rho_{I^-}(\varepsilon,A,\delta) \tag{7.14}$$

We have shown that the ratio of parallel to perpendicular photoelectron intensities is proportional to the product of the ratio computed considering only s-wave contributions and the ratio for detachment from bare I^-. Using $A = 0.4932$, $\cos\delta \approx 0.8617$ as reported by Mabbs et al., the asymptotic eKE of 0.12 eV and equation 4.23 yields $\rho_{I^-} \approx 0.733$. Combining this with the result for $\rho_s(R, \lambda, \alpha)$ from the previous section (equation 7.7) yields

$$\rho_{s,d} = 0.733 \cdot \frac{\frac{1+\cos\left(\frac{2\pi R}{\lambda}+\alpha\right)}{2}-1}{1+\frac{1+\cos\left(\frac{2\pi R}{\lambda}+\alpha\right)}{4}}, \tag{7.15}$$

where the inclusion of d-waves has set an upper bound of $\beta_2 \approx -0.20$, the anisotropy corresponding to photodetachment of bare I^- at the probe photon energy (3.18 eV). This result is plotted as a grey line vs. R and Δt in Figures 7.3 (a) and (b), respectively, with a arbitrarily set to zero.

7.2.5 Discussion of the simple two-centered partial-wave interference models

In the previous sections, we derived a simple model for the anisotropy parameters resulting from two-centered interference in photodetachment from I_2^- dissocating along the laboratory frame z-axis. These results are plotted in Figure 7.3 (a) and (b), respectively. Both results demonstrate an oscillation on the timescale corresponding to the far-field de Broglie wavelength of the photoelectron (35.4 Å). The two predictions differ in their maxima ($\beta_2 = 0$ for s-waves, $\beta_2 = -0.20$ for inclusion of d-waves).

There are two significant differences between the predictions of these models and the experimental results of Mabbs et al.[10] First, the minimum value in these idealized interference models is $\beta_2 \approx -1$, reflecting a complete cancellation of the perpendicular photoelectron intensity; the minimum observed experimentally is $\beta_2 \approx -0.35$. Several limitations of the model as well as certain experimental factors could contribute to this discrepancy. First, we note the models have so far neglected the effect of orientation averaging (i.e. contributions from molecules not perfectly aligned along the laboratory frame's z-axis), the loss of coherence and additional phase shifts between the partial-waves emitted from the two centers. Additionally, the asymptotic (far field) de Broglie wavelength is expected to differ somewhat from the effective de Broglie wavelength in the region defining the phase difference between the wave fronts emitted from I_a and I_b. Finally, from the experimental perspective, the accuracy of the time-dependent β_2 parameters is subject to the experiment's temporal resolution (not better than 150 fs FWHM) and the signal to noise in the experiment.

7.2.6 Orientation averaging

Now we consider the contributions due to deviations from the principal orientation. Because dissociation takes places preferentially parallel to the laboratory frame z-axis, we may expect a $\cos^2\gamma$ probability density distribution of dissociating molecules, where angle γ is the deviation from the parallel orientation. Consideration of these deviations is important because effects of the R-dependent interference on β depend upon the molecular orientation. The internuclear coordinate is now the vector $\boldsymbol{R}$,

with $R_{par} = R\cdot\cos(\gamma)$ and $R_{perp} = R\cdot\sin(\gamma)$. We have already shown that, for a given orientation, we may separate the intensities into R-dependent and R-independent terms, so a simple substitution may be made.

$$\rho_{OA} = \rho_s(\boldsymbol{R}, \alpha, \lambda)\rho_{I^-}(\varepsilon, A, \delta). \tag{7.16}$$

$$\rho_{OA} = \frac{\int_{0^\circ}^{90^\circ} I_{par,s}\left(\gamma, R_{par}, \lambda, \alpha\right)\cdot\cos^4(\gamma)\sin(\gamma)d\gamma}{\int_{0^\circ}^{90^\circ} I_{perp,s}\left(\gamma, R_{perp}, \lambda, \alpha\right)\cdot\cos^4(\gamma)\sin(\gamma)d\gamma}\cdot\rho_{I-}(\varepsilon, A, \delta). \tag{7.17}$$

One factor of $\cos^2\gamma$ is due to the orientation distribution of dissociating I_2^- with respect to the pump beam's polarization. The second is due to the scaling of the relative contribution of partial-waves upon deviation from the principal (z) orientation of the molecule. The $\sin\gamma$ term is required to scale the relative abundance of dissociating molecules in a given orientation. Consideration of the γ-dependence of the interference yields

$$\rho_{OA} = \rho_{I-}\frac{\int_{0^\circ}^{90^\circ}\left[1+\cos\left(\frac{2\pi R\cos(\gamma)}{\lambda}+\alpha\right)\right]\cdot\cos^4(\gamma)\sin(\gamma)d\gamma}{\int_{0^\circ}^{90^\circ}\left[1+\cos\left(\frac{2\pi R\sin(\gamma)}{\lambda}+\alpha\right)\right]\cdot\cos^4(\gamma)\sin(\gamma)d\gamma}, \tag{7.18}$$

which cannot be analytically evaluated, but contains all of the information required to determine β as a function of R under the current approximations. This expression has been evaluated numerically and is plotted in Figure 7.4 with α set to zero and parameterized in Δt.

7.2.7 Decoherence

We may alternately consider the effect of decoherence on the two-centered interference of pure s waves with a localization (or decoherence) timescale of τ_{loc}. We shall define the degree of coherence as

$$C(\Delta t) = \frac{1}{1 + e^{(\Delta t - \tau_{loc})/\Gamma}} \ . \tag{7.19}$$

We then define

$$\rho_{s,dec} = \rho_s \cdot C + (1 - C) = \rho_s \frac{1}{1 + e^{(\Delta t - \tau_{loc})/\Gamma}} + \left(1 - \frac{1}{1 + e^{(\Delta t - \tau_{loc})/\Gamma}}\right), \tag{7.20}$$

where the subscript *dec* indicates that we are considering decoherence of the two fragments. For Δt = 0, the first (the interference) term dominates, but vanishes at large pump-probe delays.

We include d-waves by multiplying $\rho_{s,dec}$ by ρ_{I^-}. The anisotropy parameter is then

$$\beta_2 = \frac{\rho_{s,dec}(\alpha, t, \tau, \lambda)\rho_{I^-}(A, \varepsilon, \delta) - 1}{1 + \frac{1}{2}\rho_{s,dec}(\alpha, t, \tau, \lambda)\rho_{I^-}(A, \varepsilon, \delta)} \ . \tag{7.21}$$

This result is plotted in Figure 7.4 with $\alpha = 0$ and Γ arbitrarily set to 2.

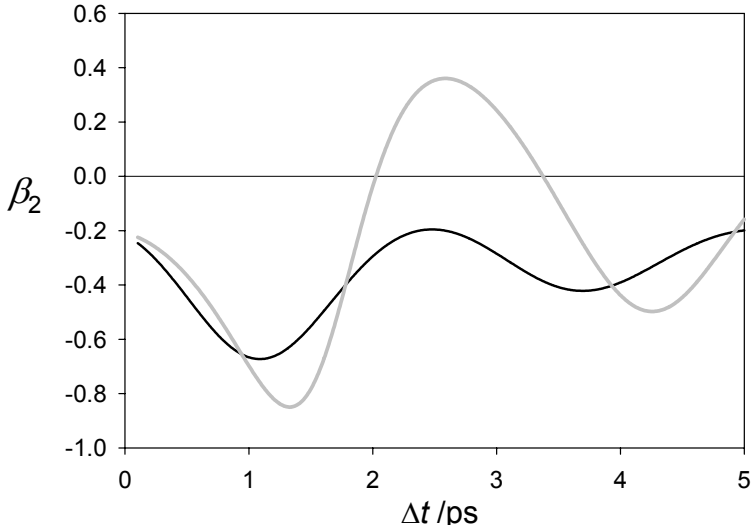

Figure 7.4 Adapted two-centered s and d partial-wave interference models of β_2 vs.Δt for 780 + 390 nm pump-probe photoelectron imaging of I_2^-. The prediction was adapted to include orientational averaging of the interference term (grey line) or generic decoherence effects (black line) assuming a characteristic decoherence timescale τ_{loc} = 2.5 ps and a de Broglie wavelength of 35.4 Å. See text for details.

7.2.8 Orientation averaging and decoherence

Finally, we may model β_2 as a function of pump-probe delay time, including both s and d waves, orientational averaging and decoherence.

$$\beta_2 = \frac{\rho_{I^-}(\rho_{s,OA} \cdot C + 1 - C) - 1}{1 + \frac{\rho_{I^-}}{2}(\rho_{s,OA} \cdot C + 1 - C)}. \tag{7.22}$$

This result was fit to the experimental results of Mabbs et al.[10] in two ways. First, λ was fixed at the far-field limit (35.4 Å) while varying α, τ_{loc} and Γ, resulting in optimal values of α = –29.3° (compared to the –40.9° from the previously reported[10] fit to equation 7.2) τ_{loc} = 1.189 ps and Γ = 552 fs. Fixing α = 0 and varying λ, τ_{loc} and Γ yielded optimal values of λ = 48.7 Å (compared to the previously reported[10] 42.7 ± 1.1 Å from a fit to equation 7.2), τ_{loc} = 1.068 fs and Γ = 692 fs. The results of both fits are plotted in Figure 7.5, along with the experimental data previously reported by Mabbs et al.[10]

7.2.9 Discussion

While we note the treatment above is approximate, its results are instructive. The simple two-centered (s and d) interference approach with the far-field λ = 35.4 Å and α = 0 predicts a minimum at 1.15 ps, while orientation-averaging predicts a minimum at 1.30 ps, much closer to the experimentally observed minimum near 1.5 ps.

The fits of equation 7.22 to the experimental data, shown in Figure 7.5, match the data quite well, especially considering the various approximations in the models and the

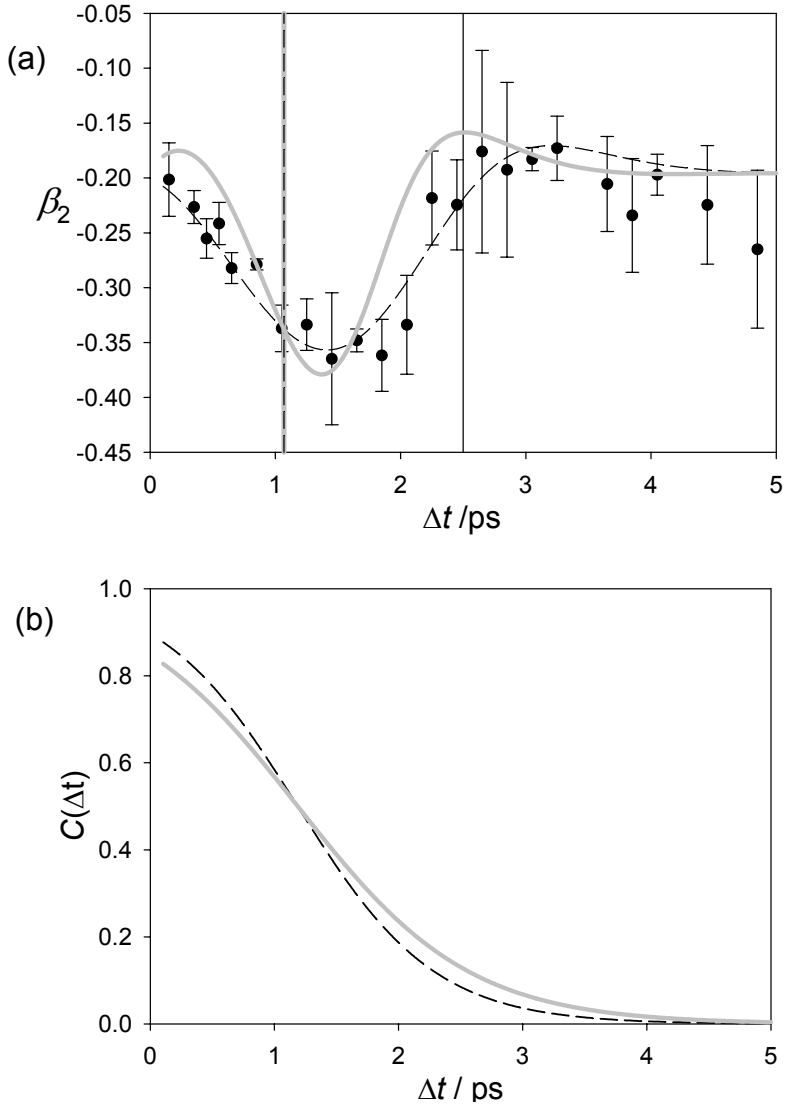

Figure 7.5 (a) Predicted and experimental β_2 vs. Δt for 780 nm+ 390 nm pump-probe photoelectron imaging of I_2^-. Data points are the results of Mabbs et al.[10] The curves are the fits of the orientation-averaged two-centered s and d partial-wave interference model, including decoherence (equation 7.22). The black curve corresponds to $\alpha = 0$, $\lambda = 48.7$ Å, $\tau_{loc} = 1.068$ ps, $\Gamma = 692$ fs. The grey curve corresponds to $\alpha = -29.3°$, $\lambda = 35.4$ Å, $\tau_{loc} = 1.189$ ps, $\Gamma = 552$ fs. The decoherence timescales, τ_{loc}, for each model are indicated as corresponding (and overlapping) vertical lines. The solid black line corresponds to the 2.5 ps decoherence timescale suggested previously.[10] (b) Coherence curves corresponding to the fits in (a). See text for more details.

temporal resolution of the experiment. One of the benefits of the fit to equation 7.22 over equation 7.2 is its inclusion of coherence timescale parameter. Within the framework of the model, the two decoherence timescales (743 fs and 145 fs) are much shorter than the 2.5 ps suggested in the previous work.[10] They are also not abrupt (as evidenced by the magnitude of the fit Γ values.); in both cases the model suggests that the system has lost some degree of coherence almost immediately after the dissociation is initiated.

These results raise several important questions: Is coherence lost during the timescale of the experiment? If so, what induces this loss?

Both Davis et al.[194] and Mabbs et al.[10] noted that localization may only occur if the system's energy is perturbed on the order of the energy splitting between the gerade dissociative state of I_2^- with an ungerade state correlated to the same asymptotic fragments. Mabbs et al. suggested that the 40 V/cm field in the laser-ion interaction region in their experiment was appropriate in magnitude to fulfill this requirement for an internuclear distance of R = 35.6 Å (coincidentally similar to the de Broglie wavelength of the photoelectron) parallel to the voltage gradient, and that the shorter duration of oscillations observed by the Neumark group results from the large field strength used in their imaging assembly. While these numbers are qualitatively consistent with the observed persistence of the oscillations in the two experiments, they overlook the fact that the dissociation should predominantly occur perpendicular to the imaging voltage gradient (parallel to the electric field vector of the pump pulse). Imaging field-induced decoherence should thus emerge at much longer delay times, arising only from individual molecules that are not aligned perfectly along the LF z-axis.

7.3 Cross-polarized pump-probe scheme

To examine the possible role of the electric field in the coherence breaking of I_2^- (which should be evidenced by a dampening or disappearance in the oscillations of β_2 with Δt within the interference paradigm), we performed a variation of the experiment by Mabbs et al. by setting the pump beam's electric field vector parallel to the imaging assembly's electric field to induce dissociation along the imaging assembly's voltage gradient.

We attempted this experiment for two different imaging field strengths with perpendicular pump-probe polarization configurations, as well as the parallel configuration as a control. The difficulty with the perpendicular configuration is that it results in the loss of cylindrical symmetry of the photoelectron distribution.[177] For the perpendicular pump-probe polarization configuration, we shall take advantage of the mirror symmetry of the photoelectron distribution to glean some information from the images. This section describes the experiment and preliminary results.

7.3.1 Experimental

General experimental considerations for time-resolved photoelectron imaging are extensively described in Chapter 2. In the following, details unique to this experiment are described.

Argon was seeded with iodine by passing ~20 psig of the buffer gas over a solid sample, with the concentration determined by the vapor pressure of iodine. The neutral

precursor gas was bombarded with high-energy electrons from the electron gun, yielding both I^- and I_2^-.

Pump-probe experiments were performed on I_2^- using the fundamental (778 nm, 1.59 eV) and second harmonic (389 nm, 3.19 eV) of a regeneratively amplified femtosecond Ti:Sapph laser, as described in detail in Chapter 2. Both parallel and perpendicular pump-probe polarization was employed. In all cases, the probe beam's polarization was parallel to the imaging detector. In brief, the zero-delay was determined by optimizing the power of the 3rd harmonic generated upon combining the pump and probe beams in a type I (parallel configuration) or type II (perpendicular configuration) BBO crystal. The zero-delay was checked multiple times each day. Pump-probe delays were induced by translation of two mirrors in the 389 nm optical line, with additional offset of 0.0975 mm on the double-pass stage (corresponding to 650 fs) employed to compensate for the additional relative delay induced when the beams pass through the Brewster window. Images were collected under two extreme focusing conditions corresponding to respective photoelectron (imaging) extraction fields of 32.9 V/cm and 228 V/cm.

Ten images (each collected for 21,300 experimental cycles minus the corresponding background signal) were collected on a single day for a given time delay. All images for a given time delay obtained on the same day were combined to yield one cumulative image. Three cumulative images were obtained for each time delay examined with the cross-polarized configuration. For the parallel configuration, one to three cumulative images were collected.

All cumulative images were analyzed using the BASEX program.[35] We note that the photoelectron distribution in the cross-polarized experiment is centrosymmetric, but lacks cylindrical symmetry.[177] Abel inversion of the 2-D projection of this distribution effectively returns the average over ϕ of the photoelectron. Strictly speaking, the 3-D photoelectron intensity in the perpendicularly-polarized experiment may be different along the laboratory x, y and z axes [i.e. $I(\theta = 0°, \varphi = 0°) \neq I(\theta = 90°, \varphi = 0°) \neq I((\theta = 90°, \varphi = 0°)$]; I($\theta = 90°$) in the reconstructed image may be thought of as the average photoelectron intensity perpendicular to the electric field vector of the pump beam.

7.3.2 Results

The average of anisotropy parameters of the cumulative images obtained for a given pump-probe delay are plotted Figure 7.6 for each polarization (parallel and perpendicular) at each extraction voltage. Error bars correspond to plus or minus one standard deviation. Points without error bars correspond to cases where only one cumulative image was obtained. Results obtained with a 32.9 V/cm photoelectron extraction field are plotted as circles; squares correspond to 228 V/cm. Filled points correspond to perpendicular pump-probe polarization. Open points correspond to parallel polarization, directly comparable to those reported by Mabbs et al.

The few data points for parallel pump-probe polarization are qualitatively similar to those of Mabbs et al.[10] though the magnitude of β_2 is smaller in the present results for both imaging fields. This is likely due to signal-to-noise issues in the current data. There

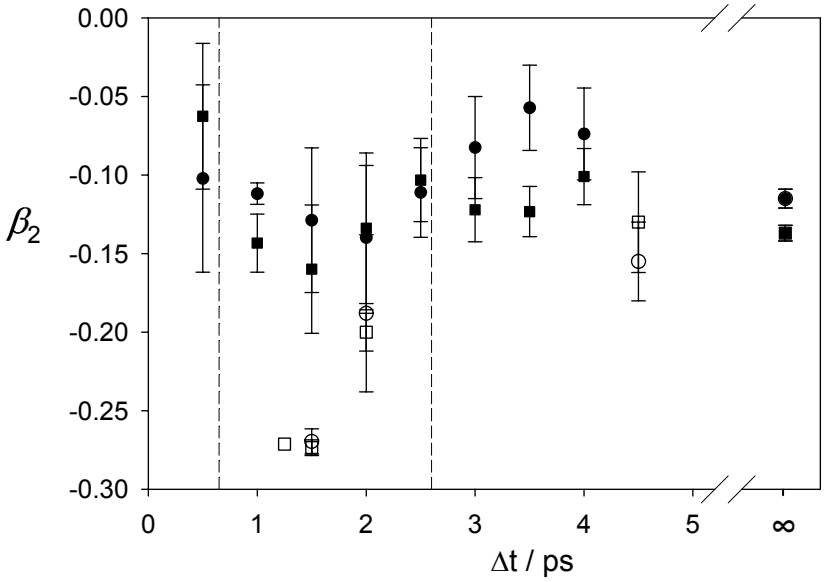

Figure 7.6 New experimental results for 778 + 389 nm pump-probe photoelectron imaging of I_2^-. Results are shown for parallel pump-probe polarization with imaging field strengths of 32.9 V/cm (open circles) and 228 V/cm (open squares) and perpendicular polarizations at E_{img} = 32.9 V/cm (filled circles) and 228 V/cm (filled squares).

is no distinguishable difference between the results for the two different electric field strengths at the time-delays probed.

The perpendicular configuration yields time-resolved β_2's smaller in magnitude than those for the parallel configuration, regardless of field strength. The smaller-magnitude imaging field resulted in slightly smaller β_2's than the larger-magnitude field. The anisotropy parameters for dissociation from bare I^- (indicated in the plot as the dissociation asymptote, $\Delta t = \infty$) were also slightly smaller in magnitude. This could be due to the higher signal-to-noise ratio for the more tightly-focused-that is, greater field strength image (noisier signal tends to lead to more isotropic reconstructions). The perpendicular results for both electric fields also seem to oscillate slightly on a timescale similar to that observed previously.[10]

7.3.3 Discussion of results

While the data set is limited, we may make several compelling observations. First, the large difference between the anisotropy parameters for the parallel and perpendicular polarization configurations most obvious near $\Delta t = 1.5$ ps indicates that the dissociative state accessed by the pump pulse is not randomly oriented. This conclusion is in agreement with a simple test performed by the Lineberger group that demonstrated the predominantly parallel nature of the transition.[187]

The interference occurs along the direction of the internuclear separation. In the parallel polarization configuration, the interference is primarily parallel to the polarization vectors (the laboratory frame z-axis). In the perpendicular configuration, we

would expect the interference to occur along the pump beam's polarization axis (the laboratory-frame x-axis, parallel to the imaging voltage gradient), perpendicular to the probe beam's polarization axis (the laboratory frame z axis). For convenience, we shall refer to the photoelectron intensity "parallel" and "perpendicular" with respect to the probe beam's electric field vector, which always parallel to imaging detector, regardless of the pump-probe polarization scheme. In the perpendicular polarization case, we are removing perpendicular intensity rather than parallel intensity, so we should expect a maximum in β_2 near Δt = 1.5 ps, rather than a minimum.

Let us assume the interference has exactly the same effect on the photoelectron intensity along the internuclear axis for both polarization configurations. The (average) interference-induced relative intensity drop in the reconstructed images at θ = 90° in the perpendicular configurations should be half of that for θ = 0° in the parallel configuration. We may thus estimate the expected maximum in β_2 for the perpendicular configuration using the experimental minimum for the parallel configuration, $\beta_2 = -0.27$.

$$\rho_{tot} = \rho_s \rho_{I^-} = \frac{1+\beta_2}{1-\beta_2/2} = \frac{1-0.27}{1+0.135} = 0.64 \tag{7.23}$$

Substituting the value of ρ_{I^-} at this photon energy (see section 7.2.4) yields

$$0.733 \cdot \rho_s = 0.64\,, \tag{7.24}$$

Meaning that the pure two-centered interference term (i.e. neglecting d-type partial-waves) is

$$\rho_s = 0.873\,. \tag{7.25}$$

Half of this degree of interference in the parallel direction would correspond to ρ_s = 0.937. If the interference were instead along the perpendicular direction, ρ_s should be replaced with its reciprocal. This yields a predicted ratio of parallel to perpendicular photoelectron signal intensity at Δt = 1.5 ps in the perpendicular polarization configuration of

$$\rho_{tot,cp} = 1.07 \cdot 0.733 = 0.784, \tag{7.26}$$

corresponding to $\beta_2 \approx -0.16$. This value falls within the error bars of the data points for cross-polarized pump and probe beams Δt = 1.5 ps. The new results are thus consistent with two-centered photoelectron interference along the internuclear axis of dissociating I_2^-, parallel to the pump beam's electric field vector, whether it is aligned along the laboratory frame x- or z-axis; they are also consistent with the experiment value for bare I^-.

Treating the perpendicular dissociation as was done for the parallel configuration in section 7.2.1 suggests that no partial-waves need be considered if the probe beam's polarization is perpendicular the internuclear axis. This suggests that either the approximations in this approach are not valid or that the dominant molecular orientations yielding photoelectron signal are those for which γ = 45°, 135°, which would affect the period and phase of the interference-induced oscillation in β_2.

It is difficult to discern oscillations in β_2 as a function of Δt for the perpendicular polarization configuration given the size of the error bars. However, if anything, the data seem to oscillate in-phase with the results for the parallel configuration regardless of the

imaging field used, with the lower-voltage results reaching higher values than those obtained with the higher imaging lens voltages.

Given the $E^{-1/5}$ scaling of the delocalization distance and the value of 35.6 Å previously computed for an imaging field of E_{img} = 40 V/cm[10], we predict characteristic field delocalization lengths of ~11Å and ~37 Å for the 228 V/cm and 32.9 V/cm fields used in the present experiment. Converting these internuclear distances to time using equation 7.9 yields projected delocalization timescales of 650 fs and 2.6 ps, respectively. These limits are indicated by the vertical lines in Figure 7.6. If the field played a major role in symmetry-breaking (and thus interference dampening) we would expect the oscillations for the smaller-field results to persist for longer than those for the larger field, with relative timescales close to those indicated. While the 3.5 ps data points for the two extraction field strengths appear to be significantly different, no definitive conclusions may be drawn about the role of the imaging assembly's electric field on the delocalization timescale.

7.4 Conclusions

While the conceptual models and new results presented in this chapter are consistent with the interferometic interpretation of the previously reported oscillation in β_2 as a function of pump-probe delay time in dissociating I_2^-, there is no convincing evidence of correlation between the decoherence timescale and the electric field strength due to the imaging assembly. A number of questions remain. First, what is the nature and source of the decoherence of the dissociating state? Second, does two-centered

photoelectron interference have a measurable effect on the photoelectron angular distribution in the cross-polarized experiment? Both questions could be addressed by obtaining more data (at multiple pump-probe delays) in both polarization configurations at both imaging field strengths. More statistics could assist in illuminating the nature of the photodetachment dynamics in the cross-polarized experiment. More extensive modeling (including using more rigorous quantum formalisms) should be performed. Additionally, a new reconstruction routine should be created to analyze the 2-D projections of distributions that are centrosymmetric but not cylindrically symmetric to assist in the analysis of future cross-polarized pump-probe experiments.

Another direction for this research is in the area of coherent wave packet control via pump pulse shaping. A first version of this could in principle be achieved by using a pump-pump-probe configuration, analogous to the approach taken in the wavepacket dynamics studies on dissociating I_2.[196] The interference in a four-centered wave packet would be controlled by the pump-pump and pump-probe delay times. The relevant experimental considerations for this scheme are briefly discussed in the following chapter. In general, the field of pump-probe photoelectron imaging has much to offer, both from the perspective of monitoring chemical dynamics (such as bond photodissociation) and the physics of multiphoton photodetachment.

CHAPTER 8

SUMMARY AND FUTURE DIRECTIONS

8.1 Summary of this Dissertation

In this dissertation, specific photoelectron imaging results have been reported for a variety of gas-phase anions, including atomic, molecular and cluster species. While some of the systems studied may be of particular interest in and of themselves, they have primarily served as models for examining the fundamental electronic properties and dynamics. Specifically, we have probed orbital symmetries, identified structural isomers and bonding motifs in clusters, characterized solvent-solute interactions, and seen evidence of charge-transfer, photoelectron interference and electron scattering interactions. These results demonstrate the rich complexity of electronic interactions in chemical systems and demonstrate the ability of photoelectron imaging to yield fundamental insight into chemical physics.

8.2 Ideas for further studies

One of the great benefits of writing a dissertation is that it provides a new perspective on work that spanned a number of years, breeding ideas for new experiments. Writing this dissertation has yielded no shortage of ideas for future work. In this section, I outline some experiments that could be performed, either to address unanswered questions encountered in previous work, or as new approaches to observing familiar but exciting phenomena. Some of these ideas build on previously published

results. Others are a bit more whimsical. It is my hope that some of these ideas will be visited in the near future.

8.2.1 Evaluation of relativistic effects on PAD's for closed-shell atomic anions

As discussed in Chapter 4, the one-electron orbital approach to interpreting photoelectron images is approximate. Much theoretical work has been performed using more rigorous models, particularly predicting the energy-dependence of deviations from $\beta = 2$ for photoionization of closed-shell, ns^2 atomic species.[53] However, few corresponding experimental studies have been performed, inhibiting a thorough test of the theoretical predictions. There is thus some imperative for experimentalists to systematically examine the energy-dependence of photoelectron anisotropy parameters for, at first, photodetachment from the simplest of systems.

Systematic photodetachment experiments on group I atomic anions over a range of wavelengths would test the theoretical predictions for the energy-dependence of the anisotropy parameters. The atomic hydrogen anion is an ideal first system because of its relative simplicity and because it is easily generated from ammonia (neat or seeded in argon), as discussed in Chapters 2-4; the heavier group I anions would likely need to be formed in a more selective ion source. For energies at which s-orbital detachment is the only exit channel, relativistic effects are expected to be the sole cause of deviations in photoelectron anisotropy from the Cooper-Zare limit.

Systematic application of a tunable light source (such as a dye-laser or an OPA), would allow for examining an effectively continuous range of electron kinetic energies.

This process, though tedious, is quite straightforward.[197,198] Alternately, a new approach, described in the next section, could be taken.

8.2.2 Broadband photoelectron imaging

Focusing a linearly polarized laser pulse in an isotropic, transparent condensed medium such as water or BK1 has been shown to yield a continuum broadband, or white light, pulse without altering the linear polarization.[199] Such white light generation, increasingly applied for the purpose of various femtosecond spectroscopies, could prove an incredibly useful probe source for photodetachment imaging.

Broadband photoelectron imaging would be performed exactly as a traditional photoelectron imaging experiment except the probe laser beam is replaced by a pulse of white light. This scheme would uniquely allow for examination of a single photodetachment transition over a continuous range of electron kinetic energies. The resulting photoelectron energy spectrum could be normalized to the spectral profile of the white light to yield accurate relative photodetachment cross-sections for range of photon energies used. Analysis of photoelectron anisotropy will yield β as a function of eKE, which could be deconvolved with a proper instrumental energy resolution function (taking into account the energy-scaling of the detector's resolution and the energy-dependent broadening due to the ion velocity dispersion). The detachment cross-sections could be similarly deconvolved.

This approach would require longer data collection times than typically required in one-color photoelectron imaging due to loss of power in the white-light generation

process and the spectral dispersion of the signal, but would remove the need for the systematic scanning and reoptimization of a tunable light source typically used for energy-dependence experiments. It also has the benefit of providing quantitative relative cross-sections. A careful choice of systems and photon energy ranges is required in order to prevent the overlap of signal corresponding to multiple channels (if this is desired). The accuracy of this approach should be tested using a standard such as O^-, for which the energy-dependence of both photodetachment cross-sections[200-204] and angular distributions have been characterized.[1,101]

Broadband (or white-light) photoelectron imaging would have the effect of yielding quantitative relative photodetachment cross-sections and anisotropy parameters over a continuous energy range, all from a single set of experimental conditions. Further, with sufficient white-light intensity, it could be used as a probe in time-resolved experiments. For example, probing dissociating I_2^- (discussed in Chapter 7) with white light would allow for an examination of the energy-dependence of β_2 at any given pump-probe delay time. This would allow for an alternate examination of the photoelectron interference. The relevant parameter for the interference is R/λ, where R is the internuclear distance and λ is the photoelectron's deBroglie wavelength. In the original experiment,[10] R was varied by varying the pump-probe delay time, with λ fixed by the essentially constant photoelectron kinetic energy. For a given Δt, R is fixed. A broadband probe would provide anisotropy parameters for a continuous range of λ's, which should demonstrate a corresponding oscillation.

8.2.3 Stern-Gerlach experiment on a photoelectron?

In the classic Stern-Gerlach experiment,[205,206] a beam of spin ½-particles passed through an inhomogeneous magnetic field that acted as a filter, separating the beam into two components according to the spin projections along the field gradient. This experiment was first performed on a beam of silver atoms with the intent of testing the proposed quantization of orbital angular momentum in atoms (at that time, silver's ground-state electron configuration was not understood). The beam was found to be split into two components, which was inconsistent with either the classical or unpaired d-electron hypothesis. This experiment ultimately resulted in the discovery and identification of quantum spin (and the ground-state electron-configuration of silver).

It was once heavily debated whether quantum spin was intrinsic to an electron or arose only in the presence of an external field, analogous to quantum orbital angular momentum, and whether uncertainty (in conjunction with the Lorentz force) fundamentally limits the observation of electron separation by spin in a magnetic field. Today, it is accepted that spin is an intrinsic property of an electron. It has been shown using quantum mechanics that separating a beam of electrons by spin using a classic Stern-Gerlach filter is in principle possible, but that the necessary practical control of the experimental conditions may be unachievable. While experimental determination of the gyromagnetic ratio for free electrons has been performed on electromagnetically trapped electrons, a Stern-Gerlach filter has not been successful with free electrons. [207,208]

Calculations suggest that, while spatial separation in a traditional Stern-Gerlach experiment depends upon the trajectory (and thus time) after exposure to the magnetic

field, the momentum space splitting is complete immediately after exposure to the filter.[207,208] Thus detection of momentum- (or velocity-) space separation could prove advantageous. Incorporating velocity-mapping into a free-electron spin-filtering experiment could yield new information or assist in preparation of spatially resolved, spin-separated free electrons. For example, placement of a velocity-map imaging assembly downstream of a traditional Stern-Gerlach filter in a collinear configuration (with respect to the beam) could overcome some of the spatial blurring. Thus, optimizing the electron trajectory and the filter's magnetic field for optimal resolution in momentum space could assist in resolving the electron spin components upon velocity-mapping.

It could also be interesting to attempt Stern-Gerlach-type filtering on electrons emitted from an effective point source, such as upon photodetachment. Such experiments would require extensive modeling and crafting of a magnetic field. One aim of such an experiment would be to detect magnetic moment separation due to the orbital component (in addition to that of spin) of the photoelectrons, the simplest case of which is detachment from atomic s-orbitals (for which the free electron wave has $l = 1$) and p-orbitals (free electrons in a superposition of $l = 0$ and $l = 2$ states). This would be of particular interest for examining the partial-wave composition of photoelectrons generated from molecular anions. Gating of the filter's magnetic field could be achieved using an ultrafast laser pulse-driven photoconductive switch,[209] which could replace the need for the electron beam trajectory to define the time of exposure to the magnetic field. Though these ideas may be fundamentally possible, they could be effectively impossible to implement; nonetheless it is an exciting thought experiment. Further discussion of

spin-separation of free electrons using a classic Stern-Gerlach approach may be found elsewhere.[207,208,210-214]

8.2.4 Polynitrogen anions

Polynitrogen compounds have been of great interest to chemists due their relevance to energy storage. Polynitrogens ($N_{n>2}$) are generally expected to be high-energy and often unstable, due to their penchant for exothermic release of stable N_2. Few polynitrogen species have been isolated and characterized spectroscopically.

If polynitrogen anions can be generated in the gas-phase, photoelectron imaging would be uniquely suited for characterization of orbital energies and symmetries, for comparison with theoretical studies.[215,216] Possible stable polynitrogen anions include N_3^-, N_5^- and N_6^-. Azide (N_3^-) is relatively stable and has been well characterized (including via photoelectron imaging as reported in Chapter 4). The aromatic pentazole anion, N_5^-, would complement the N-substituted cyclopentadienyl series that has so far been studied by the Lineberger group for up to three nitrogen atoms.[217-221] The N_5 moiety is relatively stable as a substituent in organic chemistry; mass spectrometric detection of N_5^- has been reported by other workers upon 1) electrospray ionization or a solution containing the conjugate base of *p*-hydroxyphenyl pentazole and 2) high-energy electron collision-induced dissociation.[222]

We attempted to generate N_5^- in our spectrometer. With the help of Dr. Ian Jones, the neutral precursor, p-hydroxyphenyl pentazole was synthesized (CAUTION: this compound and difficult synthesis are potentially EXPLOSIVE) based on a previously

reported procedure.[223] The compound was identified via NMR spectroscopy. Unfortunately, it decomposed on the order of minutes in solution unless kept on ice. We isolated a small amount of solid and placed a fraction in our pulsed nozzle as a sample but were unable to detect N_5^- in the mass spectrum. The remainder of the sample, left in the hood, quickly decomposed from an off-white solid to a brown oil (under 20 minutes at room temperature, somewhat longer for a portion left on ice). Due to the instability and involatility of this compound, electrospray ionization is likely required for generation of the gas-phase precursor. This experiment could be revisited in the group if the workers were to construct an electrospray ionization source.

Evidence has been reported in support of a N_6^- species in aprotic solution, in the form of a "pseudohalide" N_3 dimer anion in which the charge is shared equally between the two moieties.[224] Spectroscopic characterization of gas-phase N_6^- could verify the existence of this species. Unfortunately, no 84 amu peaks were observed in our mass spectrum upon electron-bombardment of benzyl azide, only 42 amu peaks (corresponding to azide) and various organic fragments.

These polynitrogens should be further pursued with the goal of photoelectron imaging.

8.2.5 Time-resolved examination of charge-transfer in $NH_2^-(NH_3)_n$ clusters

The 532 nm photoelectron images for $NH_2^-(NH_3)_{n=3\text{-}5}$ presented in Chapter 5 display signatures of autodetachment. As previously discussed, these features may be due to photoinduced electron-transfer to the ammonia solvent network, analogous to that

observed by the Neumark group[126,127] for $I^-(NH_3)_n$, followed by loss of the electron. The nature of the intermediate state could be further examined using a pump-probe approach. Ironically, our initial interest in ammonia was identifying such a process for homogeneous clusters in the pump-probe regime, but we did not find evidence of any two-photon signal. We attempted 400 + 800 nm and 800 + 400 nm time-resolved schemes for some members of the $H^-(NH_3)_n$ and $NH_2^-(NH_3)_n$ cluster series but observed no two-photon signal. Upon consideration of the 355 and 532 nm images in Chapter 5 it seems that lower-energy photoelectrons are in general more likely to induce charge-transfer-to-solvent, and that the initial charge-transfer state is likely very weakly bound [similar to the Neumark group's observations for $I^-(NH_3)_n$]. A more better approach would thus be an 800 nm + 800 nm pump-probe configuration.

Re-examining the 800 nm pump-only image obtained in an attempted 800 nm + 400 nm pump-probe experiment suggests that autodetachment signal may have been overlooked. Figure 8.1 contains the energy spectra, on the binding energy scale, for photodetachment from $NH_2^-(NH_3)_3$ at 532 nm and 800 nm, overlayed for comparison. The images are also displayed. The signal in the 800 nm image looks very much like the pure autodetachment signal observed at 532 nm for $n = 5$, also displayed in Figure 8.1 for comparison; the energy spectrum displays a sharp feature that is not coincident with that for direct detachment from that cluster. The pump + probe images for $NH_2^-(NH_3)_n$, corresponding to ~10,000 experimental cycles for time delays of 500 fs, 1 ps and 10 ps display no two-photon features, suggesting that charge transfer occurs on a different timescale. More attempts should be made to detect an intermediate charge-transfer state.

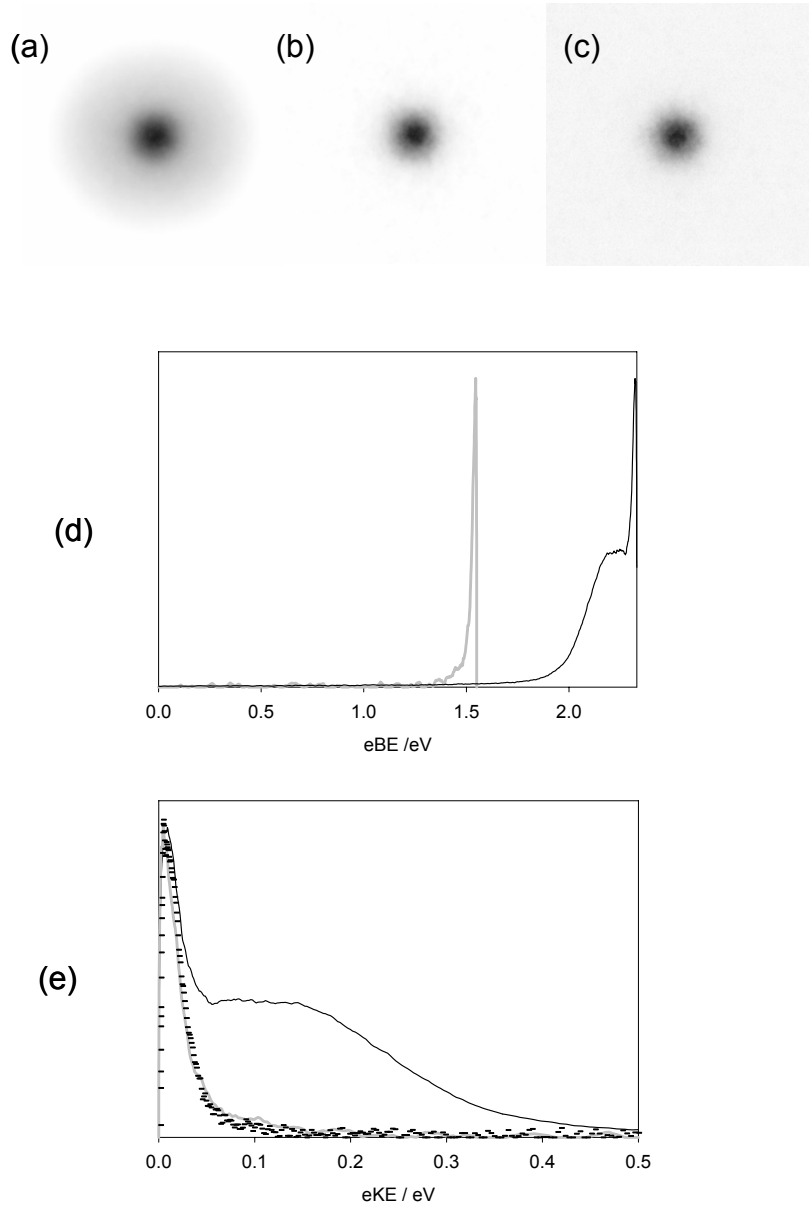

Figure 8.1 (a) 532 nm photoelectron image for $NH_2^-(NH_3)_3$ (b) 800 nm photoelectron image for $NH_2^-(NH_3)_3$. (c) 532 nm photoelectron image for $NH_2^-(NH_3)_5$. (d) Photoelectron energy spectra for $NH_2^-(NH_3)_3$ at 800 nm (grey) and 532 nm (black) on the binding energy scale, demonstrating that the signal obtained at 800 nm signal does not correspond to direct photodetachment. (e) The same energy spectra on the eKE scale, with the addition of the 532 nm spectrum for $NH_2^-(NH_3)_5$ (dashes). All three traces share similar low-eKE features consistent with autodetachment. Image and spectral scaling was chosen for comparable intensities.

Looking at larger clusters ($n > 3$) might yield longer-lived states (extra solvent molecules would better solvate an electron, as suggested by the Neumark group's results) detectable on the timescale of the experiment. Additionally, a lower photon energy would yield lower-eKE probe signal which would have a better signal-to-noise ratio due to the scaling of our detector. The one-photon studies on this cluster series presented in Chapter 5 may provide additional clues on how to obtain two-photon signal for heterogeneous ammonia clusters.

8.2.6 Time-resolved photoelectron imaging of NNO_2^-: the $N + NO_2^-$ fragmentation pathway

As discussed in Chapter 6, the 355 nm photoelectron energy spectrum for detachment from NNO_2^- displays some two-photon signal near the binding energy for NO_2^-, suggesting that the following photodissociation may occur:

$$NNO_2^- + h\nu\ (3.49\ eV) \rightarrow N + NO_2^-. \quad (8.1)$$

Because the O-N-O moiety is bent in both NO_2^- and NNO_2^- (with computed O-N-O angles of 134.1° and ~120°, respectively)[140], it is feasible that the NO_2^- fragment would be formed with moderate vibrational excitation, and thus display a vertical detachment energy close to that observed for cold NO_2^- (~2.8 eV[6]).

We previously performed 390 nm + 780 nm time-resolved photoelectron imaging on NNO_2^- for the purpose of monitoring the O^- fragment channel; this dissociation timescale turned out to be shorter than the temporal resolution of the experiment. However, the 780 nm probe in this scheme would have been insufficient to detect an

NO_2^- fragment. Repeating this experiment using a 390 nm + 390 nm pump-probe scheme could potentially elucidate an NO_2^- fragment channel.

8.2.7 New systems for molecular-scale electron interferometry experiments

Photodetachment from dissociating I_2^- yielded evidence of two-centered photoelectron interference, with the period of oscillation in β_2 approximately corresponding to internuclear displacement of the photoelectron's de Broglie wavelength, λ.[10] In the time-resolved experiment, time-dependent oscillations in β observed at the asymptotic photoelectron kinetic energy corresponding to detachment from bare I^-, were attributed to the temporal variation in R. In an alternate approach two observation of two-centered interference recently taken by a coworker, varying the photon energy (and thus the photoelectron kinetic energy and de Broglie wavelength) for one-photon detachment from various isomers of the dinitrobenzene anion induced oscillations in β as a function of eKE.[6] In the case of a symmetry plane, a molecular anion can be divided into two identical segments from which photodetachment may be considered to occur simultaneously in a coherent fashion with allowed partial-waves defined by the relative phases of the molecular orbital fragments with an additional phase shift of $2\pi R/\lambda$, where R in this case is the distance between the fragment orbital centroids. However, this interpretation is less rigorous when the two fragment orbitals are close together, as their combination may result in an additional symmetry component which should produce additional partial-waves. Additionally, the effects of interference

on the laboratory-frame photoelectron angular distributions must be considered for all orientations of the molecule in the laboratory frame.

While the one-photon nature of this approach allows for a much faster acquisition of data with greatly improved signal-to-noise, the analysis of any oscillations in β is further complicated due to the lack of explicit knowledge of the energy-dependence of β in the absence of interference. This problem could in theory be overcome in a photoionization (rather than photodetachment) experiment; according to the Wigner threshold law, the relative partial-waves cross-sections for photoionization from a neutral should in principle be independent of energy in the vicinity of the threshold (though the absolute cross-sections are not).

Further examination of two-centered interference in photodetachment from anions could be performed on benzoquinone and dinitrenobenze anions. The former could be performed via electron attachment (in the ion source) to benzoquinone or selective H_2^+ abstraction from hydroquinone using O^- (though achieving the appropriate selectivity could be challenging). The latter would be formed via dissociative electron attachment (in the ion source) to di-azidobenzene, analogous to the process identified for phenyl azide.[225] However, this precursor is likely unstable and potentially explosive.[82] The ortho and para isomers could be examined at all accessible wavelengths (a tuneable photon source such as a dye laser or an OPA would be ideal) in an approach similar to the one taken for the dinitrobenzene anions.[6] The benzoquinone anion and dinitrenobenzene anions ($[O\text{-}C_6H_4\text{-}O]^-$ and $[N\text{-}C_6H_4\text{-}N]^-$) have the benefit of being simpler than dinitrobenzene anions, while similarly taking advantage of the rigid

geometry provided by the benzene ring. On the other hand, known anionic (shape and Feshbach) resonances of benzoquinone exist that, while narrow, would need to be considered in the analysis.[226]

8.2.8 More time-resolved experiments with I_2^-

As I_2^- has proven an excellent model system for pump-probe experiments and monitoring dynamic photoelectron interference (particularly in conjunction with a titanium:sapphire fs system), it could be further taken advantage of. The first steps towards pulse-shaping (and thus shaping of the dissociative nuclear wave packet) experiments could be attained via a pump-pump-probe scheme. Specifically, splitting the 780 nm pump into two identical pulses and precise delay of one with respect to the other would be akin to creating a double-gaussian pump pulse profile. If successful, this could allow for creation of a four-centered molecular interferometer mentioned in Chapter 7. The challenge with such a scheme would be in precisely maintaining the temporal pump-pump delay in order to reliably control the phase relationship between the two pulses.

Preliminary tests of phase-stability were conducted by splitting, offsetting and recombining the 780 nm pump beam in a Mach-Zender interferometer (as illustrated in Figure 8.2 (a). When the two arms of the interferometer are exactly the same length, the beams interfere entirely constructively via path 1 and entirely deconstructively through output 2 due to the additional phase shifts of π incurred at the reflective surfaces. Translating the delay stage by $\lambda/4$ induces a change in relative path length of $\lambda/2$ (equivalent to introducing an additional, relative phase shift of π) results in signal

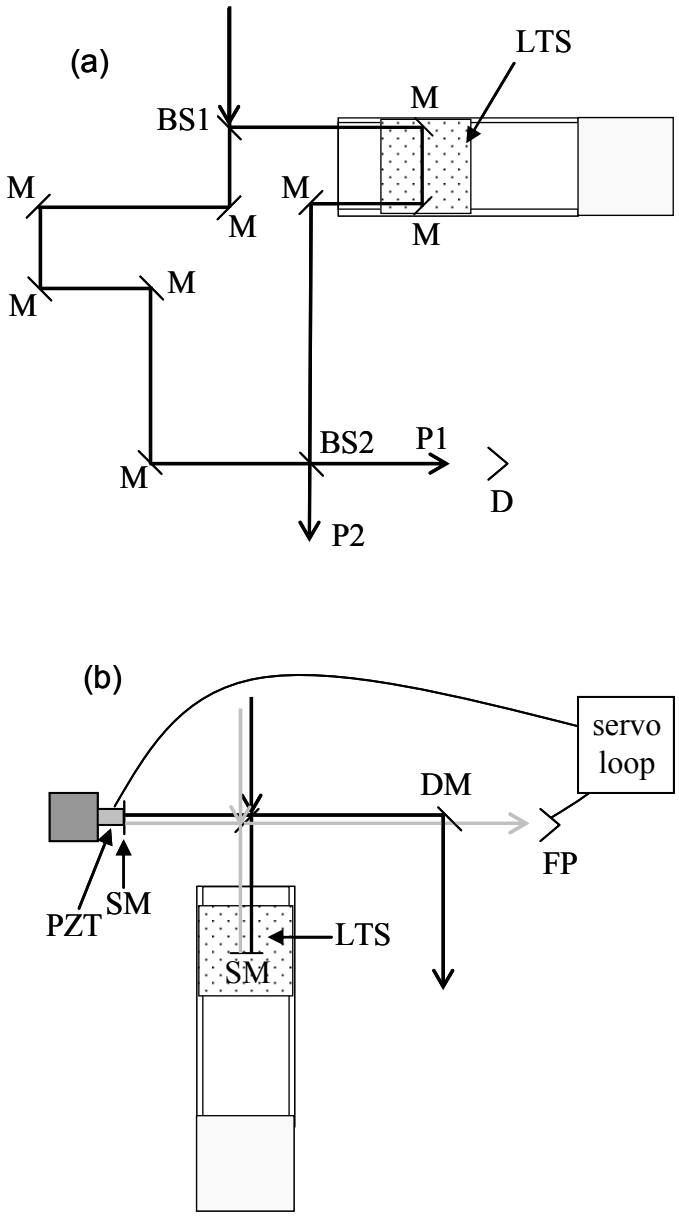

Figure 8.2 (a) Mach-Zender type interferometer used in pump-probe experiments, including the following components: beamsplitters (BS1 and BS2), dichroic mirrors (M) a linear delay stage (LDS), output paths (P1, P2). (b) Michelson interferometer for proposed pump-pump-probe experiment, including a fs beam (black line), a He/Ne beam (grey line), a beamsplitter (BS), silvered mirrors (SM), a dichroic mirror (DM), fast photodiode (FP) active servo loop, and piezo crystal (PZT).

transmission via path 2 only. Intermediate phases yield some transmission through each output path. For approximate overlap of the two pulses, the power through either output was determined to be unstable under ambient conditions (fluctuating from near zero to essentially the total input power), indicating that that passive phase-locking would only be feasible if extreme care were taken to shield against drafts, temperature fluctuations and vibrations.

Active phase-locking could be performed using a Michelson-type interferometer configuration, as displayed in Figure 8.2 (b) and described in the following. The fs beam (black line) and a He/Ne beam (grey line) are both split by a beamsplitter (BS), reflected off of silvered mirrors (SM) and recombined in the beamsplitter. The transmitted beams are separated using a dichroic mirror (DM), allowing for the He/Ne intensity to be monitored using a fast photodiode. The He/Ne intensity is fed into an active servo loop specifically designed to drive the piezo crystal (PZT) upon which one of the silvered mirrors is mounted to correct for path-length fluctuations. This active control of the relative interferometer path lengths could be sufficient for active phase-locking an facilitate performance of the pump-pump-probe experiment While obstacles to this experiment remain, such as determining the exact beam path difference as opposed to some change in path difference, these tools and this schematic could prove an adequate starting point for a future experiment.

8.3 The future

In the past decade, anion photoelectron imaging has become an increasingly popular technique for probing electronic and chemical dynamics. Today, there is a need for systematic studies for the purpose of further advancing our understanding of photodetachment dynamics and imaging results in general. In particular, coupling photoelectron imaging with either a tunable laser allows for more comprehensive characterization of the energy-dependence of the photoelectron angular distributions for detachment from a variety of systems. For the past few years, this angle has been pursued by the Mabbs group, and has so far further (and quite clearly) identified detachment resonances that affect photoelectron angular distributions.[197,198] A widespread adoption of this systematic approach to energy dependence will greatly advance the power and application of photoelectron imaging. Adoption of the broadband approach proposed in section 8.2.1 could yield quantitative photodetachment cross-sections as a function of energy, in addition to energy-dependent anisotropy parameters, in a single image.

Applying photoelectron imaging to larger chemical systems is also an exciting new prospect. For example, imaging may yield new insight (via photoelectron angular distributions) into biologically relevant systems such as DNA base pair dimers or protein fragments, systems that have recently been studied using traditional gas-phase photoelectron spectroscopy.[227] Recently, angle-resolved photoelectron spectroscopy has been applied to photodetachment from ions in solution,[228,229] allowing for comparison with imaging results for the analogous cluster anions. In general, there is a need for

wider collaboration between experimentalists and theorists in order to interpret the energy-dependence of photoelectron angular distributions, particularly for complex chemical systems.

As demonstrated in a growing number of works, including this dissertation, photoelectron imaging has the capacity to elucidate the nature of chemical bonding, orbital symmetries, photochemical reactions and electron-molecule interactions including charge-transfer and scattering. This powerful technique has great potential to be expanded or applied in new ways to further probe exciting fundamental phenomena in chemical physics.

REFERENCES

(1) Hanstorp, D.; Bengtsson, C.; Larson, D. J. *Physical Review A* **1989**, *40*, 670.

(2) Celotta, R. J.; Bennett, R. A.; Hall, J. L. *Journal of Chemical Physics* **1974**, *60*, 1740.

(3) Wickham-Jones, C. T.; Ervin, K. M.; Ellison, G. B.; Lineberger, W. C. *Journal of Chemical Physics* **1989**, *91*, 2762.

(4) Pichugin, K.; Grumbling, E.; Velarde, L.; Sanov, A. *Journal of Chemical Physics* **2008**, *129*, 044311.

(5) Grumbling, E. R.; Pichugin, K.; Velarde, L.; Sanov, A. *Journal of Physical Chemistry A* **2010**, *114*, 1367.

(6) Pichugin, K. Ph.D. dissertation, University of Arizona, 2010.

(7) Hiraoka, K.; Fujimaki, S.; Aruga, K.; Yamabe, S. *Journal of Physical Chemistry* **1994**, *98*, 8295.

(8) Velarde, L.; Habteyes, T.; Grumbling, E. R.; Pichugin, K.; Sanov, A. *Journal of Chemical Physics* **2007**, *127*, 084302.

(9) Winstead, C.; McKoy, V. *Physical Review A* **1998**, *57*, 3589.

(10) Mabbs, R.; Pichugin, K.; Sanov, A. *Journal of Chemical Physics* **2005**, *123*, 054329.

(11) Chandler, D. W.; Houston, P. L. *Journal of Chemical Physics* **1987**, *87*, 1445.

(12) Helm, H.; Bjerre, N.; Dyer, M. J.; Huestis, D. L.; Saeed, M. *Physical Review Letters* **1993**, *70*, 3221.

(13) Eppink, A.; Parker, D. H. *Review of Scientific Instruments* **1997**, *68*, 3477.

(14) Parker, D. H.; Eppink, A. T. J. B. *Journal Of Chemical Physics* **1997**, *107*, 2357.

(15) Sanov, A.; Mabbs, R. *International Reviews in Physical Chemistry* **2008**, *27*, 53.

(16) Ervin, K. M.; Lineberger, W. C. Photoelectron Spectroscopy of Negative Ions. In *Advances in Gas Phase Ion Chemistry*; Adams, N. G., Babcock, L. M., Eds.; JAI Press: Greenwich, 1992; Vol. 1; pp 121.

(17) Bowen, K. H.; Eaton, J. G. Photodetachment Spectroscopy of Negative Cluster Ions. In *The Structure of Small Molecules and Ions*; Naaman, R., Vager, Z., Eds.; Plenum: New York, 1988; pp 147.

(18) Castleman, A. W.; Bowen, K. H. *Journal Of Physical Chemistry* **1996**, *100*, 12911.

(19) Grumbling, E. R.; Mabbs, R.; Sanov, A. *Journal of Chemical Education* **in revision**.

(20) Mabbs, R.; Grumbling, E. R.; Pichugin, K.; Sanov, A. *Chemical Society Reviews* **2009**, *38*, 2169.

(21) Surber, E.; Ananthavel, S. P.; Sanov, A. *Journal of Chemical Physics* **2002**, *116*, 1920.

(22) Mabbs, R.; Surber, E.; Sanov, A. *Analyst* **2003**, *128*, 765.

(23) Surber, E. Photoelectron imaging of molecular and cluster anions. Ph.D. Dissertation, University of Arizona, 2005.

(24) Johnson, M. A.; Lineberger, W. C. Pulsed Methods for Cluster Ion Spectroscopy. In *Techniques for the Study of Ion Molecule Reactions*; Farrar, J. M., Saunders, W. H., Eds.; Wiley: New York, 1988; pp 591.

(25) Klots, C. E.; Compton, R. N. *Journal of Chemical Physics* **1978**, *69*, 1636.

(26) Klots, C. E. *J. Chem. Phys.* **1985**, *83*, 5854.

(27) Alexander, M. L.; Levinger, N. E.; Johnson, M. A.; Ray, D.; Lineberger, W. C. *Journal of Chemical Physics* **1988**, *88*, 6200.

(28) Robertson, W. H.; Kelley, J. A.; Johnson, M. A. *Review of Scientific Instruments* **2000**, *71*, 4431.

(29) Johnson, M. A.; Alexander, M. L.; Lineberger, W. C. *Chemical Physics Letters* **1984**, *112*, 285.

(30) Wiley, W. C.; McLaren, I. H. *Review of Scientific Instruments* **1955**, *26*, 1150.

(31) Posey, L. A.; DeLuca, M. J.; Johnson, M. A. *Chemical Physics Letters* **1986**, *131*, 170.

(32) Lepetit, L.; Cheriaux, G.; Joffre, M. *Journal of the Optical Society of America B-Optical Physics* **1995**, *12*, 2467.

(33) Bordas, C.; Paulig, F.; Helm, H.; Huestis, D. L. *Review of Scientific Instruments* **1996**, *67*, 2257.

(34) Heck, A. J. R.; Chandler, D. W. *Annual Review Of Physical Chemistry* **1995**, *46*, 335.

(35) Dribinski, V.; Ossadtchi, A.; Mandelshtam, V. A.; Reisler, H. *Review of Scientific Instruments* **2002**, *73*, 2634.

(36) Yang, C. N. *Physical Review* **1948**, *74*, 764.

(37) Cooper, J.; Zare, R. N. Photoelectron angular distributions. In *Atomic collision processes*; Geltman, S., Mahanthappa, K. T., Brittin, W. E., Eds.; Gordon and Breach, Science Publishers: New York, London, Paris, 1968; Vol. XI-C; pp 317.

(38) Blatt, J. M.; Biedenharn, L. C. *Reviews of Modern Physics* **1952**, *24*, 258.

(39) Telnov, D.; Chu, S. I. *Journal of Physics B-Atomic Molecular and Optical Physics* **1996**, *29*, 4401.

(40) Seideman, T. *Annual Review of Physical Chemistry* **2002**, *53*, 41.

(41) Einstein, A. *Ann. Physik* **1905**, *17*, 132.

(42) Reichle, R.; Helm, H.; Kiyan, I. Y. *Physical Review Letters* **2001**, *8724*, 243001.

(43) Bethe, H. A. S., E. E *Quantum Mechanics of One- and Two-Electron Atoms*; Springer-Verlag: Berlin, 1957.

(44) Cooper, J.; Zare, R. N. *J. Chem. Phys.* **1968**, *48*, 942.

(45) Cooper, J.; Zare, R. N. *J. Chem. Phys.* **1968**, *49*, 4252.

(46) Reed, K. J.; Zimmerman, A. H.; Andersen, H. C.; Brauman, J. I. *Journal of Chemical Physics* **1976**, *64*, 1368.

(47) Kaplan, I. G.; Markin, A. P. *Optics and Spectroscopy-Ussr* **1968**, *24*, 475.

(48) Kaplan, I. G.; Markin, A. P. *Optics and Spectroscopy-Ussr* **1968**, *25*, 275.

(49) Schweig, A.; Thiel, W. *Journal of Chemical Physics* **1974**, *60*, 951.

(50) Oana, C. M.; Krylov, A. I. *Journal of Chemical Physics* **2009**, *131*, 124114.

(51) Bethe, H. A. *Handbuch der Physik* **1933**, *24*, 483.

(52) Wigner, E. P. *Physical Review* **1948**, *73*, 1002.

(53) Manson, S. T.; Starace, A. F. *Reviews of Modern Physics* **1982**, *54*, 389.

(54) Tully, J. C.; Berry, R. S.; Dalton, B. J. *Physical Review* **1968**, *176*, 95.

(55) Lohr, L. L.; Robin, M. B. *Journal of the American Chemical Society* **1970**, *92*, 7241.

(56) Sichel, J. M. *Molecular Physics* **1970**, *18*, 95.

(57) Thiel, W.; Schweig, A. *Chemical Physics Letters* **1971**, *12*, 49.

(58) Thiel, W.; Schweig, A. *Chemical Physics Letters* **1972**, *16*, 409.

(59) Dill, D.; Manson, S. T.; Starace, A. F. *Physical Review Letters* **1974**, *32*, 971.

(60) Greene, C. H. *Physical Review Letters* **1980**, *44*, 869.

(61) Zhang, J. T.; van Woerkom, L. D.; Guo, D. S.; Freeman, R. R. *Physical Review A* **2007**, *76*.

(62) Sharp, T. E.; Dowell, J. T. *Journal of Chemical Physics* **1969**, *50*, 3024.

(63) Compton, R. N.; Stockdal.Ja; Reinhard.Pw. *Physical Review* **1969**, *180*, 111.

(64) Smyth, D. C.; Brauman, J. I. *Journal of Chemical Physics* **1972**, *56*, 4620.

(65) Snodgrass, J. T.; Coe, J. V.; Friedhoff, C. B.; McHugh, K. M.; Bowen, K. H. *Faraday Discussions of the Chemical Society* **1988**, *86*, 241.

(66) Snodgrass, J. T.; Coe, J. V.; Freidhoff, C. B.; McHugh, K. M.; Arnold, S. T.; Bowen, K. H. *Journal Of Physical Chemistry* **1995**, *99*, 9675.

(67) Warman, J. M.; Bakale, G.; Fessende.Rw. *Journal of Chemical Physics* **1972**, *57*, 2702.

(68) Dressler, R.; Allan, M. *Chemical Physics* **1985**, *92*, 449.

(69) Kryachko, E. S.; Vinckier, C.; Nguyen, M. T. *Journal of Chemical Physics* **2001**, *114*, 7911.

(70) Hanel, G.; Fiegele, T.; Stamatovic, A.; Mark, T. D. *International Journal of Mass Spectrometry* **2001**, *205*, 65.

(71) Allan, M.; Skalicky, T. *Journal of Physics B-Atomic Molecular and Optical Physics* **2003**, *36*, 3397.

(72) Illenberger, E.; Comita, P. B.; Brauman, J. I.; Fenzlaff, H. P.; Heni, M.; Heinrich, N.; Koch, W.; Frenking, G. *Berichte Der Bunsen-Gesellschaft-Physical Chemistry Chemical Physics* **1985**, *89*, 1026.

(73) Continetti, R. E.; Cyr, D. R.; Metz, R. B.; Neumark, D. M. *Chemical Physics Letters* **1991**, *182*, 406.

(74) Alvarez, S. G.; Alvarez, M. T. *Synthesis-Stuttgart* **1997**, 413.

(75) Peet, N. P.; Weintraub, P. M. *Chemical & Engineering News* **1993**, *71*, 4.

(76) Hruby, V. J.; Boteju, L.; Li, G. G. *Chemical & Engineering News* **1993**, *71*, 2.

(77) Peet, N. P.; Weintraub, P. M. *Chemical & Engineering News* **1994**, *72*, 4.

(78) Urben, P. G. *Chemical & Engineering News* **1993**, *71*, 4.

(79) Hassner, A.; Stern, M. *Angewandte Chemie-International Edition in English* **1986**, *25*, 478.

(80) Hassner, A.; Stern, M.; Gottlieb, H. E.; Frolow, F. *Journal of Organic Chemistry* **1990**, *55*, 2304.

(81) Aduev, B. P.; Aluker, E. D.; Belokurov, G. M.; Zakharov, Y. A.; Krechetov, A. G. *Journal of Experimental and Theoretical Physics* **1999**, *89*, 906.

(82) Churchill, D. G. *Journal of Chemical Education* **2006**, *83*, 1798.

(83) Hotop, H.; Lineberger, W. C. *Journal of Physical and Chemical Reference Data* **1985**, *14*, 731.

(84) Lykke, K. R.; Murray, K. K.; Lineberger, W. C. *Physical Review A (Atomic, Molecular, and Optical Physics)* **1991**, *43*, 6104.

(85) Hall, J. L.; Siegel, M. W. *Journal of Chemical Physics* **1968**, *48*, 943.

(86) Reichle, R.; Helm, H.; Kiyan, I. Y. *Physical Review A* **2003**, *68*, 063404.

(87) Sobhy, M. A.; Castleman, A. W. *Journal of Chemical Physics* **2007**, *126*, 154314.

(88) Aravind, G.; Ram, N. B.; Gupta, A. K.; Krishnakumar, E. *Physical Review A* **2009**, *79*.

(89) Covington, A. M.; Duvvuri, S. S.; Emmons, E. D.; Kraus, R. G.; Williams, W. W.; Thompson, J. S.; Calabrese, D.; Carpenter, D. L.; Collier, R. D.; Kvale, T. J.; Davis, V. T. *Physical Review A* **2007**, *75*.

(90) Chaffee, M. A. *Physical Review* **1931**, *37*, 1233.

(91) Lin, C. D. *Physical Review Letters* **1975**, *35*, 1150.

(92) Bryant, H. C.; Dieterle, B. D.; Donahue, J.; Sharifian, H.; Tootoonchi, H.; Wolfe, D. M.; Gram, P. A. M.; Yateswilliams, M. A. *Physical Review Letters* **1977**, *38*, 228.

(93) Hamm, M. E.; Hamm, R. W.; Donahue, J.; Gram, P. A. M.; Pratt, J. C.; Yates, M. A.; Bolton, R. D.; Clark, D. A.; Bryant, H. C.; Frost, C. A.; Smith, W. W. *Physical Review Letters* **1979**, *43*, 1715.

(94) Cortes, M.; Martin, F. *Physical Review A* **1994**, *50*, 1287.

(95) Lindroth, E. *Physical Review A* **1995**, *52*, 2737.

(96) Kuan, W. H.; Jiang, T. F.; Chung, K. T. *Physical Review A* **1999**, *60*, 364.

(97) Neumark, D. M.; Lykke, K. R.; Andersen, T.; Lineberger, W. C. *Physical Review A* **1985**, *32*, 1890.

(98) Domesle, C.; Jordon-Thaden, B.; Lammich, L.; Forstel, M.; Hergenhahn, U.; Wolf, A.; Pedersen, H. B. *Physical Review A* **2010**, *82*.

(99) Breyer, F.; Frey, P.; Hotop, H. *Zeitschrift Fur Physik a-Hadrons and Nuclei* **1978**, *286*, 133.

(100) Velarde, L. Ph. D. dissertation. Ph.D., University of Arizona, 2008.

(101) Cavanagh, S. J.; Gibson, S. T.; Gale, M. N.; Dedman, C. J.; Roberts, E. H.; Lewis, B. R. *Physical Review A* **2007**, *76*, 052708.

(102) O'Malley, T. F. *Physical Review* **1965**, *137*, A1668.

(103) Farley, J. W. *Physical Review A* **1989**, *40*, 6286.

(104) Mabbs, R.; Surber, E.; Sanov, A. *The Journal of Chemical Physics* **2005**, *122*, 054308.

(105) Surber, E.; Mabbs, R.; Sanov, A. *J. Phys. Chem. A* **2003**, *107*, 8215.

(106) Cohen, H. D.; Fano, U. *Physical Review* **1966**, *150*, 30.

(107) Herzberg, G. *Electronic Spectra and Electronic Structure of Polyatomic Molecules*; van Nostrand Reinhold Company: New York, 1966.

(108) Bachir, I. H.; Huet, T. R.; Destombes, J. L.; Vervloet, M. *Journal of Molecular Spectroscopy* **1999**, *193*, 326.

(109) Roszak, S. *Journal of Chemical Physics* **1996**, *105*, 7569.

(110) Dixon, R. N. *Molecular Physics* **1965**, *9*, 357.

(111) Frisch, M. J. *et al.* Gaussian 03; Rev. B.01 ed.; Gaussian, Inc.: Wallingford CT, 2004.

(112) Yang, X.; Kiran, B.; Wang, X. B.; Wang, L. S.; Mucha, M.; Jungwirth, P. *Journal of Physical Chemistry A* **2004**, *108*, 7820.

(113) Frisch, M. J. *et al.* Gaussian 03, Revision C.02; Gaussian, Inc.: Wallingford CT, 2004.

(114) Coe, J. V.; Snodgrass, J. T.; Friedhoff, C. B.; McHugh, K. M.; Bowen, K. H. *Journal of Chemical Physics* **1985**, *83*, 3169.

(115) Ritchie, C. D.; King, H. F. *Journal of the American Chemical Society* **1968**, *90*, 838.

(116) Kalcher, J.; Rosmus, P.; Quack, M. *Canadian Journal of Physics* **1984**, *62*, 1323.

(117) Squires, R. R. In *Ionic Processes in the Gas Phase*; Amoster Ferreira, M. A., Ed.; Reidel: Dordrecht, 1984; Vol. 118.

(118) Cremer, D.; Kraka, E. *Journal of Physical Chemistry* **1986**, *90*, 33.

(119) Cardy, H.; Larrieu, C.; Dargelos, A. *Chemical Physics Letters* **1986**, *131*, 507.

(120) Hirao, K.; Kawai, E. *Journal of Molecular Structure-Theochem* **1987**, *34*, 391.

(121) Ortiz, J. V. *Journal of Chemical Physics* **1987**, *87*, 3557.

(122) Gutowski, M.; Simons, J.; Hernandez, R.; Taylor, H. L. *Journal of Physical Chemistry* **1988**, *92*, 6179.

(123) Glidewell, C. *Journal of Molecular Structure* **1980**, *67*, 121.

(124) Tack, L. M.; Rosenbaum, N. H.; Owrutsky, J. C.; Saykally, R. J. *Journal of Chemical Physics* **1986**, *85*, 4222.

(125) Schwartz, R. L.; Davico, G. E.; Kim, J. B.; Lineberger, C. W. *Journal of Chemical Physics* **2000**, *112*, 4966.

(126) Frischkorn, C.; Zanni, M. T.; Davis, A. V.; Neumark, D. M. *Faraday Discussions* **2000**, *115*, 49.

(127) Davis, A. V.; Zanni, M. T.; Frischkorn, C.; Neumark, D. M. *Journal of Electron Spectroscopy and Related Phenomena* **2000**, *108*, 203.

(128) Alle, D. T.; Gulley, R. J.; Buckman, S. J.; Brunger, M. J. *Journal of Physics B-Atomic Molecular and Optical Physics* **1992**, *25*, 1533.

(129) Yourshaw, I.; Zhao, Y. X.; Neumark, D. M. *Journal Of Chemical Physics* **1996**, *105*, 351.

(130) DeLuca, M. J.; Niu, B.; Johnson, M. A. *Journal of Chemical Physics* **1988**, *88*, 5857.

(131) Tsukuda, T.; Johnson, M. A.; Nagata, T. *Chemical Physics Letters* **1997**, *268*, 429.

(132) Fleischman, S. H.; Jordan, K. D. *Journal of Physical Chemistry* **1987**, *91*, 1300.

(133) Tsukuda, T.; Saeki, M.; Zhu, L.; Nagata, T. *Chemical Physics Letters* **1998**, *295*, 416.

(134) Posey, L. A.; Johnson, M. A. *Journal of Chemical Physics* **1988**, *88*, 5383.

(135) Hacaloglu, J.; Suzer, S.; Andrews, L. *Journal of Physical Chemistry* **1990**, *94*, 1759.

(136) Jacox, M. E. *Journal of Chemical Physics* **1990**, *93*, 7622.

(137) Jacox, M. E.; Thompson, W. E. *Journal of Chemical Physics* **1990**, *93*, 7609.

(138) Arnold, D. W.; Neumark, D. M. *Journal Of Chemical Physics* **1995**, *102*, 7035.

(139) Osborn, D. L.; Leahy, D. J.; Cyr, D. R.; Neumark, D. M. *Journal Of Chemical Physics* **1996**, *104*, 5026.

(140) Li, R. J.; Continetti, R. E. *Journal of Physical Chemistry A* **2002**, *106*, 1183.

(141) Knapp, M.; Echt, O.; Kreisle, D.; Mark, T. D.; Recknagel, E. *Chemical Physics Letters* **1986**, *126*, 225.

(142) Sojka, Z.; Che, M. *Journal of Physical Chemistry* **1996**, *100*, 14776.

(143) Bass, A. D.; Lezius, M.; Ayotte, P.; Parenteau, L.; Cloutier, P.; Sanche, L. *Journal of Physics B-Atomic Molecular and Optical Physics* **1997**, *30*, 3527.

(144) Weber, J. M.; Leber, E.; Ruf, M. W.; Hotop, H. *Physical Review Letters* **1999**, *82*, 516.

(145) Leber, E.; Barsotti, S.; Bommels, J.; Weber, J. M.; Fabrikant, I. I.; Ruf, M. W.; Hotop, H. *Chemical Physics Letters* **2000**, *325*, 345.

(146) Suter, H. U.; Greber, T. *Journal of Physical Chemistry B* **2004**, *108*, 14511.

(147) Yamamoto, S.; Mitsuke, K.; Misaizu, F.; Kondow, T.; Kuchitsu, K. *Journal of Physical Chemistry* **1990**, *94*, 8250.

(148) Sanov, A.; Lineberger, W. C. *Physical Chemistry Chemical Physics* **2004**, *6*, 2018.

(149) Arnold, D. W.; Bradforth, S. E.; Kim, E. H.; Neumark, D. M. *Journal of Chemical Physics* **1992**, *97*, 9468.

(150) Benitez, A.; Moore, J. H.; Tossell, J. A. *Journal of Chemical Physics* **1988**, *88*, 6691.

(151) Nakanishi, R.; Muraoka, A.; Nagata, T. *Chemical Physics Letters* **2006**, *427*, 56.

(152) Resat, M. S.; Zengin, V.; Garner, M. C.; Continetti, R. E. *Journal Of Physical Chemistry A* **1998**, *102*, 1719.

(153) Shin, J. W.; Hammer, N. I.; Johnson, M. A.; Schneider, H.; Gloss, A.; Weber, J. M. *Journal of Physical Chemistry A* **2005**, *109*, 3146.

(154) Thoman, J. W.; Chandler, D. W.; Parker, D. H.; Janssen, M. H. M. *Laser Chemistry* **1988**, *9*, 27.

(155) Eland, J. H. D. *Photoelectron spectroscopy: an introduction to ultraviolet photoelectron spectroscopy in the gas phase*; Butterworths: London, 1984.

(156) Coe, J. V.; Snodgrass, J. T.; Friedhoff, K. M.; Bowen, K. H. *Journal of Chemical Physics* **1987**, *87*, 4302.

(157) Hendricks, J. H.; de Clercq, H. L.; Freidhoff, C. B.; Arnold, S. T.; Eaton, J. G.; Fancher, C.; Lyapustina, S. A.; Snodgrass, J. T.; Bowen, K. H. *Journal of Chemical Physics* **2002**, *116*, 7926.

(158) Roszak, S.; Leszczynski, J. *Computational Chemistry (Singapore, Singapore)* **2001**, *6*, 179.

(159) Kim, J. B.; Wenthold, P. G.; Lineberger, W. C. *Journal of Chemical Physics* **1998**, *108*, 830.

(160) Boys, S. F.; Bernardi, F. *Molecular Physics* **1970**, *19*, 553.

(161) Seeger, R.; Pople, J. A. *Journal of Chemical Physics* **1977**, *66*, 3045.

(162) Fukutome, H. *International Journal of Quantum Chemistry* **1981**, *20*, 955.

(163) Snodgrass, J. T.; Kim, H. S.; Bowers, M. T. *Journal of Chemical Physics* **1988**, *88*, 3072.

(164) Roehl, C. M.; Snodgrass, J. T.; Deakyne, C. A.; Bowers, M. T. *Journal of Chemical Physics* **1991**, *94*, 6546.

(165) Snis, A.; Panas, I. *Chemical Physics Letters* **1999**, *305*, 285.

(166) Alijah, A.; Kryachko, E. S. *Journal of Molecular Structure* **2007**, *844*, 193.

(167) Ervin, K. M.; Ho, J.; Lineberger, W. C. *Journal of Physical Chemistry* **1988**, *92*, 5405.

(168) Weaver, A.; Metz, R. B.; Bradforth, S. E.; Neumark, D. M. *Journal of Chemical Physics* **1989**, *90*, 2070.

(169) Luong, A. K.; Clements, T. G.; Continetti, R. E. *International Journal of Mass Spectrometry* **2002**, *220*, 253.

(170) Surber, E.; Sanov, A. *Journal of Chemical Physics* **2002**, *116*, 5921.

(171) Surber, E.; Sanov, A. *J. Chem. Phys.* **2003**, *118*, 9192.

(172) Lineberger, W. C.; Hotop, H.; Patterson, T. A. Photodetachment Threshold Processes. In *Electron and Photon Interactions with Atoms*; Kleinpoppen, H., McDowell, M. R. C., Eds.; Plenum Publishing Corporation: New York, 1976; pp 125.

(173) *Electron-Molecule Collisions*; Shimamura, I.; Takahashi, K., Eds.; Plenum Press: New York, 1984, pp 570.

(174) Dube, L.; Herzenberg, A. *Physical Review A* **1975**, *11*, 1314.

(175) Uiberacker, M.; Uphues, T.; Schultze, M.; Verhoef, A. J.; Yakovlev, V.; Kling, M. F.; Rauschenberger, J.; Kabachnik, N. M.; Schroder, H.; Lezius, M.; Kompa, K. L.; Muller, H. G.; Vrakking, M. J. J.; Hendel, S.; Kleineberg, U.; Heinzmann, U.; Drescher, M.; Krausz, F. *Nature* **2007**, *446*, 627.

(176) Kitajima, M.; Sakamoto, Y.; Watanabe, S.; Suzuki, T.; Ishikawa, T.; Tanaka, H.; Kimura, M. *Chemical Physics Letters* **1999**, *309*, 414.

(177) Reid, K. L. *Annual Review of Physical Chemistry* **2003**, *54*, 397.

(178) Greenblatt, B. J.; Zanni, M. T.; Neumark, D. M. *Chemical Physics Letters* **1996**, *258*, 523.

(179) Zanni, M. T.; Taylor, T. R.; Greenblatt, B. J.; Soep, B.; Neumark, D. M. *Journal of Chemical Physics* **1997**, *107*, 7613.

(180) Zanni, M. T.; Batista, V. S.; Greenblatt, B. J.; Miller, W. H.; Neumark, D. M. *Journal of Chemical Physics* **1999**, *110*, 3748.

(181) Maslen, P. E.; Faeder, J.; Parson, R. *Chemical Physics Letters* **1996**, *263*, 63.

(182) Batista, V. S.; Zanni, M. T.; Greenblatt, B. J.; Neumark, D. M.; Miller, W. H. *Journal of Chemical Physics* **1999**, *110*, 3736.

(183) Zanni, M. T.; Davis, A. V.; Frischkorn, C.; Elhanine, M.; Neumark, D. M. *Journal of Chemical Physics* **2000**, *112*, 8847.

(184) Ray, D.; Levinger, N. E.; Papanikolas, J. M.; Lineberger, W. C. *Journal of Chemical Physics* **1989**, *91*, 6533.

(185) Papanikolas, J. M.; Gord, J. R.; Levinger, N. E.; Ray, D.; Vorsa, V.; Lineberger, W. C. *Journal of Physical Chemistry* **1991**, *95*, 8028.

(186) Papanikolas, J. M.; Vorsa, V.; Nadal, M. E.; Campagnola, P. J.; Gord, J. R.; Lineberger, W. C. *Journal of Chemical Physics* **1992**, *97*, 7002.

(187) Papanikolas, J. M.; Vorsa, V.; Nadal, M. E.; Campagnola, P. J.; Buchenau, H. K.; Lineberger, W. C. *Journal of Chemical Physics* **1993**, *99*, 8733.

(188) Kliner, D. A. V.; Alfano, J. C.; Barbara, P. F. *Journal of Chemical Physics* **1993**, *98*, 5375.

(189) Walhout, P. K.; Alfano, J. C.; Thakur, K. A. M.; Barbara, P. F. *Journal of Physical Chemistry* **1995**, *99*, 7568.

(190) Vorsa, V.; Campagnola, P. J.; Nandi, S.; Larsson, M.; Lineberger, W. C. *Journal Of Chemical Physics* **1996**, *105*, 2298.

(191) Batista, V. S.; Coker, D. F. *Journal Of Chemical Physics* **1997**, *106*, 7102.

(192) Faeder, J.; Parson, R. *Journal Of Chemical Physics* **1998**, *108*, 3909.

(193) Delaney, N.; Faeder, J.; Parson, R. *Journal of Chemical Physics* **1999**, *111*, 452.

(194) Davis, A. V.; Wester, R.; Bragg, A. E.; Neumark, D. M. *Journal of Chemical Physics* **2003**, *118*, 999.

(195) Mabbs, R.; Pichugin, K.; Sanov, A. *Journal of Chemical Physics* **2005**, *122*, 174305.

(196) Skovsen, E.; Machholm, M.; Ejdrup, T.; Thogersen, J.; Stapelfeldt, H. *Physical Review Letters* **2002**, *89*.

(197) Van Duzor, M.; Wei, J.; Mbaiwa, F.; Mabbs, R. *Journal of Chemical Physics* **2009**, *131*.

(198) Mbaiwa, F.; Wei, J.; Van Duzor, M.; Mabbs, R. *Journal of Chemical Physics* **2010**, *132*.

(199) Nagura, C.; Suda, A.; Kawano, H.; Obara, M.; Midorikawa, K. *Applied Optics* **2002**, *41*, 3735.

(200) Miecznik, G.; Greene, C. H. *Physical Review A* **1996**, *53*, 3247.

(201) Zatsarinny, O.; Bartschat, K. *Physical Review A* **2006**, *73*.

(202) Hlavenka, P.; Otto, R.; Trippel, S.; Mikosch, J.; Weidemuller, M.; Wester, R. *Journal of Chemical Physics* **2009**, *130*.

(203) Branscomb, L. M.; Burch, D. S.; Smith, S. J.; Geltman, S. *Physical Review* **1958**, *111*, 504.

(204) Branscom.Lm; Smith, S. J.; Tisone, G. *Journal of Chemical Physics* **1965**, *43*, 2906.

(205) Gerlach, W.; Stern, O. *Zeitschrift Fur Physik* **1922**, *9*, 353.

(206) Gerlach, W.; Stern, O. *Annalen Der Physik* **1924**, *74*, 673.

(207) Garraway, B. M.; Stenholm, S. *Contemporary Physics* **2002**, *43*, 147.

(208) Garraway, B. M.; Stenholm, S. *Physical Review A* **1999**, *60*, 63.

(209) Freeman, M. R.; Ruf, R. R.; Gambino, R. J. *Ieee Transactions on Magnetics* **1991**, *27*, 4840.

(210) Dehmelt, H. *Proceedings of the National Academy of Sciences of the United States of America* **1986**, *83*, 2291.

(211) Dehmelt, H. *Proceedings of the National Academy of Sciences of the United States of America* **1986**, *83*, 3074.

(212) Dehmelt, H. *Zeitschrift Fur Physik D-Atoms Molecules and Clusters* **1988**, *10*, 127.

(213) Batelaan, H.; Gay, T. J.; Schwendiman, J. J. *Physical Review Letters* **1997**, *79*, 4517.

(214) Rutherford, G. H.; Grobe, R. *Physical Review Letters* **1998**, *81*, 4772.

(215) Nguyen, M. T.; Nguyen, T. L.; Mebel, A. M.; Flammang, R. *Journal of Physical Chemistry A* **2003**, *107*, 5452.

(216) Dixon, D. A.; Feller, D.; Christe, K. O.; Wilson, W. W.; Vij, A.; Vij, V.; Jenkins, H. D. B.; Olson, R. M.; Gordon, M. S. *Journal of the American Chemical Society* **2004**, *126*, 834.

(217) Ichino, T.; Andrews, D. H.; Rathbone, G. J.; Misaizu, F.; Calvi, R. M. D.; Wren, S. W.; Kato, S.; Bierbaum, V. M.; Lineberger, W. C. *Journal of Physical Chemistry B* **2008**, *112*, 545.

(218) Ichino, T.; Wren, S. W.; Vogelhuber, K. M.; Gianola, A. J.; Lineberger, W. C.; Stanton, J. F. *Journal of Chemical Physics* **2008**, *129*.

(219) Gianola, A. J.; Ichino, T.; Hoenigman, R. L.; Kato, S.; Bierbaum, V. M.; Lineberger, W. C. *Journal of Physical Chemistry A* **2004**, *108*, 10326.

(220) Gianola, A. J.; Ichino, T.; Kato, S.; Bierbaum, V. M.; Lineberger, W. C. *Journal of Physical Chemistry A* **2006**, *110*, 8457.

(221) Gianola, A. J.; Ichino, T.; Hoenigman, R. L.; Kato, S.; Bierbaum, V. M.; Lineberger, W. C. *Journal of Physical Chemistry A* **2005**, *109*, 11504.

(222) Vij, A.; Pavlovich, J. G.; Wilson, W. W.; Vij, V.; Christe, K. O. *Angewandte Chemie-International Edition* **2002**, *41*, 3051.

(223) Benin, V.; Kaszynski, P.; Radziszewski, J. G. *Journal of Organic Chemistry* **2002**, *67*, 1354.

(224) Workentin, M. S.; Wagner, B. D.; Negri, F.; Zgierski, M. Z.; Lusztyk, J.; Siebrand, W.; Wayner, D. D. M. *Journal of Physical Chemistry* **1995**, *99*, 94.

(225) Zivanov, S.; Ibanescu, B. C.; Paech, M.; Poffet, M.; Baettig, P.; Sergenton, A. C.; Grimme, S.; Allan, M. *Journal of Physics B-Atomic Molecular and Optical Physics* **2007**, *40*, 101.

(226) Schiedt, J.; Weinkauf, R. *Journal of Chemical Physics* **1999**, *110*, 304.

(227) Ko, Y. J.; Wang, H. P.; Cao, R.; Radisic, D.; Eustis, S. N.; Stokes, S. T.; Lyapustina, S.; Tian, S. X.; Bowen, K. H. *Physical Chemistry Chemical Physics* **2010**, *12*, 3535.

(228) Winter, B.; Weber, R.; Hertel, I. V.; Faubel, M.; Jungwirth, P.; Brown, E. C.; Bradforth, S. E. *Journal of the American Chemical Society* **2005**, *127*, 7203.

(229) Ottosson, N.; Faubel, M.; Bradforth, S. E.; Jungwirth, P.; Winter, B. *Journal of Electron Spectroscopy and Related Phenomena* **2010**, *177*, 60.